Modeling and Parameter Identification for Condition Monitoring of Permanent Magnet Synchronous Machine Drive Systems

by

Fanny A. Pinto Delgado

A dissertation submitted in partial fulfillment
of the requirements for the degree of
Doctor of Philosophy
(Electrical and Computer Engineering)
in The University of Michigan
2021

Doctoral Committee:

Professor Heath Hofmann, Co-chair
Professor Jing Sun, Co-chair
Professor Al-Thaddeus Avestruz
Professor Ian Hiskens
Associate Research Scientist Jason Siegel

Fanny A. Pinto Delgado

fapd@umich.edu

ORCID iD: 0000-0003-3844-358x

To my family,
for all your love and support.

ACKNOWLEDGEMENTS

First of all, I would like to express my gratitude to my advisors, Prof. Heath Hofmann and Prof. Jing Sun, for their support, guidance, and mentorship throughout my graduate studies. It is a great honor for me to work with them. Prof. Hofmann gave me the opportunity to learn so many practical and theoretical aspects of electric machines and drives. Similarly, in addition to teaching me adaptive control, Prof. Sun helped me learn about many other topics during these years. Looking back to when I started the Ph.D., they have given me countless valuable guidance and expertise. I had few rough times during my Ph.D. journey, and I really appreciate their patience, encouragement, and support. I also would like to thank my dissertation committee members, Professor Ian Hiskens, Professor Al-Thaddeus Avestruz, and Dr. Jason Siegel, for their constructive comments and helpful suggestions.

I would also like to thank Kristen Thornton for her advice, help, and reminders for the Ph.D. departmental requirements.

I would like to gratefully and sincerely thank all of my colleagues and friends for their support and friendship. I want to express my special thanks to my labmates: Dr. Yuanying Wang, Dr. Jun Hou, Dr. Ziyou Song, Dr. Abdi Zeynu, and Jake Chung. I am really grateful for working and studying with them, for all those times we spent together in the lab, for all the research advice and discussions, and for all the times we gather for lunch, dinner, and bubble tea. I also want to thank Dr. David Reed for his valuable advice and discussions when starting my doctoral studies. As for my friends in Michigan, I want to express my special thanks to Miriam Figueroa-Santos and Angela Wu, for their support and friendship. In addition, I would like to thank all my friends and classmates here in Michigan: Ahmet Mazacioglu, Bryan Maldonado, Emily Sabo, Leandra Villegas, Ruben Villegas, Kenny Lai, Kishan Srinivasan, and Akshay Sarin. Also, I would like to thank my lifelong friends Lizmari Villegas, Leonardo Villarreal, Andres Lon, Anais Lon, Maria Jose Perdomo, and Valentina Villasmil. While they are very far from Michigan, their support and faith have been valuable to me through this journey.

Finally, I would like to thank my family for all their love and support. Especially,

I would like to thank my parents, Fanny Delgado Ramirez and Nuncio Pinto, for their love and faith in me, support, and encouragement throughout my life.

TABLE OF CONTENTS

LIST OF FIGURES

Figure

LIST OF TABLES

Table

LIST OF ABBREVIATIONS

ADC Analog-to-Digital Converter

CH Current Hexagon

CW Concentrated Winding

DE Dynamic Eccentricity

DW Distributed Winding

EMF Electromotive Force

EMI Electromagnetic Interference

EV Electric Vehicle

FEA Finite Element Analysis

FFT Fast Fourier Transform

FOC Field-Oriented Control

HEVs Hybrid Electric Vehicles

IPM Interior Permanent Magnet

ITS Inter-Turn Short

MCSA Motor Current Signature Analysis

ME Mixed Eccentricity

MEC Magnetic Equivalent Circuit

MF Magnet Function

MMF MagnetoMotive Force

MPC Model Predictive Control

MRE Mean Relative Error

MWF Modified Winding Function

PE Persistency of Excitation

PI Proportional-Integral

PM Permanent Magnet

PMSM Permanent Magnet Synchronous Machine

PWM Pulse Width Modulation

RHAID Receding Horizon Adaptive Input Design

SE Static Eccentricity

SIC Simultaneous Identification and Control

SMPM Surface-Mount Permanent Magnet

STFT Short-Time Fourier Transform

SVH Space Vector Hexagon

SVM Space Vector Modulation

UMP Unbalanced Magnetic Pull

VSI Voltage Source Inverter

ZOH Zero-Order Hold

ABSTRACT

Electric machines can be found in a variety of industrial applications, including renewable energy, transportation, and military systems. Among electric machines, Permanent Magnet Synchronous Machines (PMSMs), such as Surface-Mount Permanent Magnet (SMPM) and Interior Permanent Magnet (IPM) machines, have been preferred for high-performance applications due to their high torque density, high power density, and potential for precise control and high efficiency over a wide operating range. However, PMSMs can experience magnetic, electrical, and mechanical faults, compromising the system performance and safety.

Fault diagnosis and condition monitoring techniques aim to identify abnormal conditions and track the health status during operation. In particular, if the machine's health condition is continuously monitored, faults can be recognized at early stages, and corrective actions can be implemented. Model-based techniques use unusual changes in state variables, parameters, and outputs to monitor the machine's health and determine whether the machine is experiencing a fault. Online parameter identification offers continuous monitoring of health conditions through parameter variation during operation. Moreover, if the parameters have physical meaning, health conditions can be tracked and diagnosed more straightforwardly. However, in some cases, faults and operating conditions might have similar effects on the parameters. Additionally, each fault causes different imbalances in the PMSM dynamics that standard models do not capture. Furthermore, parameter identification has an inherent implementation challenge, since accurate estimation requires persistently exciting inputs which may conflict with control objectives and compromise control performance. This dissertation presents research that seeks to address open issues regarding the application of parameter identification to fault diagnosis and condition monitoring of SMPM machines.

The first part of this dissertation addresses the incorporation of operational constraints into the Simultaneous Identification and Control (SIC) formulation for SMPM machines. Specifically, a SIC methodology that explicitly considers the voltage and current inverter limits for SMPM machines is presented. The current and voltage

constraints are derived by mapping three-phase voltage and current constraints into their two-phase equivalents. These constraints are incorporated into a SIC formulation that consists of an adaptive current regulator and a Receding Horizon Adaptive Input Design (RHAID). The SIC formulation utilizes the quadrature-axis current for torque production, while the direct-axis current is used to inject the excitation required for accurate convergence. The inverter constraints are incorporated in the RHAID, which minimizes losses while maximizing the excitation characteristics of the reference direct current. Accurate torque regulation is performed through the adaptive current regulator. Simulations demonstrate the effectiveness of the SIC formulation on constraint enforcement at different operating conditions.

The rest of this dissertation studies the modeling and parameter identification for fault diagnosis and condition monitoring of SMPM machines. First, lumped-parameter models are formulated to capture the distinctive dynamic features of SMPM machines under demagnetization, eccentricity, and inter-turn short conditions. In addition to the standard model parameters, these parameterizations incorporate parameters that capture specific oscillations produced by the different faults. Based on these models, parameter identification strategies are formulated for detecting demagnetization, eccentricity, and inter-turn short. The inputs are designed to guarantee sufficient conditions for accurate parameter convergence while avoiding control perturbations. Afterward, a parameter identification strategy for comprehensive fault detection is formulated by incorporating the estimators for demagnetization, eccentricity, and inter-turn short into a sole strategy. Simulation and co-simulation results demonstrate the effectiveness of the proposed parameter estimators for recognizing the different fault conditions.

CHAPTER I

Introduction

1.1 Motivation and Overview

Electric machines can be found in a wide range of industrial applications, including renewable energy, transportation, and military systems. The popularity of electric machines has considerably increased over time, as many applications have progressively trended towards "more electric" systems. For instance, aircraft and ships have been moving into the so-called "more electric aircraft" and "all-electric ship" concepts, in which electrical systems are preferred over others (e.g., mechanical, hydraulic, pneumatic), seeking improved efficiency and reliability [2–4]. Similarly, in the auto industry, the trend has been toward Electric Vehicles (EVs) and Hybrid Electric Vehicles (HEVs) through the years, driven by higher fuel costs, environmental concerns, and government mandates [5, 6].

Among all electric machines, Permanent Magnet Synchronous Machines (PMSMs), such as Surface-Mount Permanent Magnet (SMPM) and Interior Permanent Magnet (IPM) machines, have been preferred for high-performance applications due to their high torque density, high power density, and potential for precise control and high efficiency over a wide operating range. For example, PMSMs can be found in industrial robots such as Yamaha's SCARA robots, which are involved in processes that require high precision [7]. Similarly, PMSMs are also employed as part of the thrust reverser in aircraft and the electric propulsion system in HEVs and EVs, in which requirements include high efficiency, reliability, fast response times, and precise regulation [8,9]. In many of these applications, a sudden machine failure can have major effects on the overall system performance and availability. In fact, consequences can go from the interruption of critical services and costly maintenance to even, in some cases, loss of life.

The faults that PMSMs can experience can be classified into magnetic, electrical, and mechanical faults [10], as shown in Fig. 1.1. Magnetic faults are related to Permanent Magnet (PM) demagnetization faults, which can occur due to thermal stress, electrical faults, environmental factors (e.g., oxidation, corrosion), and rotor faults (e.g., damaged/broken rotor magnets) [11]. Electrical faults are associated with stator winding and electric drive faults resulting from overloading, manufacturing defects, high-temperature operation, and transient high voltages. Mechanical faults refer to bearing failure and eccentricity faults caused by metal fatigue, unbalanced stress, improper installation, and environmental factors [12]. All three types of faults compromise the system's performance and safety, as they can result in reduced torque per ampere, increased torque pulsations, increased noise, increased vibrations, unbalanced voltages, unbalanced currents, increased losses, and reduced efficiency [13].

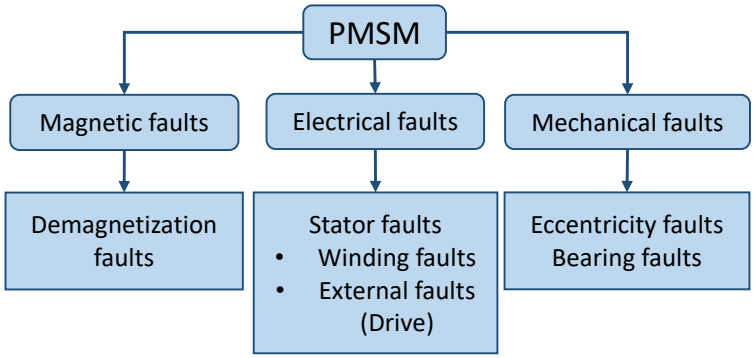

Figure 1.1: Fault categories for PMSMs.

Fault diagnosis and condition monitoring techniques aim to recognize abnormal conditions and track the health status during operation [14]. By continuously monitoring the machine's health condition, machine faults can be detected at their early stages, and corrective steps can be taken before the fault is fully developed. The maintenance of electric machines can be performed using breakdown-, fixed-time interval-, and condition-based strategies [15]. In many of the electric motor-driven applications mentioned above, breakdown maintenance (i.e., "run it until it breaks then replace it" rule) is not an option since machine failure compromises the entire system's operability [15]. In fixed-time interval-based maintenance, the machine has scheduled maintenance at fixed time periods. However, planned maintenance might be ineffective, as some components might not have a predictable time to failure. With health monitoring, machine maintenance can be carried out in a condition-based manner, allowing better outage scheduling with lower downtime and replacement costs [15].

Moreover, while the machine is still in operation, the control strategy can use the health information to adapt its strategy to continue operation and maintain performance while minimizing further machine damage [16–18].

The problem of diagnosing and monitoring the PMSM's health has been widely studied, and comprehensive reviews are presented in [11, 12, 19, 20]. In the literature, fault diagnosis and condition monitoring strategies have been proposed based on measured signals and dynamic models [14]. In signal-based techniques, particular features (e.g., mean values, frequencies) from the measured signals, such as current [21–30], voltage [22, 31–34], flux [35, 36], torque [17, 26], and vibrations [30, 37, 38], are extracted and compared against a preset combination, a.k.a. signal signature, which relates to the fault. The Fast Fourier Transform (FFT), Short-Time Fourier Transform (STFT), wavelet transform, and Cohen-class-based time-frequency analysis are some of the methods that have been used to extract the fault features [20]. The main drawback of signal-based techniques is the computational burden associated with the processing techniques for applications in which the motor operates under non-stationary conditions [39]. Moreover, in some cases, additional sensors are required to implement the fault diagnosis and condition monitoring strategies. The Motor Current Signature Analysis (MCSA) has been the most popular in practical applications among all signal-based techniques since it provides continuous monitoring without additional sensors [39]. However, the currents may be easily affected by current control loops in electric drive systems, and, hence, the effects of faults on the currents can be distorted and diminished [29]. Moreover, the current frequency spectrum under partial PM demagnetization, eccentricity, and supply/load unbalance have similar sideband frequency patterns, complicating fault classification [39, 40].

In model-based techniques, unusual changes in state variables, model parameters, and outputs are used to monitor the machine's health and determine whether the machine is experiencing a fault [39–48]. In order to ensure the robustness and reliability of these model-based fault diagnosis and condition monitoring approaches, model uncertainties and parameter variations have to be considered [47]. The disadvantages of model-based techniques include the requirement for knowledge regarding machine parameters and different models for each fault. Precisely, each fault causes different unbalanced dynamics which standard machine models do not capture. Among all model-based strategies, online parameter identification offers continuous monitoring of health conditions through parameter variations during operation. The main advantage of using online parameter identification is that health conditions can be tracked and diagnosed more straightforwardly if the parameters have physical meaning [14].

However, fault diagnosis and condition monitoring through parameter identification require a way to distinguish the root cause of the variation, as faults and operating conditions might affect the parameters similarly in some cases. Under normal operation, the parameters of PMSMs can vary due to temperature, skin effect, and magnetic saturation [49]. Additionally, parameter identification-based strategies face the challenge that each fault causes different imbalances in the PMSM, and standard models do not hold anymore. Researchers have proposed parameter identification-based fault diagnosis and condition monitoring strategies for PMSMs based on model parameterizations that capture healthy [40–46] and faulty [40, 48] operating conditions. In healthy-model-based strategies [40–46], fault diagnosis is still challenging as parameters can also be affected by operating conditions. Regarding strategies based on models for faulty conditions [40, 48], their application is limited to a particular fault.

Besides the aforementioned difficulties, parameter identification has an intrinsic implementation challenge as it requires persistently exciting inputs for estimation accuracy, which may conflict with control objectives and, therefore, compromise control performance. The control objectives typically involve tracking a set-point or trajectory, which does not necessarily produce persistently exciting inputs [50]. This trade-off between parameter identification and control for PMSMs has been addressed in the literature by exploiting actuation redundancy [50–53]. Specifically, in [50–53], the excitation required for accurate parameter estimation was constrained to the "null-space" so that sufficiently rich signals are injected without affecting the output regulation. Regarding parameter identification-based condition monitoring and fault diagnosis strategies, the inclusion of Simultaneous Identification and Control (SIC) methodologies, such as [50–53], ensures active monitoring and detection without control perturbations.

In this dissertation, we present research that seeks to address open issues regarding the application of parameter identification to fault diagnosis and condition monitoring of PMSMs. The first part of this dissertation investigates the incorporation of operational constraints to the SIC problem. Precisely, the proposed SIC methodology consists of an adaptive current regulator, which achieves accurate torque regulation, and an optimization-based adaptive input design, which determines the reference current trajectories that minimize losses and maximize excitation characteristics while considering the inverter's voltage and current limits. The rest of this dissertation covers research that studies the application of parameter identification for fault diagnosis and condition monitoring through modeling, analysis, and simulation. More

specifically, models and parameter identification strategies are developed for SMPM machines under demagnetization, eccentricity, and Inter-Turn Short (ITS) conditions. The models are devised to capture the essential dynamic behavior of SMPM machines under different faults. Based on these models, fault-related parameters are defined, and new parameterizations are formulated for parameter identification. Note that the inputs are designed for SIC. Thus, sufficient conditions for accurate parameter convergence are actively guaranteed while minimizing disturbances in the control performance.

1.2 Background

1.2.1 Background on PMSMs under Fault Conditions

As mention in Section 1.1, PMSMs can experience a variety of faults. In this dissertation, the fault conditions of interest are PM demagnetization, rotor eccentricity, and ITS in the stator windings. This section briefly describes these three PMSM fault conditions, including their causes and consequences as well as their detection, monitoring, and mitigation strategies in the existing literature.

1.2.1.1 Permanent Magnet (PM) Demagnetization Condition

Demagnetization refers to the irreversible reduction of the flux linkage produced by a PM. In an electric machine, the PMs are susceptible to irreversible demagnetization when exposed to thermal stresses, electrical faults (e.g., demagnetizing fields produced by large currents in an ITS), environmental factors (e.g., oxidation, corrosion), and unbalanced loads [54]. In the event that the PMs are irreversibly demagnetized, their flux decreases and, in some cases, becomes unbalanced, causing significant vibration and noise as well as overall performance deterioration [54, 55].

Fig. 1.2 illustrates how external demagnetizing currents and the magnet's temperature can affect a magnet's B-H curve. Note that, in Fig. 1.2, only the second quadrant of the B-H curve is shown as it is the most important one for understanding the demagnetization process. The second quadrant of the B-H curve for different materials can be found in [56]. Modern materials, such as neodymium (NdFeB) [19, 57, 58], have a linear demagnetization curve that sharply drops once approaching the knee point (H_k), as the one presented in Fig. 1.2(a). In a PMSM, the magnet's operating point corresponds to the intersection between the load line and the B-H curve. While the magnet's operating point stays within the linear region, the demagnetization is

reversible. However, if the magnet's operating point goes beyond the knee point (H_k), the magnet is irreversibly demagnetized, as it will follow another recoil line in which the remanent flux density (B_{rr}) is smaller than the original (B_r). Regarding the effect of temperature on a magnet's B-H curve, increased temperatures facilitate demagnetization since a lower field intensity is required to reach the knee point [19, 57, 58], as shown in Fig. 1.2(b).

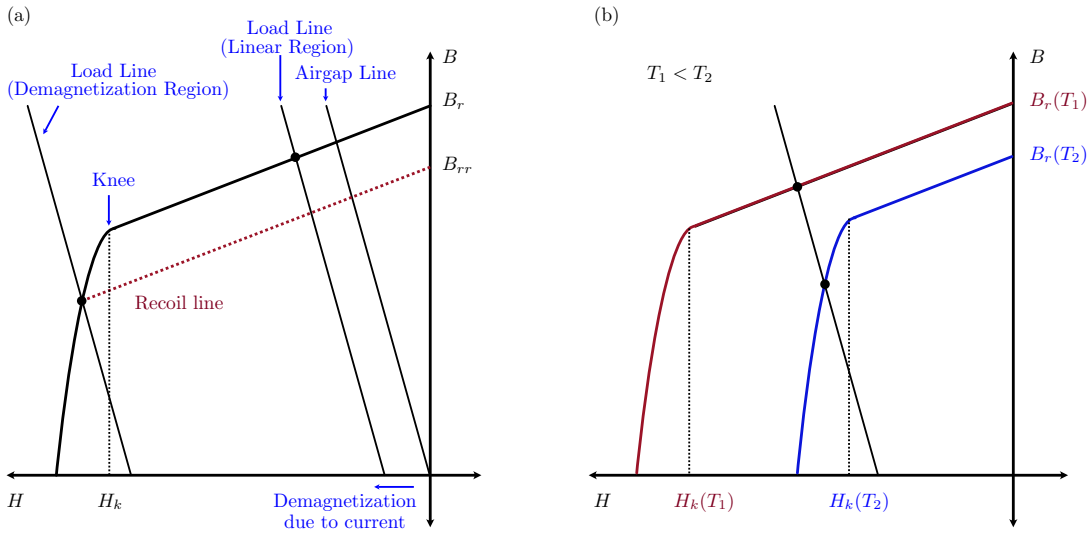

Figure 1.2: Second Quadrant of magnet's B-H curve: (a) effect of demagnetizing current, and (b) effect of temperature.

For PMSMs, demagnetization can occur evenly or unevenly in all magnets or specific ones, and, hence the dynamic response can be affected in different ways. When all magnets are evenly demagnetized, the PM flux reduces and, therefore, the torque for a given current decreases. However, no additional harmonics are expected since the rotor flux remains balanced. In the case that the magnets are unevenly demagnetized, the PM flux linkage becomes unbalanced. As a result, in addition to a decreasing torque for a given current, the system experiences additional noise and vibrations caused by the added harmonics in the rotor flux. A variety of studies have been conducted for the detection of PM demagnetization at an early stage so that performance degradation, maintenance and downtime costs, and safety hazards can be avoided [17, 19, 21, 31, 32, 35, 41–46, 54, 55, 58–67]. In the literature, researchers have studied the demagnetization mechanism [19, 54], established models for PMSMs under magnet demagnetization [58–64], and proposed condition monitoring and fault diagnosis techniques [17, 21, 31, 32, 35, 40–46, 64–67].

Regarding modeling, a comprehensive literature review on PMSMs with PM de-

magnetization can be found in [19]. Several approaches for modeling PM demagnetization have been proposed such as Finite Element Analysis (FEA) models [58], Magnetic Equivalent Circuit (MEC) models [59, 60], and lumped-parameter models [61]. The authors of [58] proposed a linear model that handles the demagnetization curve and temperature dependence of demagnetization to be used as part of the FEA simulation model of PMSMs. In [60], a MEC model was formulated and employed to investigate the impact of the motor topology on magnet defect fault signatures. Specifically, the authors studied frequency-based fault signatures on the stator Electromotive Force (EMF) and current waveforms. A three-phase lumped-parameter model for SMPM machines, in which the back-EMF captures the spatial disposition of the windings and magnets, was presented in [61].

The problem of diagnosing and monitoring the PMSM's magnet health has been widely investigated, and a comprehensive review is presented in [65]. Specific features from measured signals such as current [21], voltage [31–34], flux [35], and torque [17], have been extracted and compared against a signal signature, that is expected to correspond to PM demagnetization. In [31,32], the zero-sequence voltage component was used for online monitoring of the PMs. In [35], search coils were installed to measure the magnetic flux around the stator, and the fundamental frequency component from the measured voltages was utilized for detecting demagnetization, winding short circuit, and eccentricities. The authors of [17] proposed an online PM demagnetization fault detection strategy for IPM machines based on the torque ripple discrepancy.

In terms of model-based approaches, unusual variations in model parameters have been used to determine that the machine has a fault [41–46]. In [41], the authors proposed a demagnetization fault diagnosis strategy for IPM machines using the direct- and quadrature-axis inductances estimated from a MEC model. In [40,42,43], the authors detected rotor faults in an SMPM machine by estimating the direct-axis PM flux linkage in the rotor reference frame. However, their estimators require known stator resistance and inductances, which might affect accuracy. In [44, 45], the authors proposed parameter estimators for stator resistance and PM flux linkage monitoring based on adaline neural networks. The authors of [46] proposed a PM flux-linkage estimator based on a speed harmonic model and harmonic current injection. In [44–46], the tracking performance of the parameter estimators was validated using a healthy PMSM, as abnormal parameter deviations can indicate faults. However, for these parameter estimators, the tracking performance under magnet demagnetization was not presented.

1.2.1.2 Eccentricity Condition

When the rotor and stator are misaligned, the motor operates under eccentricity condition. Some of the causes include inaccurate manufacturing, improper alignment of the rotor or stator during commisioning, and bearing wear or misalignment. Under eccentricity conditions, the airgap between the stator and the rotor is nonuniform, causing vibrations and unbalanced magnetic forces commonly known as Unbalanced Magnetic Pull (UMP). These undesired vibrations and UMP produce additional mechanical stress in the machine and can result in performance degradation as well as reduced operating lifetime. Moreover, if the machine experiences severe eccentricity, the rotor and stator can potentially rub, leading to severe damages [36].

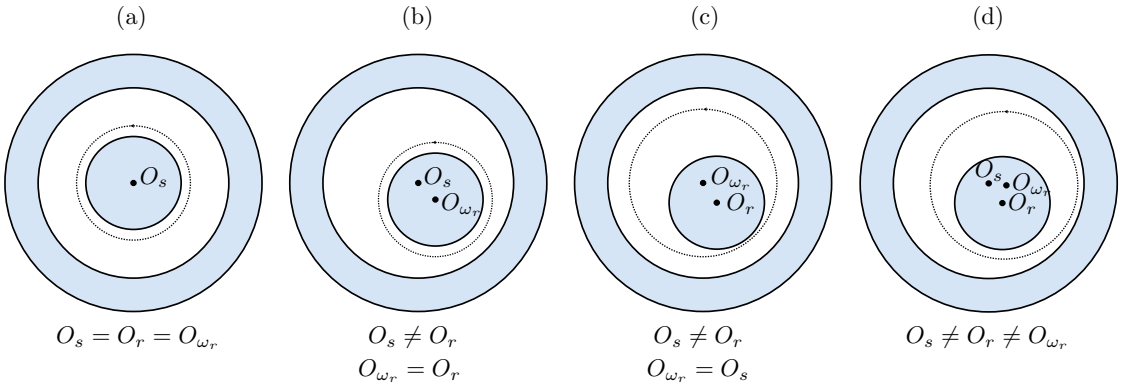

Figure 1.3: Center of the stator, rotor, and rotation under: (a) healthy, (b) static eccentricity, (c) dynamic eccentricity, and (d) mixed eccentricity conditions.

As shown in Fig. 1.3, a machine can experience three types of eccentricity: static, dynamic, and mixed eccentricity. The type of eccentricity that the machine experiences depends on whether the center of the stator, the center of the rotor, and the center of rotation coincide. Note that, in Fig. 1.3, the center of stator, rotor, and rotation are denoted by O_s, O_r, and O_{ω_r}, respectively. In a healthy machine (Fig. 1.3(a)), all three centers coincide. However, when the machine is under Static Eccentricity (SE) (Fig. 1.3(b)), the center of the rotor and rotation coincide, but they are off from the center of the stator. Similarly, when the machine experiences Dynamic Eccentricity (DE)(Fig. 1.3(c)), the center of the stator is the same as the center of rotation; however, they differ from the center of the rotor. Mixed Eccentricity (ME) occurs when the machine experiences both static and dynamic eccentricities in which case none of the three centers coincide as shown in Fig. 1.3(d). Note that, in practice, even newly manufactured motors have some level of ME due to the inherent

tolerances in the manufacturing and assembling processes.

In the literature, researchers have analyzed the performance [26], established models [23, 26, 68–70], and proposed condition monitoring and fault diagnosis techniques for PMSMs under eccentricity [23–26, 33, 35–40]. The dynamic response of PMSMs under eccentricity has been capture through FEA models [25, 26], MEC models [68], and lumped-parameter models [23,69,70]. In [25,26], a PMSM under SE, DE, and ME was modeled using a time stepping finite element method, including the non-uniform permeance of the air gap and nonlinear characteristics of the magnet material. In [68], a MEC model with saturation was proposed for an IPM machine under SE. The authors of [70] presented a lumped-parameter model for radial force and torque based on permeance functions. In the two-phase equivalent model from [69], the effect of SE on a line-start PMSM was captured using Modified Winding Function (MWF) theory for the inductance calculations; however, the eccentricity effect on the PM flux linkages was neglected. In [23], the authors proposed a model for the PMSMs electric dynamics in which they modeled the PMs as fictitious coils and captured the effects of eccentricity on the inductances by using MWF theory.

Detection of eccentricity is currently done using online and offline approaches. In terms of signal-based methodologies, specific features from signals, including current [23–26], voltage [33, 34], flux [35, 36], vibrations [37, 38], and torque [26] have been used for monitoring and detecting eccentrities. The effects of SE, DE, and ME on the stator current spectrum for PMSMs were studied in [23–26]. In [24], the configuration impacts (i.e., SMPM and IPM) on eccentricity fault detection through a particular current frequency pattern were studied. The type and degree of eccentricity were predicted in [25] using support vector machine as a classifier. In [33], the change in the commanded d- and q-axis voltages were used for fault detection and separation of PMSMs under steady-state conditions for SE, demagnetization, and ITS. The authors of [34] proposed a detection and identification method for IPM machines under demagnetization, ITS, and SE based on the variation in the load angle. In [36], the authors proposed an online detection strategy for PMSM under SE, DE, and ME based on analog hall-effect field sensors. Radial force and UMP under static and dynamic eccentricities were studied in [38] for vibration-based monitoring.

In terms of model-based approaches, unusual variations in model parameters have been used to determine that the machine is under eccentricity fault [39, 40]. The author from [39] proposed a standstill detection method for IPM machines using the equivalent d-axis inductance as the indicator. In [40], the authors proposed an online detection method for IPM machines for diagnosing and distinguishing between ec-

centricity and partial demagnetization based on the high-frequency d-axis inductance and rotor flux. In this methodology, inductance variations are used for eccentricity detection, and the d-axis inductance and rotor flux are estimated by injecting a high-frequency voltage in the d-axis and assuming a known resistance value.

1.2.1.3 Inter-Turn Short (ITS) Condition

An ITS refers to insulation failure between contiguous turns in a winding. The insulation gradually deteriorates as part of the motor's natural aging process; however, its wear and tear can be exacerbated due to overloads, manufacturing defects, thermal stresses, voltage stresses, and vibration-caused rubbing [20]. If not detected, the ITS rapidly spreads and escalates up to a phase-to-phase or phase-to-ground short circuit. Moreover, in PMSMs, stator short-circuit faults are particularly dangerous since this fault can produce a magnetic field intensity that can irreversibly demagnetize the magnets [20].

The coil insulation gradually loses its insulating characteristics and is usually modeled with an additional resistance shorting the affected turns [16, 71–73]. The decrease in the insulation-failure resistance indicates the degradation of the insulation material. Note that an insulation-failure resistance equal to zero corresponds to a perfect short, which is never reached in practice by an ITS [71]. A variety of studies including the effects of this insulation-failure resistance on the fault severity [16], modeling of PMSMs under ITS [16, 71–76], and condition monitoring and fault diagnosis techniques [27–30, 30, 33–35, 47, 48] have been conducted. A comprehensive literature review with the recent advances in modeling and online detection strategies for stator ITS can be found in [20]. Similarly, in [77], a review on ITS indexes based on current, voltage, torque, flux, and other electrical signals for PMSMs is presented.

Numerous works on modeling PMSMs under ITS have been proposed including FEA models [74], MEC models [75], and lumped parameter models [16, 71–73, 76]. Using Ansys Maxwell, Ansys Simplorer, and Simulink, the authors of [74] simulated a PMSM as part of an electric drive under ITS condition with FEA by reducing the number of turns in a phase. In [16], the authors presented an FEA-based equivalent model, in which the shorted turns are modeled as a separate winding. In [72], a dynamic model for PMSMs with an ITS fault that takes into account the fault percentage and the number of poles is proposed. The authors of [73] proposed a two-phase equivalent parametric model for SMPM machines in the rotor reference frame in which the spatial harmonics are taken into account. Dynamic models for SMPM and IPM machines under ITS condition by separating the dynamics into the positive

and negative sequences were proposed in [71, 76]. Specifically, in [76], a two-phase equivalent model for IPM machine under ITS is formulated in the positive and negative sequence synchronous reference frames while taking into account the windings' series-parallel connections.

In terms of detection and monitoring strategies for ITS conditions, signal-based methodologies employed specific features from measured signals, such as current [27–30], voltage [33, 34], flux [35], and vibrations [30]. The authors of [27] proposed a current-based detection methodology using the Extended Park's Vector approach, in which the ITS signature is the ratio between the component at twice the fundamental frequency and the one at the fundamental frequency. In [29], the authors proposed an ITS indicator based on the difference between the stator currents' fundamental component and a frequency-tracking algorithm to extract it. In [34], a detection and identification method for demagnetization, ITS, and SE in IPM machines was proposed based on the variation in the voltage angle. The authors of [30] proposed an ITS detection strategy based on both stator current and vibration signals using an improved wavelet package transform.

Regarding model-based approaches, unusual variations in state variables and model parameters have been used to determine whether the machine is experiencing an ITS [47, 48]. The authors of [47] proposed the ITS detection through a residual current vector given by the difference between the measured stator currents and the ones estimated by a state observer. In [48], the authors proposed an online parameter estimator to determine the healthy turns ratio based on a searching algorithm with the dynamic model from [76], assuming a perfect short.

1.2.2 Research Gaps

This research aims to address the application of parameter identification to fault diagnosis and condition monitoring of PMSMs through modeling, analysis, and simulation. In the literature, researchers have proposed parameter identification-based condition monitoring and fault detection strategies for PMSMs [40, 42–46, 48]; however, the existing literature solely focuses on estimating particular parameters to detect specific faults, which limits the fault-related information. This dissertation seeks to formulate comprehensive condition monitoring and fault detection methodologies of PMSMs based on simultaneous identification and control. Specifically, the goal is to develop methodologies for detecting different faults using a multi-parameter identification approach without compromising the control performance. The issues that will be addressed in this dissertation are summarized as follows:

1.2.2.1 Lumped-parameter models for analysis and fault-detection design of SMPM machines under fault conditions

Several models that capture the SMPM machine response under fault conditions have been proposed in the literature. However, the application of these models to parameter identification is not straightforward. Mathematical models provide the platform to investigate a system response under fault conditions while avoiding the costs and difficulties associated with replicating faults through special experimental setups. Models can be utilized to design, analyze, and validate fault diagnosis and condition monitoring techniques. As mentioned earlier, several approaches for modeling PMSMs under fault conditions have been proposed, including FEA, MEC, and lumped-parameter models. FEA models are preferred in terms of accuracy; however, they are computationally expensive. MEC models are more computationally efficient than FEA models and reasonably accurate, yet their computational cost can still be significant for real-time applications. Both FEA and MEC can be classified as detailed models and are typically adopted for performance verification [78]. While lumped-parameter models are not as accurate as FEA and MEC models, they are simple, which can be advantageous in terms of conceptual understanding. Moreover, lumped-parameter models are compact and can be used to design real-time fault detection and condition monitoring techniques. To this end, in this dissertation, we focus on the application of lumped-parameter models to condition monitoring and fault diagnosis.

Several lumped-parameter models for PMSMs under fault conditions have been proposed, including three-phase models [16, 23, 61], two-phase equivalent models in the stationary reference frame [72], two-phase equivalent models in the rotor reference frame [69, 70, 73], and two-phase equivalent models in the positive and negative sequence synchronous reference frames [71, 76]. While the machine model can be expressed in any of these equivalent forms, some models have advantages over the others. Three-phase models capture the behavior of the physical PMSMs, and, hence, faults can be easily incorporated. However, three-phase models are not straightforward in terms of analysis and control, and equivalent two-phase models are preferred, given their conceptual advantages. Moreover, the equivalent two-phase model representation in certain rotating reference frames is often more beneficial.

Under normal conditions, the standard machine model typically used for control design is the two-phase model in the rotor reference frame. In this standard machine model, the two-phase variables become constant under steady-state conditions, and parameters are constant. Unfortunately, under fault conditions, the machine becomes

unbalanced, and the standard model is no longer valid. Still, representing the dynamics under fault conditions using the equivalent two-phase model in the rotor reference frame is favorable. In this equivalent representation, the lack of symmetry caused by the fault corresponds to additional frequency dynamics distinguished from the healthy constant dynamics under steady-state. Moreover, if the equivalent two-phase model in the rotor reference frame is used for model-based condition monitoring and fault detection, the standard model is the baseline.

Researchers have proposed explicit equivalent two-phase models in the rotor reference frame for eccentricity and ITS in the literature [69, 73]. In terms of eccentricity, a two-phase equivalent model for a line-start PMSM under SE in the rotor reference frame is proposed [69]. However, the effect of SE on a line-start PMSM was solely captured in the inductances, neglecting its additional effect on the PM flux linkages. Regarding ITS condition, a two-phase equivalent parametric model for SMPM machines in the rotor reference frame in which the spatial harmonics are taken into account was proposed in [73]. However, the complexity of this model hinders its application to fault-detection strategies. While existing literature proposed equivalent two-phase models of PMSMs for fault conditions in the rotor reference frame, its application for condition monitoring and fault detection strategies requires further parameterization efforts. In other words, in the literature, the models do not have an appropriate parameterization for a straightforward formulation of multi-parameter identification strategies. In particular, the literature lacks simple parameterizations, in which specific parameters are formulated to capture the dynamic asymmetries caused by the faults. These simple parameterizations are crucial for implementing parameter identification-based fault detection, as the proposed parameters will carry physical meaning. The literature also lacks an explicit equivalent two-phase model for PMSMs under PM demagnetization.

1.2.2.2 Model parameterization and estimator formulation for fault detection and condition monitoring of SMPM machines

While online parameter identification is a mature field of study, its application to fault detection and condition monitoring of SMPM machines still has work to be done. Although there is previous work on this topic, most methodologies are limited to one fault [48] or are sensitive to parameter variations due to operating conditions [40, 42–46]. Hence, the existing literature provides limited information for fault diagnosis and condition monitoring.

The decrease in PM flux linkage has been used to detect demagnetization [40, 42–

46]; however, its value also reduces with increased temperature, which could lead to false positives. In [40], in addition to using the rotor flux for detecting demagnetization, estimation of the high-frequency d-axis inductance is used for eccentricity detection. However, the high-frequency d-axis inductance is extracted from a frequency spectrum analysis, which can be computationally expensive for variable-speed applications. In [48], the healthy (unshortened) turns ratio for the winding affected by ITS is estimated based on a searching algorithm with the dynamic model from [76], assuming a perfect short. Unfortunately, the application of this online fault parameter estimator is solely for detecting ITS. While the existing literature applies parameter identification to condition monitoring and fault diagnosis, they focus on a small subset of parameters, and, therefore, the fault-related information is limited. Increasing the number of estimated parameters and, hence, the fault-related information contributes to systematic and comprehensive monitoring and detection. Moreover, the integration of parameters that characterize the machine under healthy and faulty operation allows tracking and separating parameter variations due to operating conditions and faults. By including SIC, accurate parameter identification is guaranteed without compromising the control objectives, which have not been incorporated in previous condition monitoring and fault detection strategies.

1.2.3 Incorporation of operational constraints to SIC methodologies for PMSMs

Researchers have proposed SIC strategies in which the over-actuated nature of the PMSM is exploited to achieve identification and control objectives without compromise [50–53]. In [51], a robust adaptive torque controller for SMPM machines was proposed. The persistently exciting signals required for accurate parameter convergence were injected through the direct-axis current to avoid undesired ripple in the generated torque. In [50], a Lyapunov-based adaptive controller for PMSMs was designed to take advantage of over-actuation and simultaneously achieve parameter identification and torque regulation. The authors from [52] proposed an optimization-based SIC formulation for PMSM. A receding horizon control allocation was used to determine the reference current trajectories fed into an adaptive current regulator. The optimization included a metric that maximized the excitation characteristics of the reference currents, based on the Fisher information matrix. To the best of the author's knowledge, no previous work on SIC of PMSMs has accurately characterized operational limits and address them through control formulation and implementation.

1.3 Contributions

This research aims to address the application of parameter identification for comprehensive fault diagnosis and condition monitoring of PMSMs. Although condition monitoring and fault detection strategies for PMSMs through parameter identification have been investigated in the past, this is the first attempt to develop methodologies for detecting different faults while balancing parameter identification and control performance. In this sense, this work presents methodologies that exploit the system's model structure and self-excitation properties to achieve accurate identification while avoiding undesired effects on the control performance. First, parametric models are derived for SMPM machines under different fault conditions. These models seek to capture the essential SMPM machine behavior under the different faults and include parameters that capture the fault imbalances. Afterward, based on these models, parameter estimators are formulated for monitoring and detecting the different faults. The inputs are designed to guarantee sufficient conditions for accurate parameter identification without affecting the control performance. After investigating the different faults separately, a parameter estimator is proposed that establishes a more systematic and comprehensive fault diagnosis and condition monitoring strategy. Specifically, this comprehensive parameter estimator is formulated by incorporating all the previous parameter estimators into one strategy. The main contributions of this research are summarized in the following:

- *Procedures to create equivalent two-phase SMPM machine models in the rotor reference frame with fault-related parameters for parameter identification-based fault diagnosis and condition monitoring strategies [79]:* This dissertation presents procedures to create equivalent two-phase models in the rotor reference frame for SMPM machines with fault-related parameters for monitoring and detecting demagnetization, eccentricity, and inter-turn short conditions through parameter identification. The two-phase equivalent models are formulated for a four-pole three-phase SMPM machine with two coils per phase. However, the procedures can be applied to analyze other SMPM machines with different winding configurations and numbers of poles. The models assume that the machine has a smooth air gap, is balanced in construction, and is connected in an ungrounded-wye configuration. In addition, the models are derived assuming linear magnetics since magnetic saturation, eddy current, and hysteresis effect are neglected. In terms of materials, the models assume that stator and rotor irons have infinite permeability while the magnets and air have equal permeabil-

ity. The derivations start with the formulation of the physical SMPM machine model under the different fault conditions, as it is easier to incorporate the faults. Afterward, these models are mapped into the rotor reference frame using the Clarke and Park transforms. FEA simulations are used to calibrate and validate these models. These equivalent two-phase models are used to formulate new models for parameter identification that capture the "essential" behavior of SMPM machines under demagnetization, eccentricity, and inter-turn short conditions. Specifically, the distinctive dynamic features generated by the different faults are identified and further parameterized for parameter identification-based fault diagnosis and condition monitoring strategies. Expressly, in addition to the standard model parameters, these parameterizations include parameters that capture the specific oscillations produced by demagnetization, eccentricity, and inter-turn short. Under demagnetization, the fault-related parameter is the asymmetry term that captures the oscillation at three times the electrical rotor speed caused by uneven demagnetization between the north and south PM flux linkages. Similarly, under eccentricity, the fault-related parameters capture the oscillation at the rotor speed in the magnetic parameters caused by the ME air-gap asymmetry. Under ITS, the fault-related parameters are meant to capture the oscillations at twice the electrical rotor speed in the magnetic parameters due to the ITS. Note that the model for ITS is approximate since the current flowing through the shorted turns in the ITS coil is unknown. As will be seen, these equivalent two-phase models with fault-specific parameters can be easily leveraged for fault diagnosis and condition monitoring as the fault-related parameters become non-zero under the specific faults.

- *Formulation of parameter identification strategies for fault diagnosis and condition monitoring of SMPM machines based on proposed two-phase SMPM machine models [79]:* Parameter identification strategies have been formulated for monitoring and detecting demagnetization, eccentricity, and inter-turn short. Specifically, these parameter estimators are formulated based on the previously mentioned parameterizations, which include fault-related parameters. Through PE analysis, the inputs are designed to guarantee sufficient conditions for accurate parameter convergence while avoiding control perturbations. As will be seen, the dynamics associated with the fault-related parameters are self-exciting. Note that self-excitation is particularly convenient for the input design since it contributes to the PE property. Simulation and co-simulation results demonstrate the effectiveness of the proposed parameter estimators for monitoring

and detecting the different fault conditions. The results include a parameter estimator based on the standard SMPM machine model since it is used as a baseline. Compared to the parameter estimator based on the standard model, the proposed estimator offers additional fault-related information. While using the standard model parameters is problematic as their value is affected by operating conditions, the fundamental component of the different fault-related parameters is non-zero solely when the specific fault occurs. Moreover, the gradual deviation from zero in the fault-related parameters is directly linked to the progressive increase in the fault condition, advantageous for fault diagnosis and condition monitoring.

- *A comprehensive parameter identification strategy for fault diagnosis and condition monitoring of SMPM machines under different faults:* By combining all the models developed for the different faults, a multi-parameter estimator is proposed seeking a more systematic and comprehensive fault diagnosis and condition monitoring strategy. Co-simulation results assess the monitoring and detection capabilities of the proposed strategy under different conditions. The results include single- and combined-fault conditions. A discussion on the fault-related information under each condition is presented, including remarks on cases with limited diagnosis.

- *A simultaneous identification and torque control methodology for SMPM machines, including inverter current and voltage constraints* [80]: This dissertation will present an optimization-based SIC formulation for SMPM machines that explicitly considers the voltage and current inverter limits. The formulation exploits over-actuation to fix control allocation. Specifically, persistency of excitation and torque regulation are achieved through the direct- and quadrature-axis currents, respectively. An optimization-based adaptive input design determines the reference direct-axis current trajectories that minimize losses and maximize the excitation characteristics while considering the voltage and current limitations. The reference currents are fed in an adaptive current regulator for torque control. Numerical simulations demonstrate the constraint enforcement capability of the methodology.

1.4 Outline

The dissertation is organized as follows:

In Chapter II, the fundamentals of electric machines and drives, as well as parameter identification theory, are presented. First, the theory regarding electric machines and drives is discussed. Next, the reference frame transformations used for the analysis of electric machines and drives are presented. Then, the basic theory for modeling and analyzing SMPM machines, including flux-linkage/current relationships, stator voltage, and torque equations, is discussed. Afterward, relevant theory of voltage source inverters for AC motor control is presented, followed by theory on control of AC machines and, specifically, SMPM machine drive systems. Finally, following the electric machine and drives, the basics behind online parameter identification and SIC methodologies are discussed.

In Chapter III, a SIC formulation for SMPM machines with voltage and current inverter limits is presented. The SMPM machine dynamic model is first presented and followed by the control objectives. Next, the current and voltage inverter constraints are formulated for an ideal voltage source inverter. Afterward, the control algorithm, which consists of an adaptive current regulator and an optimization-based adaptive input design, is presented. Finally, simulations demonstrate the SIC formulation capabilities in terms of performance and constraint enforcement under different operating conditions.

In Chapter IV, the modeling and identification for fault diagnosis and condition monitoring of SMPM machines under demagnetization conditions are studied. Specifically, an equivalent two-phase model and an online parameter identification strategy for a three-phase four-pole SMPM machine with two windings per phase under the magnet demagnetization are presented. First, the equivalent two-phase model is formulated by superimposing the flux produced by the individual magnets. Then, FEA simulations are used to calibrate and validate the model for two SMPM machine designs. Afterward, the parameter identification strategy for monitoring and detecting demagnetization is formulated, including the linear parameterization, parameter identification algorithm, and Persistency of Excitation (PE) analysis. In this section, details on a parameter estimator based on the standard SMPM model are also presented, as it will be used as a baseline. Later, the effectiveness of both parameter estimators for monitoring and detecting demagnetization is assessed by numerical simulations and co-simulation. Finally, fault-related information that can be extracted from these estimators is discussed.

Chapter V investigates the modeling and identification for condition monitoring of SMPM machines under eccentricity conditions. An equivalent two-phase parametric model and an online parameter identification technique for monitoring SMPM ma-

chines under eccentricity are presented for a three-phase four-pole SMPM machine with two windings per phase. First, the equivalent two-phase dynamics under eccentricity are formulated by modeling the expressions for the inductances and PM flux linkages using MWF and Magnet Function (MF) theories. Then, FEA simulations are used to calibrate and validate the model's magnetic parameters for an SMPM machine design. Following the modeling section, the parameter identification strategy for monitoring and detecting eccentricity is formulated, including the parametric model and sufficient conditions for accurate convergence. Afterward, the performance of the proposed estimator and the standard-model-based parameter estimator from Chapter IV are assessed through simulations and co-simulations. For both estimators, the specific information for monitoring and detecting eccentricity conditions is discussed. This chapter ends with a discussion on the SMPM machine design limitations for detecting eccentricity.

In Chapter VI, the modeling and identification for condition monitoring of SMPM machines under ITS conditions are studied. Specifically, an equivalent two-phase model and an online parameter identification strategy for a three-phase four-pole SMPM machine with two windings in series per phase under the ITS are presented. First, an equivalent two-phase parametric model is formulated by modeling the different coils separately and integrating them into the different phases based on the winding connections. Afterward, the model's magnetic parameters are calibrated and validated against FEA simulations for an SMPM machine design. Then, the formulation of the parameter identification strategy for monitoring and detecting ITS is presented. Simulation and co-simulation results prove the effectiveness of the proposed parameter identification strategy over the standard-model-based estimator presented in Chapter IV for monitoring and detecting ITS. Finally, remarks on the parameters suitable for monitoring and detecting ITS are discussed.

Chapter VII investigates the application of parameter identification to fault diagnosis and condition monitoring of SMPM machines under demagnetization, eccentricity, and ITS. An approach based on parameter identification is presented for monitoring and detecting the different faults. A parameter estimator is formulated by combining the parameter estimators for demagnetization, eccentricity, and ITS. Co-simulations are employed to assess the performance of the parameter identification strategy for fault diagnosis and condition monitoring under the different fault conditions.

Chapter VIII provides conclusions and makes suggestions for future research directions.

CHAPTER II

Fundamentals on Electric Machines and Drives, and Parameter Identification Theories

2.1 Introduction

This chapter introduces relevant concepts on electric machines and drives theory as well as parameter identification and Simultaneous Identification and Control (SIC) strategies. First, the theory regarding electric machines and drives is discussed, followed by reference frame transformations. Then, the relevant theory of SMPM machines and voltage source inverters are discussed. Afterward, the basics behind online parameter identification and SIC methodologies are presented.

2.2 Three-Phase Electric Machines and Drives

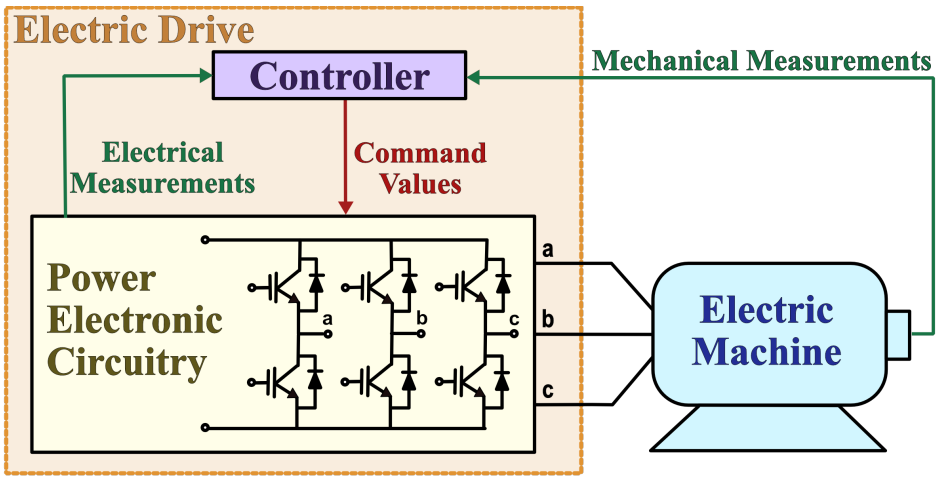

Figure 2.1: Three-phase electric machine and drive system.

An electric machine is an electromechanical energy converter that consists of stationary and rotating components, known as the stator and rotor, respectively. In variable-speed applications, the electric machine is powered through a specialized circuit known as an electric drive consisting of power electronics, controller, and sensors, as shown in Fig. 2.1. While this is physically a three-phase system, the analysis of electric machines, as well as their control, is typically based on an equivalent two-phase model as it has particular conceptual advantages over the original three-phase model in terms of modeling and understanding the dynamic response of the electric machine.

2.3 Relevant Reference Frame Transformations

The operating principle behind electric machines is the generation of a rotating magnetic field on the rotor which imposes an electromagnetic torque. The equivalent two-phase model is meant to generate the same magnetic field as the actual three-phase machine would. The three-phase variables can be mapped into their two-phase equivalents by using the Clarke transform [81], which is given by,

$$\begin{bmatrix} x_\alpha \\ x_\beta \\ x_0 \end{bmatrix} = \begin{bmatrix} \frac{2}{3} & -\frac{1}{3} & -\frac{1}{3} \\ 0 & \frac{\sqrt{3}}{3} & -\frac{\sqrt{3}}{3} \\ \frac{1}{3} & \frac{1}{3} & \frac{1}{3} \end{bmatrix} \begin{bmatrix} x_a \\ x_b \\ x_c \end{bmatrix} = \mathbf{T_{23}} \begin{bmatrix} x_a \\ x_b \\ x_c \end{bmatrix}, \tag{2.1}$$

where $\mathbf{T_{23}} \in \mathbb{R}^{3x3}$ is the Clarke transform, x_a, x_b, and x_c are the three-phase variables, x_α and x_β are the equivalent two-phase variables, and x_0 is the zero-sequence component, which is added as it allows complete analysis of the three-phase machine variables through their two-phase equivalents. Similarly, the two-phase variables can be mapped into their original three-phase variables by using the inverse Clarke transform [81], $\mathbf{T_{32}} \in \mathbb{R}^{3x3}$, which is given by,

$$\begin{bmatrix} x_a \\ x_b \\ x_c \end{bmatrix} = \begin{bmatrix} 1 & 0 & 1 \\ -\frac{1}{2} & \frac{\sqrt{3}}{2} & 1 \\ -\frac{1}{2} & -\frac{\sqrt{3}}{2} & 1 \end{bmatrix} \begin{bmatrix} x_\alpha \\ x_\beta \\ x_0 \end{bmatrix} = \mathbf{T_{32}} \begin{bmatrix} x_\alpha \\ x_\beta \\ x_0 \end{bmatrix}. \tag{2.2}$$

Note that the transformation has a scaling factor of 2/3 so that the peak values of the three-phase and equivalent two-phase sinusoidal electrical variables are the same.

The previous equivalent two-phase variables are referenced to a Cartesian coordinate system aligned with the direction of the magnetic fields generated by the stator

windings of the equivalent two-phase machine, a.k.a, the stationary reference frame. However, in the analysis of AC machines, other reference frames are often more beneficial as two-phase variables become constant in these frames under steady-state conditions. The equivalent two-phase variables can be mapped from the stationary reference frame into a rotational reference frame, a.k.a. the synchronous reference frame, by using the Park transform [82], which is given by,

$$\vec{x}^{syn} = \begin{bmatrix} x_d^{syn} \\ x_q^{syn} \end{bmatrix} = \begin{bmatrix} \cos(\theta_{syn}) & \sin(\theta_{syn}) \\ -\sin(\theta_{syn}) & \cos(\theta_{syn}) \end{bmatrix} \begin{bmatrix} x_\alpha \\ x_\beta \end{bmatrix} = e^{-\mathbf{J}\theta_{syn}}\vec{x}, \tag{2.3}$$

where $(\cdot)^{syn}$ denotes that the variable is in the rotational reference frame, and $\mathbf{J} \in \mathbb{R}^{2x2}$ is the counter-clockwise (CCW) rotation matrix, which is given by

$$\mathbf{J} = \begin{bmatrix} 0 & -1 \\ 1 & 0 \end{bmatrix}. \tag{2.4}$$

Likewise, the inverse Park transform maps the two-phase variables from rotational to stationary reference frame, and is given by,

$$\vec{x} = \begin{bmatrix} x_\alpha \\ x_\beta \end{bmatrix} = \begin{bmatrix} \cos(\theta_{syn}) & -\sin(\theta_{syn}) \\ \sin(\theta_{syn}) & \cos(\theta_{syn}) \end{bmatrix} \begin{bmatrix} x_d^{syn} \\ x_q^{syn} \end{bmatrix} = e^{\mathbf{J}\theta_{syn}}\vec{x}^{syn}. \tag{2.5}$$

2.4 Surface-Mount Permanent Magnet Machine Theory

As its name states, the Surface-Mount Permanent Magnet (SMPM) machine has magnets attached to the rotor's outer surface (e.g., see Fig. 2.2(a)). This design provides the highest air gap flux density as the magnets directly face the air gap without any other medium in between [56]. These machines can also achieve high efficiencies since the magnets do not produce losses like field windings (resistive losses). Based on its construction, SMPM machines have a relatively large gap between the stator and rotor irons, and therefore a relatively small self-inductance [83].

In this section, the basic theory of SMPM machines is presented, including flux linkage/current relationships, stator voltage, and electromagnetic torque equations. The SMPM machine is analyzed under the following assumptions:

A. The machine has a smooth air gap (i.e., slot effects are not considered), is balanced in construction, and is connected in an ungrounded-wye configuration.

B. Magnetic saturation, eddy current and hysteresis effects are neglected (i.e., lin-

ear magnetics are assumed).

C. Stator and rotor irons have infinite permeability. The magnets and air have equal permeability.

All three assumptions (A-C) are commonly used for control-oriented models [56]. Note that, regarding assumption B, the magnetics of an SMPM machine are typically linear given the large effective air gap between stator and rotor irons. In terms of assumption C, the permeability of most magnet materials (e.g., SmCo, NdFeB) is close to that of free space, and the permeability of most iron alloys used in the stator and rotor irons is much higher than that of free space. Note that all theory presented assumes a normal (i.e., fault-free) SMPM machine. Fig. 2.2 shows an example of a four-pole, three-phase, smooth-airgap SMPM machine and the equivalent two-pole, two-phase, smooth-airgap SMPM machine that is typically used for analysis. Note that in Fig. 2.2(b), the $\alpha-\beta$ coordinate system corresponds to the stationary reference frame while the $d^r - q^r$ coordinate system is the rotor reference frame, which rotates in synchronism with the rotor.

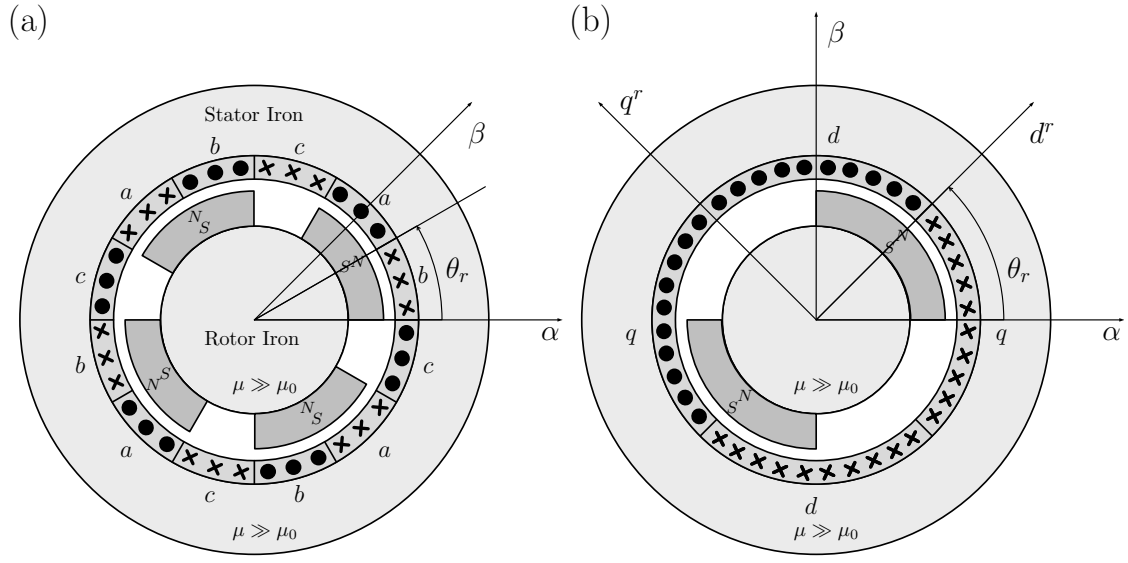

Figure 2.2: (a) Four-pole, three-phase, smooth-airgap SMPM machine, (b) Two-pole, two-phase, smooth-air-gap SMPM machine.

2.4.1 Flux-Linkage/Current Relationships

In an SMPM machine, the three-phase flux linkage/current relationships are given by:

$$\begin{bmatrix}\lambda_a\\ \lambda_b\\ \lambda_c\end{bmatrix} = \begin{bmatrix}L_s & L_m & L_m\\ L_m & L_s & L_m\\ L_m & L_m & L_s\end{bmatrix}\begin{bmatrix}i_a\\ i_b\\ i_c\end{bmatrix} + \begin{bmatrix}\lambda_{PM,a}\\ \lambda_{PM,b}\\ \lambda_{PM,c}\end{bmatrix}, \tag{2.6}$$

with

$$\begin{aligned} L_s &= L_g + L_\sigma,\\ L_m &= -\tfrac{L_g}{2},\\ \lambda_{PM,a} &= \Lambda_{PM}\cos(\theta_{re}),\\ \lambda_{PM,b} &= \Lambda_{PM}\cos(\theta_{re} - \tfrac{2\pi}{3}),\\ \lambda_{PM,c} &= \Lambda_{PM}\cos(\theta_{re} + \tfrac{2\pi}{3}), \end{aligned}$$

where the subscripts a, b, and c denote each of the three phases, L_s and L_m are the stator self- and mutual inductances, L_g is the air-gap inductance, L_σ is the leakage inductance, Λ_{PM} is the PM flux linkage, $\lambda_{PM,a}$, $\lambda_{PM,b}$, and $\lambda_{PM,c}$ are the PM flux linkages with respect to windings a, b, and c, respectively, and θ_{re} is the electrical rotor position, given by

$$\theta_{re} = \tfrac{N_p}{2}\theta_r, \tag{2.7}$$

where θ_r is the angular rotor position and N_p is the number of poles. Using the Clarke transform (Eq. (2.2)), the flux linkage/current relationships can be mapped into their two-phase equivalents in the stationary reference frame, which are given by:

$$\begin{bmatrix}\lambda_\alpha\\ \lambda_\beta\\ \lambda_0\end{bmatrix} = \begin{bmatrix}L & 0 & 0\\ 0 & L & 0\\ 0 & 0 & L_s + 2L_m\end{bmatrix}\begin{bmatrix}i_\alpha\\ i_\beta\\ i_0\end{bmatrix} + \Lambda_{PM}\begin{bmatrix}\cos(\theta_{re})\\ \sin(\theta_{re})\\ 0\end{bmatrix}, \tag{2.8}$$

where L is the equivalent two-phase inductance, which is given by

$$L = L_s - L_m = \frac{3}{2}L_g + L_\sigma. \tag{2.9}$$

For the SMPM machine, the rotor is spinning at the same velocity as the rotating magnetic field, and, therefore, a rotating coordinate system, known as the rotor reference frame, is more beneficial for analysis and control purposes. Using the Park transform (Eq. (2.3)), the electrical dynamics in the rotor reference frame are given

by,

$$\begin{bmatrix} \lambda_d^r \\ \lambda_q^r \end{bmatrix} = \begin{bmatrix} L & 0 \\ 0 & L \end{bmatrix} \begin{bmatrix} i_d^r \\ i_q^r \end{bmatrix} + \Lambda_{PM} \begin{bmatrix} 1 \\ 0 \end{bmatrix}. \tag{2.10}$$

where the superscript $(\cdot)^r$ denotes that the variable is in the rotor frame. Note that the direct-axis of the rotor reference frame is aligned with the PM flux linkage vector, and the reference frame rotates at the electrical rotor speed, ω_{re} ($\omega_{re} = \frac{N_p}{2}\omega_r$, where ω_r is the mechanical rotor speed). Also, note that, in the model, the SMPM machine is a non-salient pole ($L = L_d^r = L_q^r$) since the magnets are mounted on the rotor surface, and their permeability is equal to that of the air (Assumption C).

2.4.2 Stator Voltage Equations

The three-phase electrical dynamics of an ungrounded, wye-connected SMPM machine are given by [56]:

$$\begin{bmatrix} v_a \\ v_b \\ v_c \end{bmatrix} = \begin{bmatrix} R & 0 & 0 \\ 0 & R & 0 \\ 0 & 0 & R \end{bmatrix} \begin{bmatrix} i_a \\ i_b \\ i_c \end{bmatrix} + \begin{bmatrix} L_s & L_m & L_m \\ L_m & L_s & L_m \\ L_m & L_m & L_s \end{bmatrix} \frac{d}{dt} \begin{bmatrix} i_a \\ i_b \\ i_c \end{bmatrix} + \frac{d}{dt} \begin{bmatrix} \lambda_{PM,a} \\ \lambda_{PM,b} \\ \lambda_{PM,c} \end{bmatrix}, \tag{2.11}$$

with

$$i_0 = \frac{1}{3}(i_a + i_b + i_c) = 0, \tag{2.12}$$

where i_x and v_x are the three-phase currents and voltages ($x = \{a, b, c\}$), i_0 is the zero-sequence current component, and R is the stator winding resistance.

The electrical dynamics presented in Eq. (2.11) are typically analyzed using the standard equivalent two-phase model in which the electrical dynamics are expressed with respect to the rotor reference frame [56], as follows:

$$\boldsymbol{L}\frac{d\vec{i}^r}{dt} = -\boldsymbol{R}\vec{i}^r - \omega_{re}\boldsymbol{J}(\boldsymbol{L}\vec{i}^r + \vec{\lambda}_{PM}^r) + \vec{v}^{\,r}, \tag{2.13}$$

with $\boldsymbol{R} = R\boldsymbol{I} \in \mathbb{R}^{2x2}$, $\boldsymbol{L} = L\boldsymbol{I} \in \mathbb{R}^{2x2}$, and $\vec{\lambda}_{PM}^r = \begin{bmatrix} \Lambda_{PM} & 0 \end{bmatrix}^T \in \mathbb{R}^2$, where $\vec{i}^r$ and $\vec{v}^r$ are the equivalent two-phase current and voltage vectors (i.e., $\vec{x}^r = \begin{bmatrix} x_d^r & x_q^r \end{bmatrix}^T$ with x as the variable), $\boldsymbol{I}$ is the 2x2 identity matrix, $L = L_s - L_m$ is the two-phase equivalent stator winding self-inductance, Λ_{PM} is the PM flux linkage, and $\boldsymbol{J}$ is the counterclockwise ninety degree rotation matrix, defined in Eq. (2.4).

2.4.3 Electromagnetic Torque

The three-phase electromagnetic torque is $\frac{3}{2}$ times larger than its equivalent two-phase value and can be determined through the differentiation of co-energy with respect to the rotor angle as follows [1]:

$$\tau_{3ph} = \frac{3}{2}\tau_{2ph} = \frac{3}{2}\frac{\partial W'_{fld}}{\partial \theta_r} \tag{2.14}$$

where τ_{3ph} and τ_{2ph} are the three-phase and two-phase electromagnetic torques, and W'_{fld} is the co-energy which is given by

$$W'_{fld} = W'_{fld0} + \frac{1}{2}\mathbf{L} \mid \vec{i} \mid^2 + \vec{i}^{\intercal} e^{\mathbf{J}\theta_{re}} \vec{\lambda}^r_{PM}, \tag{2.15}$$

where W'_{fld0} is the co-energy due to the PMs themselves (i.e., with unexcited windings). Note that the co-energy due to the PMs is independent of the rotor angle if the slot effects are neglected (Assumption A). Then, the torque is therefore given by [1]:

$$\tau_{3ph} = \frac{3}{2}\frac{\partial W'_{fld}}{\partial \theta_r} = \frac{3}{2}\frac{\partial W'_{fld}}{\partial \theta_{re}}\frac{d\theta_{re}}{d\theta_r} = \frac{3N_p}{4}\vec{i}^{\intercal}\mathbf{J}\vec{\lambda}_{PM} \tag{2.16}$$

The cross-product operator is independent of the reference frame as it is based on the magnitudes and angles between the two-phase vectors. Therefore, the last torque expression can be written with respect to the rotor reference frame, in which case, the electromagnetic torque is given by

$$\tau_{3ph} = \frac{3N_p}{4}\vec{i}^{r\intercal}\mathbf{J}\vec{\lambda}^r_{PM} = \frac{3N_p}{4}\Lambda_{PM} i^r_q. \tag{2.17}$$

2.5 Voltage Source Inverters for AC Motor Control

In AC motor drives, the power electronic circuitry is typically a three-phase Voltage Source Inverter (VSI), as shown in Fig. 2.3(a). The VSI supplies a Pulse-Width Modulated version of the sinusoidal three-phase voltages calculated by the control algorithm to the electric machine. This operation is achieved through semiconductor transistors, such as MOSFETs and IGBTs, operating in "switch" mode. In switch-mode operation, the VSI transistors achieve a considerable reduction of the converter losses as they serve as switches. However, their operation generates Electromagnetic Interference (EMI), which imposes constraints in the control as it can corrupt the measurements and pollute the environment. Specifically, the Analog-to-Digital Con-

verter (ADC) sampling has to be synchronized with the switching of the transistors to avoid any spurious measurements.

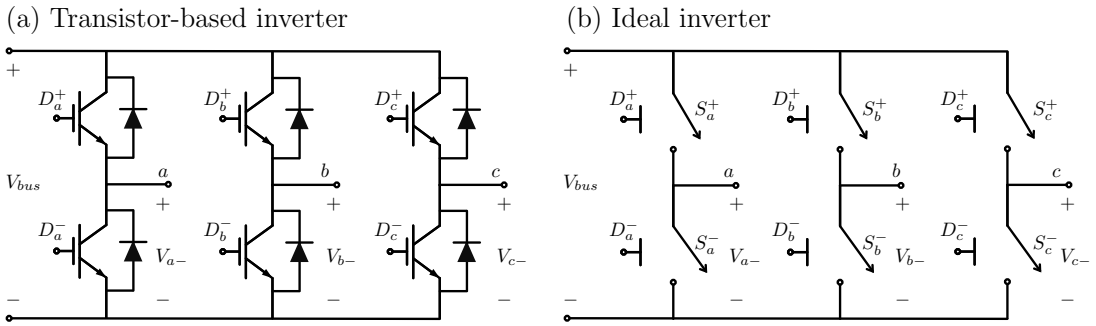

Figure 2.3: Practical and ideal three-phase VSI.

In this section, the basic theory of three-phase VSI for AC machine control, including VSI modeling for AC motor control design and space vector modulation as PWM technique, is presented. The three-phase VSI is analyzed based on its ideal model (see Fig. 2.3(b)), which neglects conduction and switching losses as well as dead-time effects.

2.5.1 Modeling Voltage Source Inverters for AC Motor Control Design

As shown in Fig. 2.3(b), the VSI's circuit consists of three half-bridges that share the same input DC supply. In each phase, two possible states can be identified:

- State 1 (Hi): S_x^+ on and S_x^- off $\Longrightarrow v_x = V_{bus}$
- State 0 (Lo): S_x^+ off and S_x^- on $\Longrightarrow v_x = 0$

where the subscript x denotes each of the phases (i.e., a, b, c), v_x is the VSI's output voltage for phase x, and V_{bus} is the input DC voltage. The desired voltage is achieved in an average-value sense through Pulse Width Modulation (PWM); in other words, by changing the duration of the VSI input voltage to the output. As a result, the output voltage is a square wave with duty cycle D and switching period T_{sw} ($T_{sw} = t_k - t_{k-1}$), as shown in Fig. 2.4.

For AC machine control design purposes, the VSI is modeled as an ideal "average-value" VSI, which applies to the electric machine average-value voltages based on the duty cycles. In this model, the main limitation is given by the two-time-scale separation assumption, which assumes that the duty cycle changes relatively slowly

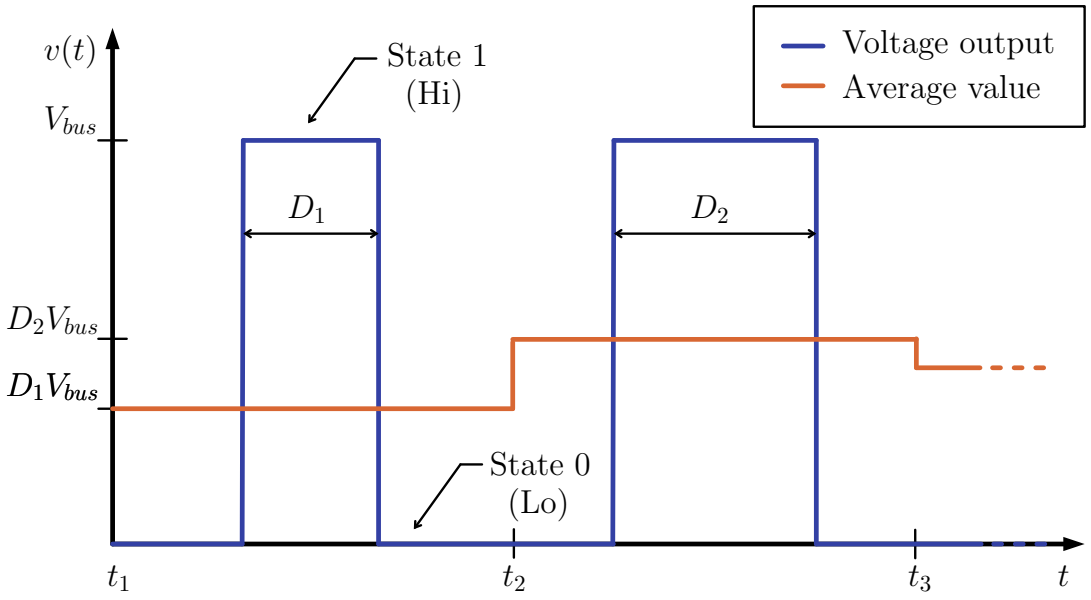

Figure 2.4: Center-based PWM output waveform and average value for an ideal VSI phase.

to such an extent that it is essentially constant during a single switching period [1]. A typical rule-of-thumb for the two-time-scale assumption to hold is that the time constants associated with the control system response are at least 20 times larger than that of the switching period [1]. For example, in an Electric Vehicle (EV), the main traction drive typically has a switching cycle of approximately $10kHz$, while the control system time constant is established by the bandwidth of the regulator, which is typically designed around $500Hz$.

In terms of AC machine control implementation, VSI operation imposes some constraints as it is inherently a sampled-data system. In particular, sampling the currents and encoder measurements has to be synchronized with a center-based PWM strategy to avoid spurious measurements due to EMI generated during voltage transitions. Therefore, the measurement sampling and duty cycle updates are performed in the middle of the Hi or Lo states, and the sampling frequency is restricted to either one or twice the switching frequency at most [56].

2.5.2 PWM technique: Space Vector Modulation

As mentioned above, the control of AC machines is typically based on the equivalent two-phase model. However, these two-phase voltages have to be implemented in an average-value sense to a three-phase system, in which the zero-sequence com-

ponent is also present. For ungrounded wye-connected machines, the average-value of the zero-sequence voltage does not affect the currents flowing through the machine since a zero-sequence current cannot exist. Space Vector Modulation (SVM) is a PWM technique that exploits this fact to increase the two-phase voltages that can be applied to the machine by the three-phase inverter [1].

The idea behind SVM is to consider the output of all three phases simultaneously. As mentioned before, in each phase, the output has two possible states (Hi and Lo), which can be represented with a binary. Then, the three-phase output voltages with respect to the negative terminal of the bus voltage can be expressed as follows [1]:

$$\begin{bmatrix} V_{a-} \\ V_{b-} \\ V_{c-} \end{bmatrix} = V_{bus} \begin{bmatrix} S_a \\ S_b \\ S_c \end{bmatrix}, \tag{2.18}$$

where S_x is a binary that is equal to one and zero for the Hi and Lo states, respectively. Note that the three-phase inverter voltages with respect to the negative terminal of the bus voltage relate to the three-phase machine voltages as follows:

$$\begin{bmatrix} V_{a-} \\ V_{b-} \\ V_{c-} \end{bmatrix} = \begin{bmatrix} V_a \\ V_b \\ V_c \end{bmatrix} + \begin{bmatrix} V_{n-} \\ V_{n-} \\ V_{n-} \end{bmatrix} \tag{2.19}$$

where V_a, V_b, and V_c are the line-to-neutral three-phase machine voltages and V_{n-} is the voltage between the machine's neutral and the inverter's negative terminal, which is a zero sequence voltage. Using the Clarke Transform [81], the equivalent two-phase voltages can be determined for all possible states (S_a, S_b, S_c), which are given by

$$V_\alpha = \frac{V_{bus}}{3}(2S_a - S_b - S_c), \tag{2.20}$$

$$V_\beta = \frac{\sqrt{3}V_{bus}}{3}(S_b - S_c). \tag{2.21}$$

The resultant $\alpha - \beta$ values for the 8 possible combinations of the output states are known as space vectors and are displayed in Fig 2.5(a). Inspection of Fig. 2.5(a) shows that the output-state combinations corresponds to the center and vertices of the hexagon, which can be divided in sectors (See Fig. 2.5(b)). Over one switching period, the desired average-value voltage is generated by switching between the space vectors that delimit the sector and zero space vectors (i.e., [111] or [000]). The interior of the hexagon represents the feasible average-value voltages which can be achieved

through SVM.

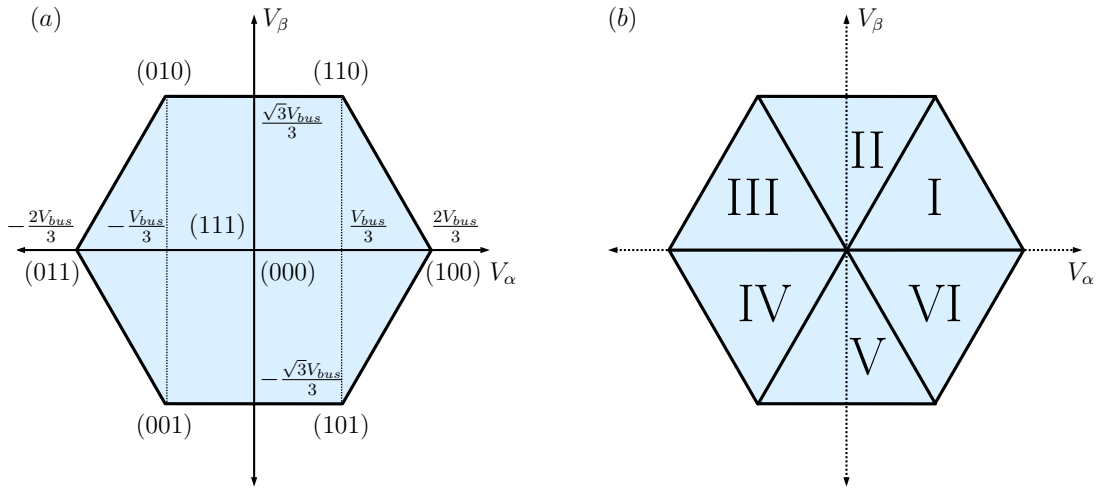

Figure 2.5: (a) Region of feasible two-phase voltages for SVM, (b) Sectors of SVM hexagon.

2.6 Control of AC Machine Drive Systems

Modern control of AC machines is typically done through Field-Oriented Control (FOC) techniques, in which the actual control is performed in a rotating reference frame in synchronism with the magnetic field (See Fig. 2.6). In these rotating reference frames, the electrical variables become constant in steady-state, facilitating current regulation through conventional control techniques (e.g., Proportional-Integral (PI) control). Moreover, the electric machine dynamics and the electromagnetic torque expression relating to electric variables are simplified, making them more suitable for control purposes.

Regarding torque control of AC machines, it is typically done indirectly through current regulation. Torque transducers are costly, and their calibration is sensitive to environmental conditions, which can be problematic for field applications (e.g., electric vehicles). Since the torque produced by an electric machine is a direct function of the currents, torque can be indirectly controlled through current regulation, which is cheaper and easier to implement in practice.

In practice, the control algorithm is typically implemented in a microprocessor. The sampled-data nature of the microprocessor used to execute the control algorithm imposes a one-period delay, which is also illustrated in Fig. 2.7.

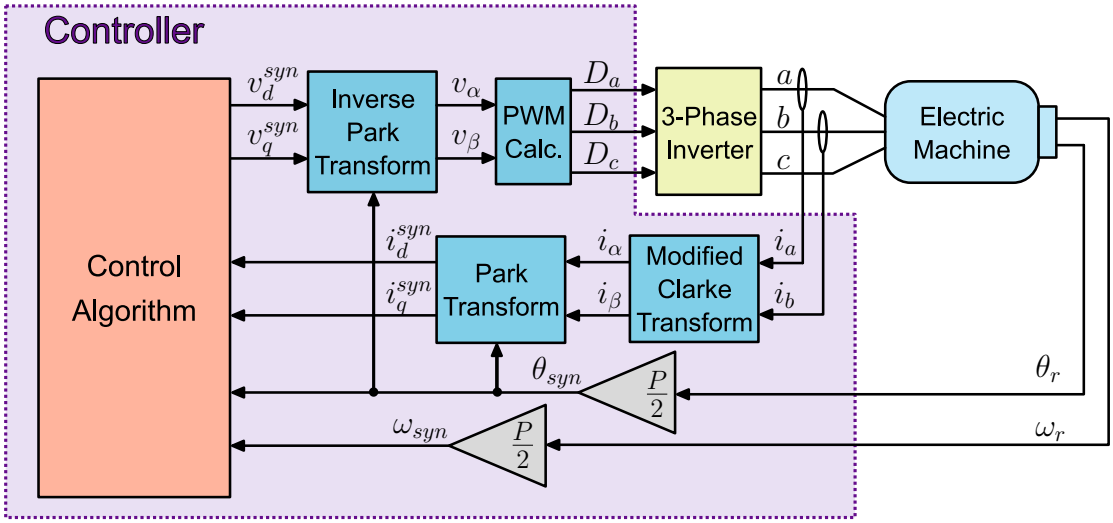

Figure 2.6: Basic control structure for AC machines.

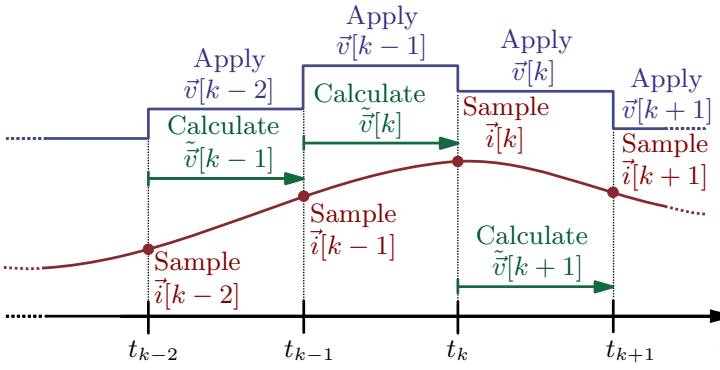

Figure 2.7: Sampled-data nature of control implementation.

2.6.1 Field-Oriented Control of SMPM Machine Drive Systems

The control algorithm for SMPM machines is typically implemented in the rotor reference frame, in which the direct axis is aligned with the PM flux linkage, as shown in Fig. 2.8. In this frame, the current regulator is designed based on the dynamics from Eq. (2.13) and the electromagnetic torque from Eq. (2.17). As seen in Eq. (2.17), the torque is solely a function of the quadrature-axis current and, hence, can be regulated by applying the following command quadrature-axis current:

$$\tilde{i}_q^r = \frac{4}{3N_p\Lambda_{PM}}\tilde{\tau}_{3ph}, \tag{2.22}$$

where the tilde $(\tilde{\cdot})$ denotes a reference signal. The direct-axis current is mainly used for field weakening, and its command value is typically set based on the rotor speed for this purpose. At low rotor speeds, the EMF is small, and the command direct-axis current should be zero (minimum loss operating point). However, as the rotor speed increases, the EMF increases, reaching the maximum available voltage. After this point, a negative direct-axis current should be commanded to reduce the voltage magnitude (i.e., field weakening). By doing so, rotor speed can be further increased while staying within the voltage limits.

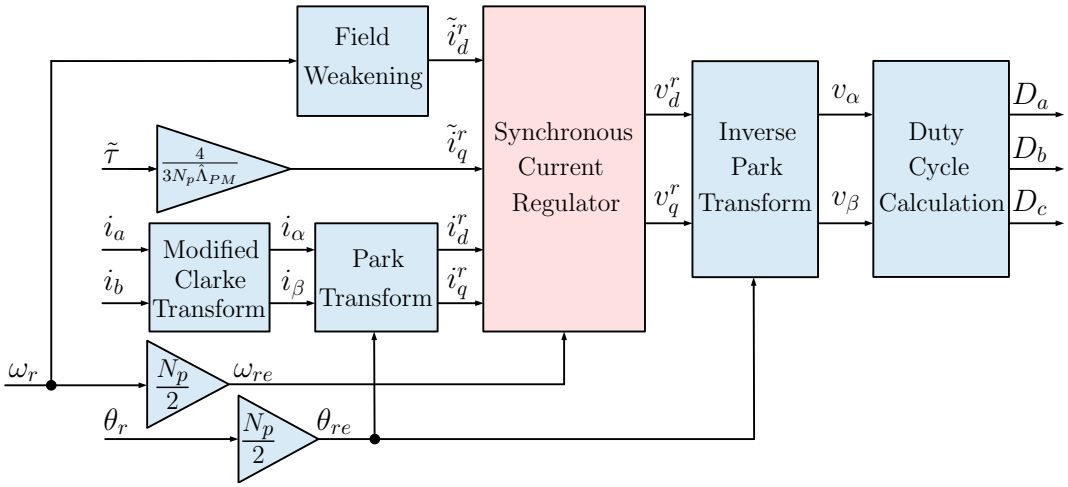

Figure 2.8: Field-oriented current regulator for SMPM machine.

2.7 Online Parameter Identification

To capture the dynamic behavior of a system for the purpose of control design, models require fairly accurate parameters. In some cases, these parameters can be

measured or calculated based on laws of physics, laws of chemistry, material properties, and others [84]. However, in many cases, these parameters have to be deduced from experiments by observing the system's dynamic response given certain inputs [84]. When the plant parameters vary negligibly or in a specific manner, the identification process may be performed "offline." However, in many cases, the parameters vary due to several causes, such as operating conditions and aging, leaving offline identification ineffective. By processing the input-output data during operation, online parameter identification techniques can provide continuous estimates and, therefore, track their variations.

The design of an online parameter estimator requires the formulation of an appropriate parameterization of the plant model, an adaptive law for parameter adjustment, and a plant input design that guarantees accurate parameter convergence [84]. In terms of the parameterizations, linear parametric models are often used, which are given by [84],

$$\vec{z} = \mathbf{\Phi}^{\intercal}\vec{\theta}, \tag{2.23}$$

where $\vec{z}$ is the observation (i.e., measurement), $\vec{\theta}$ is the parameter vector, and $\mathbf{\Phi}$ is the regressor matrix. Depending on the application, $\vec{z}$ and $\vec{\theta}$ are vectors or scalars while $\mathbf{\Phi}$ is a matrix or vector. Note that $\vec{z}$ and $\mathbf{\Phi}$ consist of measurable signals and might include time-derivatives of these measured signals. In order to avoid the undesirable effects from these derivatives, time-derivatives of signals are typically estimated through proper filtering [84]. The adaptive law is a dynamic estimation procedure that leverages the update in the measured signals to generate updated parameter estimates [85]. The law design can be based on stability considerations (e.g., Lyapunov-based algorithms) or optimization techniques (e.g., least-squares, gradient, projection algorithms). In terms of the plant input, it should provide what the adaptive law requires for accurate parameter convergence. Accurate convergence can be achieved through the sufficient condition that the regressor is persistently exciting, which is described in the following definitions for continuous- and discrete-time systems:

Definition 2.1 (Persistence of Excitation (PE) for continuous-time signals [84])**.** A piece wise continuous signal matrix $\mathbf{\Phi} : \mathbb{R}^{+} \longmapsto \mathbb{R}^{n\times m}$ is **persistently exciting** in $\mathbb{R}^n$ with a level of excitation $\alpha_0 > 0$ if there exist constants $\alpha_1, T_0 > 0$ such that

$$\alpha_1\mathbf{I} \geq \frac{1}{T_0}\int_{t}^{t+T_0} \mathbf{\Phi}(\tau)\mathbf{\Phi}^{\intercal}(\tau)d\tau \geq \alpha_0\mathbf{I}, \quad \forall t \geq 0. \tag{2.24}$$

Definition 2.2 (PE for discrete-time signals [84])**.** A bounded signal matrix $\mathbf{\Phi}[t_k]$ is said to be **persistently exciting** if there exists $N > 0$ and $\alpha_0 > 0$ such that

$$\sum_{j=1}^{N} \mathbf{\Phi}[t_{k+j}]\mathbf{\Phi}^{\intercal}[t_{k+j}] \geq \alpha_0 \mathbf{I}, \quad \forall t_k \geq t_0. \tag{2.25}$$

The PE property presented in Eq. (2.24) and (2.25) is a sufficient, but not necessary, condition to guarantee that the estimated parameters converge to their true values; additional details can be found in [84]. Based on Eq. (2.24), the regressor, $\mathbf{\Phi}$, has to be designed so that the integral of the matrix $\mathbf{\Phi}(\tau)\mathbf{\Phi}^{\intercal}(\tau)$ is uniformly positive definite over any time interval $[t, t + T_0]$. For discrete-time systems, Eq. (2.25) shows that the input has to be designed so that the summation of $\mathbf{\Phi}[t_j]\mathbf{\Phi}^{\intercal}[t_j]$ over a certain interval is full rank. Hence, if identification is performed in discrete-time domain for physical processes evolving in continuous-time domain, such as the electric machines, the PE conditions depend not only on the signals but also the sampling frequency.

The sampling theorem gives a guideline so that the sampling does not result in loss of information and is described as follows:

Theorem 2.3 (Shannon's sampling theorem [86])**.** *A time-varying signal e(t) whose Fourier transform contains no frequency components greater than f_0 Hertz is uniquely determined by the values of $e(t)$ at any set of sampling points spaced $\frac{1}{2f_0}$ seconds apart.*

Therefore, the sampling frequency should be greater than twice the highest-frequency component of significant amplitude of the signal being sampled in order to maintain the PE properties of a continuous time-varying signal.

2.8 Simultaneous Identification and Control

The term SIC refers to control methodologies that seek to achieve certain control objectives while also guaranteeing sufficient conditions for accurate parameter identification. Parameter identification can be used for control adaptation and other secondary objectives (e.g., loss minimization, condition monitoring); however, in order to be accurate, it requires persistently exciting inputs which may conflict with the control objective (e.g., tracking a set-point or trajectory). Due to this trade-off, the SIC problem is often approached through optimization-based design methodologies such as Model Predictive Control (MPC) [87–90]. While this trade-off is unavoidable for most cases, in over-actuated plants their additional degrees of freedom offer an

opportunity to achieve identification and control objectives simultaneously without compromise [50, 52, 91, 92].

Systems that have strictly more inputs than outputs to be controlled are known as over-actuated systems. Their additional inputs potentially offer an opportunity to achieve the control objectives while guaranteeing persistent excitation, possibly without compromising the control performance. Based on the fact that there is no unique input vector that yields a particular output, the excitation can be constrained to the system's "null-space," avoiding undesirable output perturbations [53]. An example of an over-actuated system is the Permanent Magnet Synchronous Machine (PMSM), which has effectively two inputs (i.e., equivalent two-phase voltages) and a single regulated output (i.e., torque). In previous work, a few methodologies [50–52] have exploited the over-actuated nature of the PMSMs to formulate SIC methodologies without the aforementioned trade-off.

CHAPTER III

Simultaneous Identification and Torque Control of Surface-Mount Permanent Magnet Synchronous Machines with Inverter Current and Voltage Constraints

3.1 Introduction

Simultaneous Identification and Control (SIC) refers to control designs that ensure sufficient conditions for accurate parameter identification while achieving a control objective. In some applications, accurate knowledge of the system parameters is desirable for control adaptation and secondary objectives such as condition monitoring. However, to be accurate, parameter identification requires persistently exciting inputs that may compromise the control objective (e.g., tracking a set-point or trajectory). Because of this trade-off, the SIC problem is often addressed using optimization-based design methodologies such as MPC [87–90]. While conflicts between the control and identification objectives are inevitable in most cases, over-actuated plants have additional degrees of freedom that can be exploited to achieve both objectives without compromise simultaneously [50, 52, 91, 92].

The PMSM is an example of an over-actuated system since it has effectively two inputs (i.e., equivalent two-phase voltages) and a single regulated output (i.e., torque). PMSMs, such as SMPM and IPM, have been preferred for high-performance applications due to their high torque density, high power density, and potential for precise control and high efficiency over a wide operating range. However, the machine parameters vary with temperature changes, skin effect, and saturation, and, hence, the control performance can be negatively affected. A few methodologies [50–52] have exploited the over-actuated nature of the PMSMs to formulate SIC methodologies

without the trade-off mentioned above.

Operational constraints are inherent in PMSMs due to physical limitations as well as safety and reliability considerations. In an electric drive, the voltages supplied by the three-phase Voltage Source Inverter (VSI) are limited by the DC bus voltage and the PWM technique. Commanding voltages outside the limits will lead to clipped output voltages and deteriorated control performance. Furthermore, exceeding the current limit will trip the over-current protection of the VSI.

This chapter investigates the incorporation of operational constraints to the SIC formulation for SMPM machines. Specifically, an optimization-based SIC formulation that explicitly considers the voltage and current inverter limits for SMPM machines is presented[1]. First, the equivalent two-phase SMPM machine model is discussed. Then, the control objectives for the SIC formulation are presented, including the voltage and current limitations for the SMPM machine as a function of the speed. Afterward, the current and voltage constraints for the SIC formulation are derived by mapping three-phase voltage and current constraints into their two-phase equivalents. Subsequently, the control algorithm is discussed, including an adaptive current regulator and a Receding Horizon Adaptive Input Design (RHAID). The RHAID determines the reference direct-axis current that minimizes losses and maximizes the excitation characteristics while considering the voltage and current limitations. The reference currents are then fed into an adaptive current regulator for torque control. Following the control algorithm section, the constraint enforcement capability of the methodology is demonstrated through numerical simulations.

3.2 SMPM Machine Model

Assuming that the direct-axis is aligned with the PM flux linkage, the electrical dynamics in the rotor reference frame are given by

$$\boldsymbol{L}\frac{d\vec{i}^{r}}{dt} = -\boldsymbol{R}\vec{i}^{r} - \omega_{re}\boldsymbol{J}(\boldsymbol{L}\vec{i}^{r} + \vec{\lambda}^{r}_{PM}) + \vec{v}^{\,r}, \tag{3.1}$$

with $\boldsymbol{R} = R\boldsymbol{I} \in \mathbb{R}^{2x2}$, $\boldsymbol{L} = L\boldsymbol{I} \in \mathbb{R}^{2x2}$, and $\vec{\lambda}^{r}_{PM} = \begin{bmatrix}\Lambda_{PM} & 0\end{bmatrix}^{T} \in \mathbb{R}^{2}$, where the superscript $(\cdot)^{r}$ denotes that the variable is in the rotor reference frame, $\vec{i}$ and $\vec{v}$ are the

[1]The information in this chapter is based on the conference paper [80]:
F. A. Pinto Delgado, D. M. Reed, H. F. Hofmann, and J. Sun, "Simultaneous Identification and Torque Control of Surface-Mount Permanent Magnet Synchronous Machines with Inverter Current and Voltage Constraints", in *2018 IEEE Conference on Control Technology and Applications (CCTA)*, IEEE, 8-2018, pp. 1185-1190.

current and voltage vectors, $\boldsymbol{I} \in \mathbb{R}^{2x2}$ is the identity matrix, R is the stator winding resistance, L is the stator winding self-inductance, Λ_{PM} is the PM flux linkage, ω_{re} is the electrical rotor speed (i.e., $\omega_{re} = \frac{N_p}{2}\omega_r$, where ω_r is the mechanical rotor speed and N_p is the number of poles), and $\boldsymbol{J}$ is the counterclockwise (CCW) 90°-rotation matrix, defined in Eq. (2.4).

The three-phase electromagnetic torque is given by

$$\tau_{3ph} = \frac{3N_p}{4}\Lambda_{PM} i_q^r. \tag{3.2}$$

3.3 Control Objectives

Since the SMPM machine is an over-actuated system, SIC can be achieved without compromise. However, doing so while considering current and voltage constraints can be challenging. The current and/or voltage limitations that might be encountered by the SMPM machine will depend on the operating condition (i.e., torque/power and speed).

If the SMPM machine is operating close to the limits (e.g., maximum power, P_{max}, condition), three regions can be identified, as shown in Fig. 3.1. At low speeds, the system is current constrained since the EMF, which is proportional to speed in steady-state, is small. At medium speeds, the system is both current-and-voltage-constrained, and the voltage is kept within its limits by using field-weakening. Specifically, negative direct current is commanded to cancel PM flux linkage and, hence, reduce the EMF, while the quadrature current is adjusted accordingly to satisfy the current limit. At high speeds, the behavior depends on whether or not the currents can completely cancel the PM flux linkage. If the PM flux linkage cannot be completely cancelled (Fig. 3.1(a)), the system continues to be current-and-voltage-constrained until a maximum speed where the current is exclusively used for field-weakening (i.e., zero power operating point). If the PM flux linkage can be completely cancelled out (Fig. 3.1(b)), the system becomes solely voltage-constrained and can operate at arbitrarily high speed.

The control objective is to simultaneously achieve accurate torque regulation and parameter identification over a wide range of operating conditions without exceeding the voltage and current limits. This is approached through a controller which consists of a RHAID and an adaptive current regulator.

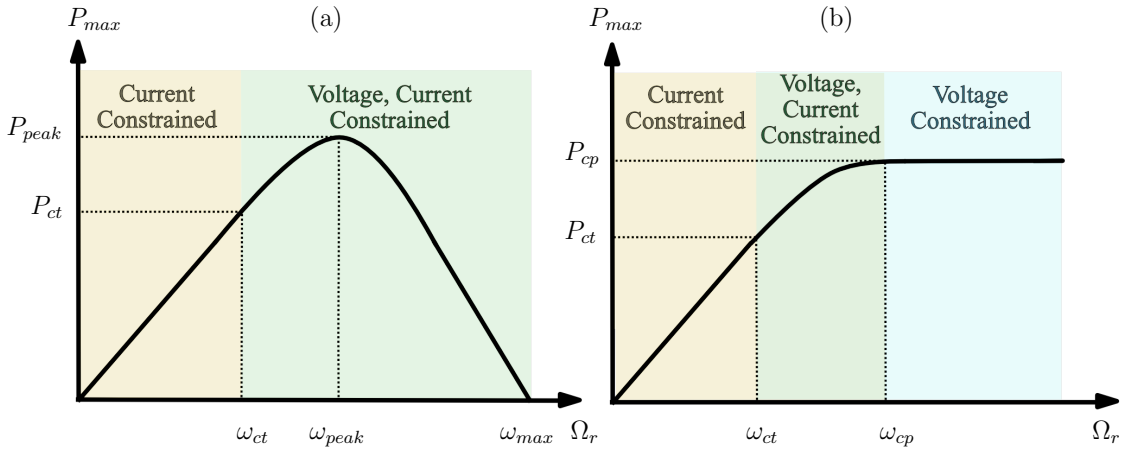

Figure 3.1: Maximum power of SMPM machine as function of rotor speed, in which (a) $I_{max} \leq \frac{\Lambda_{PM}}{L}$, (b) $I_{max} > \frac{\Lambda_{PM}}{L}$ (Additional details can be found in [1]).

3.4 Current and Voltage Constraint Formulation

In this section, the mathematical formulation of the voltage and current limitations which are inherent in an electric drive assuming an ideal three-phase Voltage Source Inverter (VSI) is presented. Fig. 3.2 shows an ideal VSI which applies to the machine the voltages determined by the control algorithm in an average-value sense [83]. In this work, SVM [83] is assumed as the PWM technique.

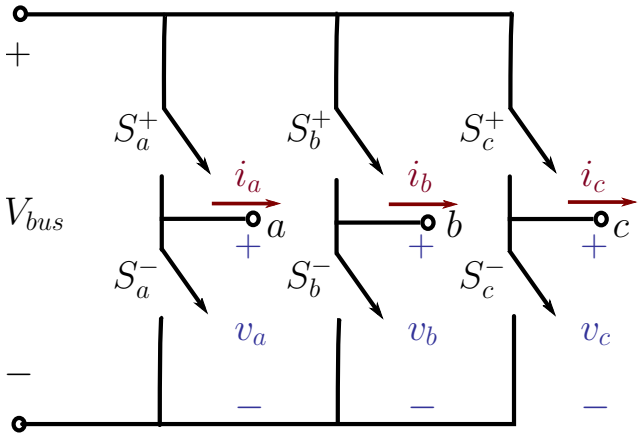

Figure 3.2: Ideal three-phase inverter.

3.4.1 Voltage Constraints

The VSI's output voltage is a square wave with duty cycle D since each phase can have two possible states:

- State $S_x = 0$: S_x^+ "off", S_x^- "on" $\implies v_x = 0$
- State $S_x = 1$: S_x^+ "on", S_x^- "off" $\implies v_x = V_{bus}$

where the subscript $(\cdot)_x$ denotes each phase (i.e., a, b, c). Then, by using the Clarke transform [81], the equivalent two-phase voltages can be determined for all possible states (S_a, S_b, S_c). The region of feasible average-value voltages is described by the Space Vector Hexagon (SVH) [83] presented in Fig. 3.3(a), which can be represented mathematically as

$$\Omega_v = \{\vec{v} : \boldsymbol{G_v}\vec{v} \leq \vec{h}_v\}, \tag{3.3}$$

where

$$\boldsymbol{G_v} = \begin{bmatrix} 0 & 1 \\ 0 & -1 \\ -\sqrt{3} & 1 \\ \sqrt{3} & 1 \\ -\sqrt{3} & -1 \\ \sqrt{3} & -1 \end{bmatrix}, \vec{h}_v = -\begin{bmatrix} 1 \\ 1 \\ 2 \\ 2 \\ 2 \\ 2 \end{bmatrix} \frac{V_{bus}}{\sqrt{3}},$$

and $\vec{v} = \begin{bmatrix} v_\alpha & v_\beta \end{bmatrix}^T$ is the equivalent two-phase stator voltage vector in the stationary reference frame.

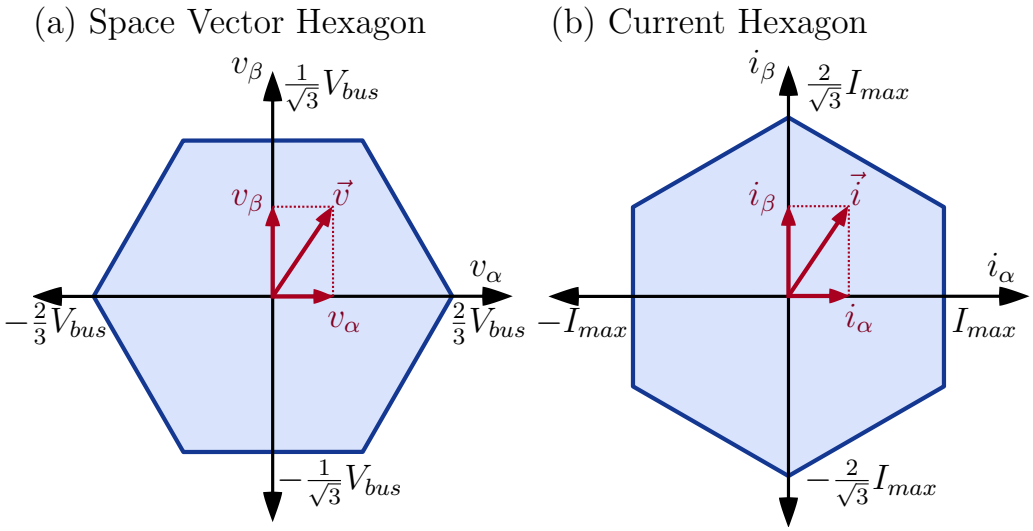

Figure 3.3: Regions of: (a) feasible voltages, and (b) feasible currents.

3.4.2 Current Constraints

The VSI is operating at its current limit when the maximum rated current, I_{max}, is flowing through any of its phases. The three-phase line currents can be mapped into their equivalent two-phase line currents (i.e., i_α, i_β) by using the Clarke transform [81]. Assuming balanced three-phase operation, the feasible current region corresponds to the Current Hexagon (CH) shown in Fig. 3.3(b) which can be characterized by:

$$\Omega_i = \{\vec{i} : \boldsymbol{G_i}\vec{i} \leq \vec{h}_i\}, \tag{3.4}$$

where

$$\boldsymbol{G_i} = \begin{bmatrix} 1 & 0 \\ -1 & 0 \\ -\frac{1}{\sqrt{3}} & 1 \\ \frac{1}{\sqrt{3}} & 1 \\ -\frac{1}{\sqrt{3}} & -1 \\ \frac{1}{\sqrt{3}} & -1 \end{bmatrix}, \vec{h}_i = -\begin{bmatrix} 1 \\ 1 \\ \frac{2}{\sqrt{3}} \\ \frac{2}{\sqrt{3}} \\ \frac{2}{\sqrt{3}} \\ \frac{2}{\sqrt{3}} \end{bmatrix} I_{max}.$$

3.5 Control Algorithm

The proposed SIC methodology, which is an extension of [52], uses an adaptive input design and an adaptive current regulator, as shown in Fig. 3.4. In this methodology, while the reference quadrature current is set to achieve the desired torque, the adaptive input design ensures persistency of excitation by generating an appropriate reference direct current.

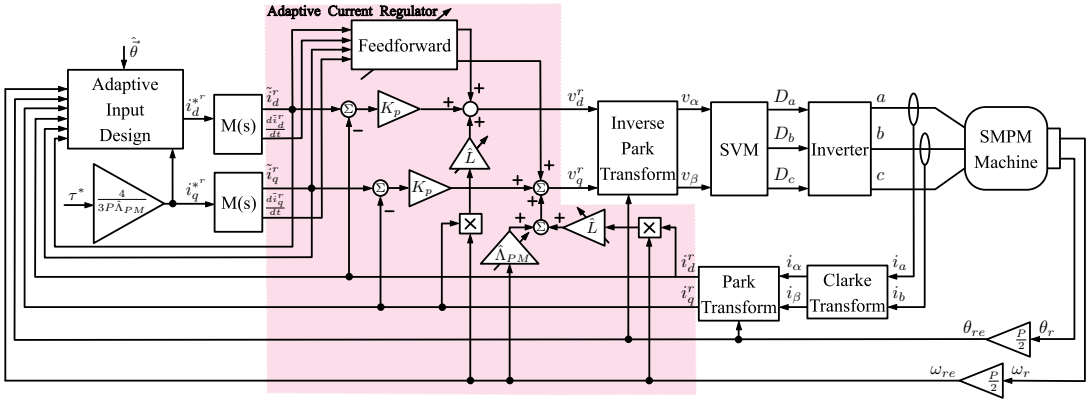

Figure 3.4: Block diagram of the proposed SIC strategy.

3.5.1 Adaptive Current Regulator

The controller is a projection-based adaptive current regulator consisting of feed-forward, back-emf compensation, and proportional feedback,

$$\vec{v}^{\,r} = \hat{\boldsymbol{R}}\tilde{\vec{i}}^{\,r} + \hat{\boldsymbol{L}}\frac{d\tilde{\vec{i}}^{\,r}}{dt} + \omega_{re}\boldsymbol{J}(\hat{\boldsymbol{L}}\vec{i}^{\,r} + \hat{\vec{\lambda}}_{PM}) + \boldsymbol{K_p}\vec{e}_i^{\,r}, \tag{3.5}$$

with $\boldsymbol{K_p} = K_p\boldsymbol{I}$ and $\vec{e}_i^{\,r} = \tilde{\vec{i}}^{\,r} - \vec{i}^{\,r}$, where the accent $(\hat{\cdot})$ denotes an estimated parameter, $\tilde{\vec{i}}^{\,r}$ and $\frac{d\tilde{\vec{i}}^{\,r}}{dt}$ are the filtered reference current vector and its derivative $\big($i.e., $\tilde{\vec{i}}^{\,r} = \{M(s)\}\vec{i}^{*r}$ and $\frac{d\tilde{\vec{i}}^{\,r}}{dt} = \{sM(s)\}\vec{i}^{*r}$, where $\vec{i}^{*r}$ is the reference current vector, $\{\cdot\}$ denotes a dynamic operator with transfer function "$\cdot$", and $M(s) = \frac{\lambda}{s+\lambda}$ $\big)$, K_p is the proportional feedback gain, and $\vec{e}_i^{\,r}$ is the stator current error vector.

The adaptive law is based on the linear parameterization of the filtered SMPM dynamics from Eq. (3.1):

$$\vec{z} = \boldsymbol{\Phi}^T\vec{\theta}, \tag{3.6}$$

where $\vec{z} = \begin{bmatrix} z_d & z_q \end{bmatrix}^T = \{M(s)\}\vec{v}^{\,r}$ is the observation, $\vec{\theta} = \begin{bmatrix} R & L & \Lambda_{PM} \end{bmatrix}^T$ is the parameter vector, and $\boldsymbol{\Phi}$ is the regressor matrix, which is given by

$$\boldsymbol{\Phi}^T = \begin{bmatrix} \vec{\phi}_d^{\,T} \\ \vec{\phi}_q^{\,T} \end{bmatrix} = \{M(s)\} \begin{bmatrix} i_d^r & (\frac{d}{dt}i_d^r - \omega_{re}i_q^r) & 0 \\ i_q^r & (\omega_{re}i_d^r + \frac{d}{dt}i_q^r) & \omega_{re} \end{bmatrix}. \tag{3.7}$$

Note that the signals have been filtered in order to avoid the derivatives of measured signals in $\boldsymbol{\Phi}$ or $\vec{z}$.

While the control formulation and design are carried out with a continuous-time model, parameter identification and update are performed at discrete time instants. Capturing the discrete-time effects is crucial for accurate parameter identification. The projection algorithm [93] aims to minimize the Euclidean norm between consecutive parameter estimates subject to the model in Eq. (3.6) and new measurements, and its estimated parameters are given by,

$$\hat{\vec{\theta}}[k] = \hat{\vec{\theta}}[k-1] + \frac{a\vec{\phi}_d[k]\big(z_d[k] - \vec{\phi}_d^{\,T}[k]\hat{\vec{\theta}}[k-1]\big)}{c + \vec{\phi}_d^{\,T}[k]\vec{\phi}_d[k]} + \frac{a\vec{\phi}_q[k]\big(z_q[k] - \vec{\phi}_q^{\,T}[k]\hat{\vec{\theta}}[k-1]\big)}{c + \vec{\phi}_q^{\,T}[k]\vec{\phi}_q[k]}, \tag{3.8}$$

where $c > 0$ is a small constant, $0 < a < 2$ is the adaption gain, and $k = 1, 2, ...$ is the time index.

3.5.2 Receding Horizon Adaptive Input Design (RHAID)

The Receding Horizon Adaptive Input Design (RHAID) determines the reference direct current trajectory to minimize ohmic losses and maximize the level of excitation. While the metric for minimizing losses is the weighted quadratic function of the reference direct current, the level of PE is measured using the "D-optimality" metric [94]:

$$J_D = \log(\det(\boldsymbol{F})), \tag{3.9}$$

where $\mathbf{F}$ is the Fisher information matrix [52],

$$\boldsymbol{F} = \sum_{k=1}^{N} \boldsymbol{\Phi}(t_k)\boldsymbol{\Phi}^T(t_k), \tag{3.10}$$

$\boldsymbol{\Phi}(t_k)$ is the regressor matrix at time t_k, and N is the total number of observations (i.e., measurements). Note that the D-optimality is a common optimization criterion often used for "optimal experiment design" [95].

The dynamic model required to predict the future states of the system is formulated using the Zero-Order Hold (ZOH) equivalent model of Eq. (3.1) given by,

$$\vec{x}[k+1] = \hat{\boldsymbol{A}}_{\boldsymbol{d}}\vec{x}[k] + \boldsymbol{B}_{\boldsymbol{d}}\vec{u}[k], \tag{3.11}$$

where

$$\hat{\boldsymbol{A}}_{\boldsymbol{d}} = \begin{bmatrix} e^{\hat{\boldsymbol{A}}T_{sw}} & \hat{\boldsymbol{B}}(\omega_{re}\boldsymbol{J}\hat{\boldsymbol{L}} - \boldsymbol{K_p}) & \hat{\boldsymbol{B}}(\hat{\boldsymbol{R}} + \boldsymbol{K_p}) & \hat{\boldsymbol{B}}\hat{\boldsymbol{L}} \\ \boldsymbol{I} & \boldsymbol{0} & \boldsymbol{0} & \boldsymbol{0} \\ \boldsymbol{0} & \boldsymbol{0} & a_f\boldsymbol{I} & \boldsymbol{0} \\ \boldsymbol{0} & \boldsymbol{0} & \boldsymbol{0} & a_f\boldsymbol{I} \end{bmatrix},$$

$$\boldsymbol{B}_{\boldsymbol{d}} = \begin{bmatrix} \boldsymbol{0} & \boldsymbol{0} \\ \boldsymbol{0} & \boldsymbol{0} \\ \boldsymbol{0} & b_f\boldsymbol{I} \\ \lambda\boldsymbol{I} & -\lambda\boldsymbol{I} \end{bmatrix}, \ \vec{x}[k] = \begin{bmatrix} \vec{i}^r[k] \\ \vec{i}^r[k-1] \\ \tilde{\vec{i}}^r[k] \\ \frac{d\tilde{\vec{i}}^r}{dt}[k] \end{bmatrix},$$

$$\vec{u}[k] = \begin{bmatrix} \vec{i}^{r^*}[k+1] \\ \vec{i}^{r^*}[k] \end{bmatrix}, \hat{\boldsymbol{A}} = \boldsymbol{L^{-1}}(\hat{\boldsymbol{R}} + w_{re}\boldsymbol{J}\hat{\boldsymbol{L}}),$$

$\hat{\boldsymbol{B}} = (e^{\hat{\boldsymbol{A}}_{\boldsymbol{d}} T_{sw}} - \boldsymbol{I})\hat{\boldsymbol{A}}^{-1}\hat{\boldsymbol{L}}^{-1}$, $\lambda > 0$ is the parameter of the first-order filter (i.e.,$M(s) = \frac{\lambda}{s+\lambda}$), T_{sw} is the sampling period, and a_f and b_f are the parameters of the ZOH model of $\{M(s)\}$ (i.e., $M(z) = \frac{b_f}{z-a_f}$). Note that $\tilde{\vec{i}}^r[k]$ and $\frac{d\tilde{\vec{i}}^r}{dt}[k]$ are the outputs from the ZOH model of $\{M(s)\}$ and $\{sM(s)\}$, respectively. We need both $\vec{i}^r[k]$ and $\vec{i}^r[k-1]$ as states of $\vec{x}[k]$ to incorporate the effect of the switching-period delay between measurement sampling and duty cycle updates (See Fig. 2.7).

Assuming that the estimated parameters, $\hat{\vec{\theta}}[k]$, the reference torque, $\tau^*[k]$, and the rotor electrical speed, $\omega_{re}[k]$, are essentially constant over the prediction horizon, the RHAID is formulated as the following,

$$
\begin{aligned}
\min_{i_d^{r^*}[k]} \quad & \sum_{k=j}^{j+N_f-1} \Big[\big(i_d^{r^*}[k]\big)^2 - \rho \cdot \log(\det(\boldsymbol{F}(\vec{x}))) \Big], \\
\text{subject to:} \quad & \vec{x}[k+1] = \hat{\boldsymbol{A}}_{\boldsymbol{d}}\vec{x}[k] + \boldsymbol{B}_{\boldsymbol{d}}\vec{u}[k], \\
& \boldsymbol{F}(\vec{x}) = \sum_{k=j-N_{pp}}^{j+N_f-1} \boldsymbol{\Phi}(\vec{x}[k])\boldsymbol{\Phi}(\vec{x}[k])^T, \\
& \boldsymbol{G_i} e^{\boldsymbol{J}\theta_{re}[k]} \tilde{\vec{i}}^r[k] \leq \vec{h}_i \ \forall k \epsilon [j \dots j+N_f-1], \\
& \boldsymbol{G_v} e^{\mathbf{J}\theta_{re}[k]} \vec{v}^r[k] \leq \vec{h}_v \ \forall k \epsilon [j \dots j+N_f-1], \\
& \vec{i}^{r^*}[k] = \begin{bmatrix} i_d^{r^*}[k] \\ i_q^{r^*}[k] \end{bmatrix} = \begin{bmatrix} i_d^{*^r}[k] \\ \frac{4\tau^*[k]}{3P\hat{\Lambda}_{PM}} \end{bmatrix},
\end{aligned}
\tag{3.12}
$$

where $\rho \geq 0$ is the weighting for the PE metric, N_f is the prediction horizon, N_{pp} is the number of past-data points required to achieve the persistently excited references (as discussed in [52]), $e^{\mathbf{J}\theta_{re}[k]}$ is a matrix exponential, and $\theta_{re}[k]$ is the predicted electrical rotor position at time t_k, which is given by:

$$
\theta_{re}[k] = \theta_{re}[j] + \Big[\frac{1}{2} + (k-j)\Big]\omega_{re}[k]T_{sw}, \forall k \neq j. \tag{3.13}
$$

Note that, in (3.12), the inverse Park transform [82] (i.e., $e^{\mathbf{J}\theta_{re}[k]}$) is used since the voltage and current constraints are formulated in the stationary reference frame. Also, note that the inverter current and voltage constraints are convex as they are given by linear functions.

3.6 Simulation Results

The constraint enforcement capability of the SIC algorithm is validated by numerical simulations using Matlab/Simulink. The methodology is tested at three operating conditions: low speed (current-constrained), medium speed (current-and-voltage-constrained), and high speed (voltage-constrained), representing the three limiting regions previously discussed.

The simulations capture the sampled-data nature of a practical implementation by modeling the controller (i.e., RHAID and adaptive current regulator) as a triggered subsystem that runs at $10kHz$, while the continuous-time SMPM dynamics are simulated with a fixed time step of 500ns using *ode3*. The RHAID formulation is solved using the interior-point method in Matlab's *fmincon*. A linear B-spline [87] is used to approximate the reference direct current trajectory and reduce the dimension of the optimization problem. An ideal "average-value" VSI is assumed, which applies to the machine the average-value voltages based on the duty cycles determined by the SVM. The initial parameter error is 20%. Table 3.1 presents the simulation parameters.

Table 3.1: SMPM machine, VSI, and control parameters for simulations.

Electrical Machine Parameters	
R	$436\,m\Omega$
L	$2\,mH$
Λ_{PM}	$12.579\,mV\cdot s$
N_p	10
VSI Parameters	
I_{max}	$7\,A$
V_{bus}	$30\,V$
Control Design Parameters	
K_p	8
a	0.005
c	1
ρ	1000
λ	600
N_f	50
N_{pp}	60

3.6.1 Effects of PE Signal and Constraint Enforcement

In order to highlight the impact of the PE signal and constraint enforcement, simulations at a current-constrained (low-speed) operating point $(200\,RPM, 0.62Nm)$

with four different control settings are presented in Fig 3.5. Fig. 3.5(a) shows the simulation without PE metric ($\rho = 0$) and without current/voltage constraints. The plots reveal that the parameters converge to the wrong values, causing inaccurate torque regulation. Fig. 3.5(b) shows that a similar result is obtained when the current and voltage constraints are included. Fig. 3.5(c) shows the simulation with the PE metric without considering current and voltage limits. In contrast to the previous cases, accurate parameter convergence and torque regulation are achieved. However, since the current limits were not considered, the constraints are violated.

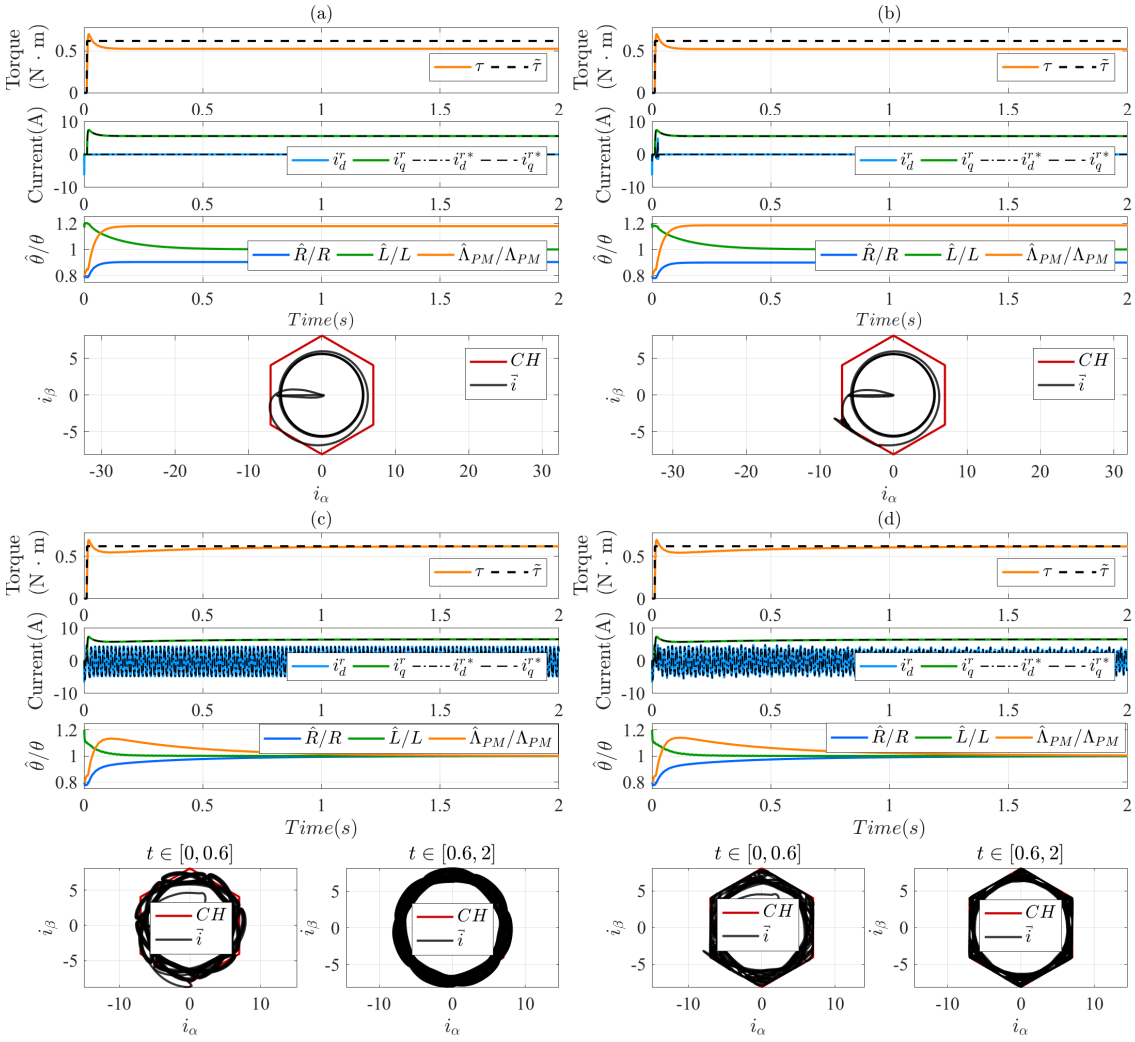

Figure 3.5: Simulations at current-constrained (low-speed) operating point with four different control settings: (a) with neither PE metric nor current/voltage constraints, (b) without PE metric and with current/voltage constraints, (c) with PE metric and without current/voltage constraints, and (d) with PE metric and current/voltage constraints. In (c) and (d), the phase plots are shown before and after the parameter errors are bounded within ±5%.

3.6.2 Constraint enforcement in three operating conditions

Figs. 3.5(d) , 3.6, and 3.7 show the effectiveness of the proposed algorithm in the following three conditions:

- Current constrained (Fig. 3.5(d)). The system operates at low-speed ($0.62 N{\cdot}m$ at $200\,RPM$). Inspection of the current phase plot reveals that the current constraints are successfully enforced after the parameters converge. Note that, while the direct current is modified to satisfy the constraints, the parameters are still able to converge and accurate torque regulation is achieved.

- Voltage constrained (Fig. 3.6). The system operates at high-speed ($0.2\,N{\cdot}m$ at $2000\,RPM$). As before, the voltage constraints are effectively enforced after the parameters converge. Note that the RHAID successfully deals with the voltage limit by using field-weakening (i.e., the direct current has a negative average-value). The torque ripple is caused by the discrete-time implementation.

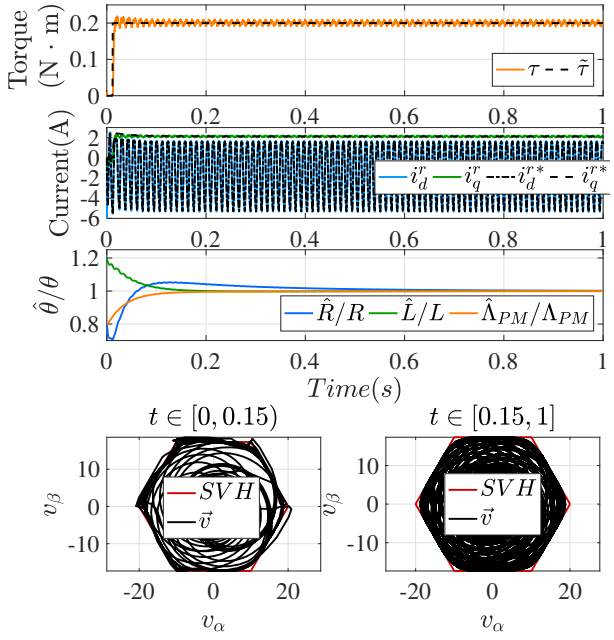

Figure 3.6: Simulation at voltage-constrained (high-speed) operating point.

- Current and voltage constrained (Fig. 3.7). The system operates at medium-speed ($0.6\,N{\cdot}m$ at $1300\,RPM$). The voltage and current phase plots show that the equivalent two-phase voltages and currents stay within their feasible regions. Accurate torque regulation is achieved after the parameters converge to their true values.

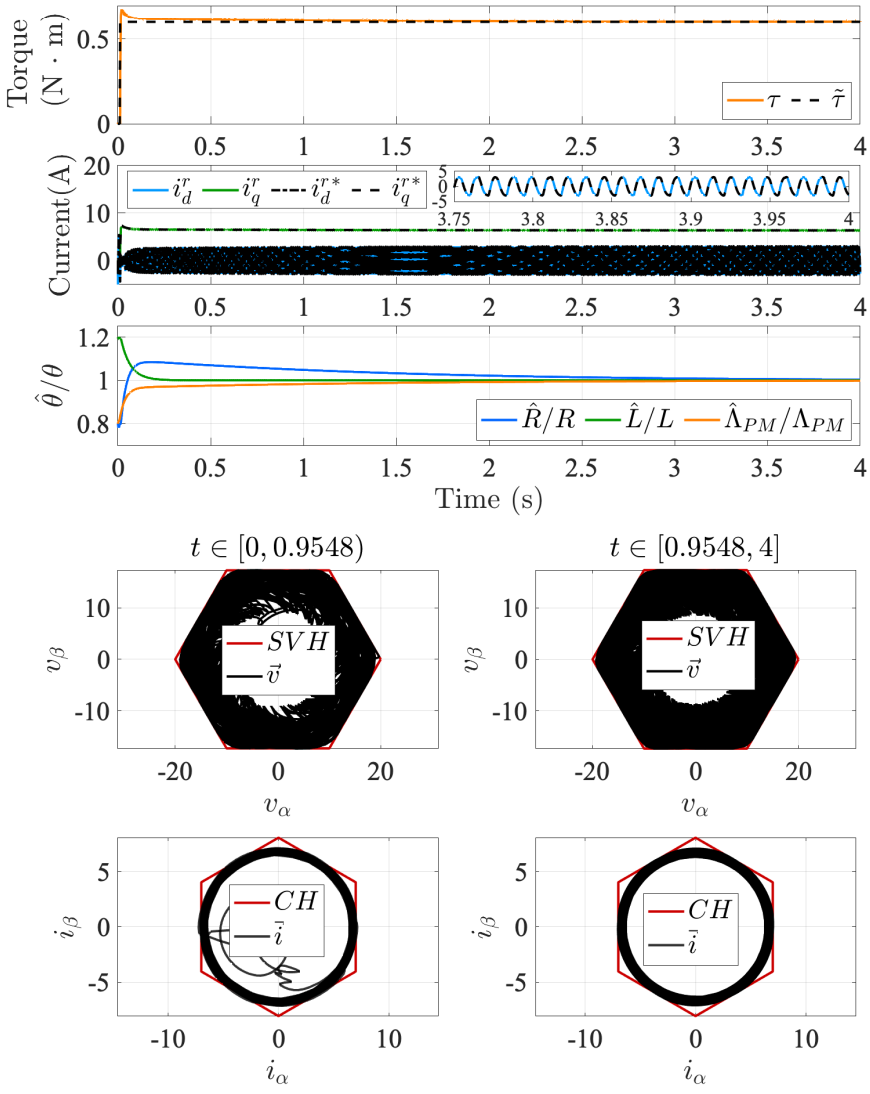

Figure 3.7: Simulation at current-and-voltage-constrained (medium-speed) operating point.

Note that the phase plots in Figs. 3.5(c), 3.5(d), 3.6, and 3.7 are shown before and after the parameter error is within ±5%.

Remark 3.1. Simulations show that occasional constraint violations can occur before parameter convergence. This could be addressed by performing a parameter calibration before use, or tightening the constraints [90].

3.7 Summary

This chapter investigated the incorporation of operational constraints into the SIC formulation for SMPM machines. Specifically, a SIC methodology that explicitly considers the voltage and current inverter limits for SMPM machines was presented. First, the current and voltage constraints for the SIC formulation were derived by mapping three-phase voltage and current constraints into their two-phase equivalents. Note that the resultant feasible region for both variables corresponds to hexagons. Afterward, these constraints were incorporated into a SIC formulation that consisted of an adaptive current regulator and an RHAID. The SIC formulation utilized the quadrature-axis current for torque production, while the direct-axis current was used to inject the excitation required for accurate convergence. The inverter current and voltage constraints were included in the RHAID, which minimizes losses while maximizing the excitation characteristics of the reference direct current trajectories. Accurate torque regulation was achieved through the adaptive current regulator. Simulations demonstrated the effectiveness of the SIC formulation on the constraint enforcement at different operating conditions.

CHAPTER IV

Modeling and Identification for Condition Monitoring of Surface-Mount Permanent Magnet Machines Under Magnet Demagnetization

4.1 Introduction

Among all components within a PMSM, the Permanent Magnets (PMs) are critically important due to their direct effect on torque production. However, the PMs are susceptible to irreversible demagnetization when exposed to thermal stresses, electrical faults (e.g., inter-turn short), environmental factors (e.g., oxidation, corrosion), and unbalanced loads [54]. In the case that PMs are irreversibly demagnetized, their flux reduces and, in some cases, becomes unbalanced, causing significant vibrations and noise as well as overall performance deterioration [54, 55].

This chapter investigates the application of parameter identification to fault diagnosis and condition monitoring of SMPM machines under demagnetization conditions. Specifically, an equivalent two-phase model and an online parameter identification strategy for a three-phase four-pole SMPM machine with two windings per phase under the magnet demagnetization are presented. First, demagnetization is incorporated into the three-phase SMPM machine model by modeling the PM flux linkages from each magnet separately. Then, the equivalent two-phase model is formulated by mapping the three-phase dynamics into their two-phase equivalents, which are referenced to the rotor reference frame. Afterward, based on FEA simulations, the model's PM flux linkage is calibrated and validated for a Distributed Winding (DW) and a Concentrated Winding (CW) SMPM machine designs. Following the model validation, the parameter estimation strategy for fault detection and condition monitoring is discussed. In this section, a parameter estimator based on the standard SMPM dynamic model [80] is also presented as it is used as the baseline. Precisely, the linear

parametric models, the parameter identification strategy, and the sufficient conditions for accurate convergence are discussed for both estimators. Afterward, the performance of both estimators is assessed through simulations and co-simulations. Finally, remarks specific to the information for detecting demagnetization are discussed, and a summary of the chapter is presented.

4.2 Modeling SMPM Machines with Magnet Demagnetization

The general equation describing the three-phase electrical dynamics of an ungrounded, wye-connected Surface-Mount Permanent Magnet (SMPM) machine is given by [56]:

$$\begin{bmatrix} v_a \\ v_b \\ v_c \end{bmatrix} = \begin{bmatrix} R & 0 & 0 \\ 0 & R & 0 \\ 0 & 0 & R \end{bmatrix} \begin{bmatrix} i_a \\ i_b \\ i_c \end{bmatrix} + \begin{bmatrix} L_s & L_m & L_m \\ L_m & L_s & L_m \\ L_m & L_m & L_s \end{bmatrix} \frac{d}{dt} \begin{bmatrix} i_a \\ i_b \\ i_c \end{bmatrix} + \frac{d}{dt} \begin{bmatrix} \lambda_{PM,a} \\ \lambda_{PM,b} \\ \lambda_{PM,c} \end{bmatrix}, \tag{4.1}$$

with

$$i_0 = \frac{1}{3}(i_a + i_b + i_c) = 0, \tag{4.2}$$

where the subscripts a, b, and c denote each of the three phases, i_x and v_x are the three-phase currents and voltages ($x = \{a, b, c\}$), i_0 is the zero-sequence current component, R is the stator winding resistance, L_s and L_m are the stator self and mutual inductances, and $\lambda_{PM,x}$ is the PM flux linkage with respect to phase x.

When the machine is operating under healthy conditions, the dynamics presented in Eq. (4.1) are typically studied using the standard equivalent two-phase model. In this model, the electrical dynamics are expressed with respect to a moving coordinate system, known as the rotor reference frame, whose direct axis is aligned with the PM flux linkage vector [56],

$$\boldsymbol{L}\frac{d\vec{i}^r}{dt} = -\boldsymbol{R}\vec{i}^r - \omega_{re}\boldsymbol{J}(\boldsymbol{L}\vec{i}^r + \vec{\lambda}^r_{PM}) + \vec{v}^r, \tag{4.3}$$

and the three-phase electromagnetic torque is given by

$$\tau_{3\phi} = \frac{3N_p}{4}\Lambda_{PM} i^r_q, \tag{4.4}$$

with $\boldsymbol{R} = R\boldsymbol{I}$, $\boldsymbol{L} = L\boldsymbol{I}$, and $\vec{\lambda}^r_{PM} = \begin{bmatrix} \Lambda_{PM} & 0 \end{bmatrix}^T$, where the superscript $(\cdot)^r$ denotes

that the variable is in the rotor frame, $\vec{i}^r$ and $\vec{v}^r$ are the equivalent two-phase current and voltage vectors (i.e., $\vec{x}^r = \begin{bmatrix} x_d^r & x_q^r \end{bmatrix}^T$ with x as the variable), $\boldsymbol{I}$ is the 2x2 identity matrix, $L = L_s - L_m$ is the two-phase equivalent stator winding self-inductance, Λ_{PM} is the PM flux linkage, ω_{re} is the electrical rotor speed (i.e., $\omega_{re} = \frac{N_p}{2}\omega_r$, where ω_r is the mechanical rotor speed and N_p is the number of poles), and $\boldsymbol{J}$ is the counterclockwise ninety degree rotation matrix (See Eq. (2.4)).

PM demagnetization in an SMPM machine can affect evenly or unevenly the different magnets. If all magnets are evenly demagnetized, the overall PM flux decreases, and no additional harmonics develop as the rotor flux remains balanced. When the magnets are unevenly demagnetized, the PM flux not only reduces but becomes unbalanced. In terms of performance, the PM flux reduction causes a decrease in the torque for a given current, while its imbalance generates additional harmonics that result in added noise and vibrations. Under magnet demagnetization, the standard model presented in Eqs. (4.3) and (4.4) is no longer valid unless all magnets are evenly demagnetized. In this section, a control-oriented SMPM machine model that can capture dynamic behavior under both healthy and demagnetized conditions is derived for analysis and simulation purposes under the following assumptions:

A. The machine has a smooth air gap (i.e., slot effects are not considered), is balanced in construction, and is connected in an ungrounded-wye configuration.

B. Magnetic saturation, eddy current, and hysteresis effects are neglected.

C. Stator and rotor irons have infinite permeability. The magnets and air have equal permeability.

D. Individual magnets are uniformly demagnetized (i.e., uneven demagnetization within an individual magnet is not considered).

The first three assumptions (A-C) are commonly used for control-oriented models [56] while the last assumption (D) restricts the scope of the model to even and uneven demagnetization affecting the magnets. From these assumptions, we point out for assumption B that the magnetics of an SMPM machine are typically linear given the large effective air gap between stator and rotor irons. We note that, regarding assumption C, the permeability of most PM materials (e.g., SmCo, NdFeB) is close to that of free space, and the permeability of most iron alloys used for the stator and rotor irons is much higher than that of free space. Also, we emphasize that assumption D is for analysis purposes, since the goal of the model is to capture asymmetries in

the overall PM flux linkage. These asymmetries will happen regardless of whether the individual magnets are evenly or unevenly demagnetized.

In the following analysis, the model is derived based on a four-pole three-phase SMPM machine with two coils per phase, as shown in Fig. 4.1. Note that the analysis can be applied to series- and parallel-connected windings and similar analysis can be performed on other SMPM machines with different winding configurations and numbers of poles. The model captures the decrease in the overall PM flux linkage, which is always present regardless of the SMPM machine design. Moreover, the model also captures the dynamics associated with additional harmonics in the PM flux linkage due to demagnetization. However, as will be seen, these additional harmonics in the PM flux linkage depend on the SMPM machine design. In this sense, analyzing SMPM machines under magnet demagnetization has to be done on a case-by-case basis since the dynamic behavior differs with different pole numbers and winding configurations [60]. Regarding SMPM machines with parallel-connected windings, we note that, under magnet demagnetization, the parallel-connected coils will experience circulating currents when the magnets are unevenly demagnetized.

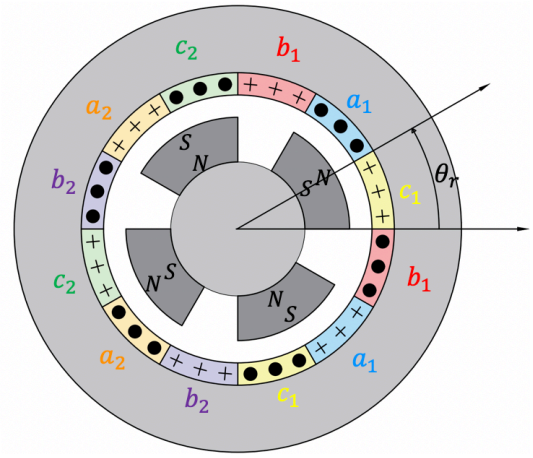

Figure 4.1: Cross-section of simplified three-phase four-pole SMPM machine with two windings per phase.

4.2.1 Modeling Permanent Magnet Demagnetization

In this section, a simple equivalent two-phase parametric model that captures demagnetization affecting evenly and unevenly the PMs is formulated for a three-phase four-pole SMPM machine with two windings per phase. The derivation starts with the formulation of a three-phase SMPM machine model as it captures the behavior

of the physical machine, making it easier to incorporate the fault. In the model, magnet demagnetization is captured in the PM flux linkage. Using superposition, the three-phase PM flux linkages are constructed from the individual contribution that each magnet provides to the different coils in each phase. After deriving the three-phase model, the equivalent two-phase model is formulated using the Clarke and Park Transforms. In this equivalent two-phase dynamic model, two parameters are identified from the harmonic content in the PM flux linkages, which can be leveraged to detect magnet demagnetization.

4.2.1.1 Three-phase SMPM machine model under PM demagnetization

A three-phase SMPM machine model under PM demagnetization is formulated in this section. Specifically, in Eq. (4.1), demagnetization solely affects the three-phase PM flux linkages. This section starts by constructing the three-phase PM flux linkages from the individual contribution that each magnet provides to the different coils in each phase so that demagnetization can be captured.

The net PM flux linkage in a coil corresponds to the superposition of the individual contribution of each magnet to each coil, and is given by

$$\lambda_{PM,x_i} = \sum_{k=1}^{4} \lambda_{PM_k,x_i}, \tag{4.5}$$

where x_i denotes the coil (e.g., a_1, a_2, b_1, b_2, c_1, or c_2), the subscript i denotes each of the coils that form a phase, the subscript k denotes the magnet (e.g., 1, 2, 3, or 4), λ_{PM,x_i} corresponds to the net PM flux with respect to the winding x_i, and λ_{PM_k,x_i} is the flux linkage in winding x_i due to magnet k.

The flux produced by each magnet linking the coils can be studied by inspection. Based on assumptions C and D, the flux is assumed to cross the air gap uniformly and radially. Therefore, two regions can be identified for the flux produced by a magnet, as shown in Fig. 4.2. In the sector that corresponds to the magnet, the flux radially crosses the air gap based on the magnet's polarity. Similarly, the remainder sector serves as the return, and, therefore, the magnet's flux crosses the air gap in the opposite direction based on the magnet's polarity. In other words, the fluxes crossing the air gap in both regions have opposite directions and sum to zero.

The flux linkage in each coil corresponds to the net flux crossing the air gap in the coil's sector. Three regions can be identified based on the magnet's position with respect to the coil, as the magnet can be fully inside, crossing, or entirely outside of

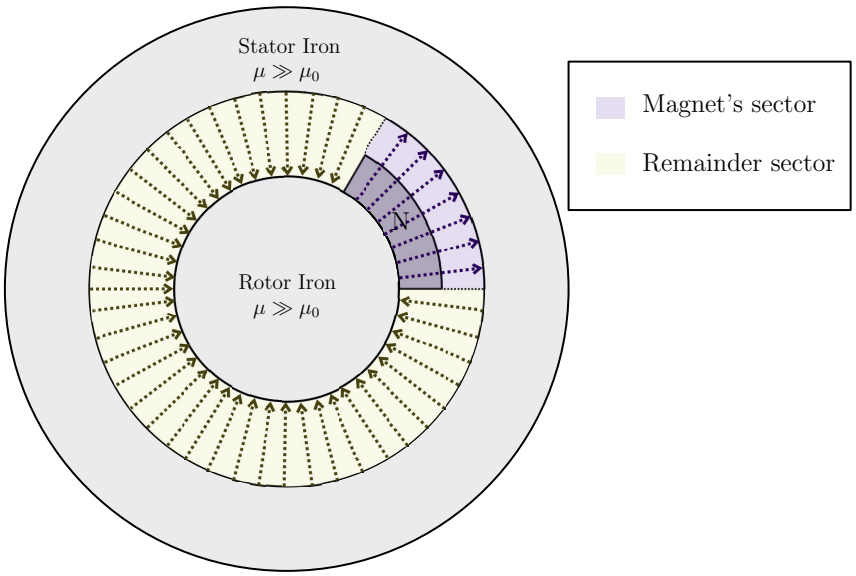

Figure 4.2: Theoretical flux produced in the air gap by a magnet.

the coil sector. This can be approximated with a trapezoidal waveform, as shown in Fig. 4.3. In order to facilitate analysis, it is helpful to express the PM flux linking a coil in terms of its Fourier components. Using Fourier Series, the PM flux linking a coil can be expressed as follows:

$$\lambda_{PM,k,x_i} = \Lambda_K \sum_{h=1}^{N_h} a_h \cos(h(\theta_r + \phi_{PM_k,x_i})), \tag{4.6}$$

where

$$a_h = \frac{4}{\pi h^2}\left(\frac{\Lambda_{in} - \Lambda_{out}}{\beta - \alpha}\right) \sin\left(\frac{(\alpha+\beta)h}{2}\right) \sin\left(\frac{(\beta-\alpha)h}{2}\right), \tag{4.7}$$

α is the position at which the magnet starts to leave the inside of the coil sector, β is the position at which the whole magnet reaches the outside of the coil sector, Λ_{in} is the net coil flux when the magnet is fully inside the coil region, Λ_{out} is the net coil flux when the magnet is entirely outside the coil region, a_h is the h-harmonic Fourier coefficient of the flux linkage produced by a healthy magnet, N_h is the total number of harmonics, ϕ_{k,x_i} is the phase shift for the corresponding magnet and winding, and $\Lambda_K \leq 1$ is the normalized flux amplitude produced by the magnet k. Note that Λ_K equal to unity represents a healthy magnet while Λ_K less than unity captures a demagnetized magnet.

Since the machine is balanced in construction, the net PM flux linkage with respect

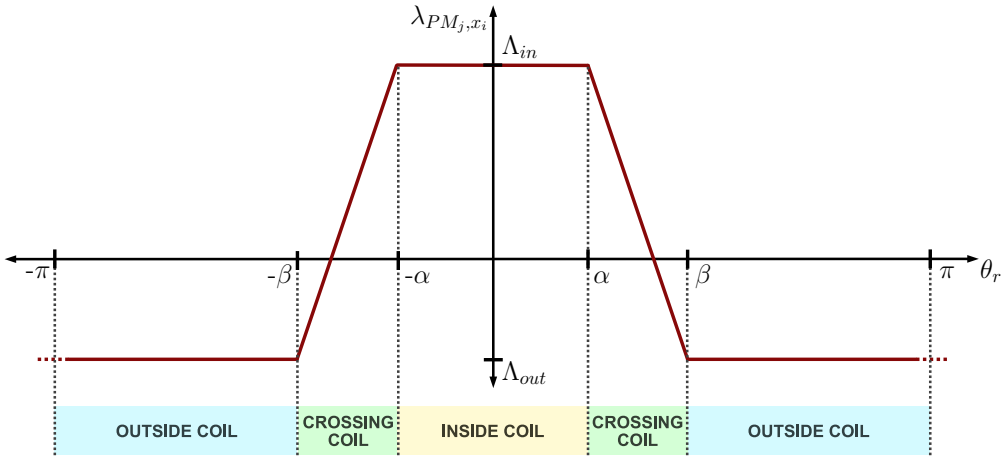

Figure 4.3: Trapezoidal approximation of the flux produced in a coil due to an individual magnet (assuming $\phi_{PM_k,x_i} = 0$).

to each phase is given by

$$\lambda_{PM,x} = K(\lambda_{PM,x_1} + \lambda_{PM,x_2}), \tag{4.8}$$

with

$$K = \begin{cases} 1, & \text{if } i_x = i_{x_1} = i_{x_2}, \text{ and } v_x = v_{x_1} + v_{x_2} \text{ (for series connection)} \\ \frac{1}{2}, & \text{if } v_x = v_{x_1} = v_{x_2}, \text{ and } i_x = i_{x_1} + i_{x_2} \text{ (for parallel connection)} \end{cases}$$

where i_{x_i} and v_{x_i} represent the current and voltage corresponding to the coil x_i, and K is a factor taking into account the series/parallel connections.

Considering that the magnets' permeability is close to that of air (assumption C), the magnets can be treated as air when calculating inductances, and, hence, demagnetization does not affect inductances. Thus, the electrical three-phase SMPM machine dynamics under magnet demagnetization can be described using Eq. (4.1) with the demagnetization effect captured in the PM flux linkages as

$$\lambda_{PM,a} = 2K \sum_{h=1}^{N_h} a_{2h} \cos(h\theta_{re}) \Big(\Lambda_{13} - \Lambda_{24} \cos(h\pi) \Big) \Big), \tag{4.9}$$

$$\lambda_{PM,b} = 2K \sum_{h=1}^{N_h} a_{2h} \cos\left(h\Big(\theta_{re} - \frac{2\pi}{3}\Big)\right) \Big(\Lambda_{13} - \Lambda_{24} \cos(h\pi) \Big) \Big), \tag{4.10}$$

$$\lambda_{PM,c} = 2K \sum_{h=1}^{N_h} a_{2h} \cos\Big(h\Big(\theta_{re} + \frac{2\pi}{3}\Big)\Big)\Big(\Lambda_{13} - \Lambda_{24}\cos(h\pi)\Big)\Big), \tag{4.11}$$

where $\Lambda_{13} = \Lambda_1 + \Lambda_3$ and $\Lambda_{24} = \Lambda_2 + \Lambda_4$ correspond to the total normalized flux produced by the north and south poles, respectively, and $\theta_{re} = \frac{N_p}{2}\theta_r$ is the electrical rotor position, with $N_p = 4$ for a four-pole machine. Note that, for the four-pole SMPM machine design, the PM flux linkage can solely have even harmonics, as shown in Eqs. (4.9), (4.10), and (4.11).

Since the PM flux linkages are modeled separately (Eq. (4.6)), this model can capture the operation of the SMPM machine under demagnetization affecting evenly or unevenly the different magnets, as well as healthy conditions. Note that this model can be easily implemented because all operating health conditions can be achieved by modifying the corresponding PM flux amplitude(s) accordingly (i.e., Λ_k with $k = 1, 2, 3, 4$). Moreover, while the winding configuration is required to formulate the PM flux linkages, the resistance and inductance information for different windings is not required. In other words, the resistance and inductance values used in the model are those of the three-phase standard model (Eq. (4.1)).

4.2.1.2 Equivalent two-phase SMPM machine model under permanent magnet demagnetization in the rotor reference frame

The three-phase electrical SMPM dynamics provide little information about the fault and cannot be implemented in simulation unless a constraint that specifies the phase configuration (i.e., delta or wye) is considered. Since the SMPM machine is assumed to be ungrounded-wye connected, the Clarke Transform [81] can be used to impose the zero current constraint (Eq. (4.2)) while mapping the three-phase variables into their equivalent two-phase stationary ($\alpha - \beta$) variables. Afterwards, by using the Park Transform [82], these variables can be mapped to the aforementioned rotor reference frame in which the electrical dynamics of the SMPM machine under PM demagnetization are given by,

$$\begin{aligned} \begin{bmatrix} v_d^r \\ v_q^r \end{bmatrix} &= \begin{bmatrix} R & 0 \\ 0 & R \end{bmatrix} \begin{bmatrix} i_d^r \\ i_q^r \end{bmatrix} + \begin{bmatrix} L & 0 \\ 0 & L \end{bmatrix} \frac{d}{dt} \begin{bmatrix} i_d^r \\ i_q^r \end{bmatrix} + \\ \omega_{re} \begin{bmatrix} 0 & -L \\ L & 0 \end{bmatrix} \begin{bmatrix} i_d^r \\ i_q^r \end{bmatrix} &+ \omega_{re} \begin{bmatrix} -\lambda_{PM,q}^r \\ \lambda_{PM,d}^r \end{bmatrix} + \frac{d}{dt} \begin{bmatrix} \lambda_{PM,d}^r \\ \lambda_{PM,q}^r \end{bmatrix}, \end{aligned} \tag{4.12}$$

where

$$\lambda^r_{PM,d} = \frac{4K}{3}\sum_{h=1}^{N_h} a_{2h}\Bigg(\Big(1-\cos\Big(\frac{2\pi h}{3}\Big)\Big)\cos(h\theta_{re})\cos(\theta_{re})+ \sqrt{3}\sin\Big(\frac{2\pi h}{3}\Big)\sin(h\theta_{re})\sin(\theta_{re})\Bigg)\Big(\Lambda_{13}-\Lambda_{24}\cos(h\pi)\Big), \tag{4.13}$$

$$\lambda^r_{PM,q} = \frac{4K}{3}\sum_{h=1}^{N_h} a_{2h}\Bigg(-\Big(1-\cos\Big(\frac{2\pi h}{3}\Big)\Big)\cos(h\theta_{re})\sin(\theta_{re})+ \sqrt{3}\sin\Big(\frac{2\pi h}{3}\Big)\sin(h\theta_{re})\cos(\theta_{re})\Bigg)\Big(\Lambda_{13}-\Lambda_{24}\cos(h\pi)\Big). \tag{4.14}$$

Equations (4.13) and (4.14) reveal that even harmonics that are multiples of three cannot exist. Moreover, in the harmonic content, two types of terms can be identified in which Λ_{13} and Λ_{24} either add or subtract. Therefore, some harmonics only exist when the north and south poles are unevenly affected by demagnetization.

In the next section, the SMPM machine model under demagnetization is compared against an FEA model. As will be seen, the winding configuration can affect the harmonic content that the machine will experience under uneven demagnetization.

4.2.2 Calibration and Validation of Proposed Model

In this section, numerical simulations of the proposed SMPM model are presented for a double-layer CW and a single-layer DW SMPM machine. The magnetic parameters are calibrated and validated using FEA simulations. The SMPM machines used in the simulations are shown in Figs. 4.4 and 4.5, and their parameters are presented in Table 4.1. The FEA simulations are performed using *Maxwell*, which is a commercial simulation software from *Ansoft Corporation*. During these FEA simulations, the SMPM machine operates at zero current and a constant speed of $1000RPM$.

4.2.2.1 Calibration of Trapezoidal Approximation for PM Flux Linkage

In this section, the trapezoidal approximation presented in Eq. (4.6) is calibrated based on the FEA simulation results of the four-pole CW and DW SMPM machines. The trapezoidal approximation captures the flux linkage in a coil produced by one magnet. Hence, for calibration purposes, the FEA simulation models all coils separately and only one north magnet (PM_1). Table 4.2 presents the calibrated parameters for the trapezoidal approximation used with the CW and DW SMPM machines.

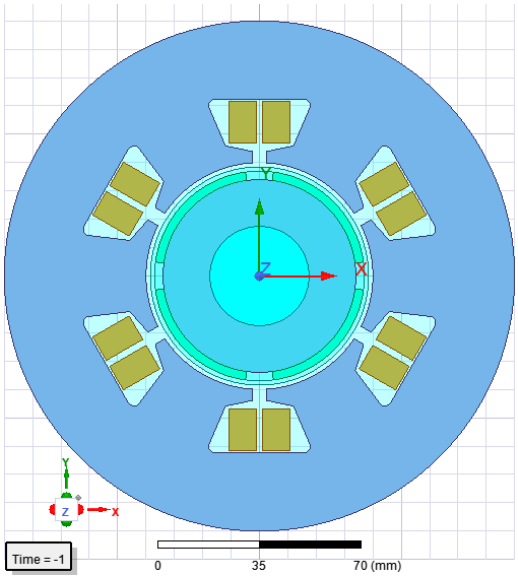

Figure 4.4: Cross-section of double-layer CW SMPM machine.

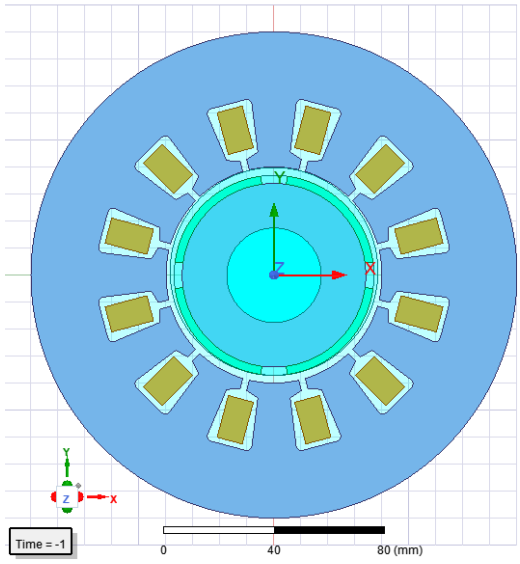

Figure 4.5: Cross-section of single-layer DW SMPM machine.

Table 4.1: SMPM machine parameters for FEA simulations

Parameter	Double-layer CW SMPM	Single-layer DW SMPM
Number of poles	4	4
Number of slots	6	12
Conductors per slot	220	100
Parallel branches	1	1
Magnet material	NdFe30	NdFe30
Steel type	Iron	Iron
Stacking factor	0.95	0.95
Stator outer diameter [mm]	180	180
Stator inner diameter [mm]	80	80
Rotor outer diameter [mm]	74	74
Magnet thickness [mm]	3	3
Magnet coverage coefficient	0.83	0.83
Machine length [mm]	80	80

Figs. 4.6 and 4.7 show the results for the flux linkage in coil a_1 produced by PM_1 for the CW and DW SMPM machines, respectively. As seen in the Figs. 4.6 and 4.7, the trapezoidal function is calibrated to reasonably match the FEA results.

Table 4.2: Parameters for trapezoidal approximation

Parameter	Double-layer CW SMPM	Single-layer DW SMPM
Magnet coverage (γ)	74.7°	74.7°
α	7.35°	7.65°
β	67.35°	82.35°
Λ_{in}	$-0.1407V \cdot s$	$-0.1519V \cdot s$
Λ_{out}	$0.03699V \cdot s$	$0.05073V \cdot s$

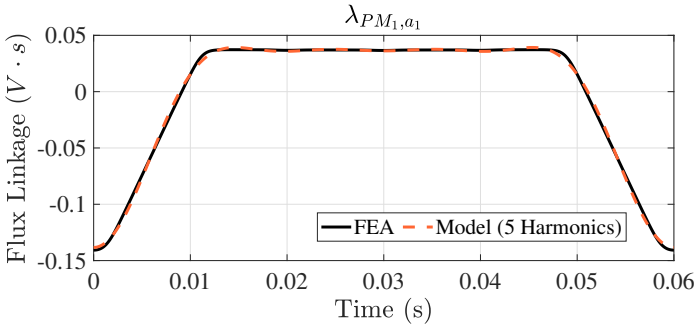

Figure 4.6: Flux linkage in coil a_1 produced by PM_1 for double-layer CW SMPM machine.

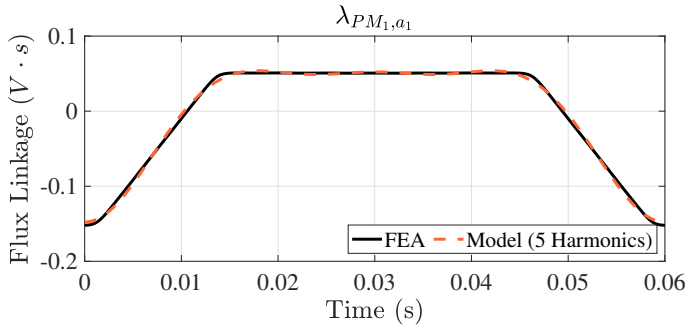

Figure 4.7: Flux linkage in coil a_1 produced by PM_1 for single-layer DW SMPM machine.

4.2.2.2 Validation of PM Flux Linkage

Based on the previous calibration, the PM flux linkage expressions in Eq. (4.13) and (4.14) are validated against FEA simulations. Figures 4.8 and 4.9 show the

simulation results for the CW and DW SMPM machines, respectively. The equivalent two-phase PM flux linkages under healthy and magnet demagnetization conditions are presented for one mechanical period. Note that, under PM demagnetization, a north pole is assumed completely demagnetized (i.e., $\Lambda_1 = 0$).

Inspection of Figs. 4.8 and 4.9 reveal that the model matches the FEA results with reasonable accuracy for both CW and DW cases. As seen in Figs. 4.8 and 4.9, the two-phase PM flux linkages behave similarly under healthy conditions for the CW and DW SMPM machines. In contrast, the PM flux linkage decreases and shows additional harmonics for the CW SMPM machine under PM demagnetization, while the PM flux linkage solely reduces for the DW case. The reason behind their difference is due to their winding configuration. The angular distance between the centers of the two sides of a coil (a.k.a, coil span) is 90 degrees (180 electrical degrees) for the DW and 60 degrees (120 electrical degrees) for the CW design, respectively. Inspection of Eq. (4.7) reveals that the coefficients that are multiples of four become zero when the machine has 180 electrical degrees between the two sides of its coils. As a consequence, the DW SMPM machine does not present new harmonics under demagnetization.

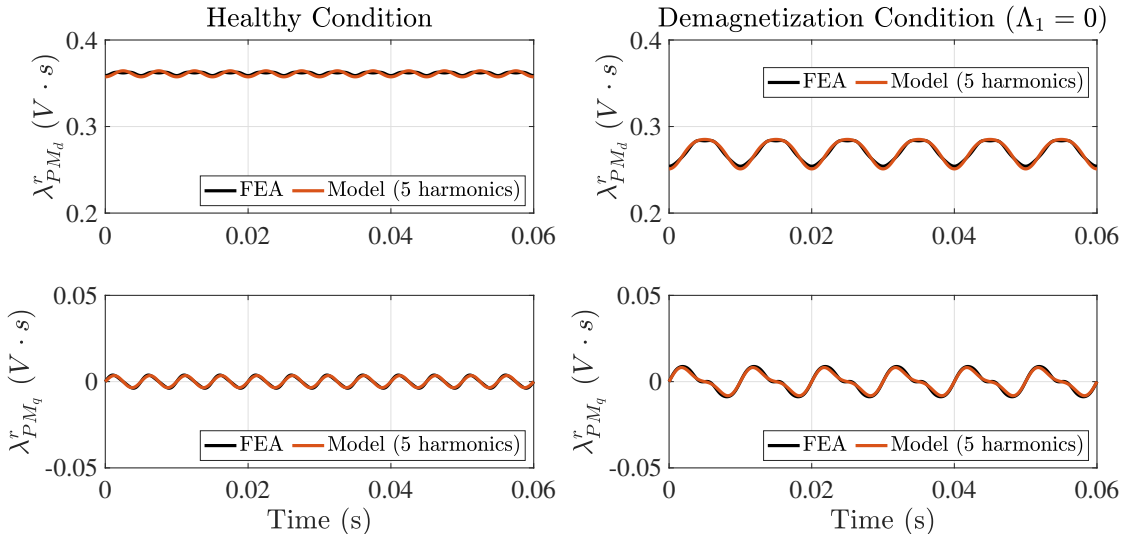

Figure 4.8: Comparison of the proposed model and FEA results of the CW SMPM machine for the PM flux linkage under healthy (left) and demagnetized (right) conditions.

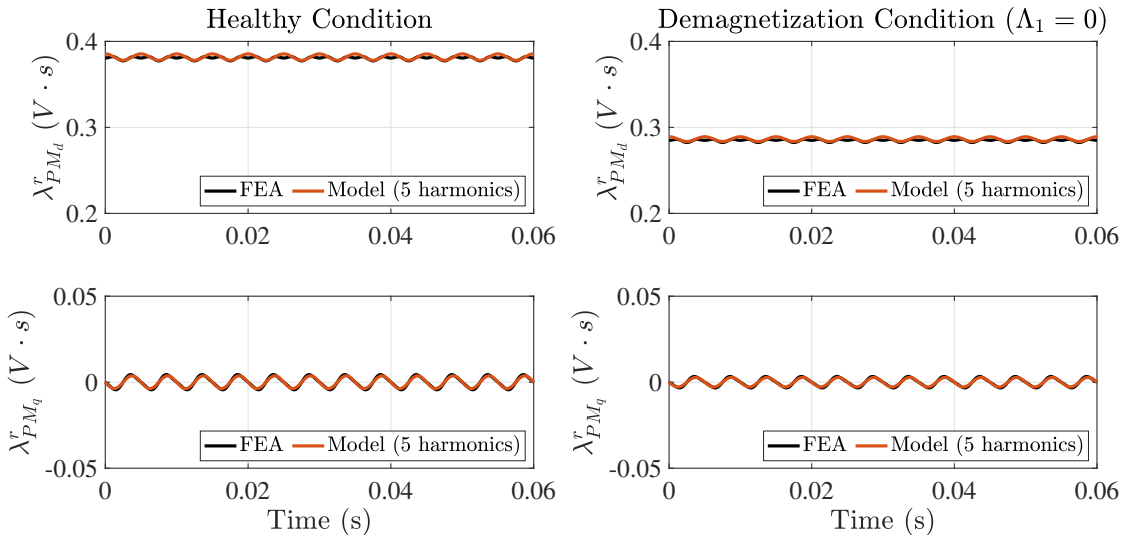

Figure 4.9: Comparison of the proposed model and FEA results of the DW SMPM machine for the PM flux linkage under healthy (left) and demagnetized (right) conditions.

4.3 Parameter Identification for Fault Diagnosis and Condition Monitoring of SMPM Machines under Magnet Demagnetization

This section presents a parameter estimator for fault detection based on the model from Eq. (4.12). Additionally, an estimator based on the standard model from Eq. (4.3) is presented as it will be used as the baseline. First, parameterizations required to formulate the parameter estimators based on the standard and proposed equivalent two-phase models are presented. In both cases, the parameter estimators are based on a linear parameterization of the filtered SMPM machine dynamics, which has the following form:

$$\vec{z} = \mathbf{\Phi}^T \vec{\theta}, \tag{4.15}$$

where $\vec{z}$ is the observation (i.e., measurement), $\vec{\theta}$ is the parameter vector, and $\mathbf{\Phi}$ is the regressor matrix. Specifically, a parameterization that includes a specific parameter related to the demagnetization condition is formulated based on the SMPM machine model presented in Eq. (4.12). Afterward, the parameter identification algorithm used for both parameter estimators is presented. This section ends with an analysis of the conditions in which the input signals ensure PE.

4.3.1 Parametric Models

4.3.1.1 Parametric Model based on Standard Dynamics

The standard-model-based parameter estimator is formulated using the following linear parameterization of the filtered SMPM dynamics from Eq. (4.3):

$$\begin{aligned}
\vec{z} &= \begin{bmatrix} z_d & z_q \end{bmatrix}^T = \{\mathcal{F}(s)\} \begin{bmatrix} v_d^r & v_q^r \end{bmatrix}^T, \\
\vec{\theta} &= \begin{bmatrix} R & L & \Lambda_{PM} \end{bmatrix}^T, \\
\mathbf{\Phi}^T &= \begin{bmatrix} \vec{\phi}_d^{\,T} \\ \vec{\phi}_q^{\,T} \end{bmatrix} = \{\mathcal{F}(s)\} \begin{bmatrix} i_d^r & (\frac{d}{dt} i_d^r - \omega_{re} i_q^r) & 0 \\ i_q^r & (\omega_{re} i_d^r + \frac{d}{dt} i_q^r) & \omega_{re} \end{bmatrix},
\end{aligned} \tag{4.16}$$

where $\{\cdot\}$ denotes a dynamic operator with transfer function "$\cdot$" and $\{\mathcal{F}(s)\} = \frac{\gamma}{s+\gamma}$ is a first-order low-pass filter with $\gamma > 0$. Note that filtered signals are used in order to avoid the derivatives appearing as signals in $\mathbf{\Phi}$.

4.3.1.2 Parametric Model for Fault Diagnosis and Condition Monitoring of SMPM Machines under Magnet Demagnetization

The equivalent two-phase SMPM machine model in the rotor reference frame from Eqs. (4.12), (4.13), and (4.14) captures the dynamic behavior under demagnetization and healthy conditions. However, its application to fault diagnosis and condition monitoring requires a more convenient parameterization. Demagnetization affects the PM flux linkage by decreasing its amplitude and adding harmonic content. Specifically, Eqs. (4.13) and (4.14) show that the north and south poles' PM flux linkages either add or subtract. The summation terms of the individual PM flux linkages directly relate to the standard-model parameter that captures the overall PM flux linkage. Regarding condition monitoring and fault diagnosis, the decrease in this total PM flux linkage indicates demagnetization. However, the total PM flux linkage also decreases with increased PM temperature, and so a method to distinguish the root cause is required. The subtraction terms between the north and south PM flux linkages refer to demagnetization asymmetries. In other words, these subtraction terms capture demagnetization in which the north and south magnets are unevenly demagnetized. These subtraction terms can provide a useful indicator for demagnetization detection and monitoring. While the individual PM flux linkages vary with PM temperature, their subtraction is insensitive, assuming magnets share similar temperatures. Parameters that model both the overall PM flux linkage and the asymmetries between

north and south PM flux linkages are of interest as they can be incorporated into a parameter identification-based fault detection strategy.

By approximating the model dynamics from Eq. (4.12) with low-order harmonics (i.e., second and fourth harmonics), the dynamics of the SMPM machine are reduced to:

$$\begin{aligned}\begin{bmatrix} v_d^r \\ v_q^r \end{bmatrix} = \begin{bmatrix} R & 0 \\ 0 & R \end{bmatrix} \begin{bmatrix} i_d^r \\ i_q^r \end{bmatrix} + \begin{bmatrix} L & 0 \\ 0 & L \end{bmatrix} \frac{d}{dt} \begin{bmatrix} i_d^r \\ i_q^r \end{bmatrix} + \omega_{re} \begin{bmatrix} 0 & -L \\ L & 0 \end{bmatrix} \begin{bmatrix} i_d^r \\ i_q^r \end{bmatrix} \\ + \omega_{re}\Lambda_{PM} \begin{bmatrix} 0 \\ 1 \end{bmatrix} - 2\omega_{re}\Delta_{PM} \begin{bmatrix} \sin(3\theta_{re}) \\ \cos(3\theta_{re}) \end{bmatrix},\end{aligned} \tag{4.17}$$

where the PM flux linkage (Λ_{PM}) and the asymmetry term (Δ_{PM}) are given by

$$\begin{aligned}\Lambda_{PM} &= 2a_2K(\Lambda_1 + \Lambda_2 + \Lambda_3 + \Lambda_4), \\ \Delta_{PM} &= 2a_4K(\Lambda_1 - \Lambda_2 + \Lambda_3 - \Lambda_4).\end{aligned}$$

Note that this model can capture variations in the PM flux linkage using Λ_{PM} and asymmetries between the north and south PM flux linkages with the asymmetry term Δ_{PM}.

Afterward, the linear parameterization of the proposed dynamics from Eq. (4.17) utilized to formulate the parameter estimator is given by

$$\begin{aligned}\vec{z} &= \begin{bmatrix} z_d & z_q \end{bmatrix}^T = \{\mathcal{F}(s)\} \begin{bmatrix} v_d^r & v_q^r \end{bmatrix}^T, \\ \vec{\theta} &= \begin{bmatrix} R & L & \Lambda_{PM} & \Delta_{PM} \end{bmatrix}^T, \\ \mathbf{\Phi} &= \begin{bmatrix} \vec{\phi_d} & \vec{\phi_q} \end{bmatrix}, \\ \vec{\phi_d} &= \{\mathcal{F}(s)\} \begin{bmatrix} i_d^r \\ (\frac{d}{dt}i_d^r - \omega_{re}i_q^r) \\ 0 \\ -2\omega_{re}\sin(3\theta_{re}) \end{bmatrix}, \vec{\phi_q} = \{\mathcal{F}(s)\} \begin{bmatrix} i_q^r \\ (\omega_{re}i_d^r + \frac{d}{dt}i_q^r) \\ \omega_{re} \\ -2\omega_{re}\cos(3\theta_{re}) \end{bmatrix}.\end{aligned} \tag{4.18}$$

4.3.2 Parameter Identification Algorithm

The projection algorithm is employed to formulate the parameter estimators, as accounting for discrete-time implementation effects is crucial for accuracy. This algorithm [93] aims at minimizing the Euclidean norm between consecutive parameter estimates subject to the model in Eq. (4.15), and the estimated parameters, $\vec{\theta}$, are

derived as follows:

$$\hat{\vec{\theta}}[k] = \hat{\vec{\theta}}[k-1] + \frac{a\vec{\phi}_d[k]\big(z_d[k] - \vec{\phi}_d^T[k]\hat{\vec{\theta}}[k-1]\big)}{c + \vec{\phi}_d^T[k]\vec{\phi}_d[k]} + \frac{a\vec{\phi}_q[k]\big(z_q[k] - \vec{\phi}_q^T[k]\hat{\vec{\theta}}[k-1]\big)}{c + \vec{\phi}_q^T[k]\vec{\phi}_q[k]}, \quad (4.19)$$

where $c > 0$ is a small constant to avoid division by zero, $0 < a < 2$ is the adaptation gain, and $k = 1, 2, ...$ is the time index. We note that other algorithms (e.g., least-squares) can be used for formulating the parameter estimator, and that the goal of this work is to compare the performance of the models rather than different estimation algorithms.

4.3.3 Persistently Exciting Inputs

This section investigates the sufficient conditions in which accurate parameter estimation is achieved for the estimators based on the standard and demagnetization models presented in Section 4.3.1. Since the parameter identification algorithm is formulated in discrete time, the PE conditions should be studied using Definition 2.2. However, a connection can be made between the continuous- and discrete-time PE properties. Assuming the regressor is sampled with a frequency more than twice the highest-frequency component (Theorem 2.3), the discrete- and continuous-time regressors carry the same information. Hence, if the continuous-time signal is PE, its discrete-time version is also PE. Based on this, the continuous-time definition of persistent excitation presented in Section 2.7 (Definition 2.1) will be used to determine the sufficient conditions for PE. Note that, in the case of the estimator based on the standard model (Eq. (4.16)) and demagnetization model (Eq. (4.18)), the integral of the matrix $\mathbf{\Phi}(\tau)\mathbf{\Phi}^\intercal(\tau)$ can be written as:

$$\frac{1}{T_0}\int_t^{t+T_0} \mathbf{\Phi}(\tau)\mathbf{\Phi}^\intercal(\tau)d\tau = \frac{1}{T_0}\int_t^{t+T_0} \vec{\phi}_d(\tau)\vec{\phi}_d^\intercal(\tau)d\tau + \frac{1}{T_0}\int_t^{t+T_0} \vec{\phi}_q(\tau)\vec{\phi}_q^\intercal(\tau)d\tau. \quad (4.20)$$

Therefore, a sufficient condition to guarantee that the estimated parameters converge to their actual values is that $\vec{\phi}_d$, $\vec{\phi}_q$, or both are persistently exciting.

The torque and electrical rotor speed will be assumed constant to simplify the analysis. These assumptions fairly represent a "worst-case" scenario as time-varying torque and electrical rotor speed will produce additional excitation and, hence, help

identification. Similarly, the analysis will utilize the healthy torque expression from Eq. (4.4), as the torque under demagnetization can have additional harmonic content aiding the estimation. Based on Eq. (4.4), the torque is solely a function of the quadrature-axis current. Hence, to avoid torque perturbations, the persistently exciting input required for accurate parameter identification is injected through the direct-axis current. A sinusoidal direct-axis current and a constant quadrature current will be assumed, which are given by:

$$i_d^r = A\sin(\omega t), \tag{4.21}$$

$$i_q^r = I_q, \tag{4.22}$$

where A and ω are the amplitude and frequency of the injected PE signal, and I_q is the corresponding quadrature-axis current that achieves the desired torque (i.e., $I_q = \frac{4\tau}{3N_p\Lambda_{PM}}$). Note that, in practice, these currents are implemented as the reference signals ($\tilde{i}_d^r$,$\tilde{i}_q^r$) that the control algorithm aims to track. In the following analysis, we assume a good control performance so that $i_d^r \approx \tilde{i}_d^r$, $i_q^r \approx \tilde{i}_q^r$. Additionally, the low-pass filter ($\{\mathcal{F}(s)\}$) will be neglected in the analysis as it is only used to avoid differentiation and has no effect on the results.

Remark 4.1. The parameter estimators can suffer convergence issues as orders of magnitude typically separate the machine parameters, causing poor numerical conditioning. Hence, for pre-conditioning purposes, the rows of the regressor matrix should be normalized so that the peak values are all around unity. Note that this scaling also affects the parameters.

4.3.3.1 Persistency of Excitation Analysis for Estimator based on Standard Dynamic Model

Based on the previous assumptions, the regressor of the standard-model-based parameter estimator (Eq. (4.16)) is given by:

$$\mathbf{\Phi}(t) = \begin{bmatrix} A\sin(\omega t) & I_q \\ A\omega\cos(\omega t) - \omega_{re} I_q & A\omega_{re}\sin(\omega t) \\ 0 & \omega_{re} \end{bmatrix}. \tag{4.23}$$

Note that the regressor is periodic with period $T = \frac{2\pi}{\omega}$. To obtain the conditions in which the integral of the matrix $\mathbf{\Phi}(\tau)\mathbf{\Phi}(\tau)^\intercal$ is uniformly positive definite, we calculate

its determinant:

$$\det\left(\frac{\omega}{2\pi}\int_0^{\frac{2\pi}{\omega}}\mathbf{\Phi}(\tau)\mathbf{\Phi}(\tau)^\intercal d\tau\right)=\frac{A^2\omega_{re}^2}{4}\Big(A^2\omega^2+\omega_{re}^2(A^2+2I_q^2)\Big). \tag{4.24}$$

Thus, Eq. (4.24) shows that the regressor, $\mathbf{\Phi}(t)$, is persistently exciting if the following conditions are guarateed:

1. The rotor speed is non-zero (i.e., $\omega_r=\frac{\omega_{re}}{2}\neq 0$).
2. At least one sinusoidal component is injected into the direct-axis current (i.e., $A\neq 0$).

4.3.3.2 Persistency of Excitation Analysis for Estimator based on Proposed Dynamic Model

Similarly, based on the assumptions mentioned above, the estimator based on the proposed dynamics (Eq. (4.18)) has the regressor given by:

$$\mathbf{\Phi}=\begin{bmatrix} A\sin(\omega t) & I_q \\ A\omega\cos(\omega t)-\omega_{re}I_q & A\omega_{re}\sin(\omega t) \\ 0 & \omega_{re} \\ -2\omega_{re}\sin(3\omega_{re}t) & -2\omega_{re}\cos(3\omega_{re}t)\end{bmatrix} \tag{4.25}$$

Note that, in this case, the regressor is a function of the excitation and (electrical) rotor frequencies. Assuming that the regressor is periodic with $T_0=\frac{2\pi}{\omega_0}$, the integral of the matrix $\mathbf{\Phi}(\tau)\mathbf{\Phi}^\intercal(\tau)$ can be calculated using the interval $[0,T_0]$ as follows

$$\frac{1}{T_0}\int_0^{T_0}\mathbf{\Phi}(\tau)\mathbf{\Phi}(\tau)^\intercal d\tau=\begin{bmatrix}\frac{A^2}{2}+I_q^2 & 0 & \omega_{re}I_q & 0\\ 0 & \frac{A^2(\omega^2+\omega_{re}^2)}{2}+\omega_{re}^2I_q^2 & 0 & 0\\ \omega_{re}I_q & 0 & \omega_{re}^2 & 0\\ 0 & 0 & 0 & 4\omega_{re}^2\end{bmatrix}. \tag{4.26}$$

Afterward, the sufficient conditions for accurate identification are determined by calculating the determinant, which is given by:

$$\det\left(\frac{1}{T_0}\int_0^{T_0}\mathbf{\Phi}(\tau)\mathbf{\Phi}(\tau)^\intercal d\tau\right)=A^2\omega_{re}^4\Big(A^2\omega^2+\omega_{re}^2(A^2+2I_q^2)\Big). \tag{4.27}$$

Based on Eq. (4.27), the regressor, $\mathbf{\Phi}$, is persistently exciting if the following conditions are met:

1. The rotor speed is non-zero (i.e., $\omega_r = \frac{\omega_{re}}{2} \neq 0$).

2. At least one sinusoidal component is injected into the direct-axis current (i.e., $A \neq 0$).

As seen in this analysis, the estimator based on the demagnetization model requires the same excitation as the estimator based on the standard model. Typically, adding more parameters implies the need for more excitation to guarantee accurate convergence. However, for the estimator based on the demagnetization model, there is no need for additional excitation as the regressor terms associated with the asymmetry term are self-excited. Specifically, these regressor terms introduce sinusoids with a frequency equal to three times the electrical rotor speed, as long as the SMPM machine is spinning.

4.4 Simulation Results Assuming Linear Magnetics

The performance of the parameter estimators is evaluated by numerical simulations conducted in Matlab/Simulink for the CW and DW SMPM machines presented in Section 4.2.2 (Figs. 4.4 and 4.5). Both parameter estimators are investigated with different gains while the SMPM machines operate under healthy and demagnetized conditions using the model from Eq. (4.12). Under the demagnetized condition, Magnet 1 is assumed to be 100% demagnetized ($\Lambda_1 = 0$). In the simulations, the parameters are estimated while the SMPM machines operate at different current levels and a constant speed of $1000\,RPM$. Proportional-Integral (PI) regulators with cross-coupling compensation are used to regulate the two-phase currents in the rotor reference frame. Since torque is solely a function of quadrature current (Eq. (4.4)), a persistently exciting signal is injected in the direct axis to guarantee accurate parameter convergence [51, 80], which is given by

$$\tilde{i}_d^r = 10\sin(2\pi 40t), \tag{4.28}$$

where the tilde ($\tilde{\cdot}$) denotes a reference signal. The estimated parameters are assumed to have an initial 20% deviation from the actual, healthy parameters.

In the simulations the discrete-time behavior of an actual practical implementation is captured by modeling the PI-based controller and the parameter estimators with

a triggered subsystem which operates at $10kHz$, and the continuous-time SMPM dynamics are captured with a fixed time step of $2\mu s$ using *ode4*. The command voltages determined by the controller are converted into duty cycles using Space Vector Modulation (SVM) [83]. The SMPM machines are assumed to be driven by an ideal "average-value" Voltage-Source Inverter (VSI) which provides average-value voltages to the machine based on duty cycles using SVM. Table 4.3 presents the control, adaptation, and machine parameters.

Table 4.3: Control and adaptation parameters for simulation

Parameter	DW SMPM Machine	CW SMPM Machine
SMPM machine Parameters:		
R	0.785Ω	0.919Ω
L	$24.864mH$	$28.095mH$
Λ_{PM}	$0.38175V \cdot s$	$0.36142V \cdot s$
K	1	1
Control Parameters:		
K_p	24.864	28.095
K_i	0.0785	0.0919
V_{bus}	$480V$	$480V$
Switching frequency (f_{sw})	$10kHz$	$10kHz$
Sampling frequency (f_s)	$10kHz$	$10kHz$
Adaptation Parameters:		
a	0.002/0.001/0.0005	0.002/0.001/0.0005
c	1	1

4.4.1 Performance of the Parameter Estimator Based on Standard Dynamic Model

In Figs. 4.10 and 4.11, the performance of the parameter estimator from Eq. (4.16) under healthy and demagnetized conditions is presented for the DW and CW SMPM machines, respectively. In the figures, note that the black dashed line corresponds to the actual parameters. In the demagnetization case, the black dash line for the PM flux linkage corresponds to average value of the actual PM flux linkage. Specifically, under demagnetization, the PM flux linkage is reduced by 25% compared to the healthy case.

Regarding the DW SMPM machine, the parameters converge to their actual values for both healthy and demagnetized conditions. As shown in Fig. 4.10, the estimator can track the 25% reduction in the PM flux linkage. Similar behavior is seen in both

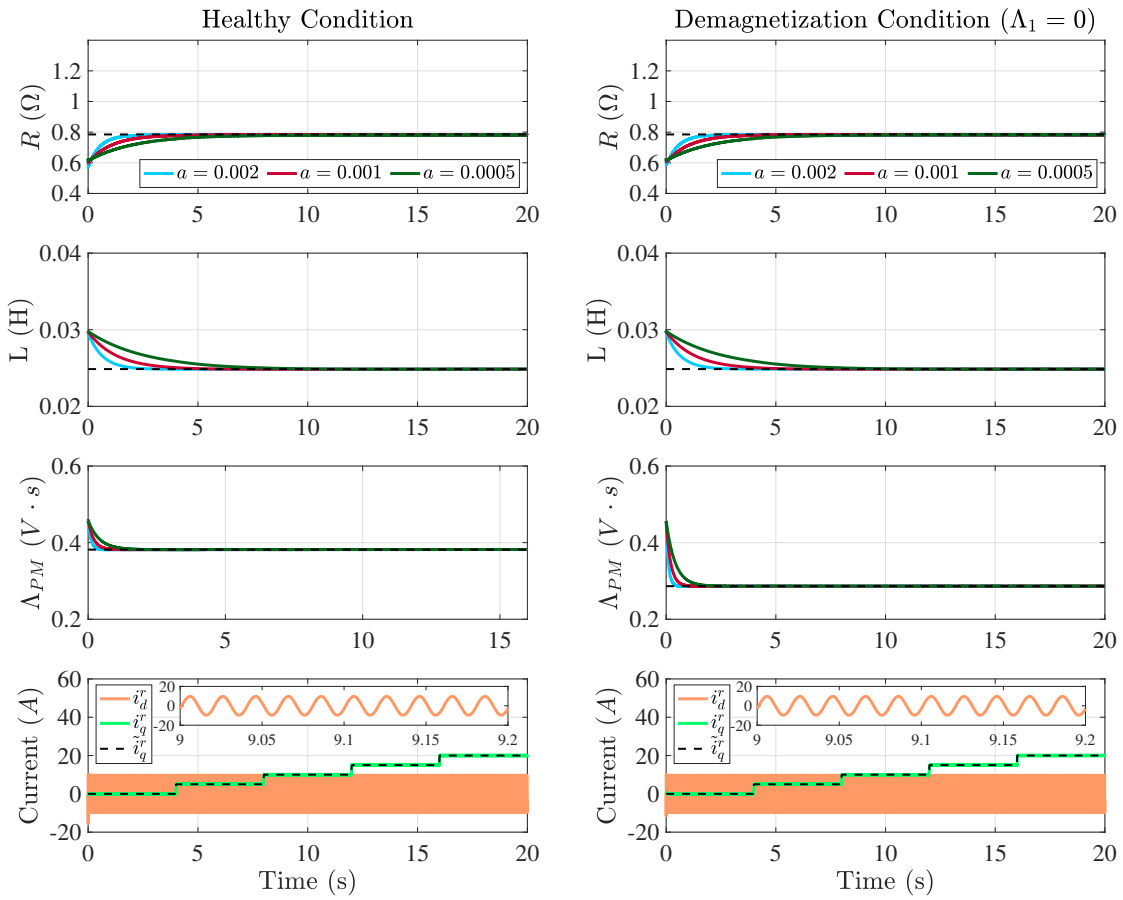

Figure 4.10: Simulation results of the parameter estimator based on the standard dynamics for different adaptation gains when the DW SMPM machine is operating under healthy (left) and demagnetized (right) conditions. Note that the black dashed line corresponds to the actual parameters.

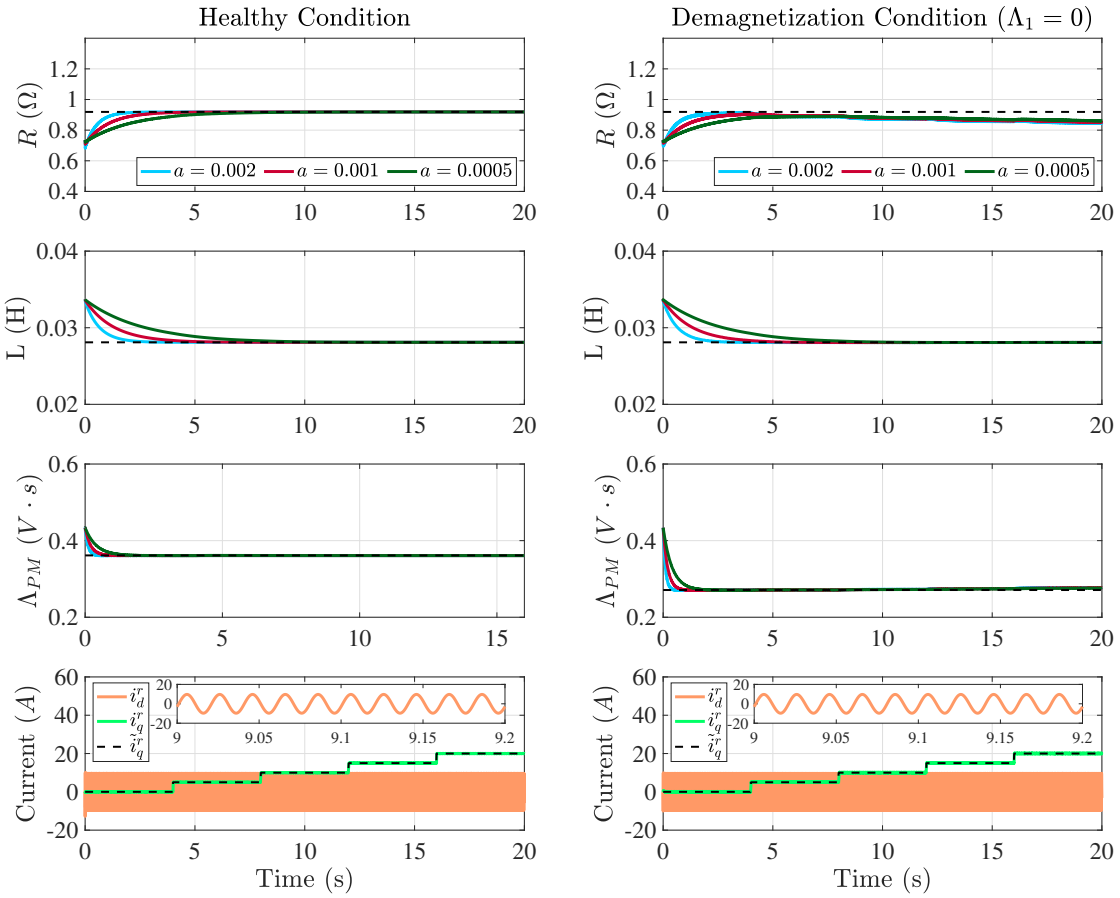

Figure 4.11: Simulation results of the parameter estimator based on the standard dynamics for different adaptation gains when the CW SMPM machine is operating under healthy (left) and demagnetized (right) conditions. Note that the black dashed line corresponds to the actual parameters.

conditions as no additional harmonics are expected in the PM flux linkage under demagnetization. Fig. 4.11 shows the simulation results for the CW SMPM machine. In the case that the SMPM machine is healthy, the parameters converge to their actual values. Regarding the unhealthy SMPM machine simulations, the parameter estimator can also track the 25% decrease on the PM flux linkage. However, the plots show a deviation in the estimated resistance from its actual value, which is within 10% of error. For the simulated SMPM machine, the resistance represents a considerably small portion of the voltage compared to the total voltage. This fact makes the resistance prone to inaccuracies due to noise or unmodeled dynamics. Regarding the simulation results under demagnetization, the resistance deviates from its actual value due to unmodeled dynamics. Since demagnetization solely affects Magnet 1, the PM flux reduction is accompanied by oscillations in both direct and quadrature axes, which the model does not capture. Given that the resistance does not contribute significantly to the voltage equation, a possible modification to the presented estimator is to fix the resistance value and include it in the observation.

As a validation for the discrete PE analysis, Figs. 4.12, 4.13, 4.14, and 4.15 show the condition number of the PE condition matrix (See Definition 2.2) for the DW and CW SMPM machines. Note that the moving window (N) is given by 250 samples ($0.025s$), corresponding to the injected PE signal period. As seen in Figs. 4.12 and 4.13, the condition number is not infinite, indicating that the system is persistently excited. Figs. 4.14 and 4.15 show condition numbers of the PE condition matrix for the DW and CW SMPM machines when the regressor is scaled, as previously discussed in Remark 4.1. As shown in Figs. 4.14 and 4.15, scaling the regressor successfully improves the condition number of the PE condition matrix.

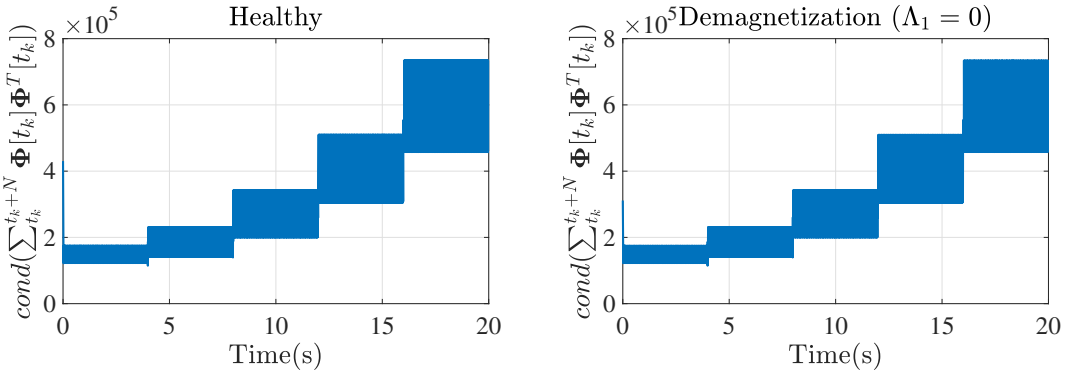

Figure 4.12: Condition number of the discrete-time PE condition matrix for the estimator based on the standard dynamics when the DW SMPM machine is operating under healthy (left) and demagnetized (right) conditions.

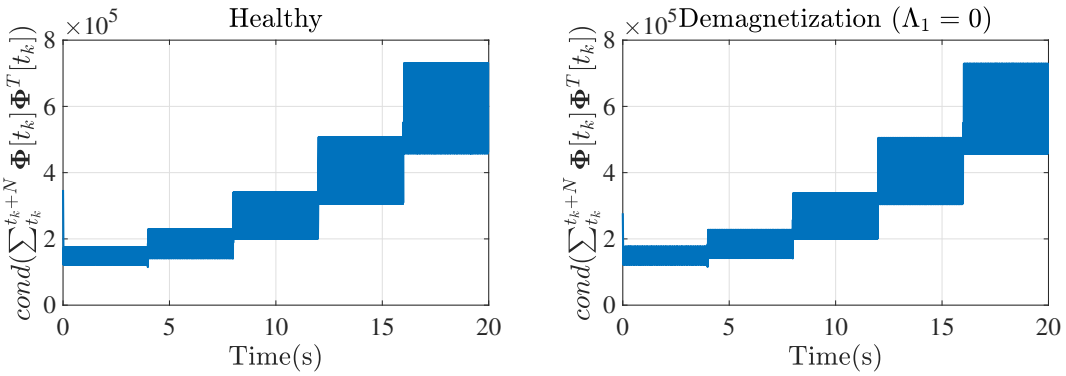

Figure 4.13: Condition number of the discrete-time PE condition matrix for the estimator based on the standard dynamics when the CW SMPM machine is operating under healthy (left) and demagnetized (right) conditions.

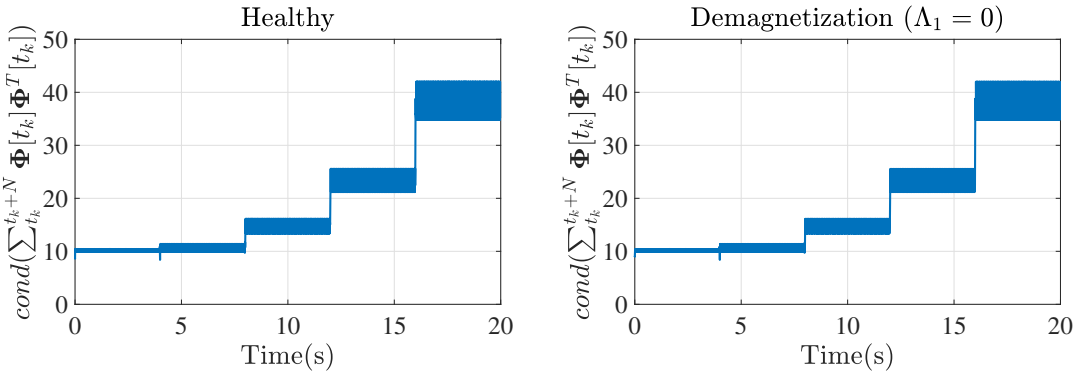

Figure 4.14: Condition number of the discrete-time PE condition matrix with scaled regressor for the estimator based on the standard dynamics when the DW SMPM machine is operating under healthy (left) and demagnetized (right) conditions.

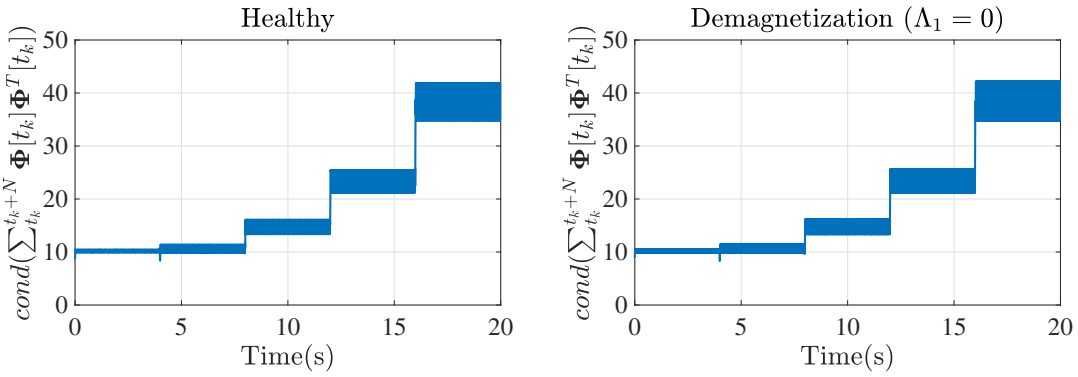

Figure 4.15: Condition number of the discrete-time PE condition matrix with scaled regressor for the estimator based on the standard dynamics when the CW SMPM machine is operating under healthy (left) and demagnetized (right) conditions.

4.4.2 Performance of the Parameter Estimator Based on Proposed Dynamic Model

The performance of the parameter estimator from Eq. (4.18) under healthy and demagnetized conditions for the DW and CW SMPM machines is shown in Figs. 4.16 and 4.17, respectively. Fig. 4.16 reveals that accurate parameter convergence is achieved when the DW SMPM machine is operating under both healthy and demagnetized conditions. As expected from Section 4.2.2.2, the PM flux linkage does not have additional harmonics under the demagnetization condition, and, hence, the asymmetry term is zero.

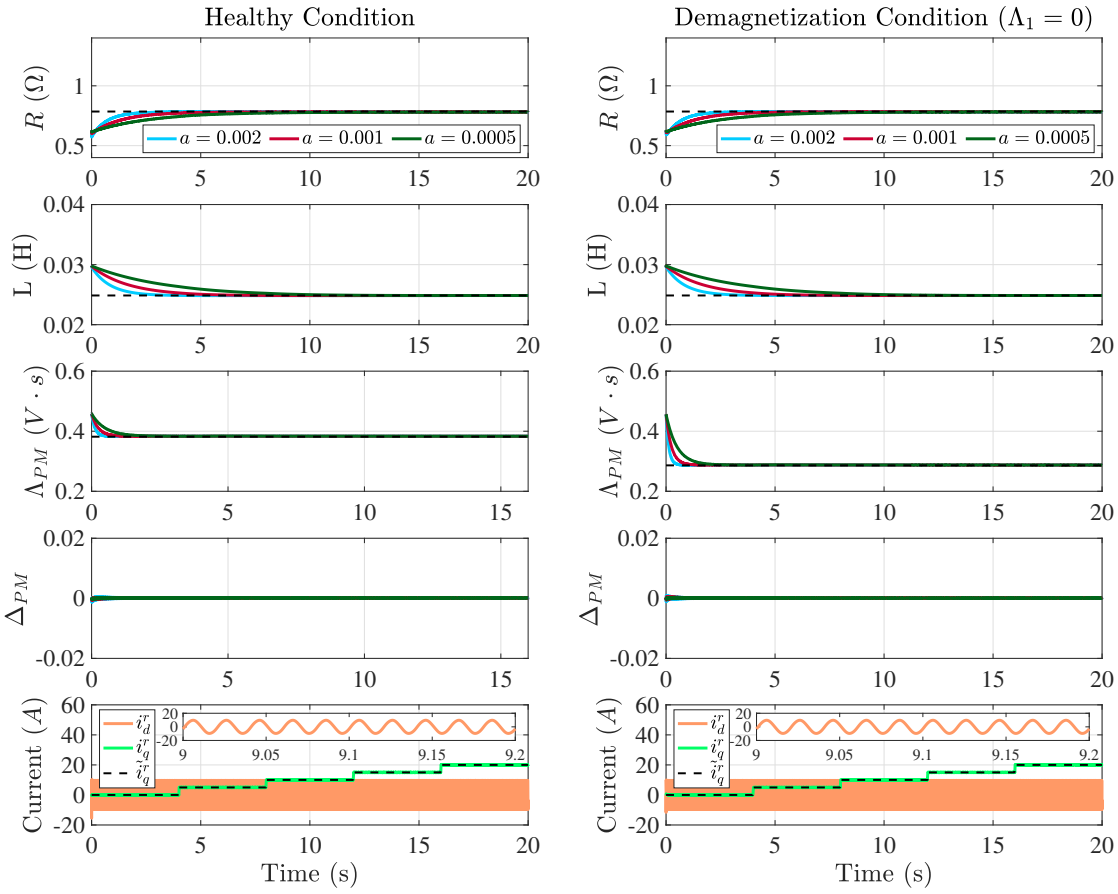

Figure 4.16: Simulation results of the parameter estimator based on the proposed dynamics for different adaptation gains when the DW SMPM machine is operating under healthy (left) and demagnetized (right) conditions. Note that the black dashed line corresponds to the actual parameters.

Fig. 4.17 shows the simulation results for the CW SMPM machine. As shown in Fig. 4.17, the parameters converge to their actual values under healthy and de-

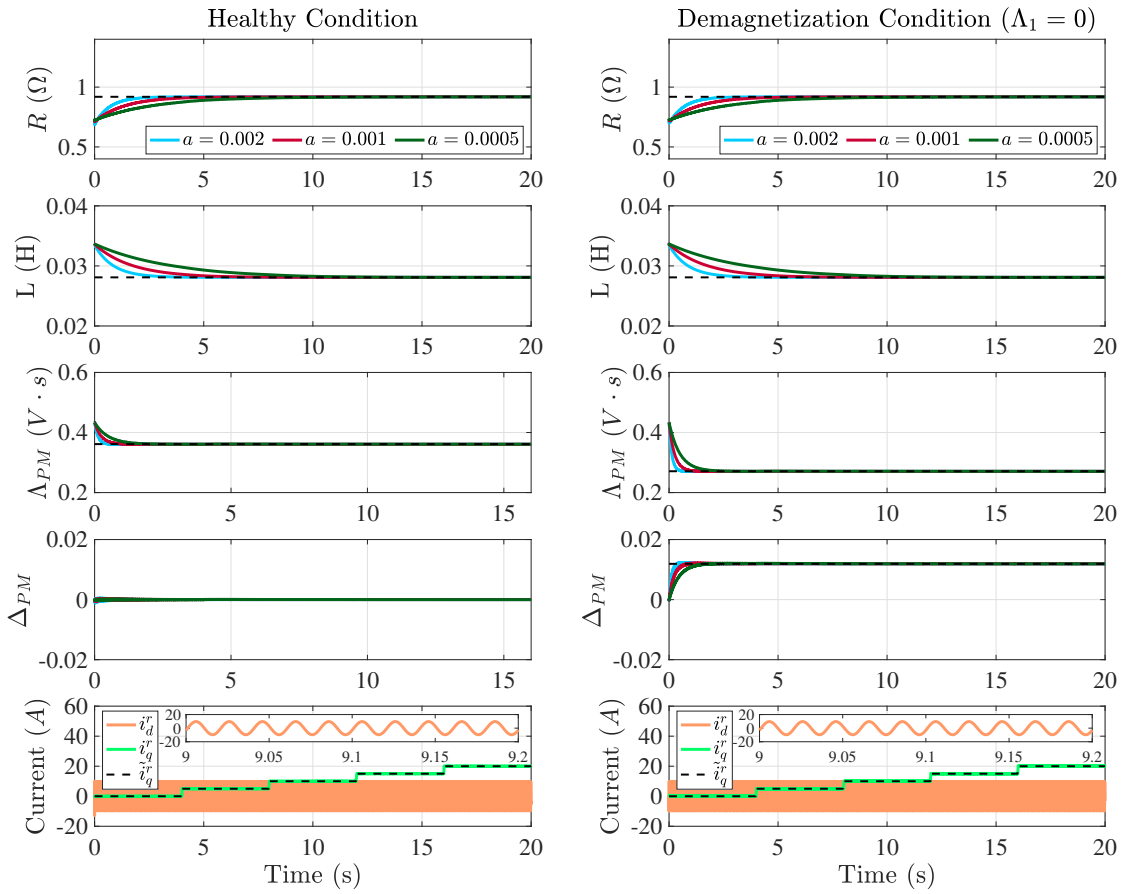

Figure 4.17: Simulation results of the parameter estimator based on the proposed dynamics for different adaptation gains when the CW SMPM machine is operating under healthy (left) and demagnetized (right) conditions. Note that the black dashed line corresponds to the actual parameters.

magnetized conditions. In contrast to the DW SMPM machine case, the CW SMPM machine has additional harmonics in its PM flux linkage under demagnetization, which causes a non-zero asymmetry term. Fig. 4.18 shows that the estimated PM flux linkage and asymmetry term successfully reconstruct the PM flux linkage. In addition, note that the resistance does not deviate from its actual value as in the standard-model-based estimator results. The asymmetry term helps to reduce the unmodeled dynamics and, therefore, alleviates the resistance from inaccuracies.

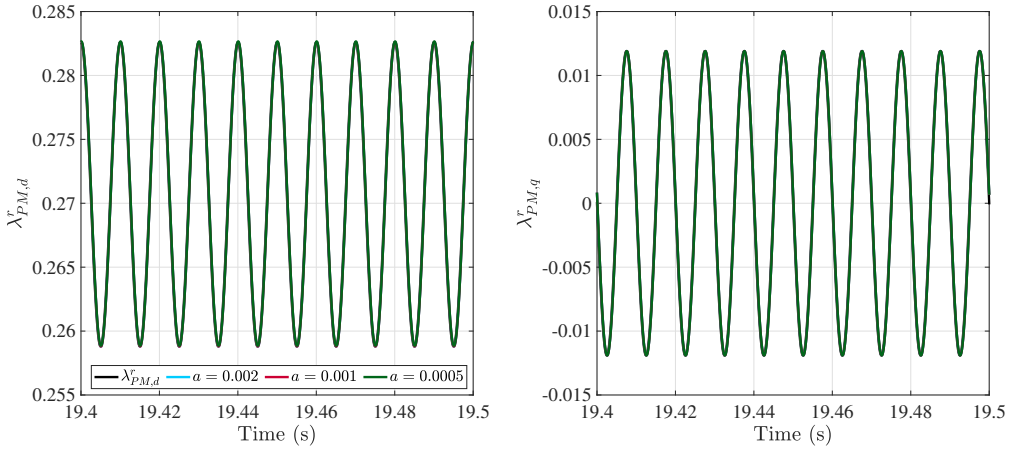

Figure 4.18: Comparison between the model and estimated direct (left) and quadrature-axis (right) PM flux linkage with the CW SMPM machine operating under demagnetization. The PM flux linkage is reconstructed based on the estimated parameters from the proposed-model-based parameter estimator for different adaptation gains.

In terms of the PE condition, Figs. 4.19, 4.20, 4.21, and 4.22 show the condition number of the PE condition matrix for the DW and CW SMPM machines. The moving window is given by 500 samples (0.05 s), corresponding to the regressor's period. In this case, the regressor period depends on the frequency of the injected PE signal and the electrical rotor frequency (See Eq. (4.25)). Figs. 4.19 and 4.20 show that the system is PE as the condition number for the PE condition matrix is not infinite. As previously seen in the PE analysis, the parameter estimator based on the demagnetization model can achieve sufficient conditions for accurate identification with the same excitation as the estimator based on the standard model. Figs. 4.21, and 4.22 show the condition numbers of the PE condition matrix for the DW and CW SMPM machines when the regressor is scaled. Similar to the parameter estimator based on the standard model, scaling the regressor improves the condition number of the PE condition matrix.

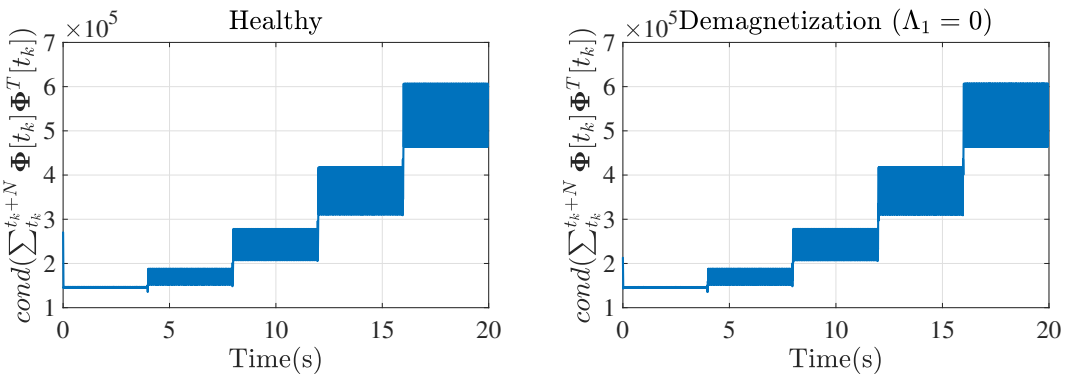

Figure 4.19: Condition number of the discrete-time PE condition matrix for the estimator based on the proposed dynamics when the DW SMPM machine is operating under healthy (left) and demagnetized (right) conditions.

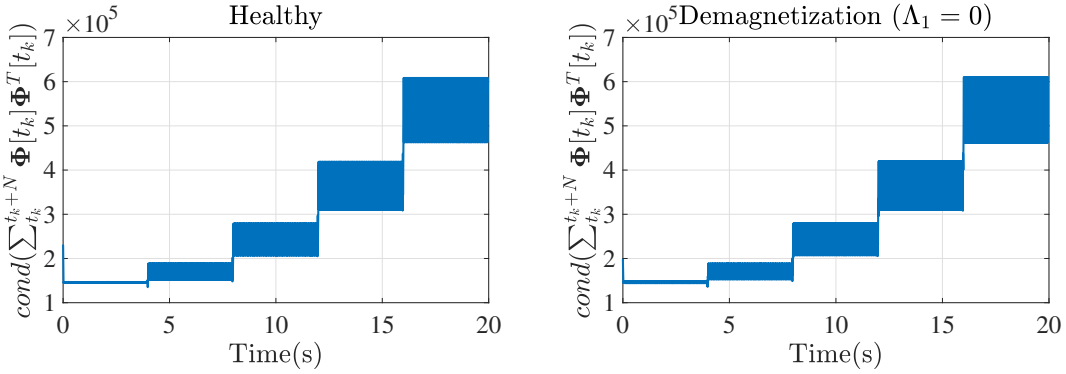

Figure 4.20: Condition number of the discrete-time PE condition matrix for the estimator based on the proposed dynamics when the CW SMPM machine is operating under healthy (left) and demagnetized (right) conditions.

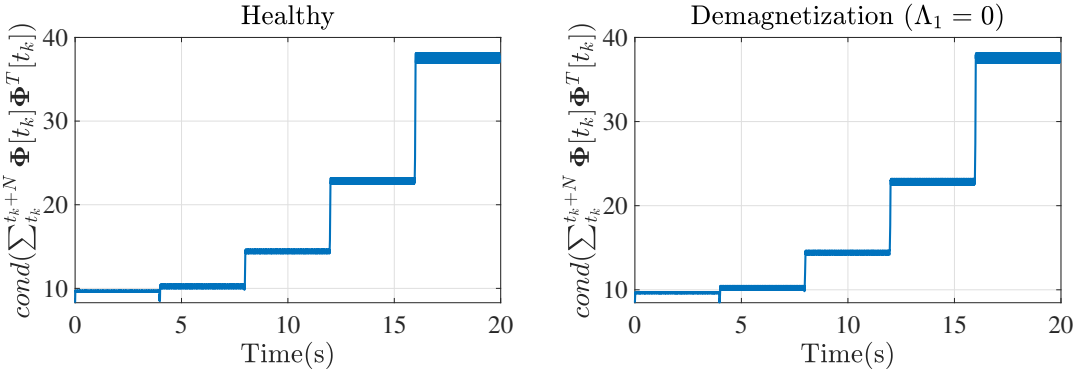

Figure 4.21: Condition number of the discrete-time PE condition matrix for the estimator based on the proposed dynamics with scaled regressor when the DW SMPM machine is operating under healthy (left) and demagnetized (right) conditions.

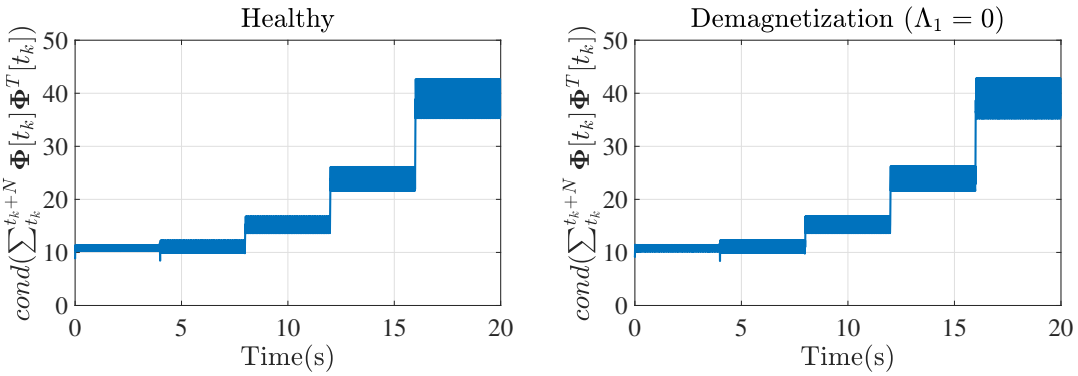

Figure 4.22: Condition number of the discrete-time PE condition matrix with scaled regressor for the estimator based on the proposed dynamics when the CW SMPM machine is operating under healthy (left) and demagnetized (right) conditions.

Regarding the design of the parameter estimator, smaller adaptation gains are preferable as the estimator acts as a filter under these conditions. The purpose of the parameter estimator from Eq. (4.18) is to capture possible asymmetries between the north and south poles, and it is based on an approximation of the model in Eq. (4.12). In other words, there are still some unmodeled dynamics which will still appear in the parameters as oscillations. By using smaller gains, the identification results are more robust to these unmodeled dynamics and noises [84].

Note that, while the proposed model assumes uniform demagnetization within individual poles (assumption D), the effectiveness of the parameter estimator based on this proposed model for fault detection does not rely on this assumption. In practice, an overall decrease in the individual magnet flux linkage is expected regardless of the demagnetization scenarios.

4.5 Co-Simulation Results Considering Nonlinearities

The performance of the parameter estimators is validated through co-simulation, as experimental results would require damaging an actual machine. In these co-simulations, the FEA machine models are integrated with an electric drive. The FEA-based SMPM machine models correspond to the DW and CW SMPM machine models presented in Section 4.2.2 and are simulated in Maxwell. Note that the steel type was modified from "Iron" to "M19", which corresponds to a practical material for electric machines. The B-H curve for "M19" is presented in Fig. 4.23. The co-simulation interface and inverter model are implemented in *Twin Builder*, which is a

commercial simulation software from *Ansoft Corporation*. The inverter is modeled as an ideal "average-value" VSI. The control model is developed in Matlab/Simulink and exported as a Twin Builder component. Specifically, PI regulators with cross-coupling compensation are used to regulate the two-phase currents in the rotor reference frame.

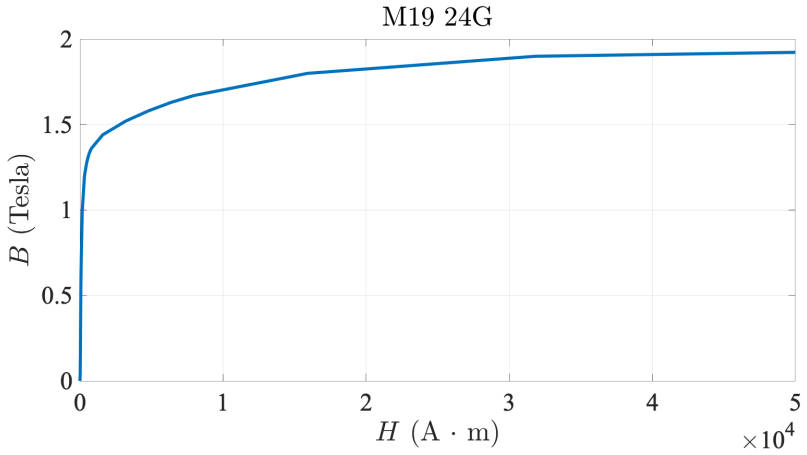

Figure 4.23: B-H curve for M19 24G.

Similar to the simulations presented in the previous section (Section 4.4), the parameters are estimated while the SMPM machines operate at different current levels and a constant speed of $1000RPM$. The PE signal required for accurate parameter convergence is injected in the direct axis and given by:

$$\tilde{i}_d^r = 5\sin(2\pi 40t). \tag{4.29}$$

The estimated parameters are assumed to have an initial 20% deviation from the linear parameters presented in Section 4.2.2.2. The FEA-based machine model as well as the electric drive are executed at $10kHz$.

4.5.1 Performance of Parameter Estimator Based on Standard Dynamic Model

In Figs. 4.24 and 4.25, the co-simulation results for the standard-model-based parameter estimator are presented. Note that the black dashed line corresponds to the average value of the actual parameters assuming linear magnetics from Section 4.2.2.2. Fig. 4.24 presents the results for the DW SMPM machine under healthy and demagnetized conditions. As seen in Fig. 4.24, the parameters have similar behavior under both conditions as no new harmonics are expected under demagnetization. In addition, the magnetic parameters track the linear values for most of the current values.

However, once the machine operates at higher currents, the magnetic parameters decrease, implying saturation. Under saturation, the magnetics are no longer linear, and the resistance gets affected by these unmodeled dynamics. As mentioned above, the resistance is prone to inaccuracies due to unmodeled dynamics since its voltage drop is considerably small compared to the total voltage.

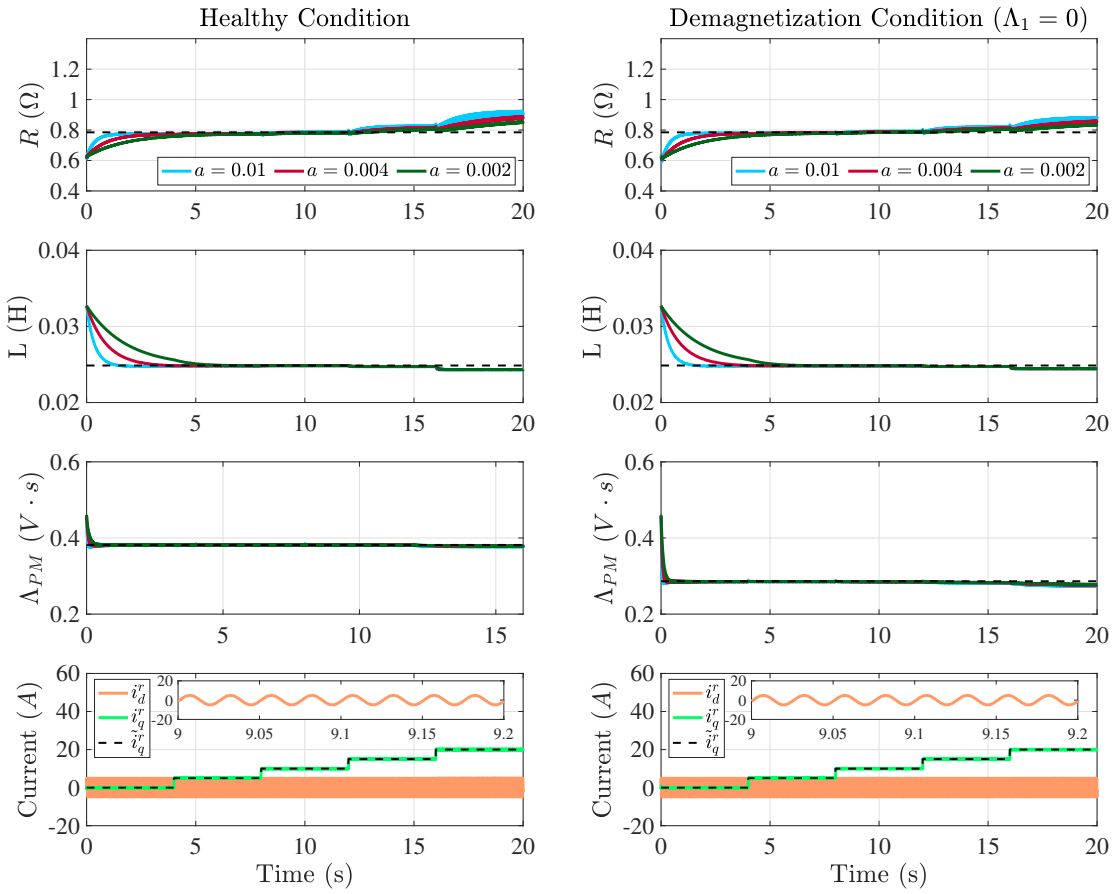

Figure 4.24: Co-simulation results of the parameter estimator based on standard dynamics for different adaptation gains when the DW machine is operating under healthy (left) and demagnetized (right) conditions. Note that the black dashed line corresponds to the expected "linear" parameter value.

The co-simulation results of the parameter estimator based on standard dynamics for the CW SMPM machine operating under healthy and demagnetized conditions are presented in Fig. 4.25. Under healthy conditions, the estimated parameters match their linear values for most current values, as seen in Fig. 4.25. However, under demagnetization, the unmodeled dynamics cause the resistance to deviate within 10% from its actual value. In addition, similar to the DW SMPM machine results, the estimated inductance and PM flux linkage slightly reduce at high currents, which

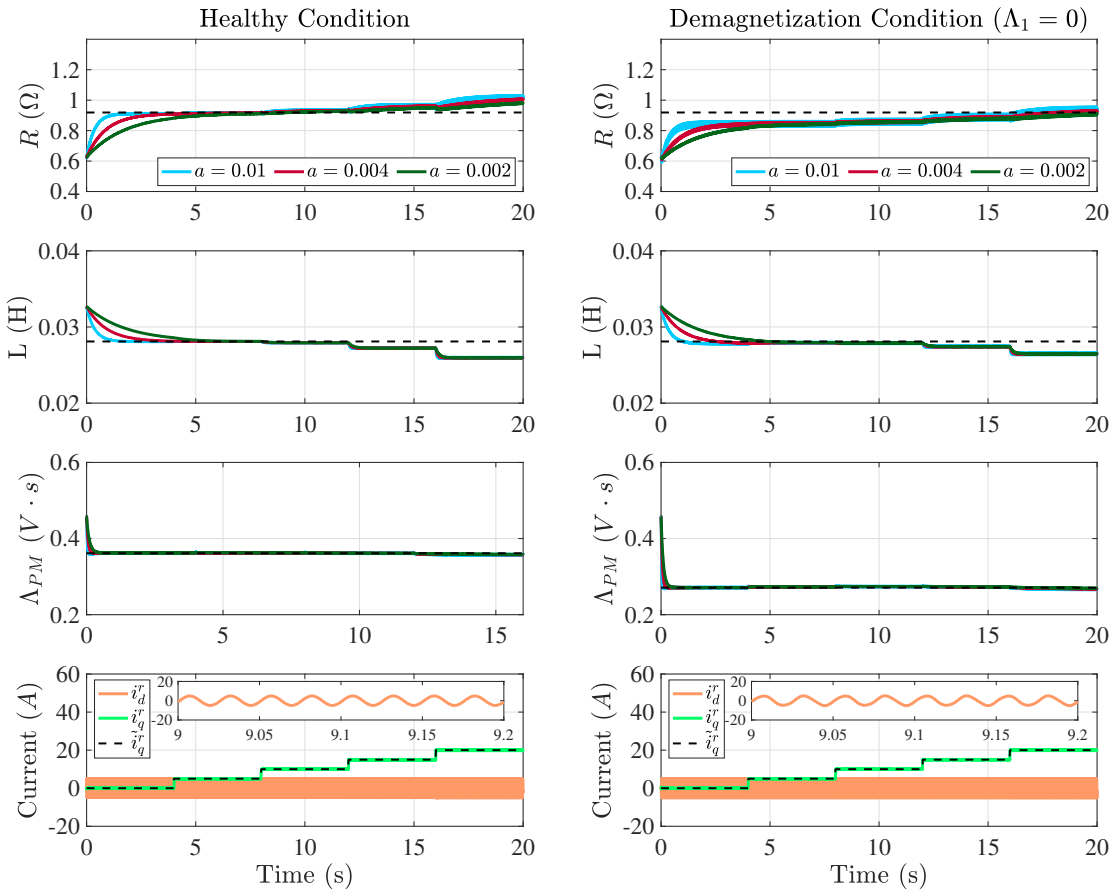

Figure 4.25: Co-simulation results of the parameter estimator based on standard dynamics for different adaptation gains when the CW machine is operating under healthy (left) and demagnetized (right) conditions. Note that the black dashed line corresponds to the expected "linear" parameter value.

indicates saturation.

These results indicate that the parameter estimator based on the standard equivalent two-phase model provides some information for fault diagnosis and condition monitoring of SMPM machines under magnet demagnetization. In terms of the fundamental component of the estimated PM flux linkage, its decrease can be used to quantify the demagnetization. The main challenge of using this reduction as an indicator is that, under healthy conditions, increasing PM temperature also causes a decrease in the PM flux linkage, and so a method to distinguish the root cause is required. In terms of the CW SMPM machine, the resistance's accuracy is affected by the demagnetization fault. However, since the resistance is not used as an indicator for demagnetization, it should not affect the detection and monitoring capabilities of this parameter identification strategy.

4.5.2 Performance of Parameter Estimator Based on Proposed Dynamic Model

The co-simulation results for the parameter estimator based on the proposed dynamics are presented in Figs. 4.26 and 4.27. Fig. 4.26 reveals that the parameters converge to their actual values for the DW SMPM machine case. Under demagnetization, the asymmetry term is zero, which is expected as no new harmonics should exist. Similar to the standard-model-based simulations, saturation is observed for the higher current region.

The co-simulation results of the proposed parameter identification strategy for the CW SMPM machine are presented in Fig. 4.27. As in previous cases, a linear region is identified in which the parameters converge to their actual linear values. As the current increases, the magnetics reach saturation, at which point the magnetic parameters slightly reduce. Under demagnetization, the asymmetry term is non-zero, indicating asymmetric demagnetization between the north and south poles. Similar to the simulation results, the inclusion of the asymmetry term helps the resistance accuracy.

In terms of the information that can be extracted for fault diagnosis and condition monitoring of SMPM machines under magnet demagnetization, the parameter estimator based on the proposed dynamics can provide more details when compared to the standard-model-based estimator. Similar to the standard-model-based estimator, the estimator based on the proposed dynamics can track variations of the fundamental component of the PM flux linkage, which can be used as an indicator for demagnetization. In addition, unlike the standard-model-based estimator, the

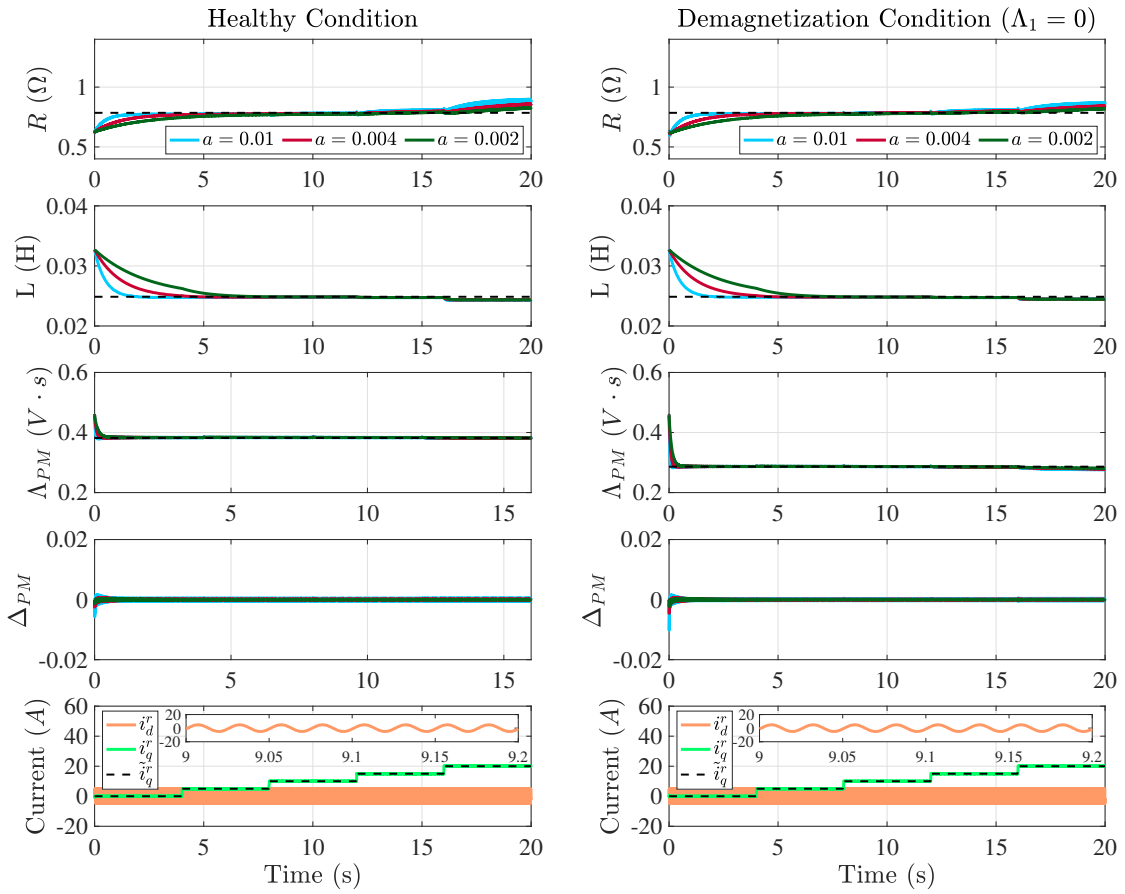

Figure 4.26: Co-simulation results of the parameter estimator based on proposed dynamics for different adaptation gains when the DW machine is operating under healthy (left) and demagnetized (right) conditions. Note that the black dashed line corresponds to the expected "linear" parameter value.

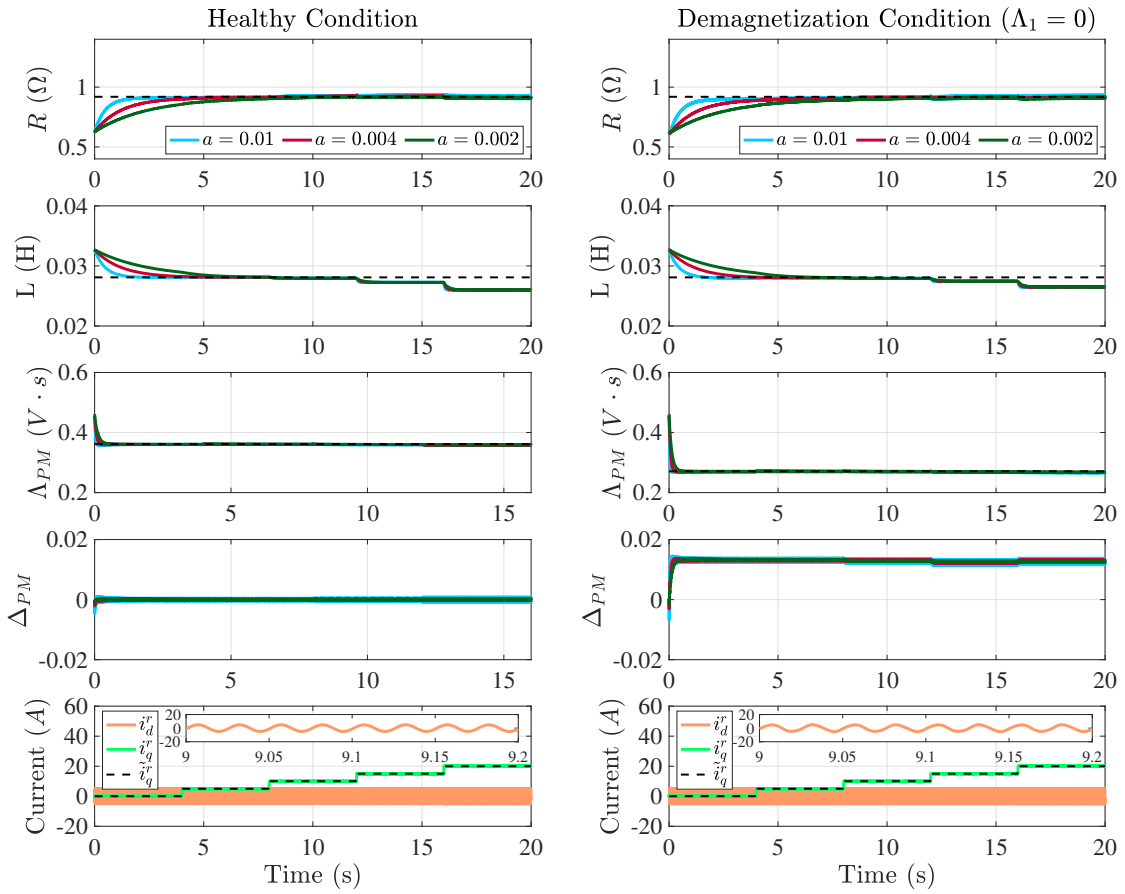

Figure 4.27: Co-simulation results of the parameter estimator based on proposed dynamics for different adaptation gains when the CW machine is operating under healthy (left) and demagnetized (right) conditions. Note that the black dashed line corresponds to the expected "linear" parameter value.

added parameter Δ_{PM} can provide useful information to distinguish between even and uneven demagnetization among the magnets when there is an asymmetry between the north (Λ_{13}) and south (Λ_{24}) poles. Note that Δ_{PM} can be potentially used to overcome the difficulty mentioned above for fault detection and monitoring caused by the dependency of the PM flux linkage on its temperature. The main limitation of this approach is that when there is no asymmetry between the north and south poles (i.e., Λ_{13} and Λ_{24} are identically demagnetized), Δ_{PM} is equal to zero, and the only information that can be used to monitor and detect demagnetization is the average value of the PM flux linkage. Additionally, as seen in the DW SMPM machine results, there can be machine designs with no new harmonics under demagnetization.

Regarding modeling, the equivalent two-phase model offers computational and conceptual advantages for studying the demagnetization conditions compared with the FEA model. In addition to the findings from the model validation section (Section 4.2.2.2), comparing the co-simulation results and the simulation results suggests that the proposed equivalent two-phase model properly captures the SMPM machine behavior under demagnetization in the linear region. Note that the magnetics of SMPM machines are typically linear given the large effective air gap between the stator and rotor irons. Therefore, the proposed equivalent two-phase model is a suitable tool for studying the demagnetization conditions and can be used for initial control development.

4.6 Summary

This chapter investigated the application of parameter identification to fault diagnosis and condition monitoring of SMPM machines under demagnetization conditions. Specifically, an equivalent two-phase parametric model and an online parameter identification technique for a three-phase four-pole SMPM machine with two windings per phase were formulated. Demagnetization mainly affects the PM flux linkage. So first, the equivalent two-phase model was formulated by superposing the individual magnets. Then, FEA simulations were used to calibrate and validate the model's PM flux linkage for DW and CW SMPM machine designs. Afterward, the formulation of the parameter estimator based on the proposed model together with a parameter estimator based on the standard model was discussed, including the parametric models, the parameter identification algorithm, and the sufficient conditions for accurate convergence. Simulation and co-simulation results proved the effectiveness of the proposed parameter identification strategy over the standard-model-based identification

strategy for monitoring and detecting demagnetization. In addition, a comparison between simulation and co-simulation results showed that the proposed model is a suitable tool for studying the SMPM machine behavior under demagnetization in the linear operating region. Finally, remarks on the information for detecting demagnetization were discussed.

CHAPTER V

Modeling and Identification for Condition Monitoring of Surface-Mount Permanent Magnet Machines Under Eccentricity Condition

5.1 Introduction

In an SMPM machine, the stator and rotor are aligned so that the air-gap length is symmetrical. However, the rotor and stator can experience misalignments due to inaccurate manufacturing, improper alignment of the rotor or stator during commissioning, and bearing wear or misalignment. If the rotor and stator are misaligned, the air gap between the stator and rotor is non-uniform, in which case the SMPM machine operates under eccentricity conditions. The non-uniform air gap due to eccentricity generates vibrations and UMP, causing additional mechanical stress and performance degradation in the SMPM machine. Furthermore, under severe eccentricity, the rotor and stator can potentially rub, leading to severe damages.

This chapter studies modeling and parameter identification for fault diagnosis and condition monitoring of SMPM machines under eccentricity conditions. Specifically, an equivalent two-phase model and an online parameter identification strategy for a three-phase four-pole SMPM machine with two windings in series per phase under eccentricity conditions are presented. Eccentricity mainly affects the magnetic parameters in the three-phase SMPM machine dynamics. So first, Modified Winding Function (MWF) and Magnet Function (MF) theories are used to determine the expressions for the three-phase inductances and PM flux linkages under eccentricity. Particularly, in MWF and MF theories, the effect of eccentricity on the magnetic parameters is captured in the air-gap function. Then, the equivalent two-phase model is formulated by mapping the three-phase dynamics under eccentricity into their two-phase equivalents, which are referenced to the rotor reference frame. Afterward, the

model's magnetic parameters are calibrated and validated against FEA simulations for an SMPM machine design. Following the model validation, the parameter identification strategy for monitoring and detecting eccentricity is discussed, including the parametric model and sufficient conditions for accurate convergence. Next, simulation and co-simulation results are presented for the proposed parameter identification strategy and the standard-model-based estimator presented in Section 4.3. For both estimators, the specific information for monitoring and detecting eccentricity conditions is discussed. Finally, comments on the SMPM machine design limitations for detecting eccentricity are discussed, and a summary of the chapter is presented.

5.2 Modeling SMPM Machines with Eccentricity Condition

Under healthy conditions, the electrical dynamics are typically analyzed using the standard equivalent two-phase model in which the electrical dynamics are expressed with respect to the rotor reference frame [56], as previously presented in Eq. (4.3). When the SMPM machine is operating under healthy conditions, the center of the stator, rotor, and rotation coincide and, hence, the air-gap length is symmetrical. Unfortunately, under eccentricity the air gap becomes asymmetrical and the standard model presented in Eq. (4.3) is no longer valid. In this section, a simple SMPM machine model that captures the dynamic behavior under static, dynamic, and mixed eccentricity conditions using the Modified Winding Function and Magnet Function theories is derived for analysis and simulation purposes under the following assumptions:

A. The machine has a smooth air gap (i.e., slot effects are not considered), is balanced in construction, and is connected in an ungrounded-wye configuration.

B. Magnetic saturation, eddy current, and hysteresis effects are neglected (i.e., linear magnetics are assumed).

C. Stator and rotor irons have infinite permeability. The magnets and air have equal permeability.

All three assumptions (A-C) are commonly used for control-oriented models [56]. Note that, regarding assumption B, the magnetics of an SMPM machine are typically linear given the large effective air gap between stator and rotor irons. In terms of assumption C, the permeability of most PM materials (e.g., SmCo, NdFeB) is close to that of free space, and the permeability of most iron alloys used in the stator and rotor irons is much higher than that of free space.

In the following analysis, the model is derived based on a four-pole three-phase SMPM machine with two coils per phase, as shown in Fig. 4.1. As will be seen, eccentricity affects all the Fourier components in the magnetic parameters. The model captures the eccentricity based on the fundamental Fourier coefficient of the magnetic parameters, which is always present regardless of the SMPM machine design. Additional harmonics can be easily included based on the procedure that will be presented. However, note that these additional harmonics will depend on the SMPM machine design.

5.2.1 Modeling Eccentricity

Eccentricity mainly affects the magnetic components (i.e., inductances and PM flux linkages) in the general three-phase dynamics of Eq. (4.1). Using MWF theory, expressions for the stator winding magnetizing and mutual inductances under the different eccentricity conditions can be calculated [96, 97]. Similarly, the MF theory from [98] can be applied to determine the PM flux linkages under eccentricity conditions.

This section presents a simple equivalent two-phase parametric model for a three-phase four-pole SMPM machine with two windings in series per phase under eccentricity conditions. The derivation starts with the air-gap function for SMPM machines under eccentricity conditions. Afterward, the theory for calculating the magnetic parameters using MWF and MF is presented. In these calculations, the inverse air-gap function is used to capture the eccentricity conditions. Based on these magnetic parameters, the three-phase and equivalent two-phase models for SMPM under eccentricity conditions are formulated. FEA simulations are used to validate the proposed two-phase equivalent model for SMPM machines in the rotor reference frame under eccentricity conditions.

5.2.1.1 Air-gap Function and its Inverse under Eccentricity Conditions

In both MWF and MF approaches, the effects of eccentricity on the magnetic components are captured in the air-gap function and its inverse. In Fig. 5.1, a stator and rotor cross-section that shows the position of the center of stator (O_s), rotor (O_r) and rotation (O_{ω_r}) with respect to the stator reference frame under healthy, SE, DE, and ME conditions is presented. In general, the air-gap length is a function of ϕ, the stator reference position, and θ_r, the rotor position. In healthy conditions, the center of the rotor, stator, and rotation coincide as shown in Fig. 5.1(a), and, hence, the

effective air-gap length (i.e., including magnet thickness) is symmetrical and given by,

$$g(\phi, \theta_r) = g_0, \tag{5.1}$$

where g_0 is the symmetrical air-gap length.

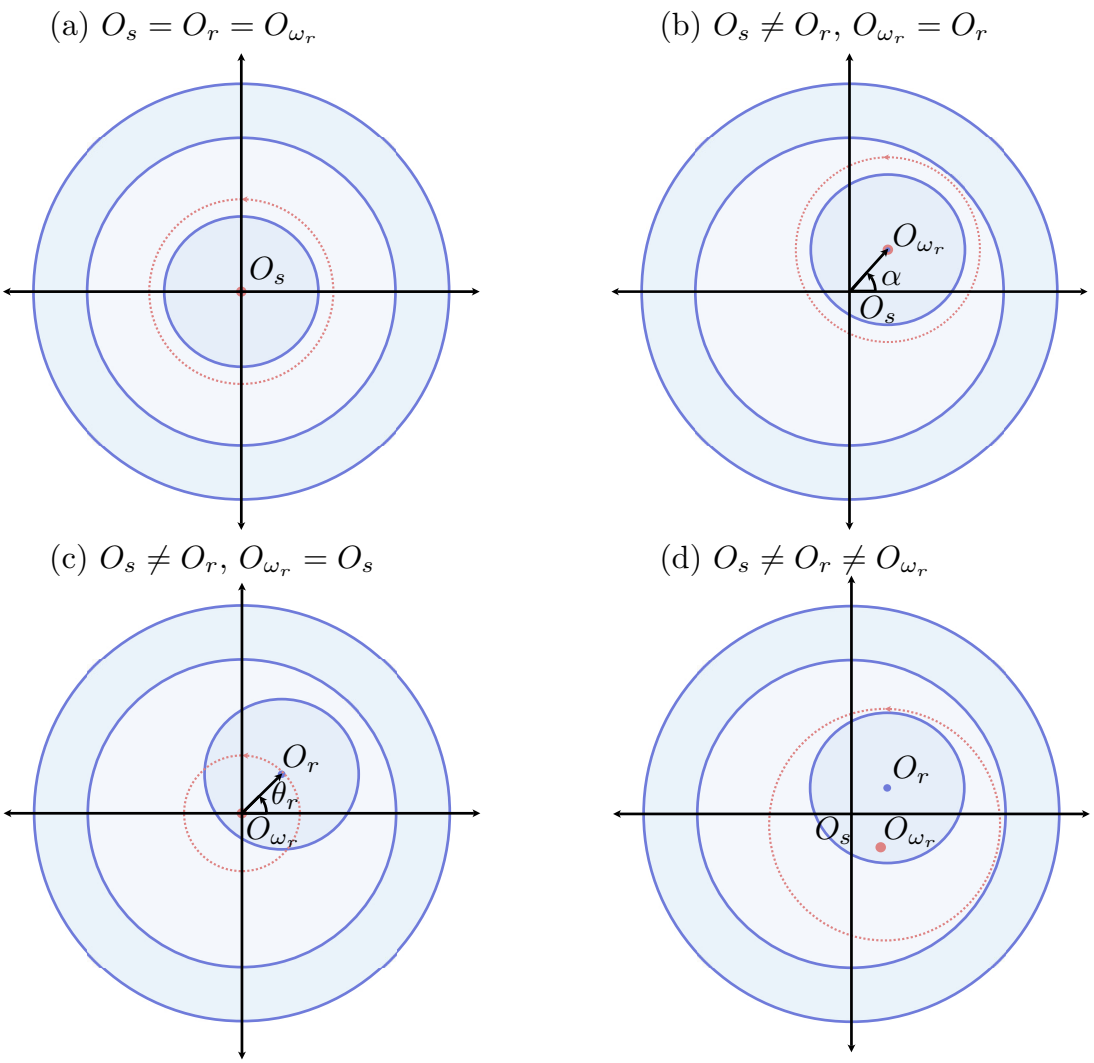

Figure 5.1: Center of stator, rotor and rotation under (a) healthy, (b) SE, (c) DE, and (d) ME conditions. The coordinate system corresponds to the stator reference frame.

Under Static Eccentricity (SE) condition (Fig. 5.1(b)), the center of the rotor and rotation coincide, but they are displaced from the center of the stator. In this case, the air-gap length is not uniformly distributed around the rotor, depends on ϕ and

constants α, δ_s, and is given by

$$g(\phi, \theta_r) = g_0(1 - \delta_s \cos(\phi - \alpha)), \tag{5.2}$$

where α is the angle between the vector O_sO_r and the horizontal axis, and δ_s is the degree of static eccentricity [10], which is defined as

$$\delta_s = \frac{\mid O_sO_r \mid}{g_0}. \tag{5.3}$$

Note that α is fixed for all rotor positions and, therefore, the air-gap length under SE is time independent. When the machine is under Dynamic Eccentricity (DE), the center of the stator coincides with the center of rotation; however, they differ from the center of the rotor as shown in Fig. 5.1(c). Under this condition, the air-gap length around the rotor is nonuniform and is given by

$$g(\phi, \theta_r) = g_0(1 - \delta_d \cos(\phi - \theta_r)), \tag{5.4}$$

where δ_d is the degree of dynamic eccentricity [10], which is defined as

$$\delta_d = \frac{\mid O_{\omega_r}O_r \mid}{g_0}. \tag{5.5}$$

When the machine experiences some degree of SE and DE simultaneously, it operates under the Mixed Eccentricity (ME) condition (Fig. 5.1(d)). In this case, the air-gap function is given by the superposition of both SE and DE conditions [97]:

$$g(\phi, \theta_r) = g_0(1 - \delta_s \cos(\phi - \alpha) - \delta_d \cos(\phi - \theta_r)) = g_0(1 - \delta_M \cos(\phi - \alpha_M)), \tag{5.6}$$

where

$$\delta_M = \sqrt{\delta_s^2 + \delta_d^2 + 2\delta_s\delta_d \cos(\theta_r - \alpha)},$$
$$\alpha_M = \arctan\left(\frac{\delta_s \sin(\alpha) + \delta_d \sin(\theta_r)}{\delta_s \cos(\alpha) + \delta_d \cos(\theta_r)}\right).$$

Thus, the inverse air-gap function is given by

$$g^{-1}(\phi, \theta_r) = \frac{1}{g_0(1 - \delta_M \cos(\phi - \alpha_M))}, \tag{5.7}$$

Note that the air-gap function and its inverse presented in Eqs. (5.6) and (5.7) can capture the air-gap length variations due to SE, DE, and ME by modifying accordingly the degrees of static and dynamic eccentricity. Additionally, it should be noted that, while slot effects were neglected in the previous analysis, they can be easily incorporated into the air-gap function and its inverse by modifying the healthy air-gap length, g_0, with

$$g_e = k_c g_0, \tag{5.8}$$

where k_c is the Carter's coefficient, and g_e is the modified equivalent air gap which allows one to model a slotted surface with an equivalent unslotted surface with the same cross-section [99].

5.2.1.2 Magnetic Parameter Calculations using Modified Winding Function (MWF) and Magnet Function (MF) Theories

This section describes how to calculate inductances and PM flux linkages based on MWF and MF theories. MWF theory provides a computationally efficient method to estimate inductances based on the machine winding and the air-gap data [96]. Using MWF theory, the magnetizing and mutual inductances can be calculated through the following expressions [96]:

$$L_{xx} = \mu_0 r l \int_0^{2\pi} n_x(\phi, \theta_r) M_x(\phi, \theta_r) g^{-1}(\phi, \theta_r) d\phi, \tag{5.9}$$

$$L_{xy} = \mu_0 r l \int_0^{2\pi} n_y(\phi, \theta_r) M_x(\phi, \theta_r) g^{-1}(\phi, \theta_r) d\phi, \tag{5.10}$$

where μ_0 is the magnetic constant (a.k.a., permeability of free space), r is the mean radius, l is the machine axial length, $n_x(\phi, \theta_r)$ is the turns function for winding x, and $M_x(\phi, \theta_r)$ is the modified winding function for winding x given by,

$$M_x(\phi, \theta_r) = n_x(\phi, \theta_r) - \langle M_x(\phi, \theta_r) \rangle, \tag{5.11}$$

with the average component of the MWF given by,

$$\langle M_x(\phi, \theta_r) \rangle = \frac{1}{2\pi \langle g^{-1}(\phi, \theta_r) \rangle} \int_0^{2\pi} n_x(\phi, \theta_r) g^{-1}(\phi, \theta_r) d\phi.$$

A detailed derivation and discussion about inductance calculations using MWF theory can be found in [96, 100]. Note that, under the presence of non-uniform air gaps, the reciprocity theorem holds for mutual inductances (i.e., $L_{xy} = L_{yx}$) (proof in [96]). Also, note that MWF theory only calculates the inductance related to the flux linkage involved in the electromagnetic torque generation, a.k.a, the magnetizing or air-gap inductance. In order to determine the winding self-inductance, the leakage inductance, which does not contribute to torque generation, has to be added to the magnetizing inductance [99, 100].

Similarly, using MF theory [98], the PM flux linkages can be calculated as:

$$\lambda_{PM,x} = \mu_0 r l \int_0^{2\pi} n_x(\phi, \theta_r) F_{mag}(\phi, \theta_r) g^{-1}(\phi, \theta_r) d\phi \tag{5.12}$$

where $F_{mag}(\phi, \theta_r)$, a.k.a the magnet function, is the air-gap MagnetoMotive Force (MMF) produced by the magnets. In terms of analysis, it is useful to describe the turn, magnet and inverse air-gap functions with a Fourier Series. Based on these Fourier Series, general expressions for the inductances and PM flux linkages are provided in the Appendix.

5.2.1.3 Three-phase SMPM Machine Model under Eccentricity Conditions

A three-phase SMPM machine model under eccentricity conditions is formulated in this section. By approximating the general expressions for the magnetic parameters (Eqs. (5.44) and (5.45) in the Appendix) to their low-order harmonics, the electrical three-phase SMPM dynamics under the eccentricity condition can be described using Eq. (4.1) with the eccentricity capture in the inductances and PM flux linkages as

$$L_s = L_{mag} + L_\sigma \approx \pi \mu_0 r l A_1^2 G_0 + L_\sigma, \tag{5.13}$$

$$L_m = L_{ab} = L_{bc} = L_{ca} \approx -\frac{\pi \mu_0 r l A_1^2 G_0}{2}, \tag{5.14}$$

$$\lambda_{PM,a} \approx \pi \mu_0 r l A_1 F_1 G_0 \cos(2\theta_r), \tag{5.15}$$

$$\lambda_{PM,b} \approx -\pi \mu_0 r l A_1 F_1 G_0 \cos\left(2\left(\theta_r + \frac{\pi}{6}\right)\right), \tag{5.16}$$

$$\lambda_{PM,c} \approx -\pi \mu_0 r l A_1 F_1 G_0 \cos\left(2\left(\theta_r - \frac{\pi}{6}\right)\right), \tag{5.17}$$

where $L_{mag} = L_{aa} = L_{bb} = L_{cc}$ is the magnetizing inductance, L_σ is the leakage inductance, F_1 is the first-harmonic Fourier coefficient of the magnet function, A_1 is

the first-harmonic Fourier coefficient of the turns function, and G_0 is the fundamental Fourier coefficient of the inverse gap function (See Eqs. (5.41), (5.42), and (5.43) in the Appendix).

5.2.1.4 Equivalent Two-phase SMPM Machine Model in the rotor reference frame under Eccentricity Conditions

For the three-phase SMPM machine model to provide information about the eccentricity fault and be implemented in simulation, a constraint that specifies the winding configuration (i.e., wye or delta) has to be included. Since an ungrounded-wye connected SMPM machine is assumed, the Clarke Transform [81], which maps the three-phase variables into their equivalent two-phase stationary ($\alpha - \beta$) variables, is used to enforce the zero current constraint from Eq. (2.12). After converting the three-phase dynamics into two-phase stationary equivalent dynamics, they are mapped into the rotor reference frame by using the Park Transform [82]. The equivalent two-phase electrical dynamics of the SMPM machine under eccentricity in the rotor reference frame are given by

$$\begin{bmatrix} v_d^r \\ v_q^r \end{bmatrix} = \begin{bmatrix} R & 0 \\ 0 & R \end{bmatrix} \begin{bmatrix} i_d^r \\ i_q^r \end{bmatrix} + \begin{bmatrix} L^r & 0 \\ 0 & L^r \end{bmatrix} \frac{d}{dt} \begin{bmatrix} i_d^r \\ i_q^r \end{bmatrix} + \frac{d}{dt} \begin{bmatrix} L^r & 0 \\ 0 & L^r \end{bmatrix} \begin{bmatrix} i_d^r \\ i_q^r \end{bmatrix} + \omega_{re} \begin{bmatrix} 0 & -L^r \\ L^r & 0 \end{bmatrix} \begin{bmatrix} i_d^r \\ i_q^r \end{bmatrix} + \omega_{re} \begin{bmatrix} 0 \\ \lambda_{PM}^r \end{bmatrix} + \frac{d}{dt} \begin{bmatrix} \lambda_{PM}^r \\ 0 \end{bmatrix}, \tag{5.18}$$

where

$$L^r = L_s - L_m = \frac{3}{2}\pi\mu_0 r l A_1^2 G_0 + L_\sigma \tag{5.19}$$

$$\lambda_{PM}^r = \pi\mu_0 r l A_1 F_1 G_0 \tag{5.20}$$

Equations (5.19) and (5.20) reveal that the variation in the equivalent two-phase inductance and PM flux linkage under eccentricity with respect to the healthy ones are driven by the air-gap asymmetry with the term,

$$G_0 = \frac{1}{g_0\sqrt{1-\delta_M^2}}. \tag{5.21}$$

Based on this term, the equivalent two-phase inductance and PM flux linkage are expected to increase under SE and DE. In the case of ME, the increment will vary with the rotor position, as shown in Fig. 5.2.

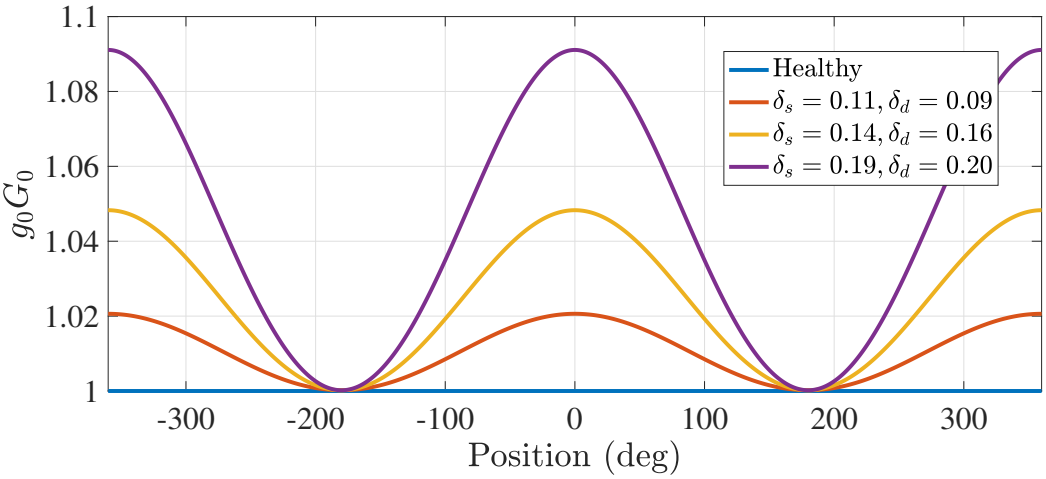

Figure 5.2: Normalized ME air-gap asymmetry term for different degrees of SE and DE with $\alpha = 0$.

5.2.2 Calibration and Validation of Proposed Model

In this section, numerical simulations of the proposed SMPM machine model are presented. The magnetic parameters are calibrated and validated using the dimensions of the SMPM machine and FEA simulations. Note that, under ME condition, the rotor is assumed to have degrees of 21.5% for SE and 23.15% for DE. The SMPM machine used in the simulations is shown in Figs. 5.3 and 5.4, and its parameters are presented in Table 5.1.

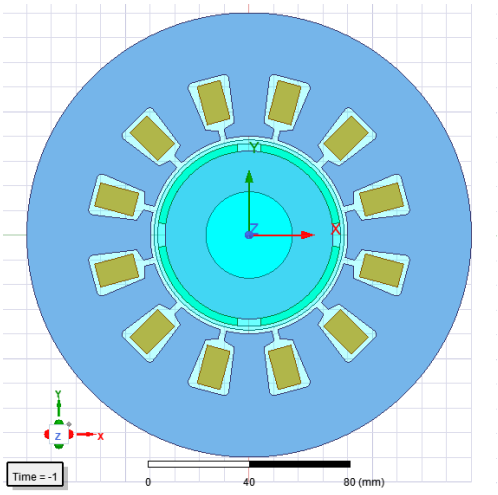

Figure 5.3: Cross-section of SMPM machine without ME in Maxwell.

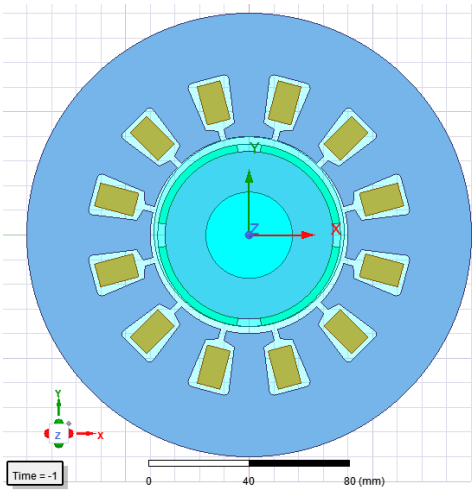

Figure 5.4: Cross-section of SMPM machine with ME in Maxwell.

Table 5.1: SMPM machine parameters for simulation.

Parameter	Value
Number of poles	4
Number of slots	12
Conductors per slot	100
Parallel branches	1
Magnet material	NdFe30
Steel type	Iron
Stacking factor	0.95
Stator outer diameter [mm]	180
Stator inner diameter [mm]	80
Rotor outer diameter [mm]	74
Magnet thickness [mm]	3
Magnet coverage coefficient	0.83
Machine length [mm]	80

5.2.2.1 Calibration of Magnetic Parameters

The magnetic parameters are calibrated based on the dimensions of the four-pole SMPM machine. The slot effects are taken into account by using the Carter coefficient [99]:

$$k_c = \frac{\tau_s}{\tau_s - b_0 + \frac{4g}{\pi} \ln\left(1 + \frac{\pi}{4}\frac{b_0}{g}\right)}. \tag{5.22}$$

Similarly, the leakage inductance is assumed to be solely the slot leakage which is calculated with the method from [99]. Assuming that all conductors in a slot are series connected and approximating the slot to a rectangle (Fig. 5.5), the phase slot inductance is given by [99]

$$L_{slot} = 4N_t^2 l_e \mathcal{P}, \tag{5.23}$$

where l_e is the effective length and $\mathcal{P}$ is the slot leakage permeance, which are given by,

$$l_e = l + 2g_e, \tag{5.24}$$

$$\mathcal{P} = \mu_0 \left(\frac{d_0}{b_0} + \frac{d_2}{b_s} + \frac{d_3}{3b_s} + \frac{d_1}{b_s - b_0} \log\left(\frac{b_s}{b_0}\right) \right). \tag{5.25}$$

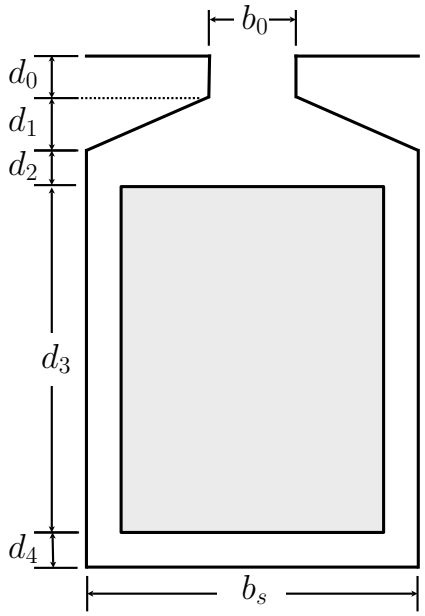

Figure 5.5: Slot dimensions for slot leakage inductance calculation.

5.2.2.2 Validation of Magnetic Parameters

FEA simulations are used to validate the magnetic parameters. The FEA simulations are performed using *Maxwell* from *Ansoft Corporation*. The SMPM machine operates at zero current and a constant speed of 1000 RPM. Note that, for the PM flux linkage, the shape is determined based on the dimensions (i.e., normalized PM flux linkage); however, the amplitude is calculated using the healthy case from FEA simulations. Another approach is to scale the magnet function using an open circuit test, as presented by [98].

Fig. 5.6 shows the equivalent two-phase magnetic parameters under healthy and ME conditions for one mechanical period. Note that the equivalent direct- and quadrature-axis inductances calculated using FEA simulations are slightly different since the permeability of the magnet lightly differs from the one of the air. Also, we point out that the ripple in the magnetic parameters calculated through FEA simulations is due to the slot harmonics which were neglected in the model derivation. The magnetic values calculated by the model and the FEA simulation are compared using the Mean Relative Error (MRE), which is given by

$$MRE = \sum_{k=1}^{K} \frac{\mid m_k - d_k \mid}{n_k \langle d_k \rangle}, \tag{5.26}$$

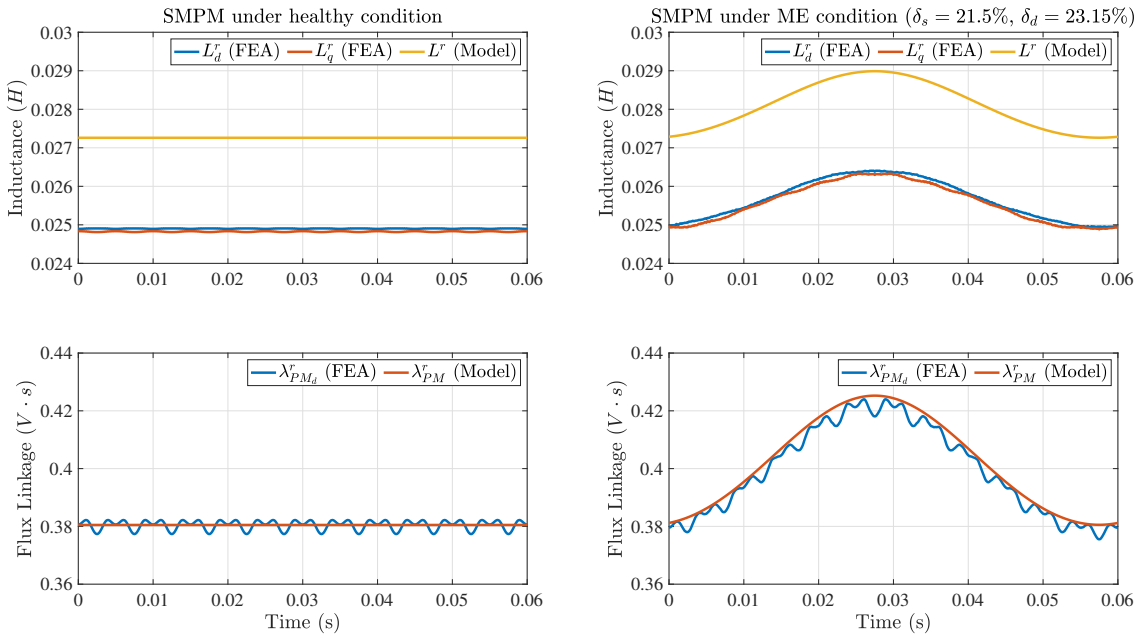

Figure 5.6: Comparison of the proposed model and FEA results for the magnetic parameters under healthy (left) and ME (right) conditions.

where m_k is the model prediction, d_k is the data (i.e., FEA data), n_k is the number of data points, and $\langle d_k \rangle$ is the average of all data points, which is given by,

$$\langle d_k \rangle = \frac{1}{n_k} \sum_{k=1}^{K} d_k.$$

Table 5.2 presents a summary of the MREs for healthy and eccentric conditions. As shown in Table 5.2, the inductance is calculated approximately within a 10% MRE. Note that, while there is a 10% error in the inductances, it is a constant difference, mainly due to the leakage inductance approximation. In the case of the PM flux linkage, the MRE is considerably smaller (0.64%). Note that the main goal of the model is to capture the "essential" behavior of the eccentricity fault. In other words, the model seeks to capture the distinctive features of the eccentricity fault rather than details. In the healthy case, inductance and PM flux linkage are expected to be essentially constant, and the model captures them. Similarly, in the ME case, the characteristic feature is the oscillation at the rotor speed and the increase in the magnetic parameters, also captured by the model. Note that the model captures the eccentricity based on the fundamental Fourier coefficient of the magnetic parameters, always present regardless of the SMPM machine design.

Table 5.2: MREs under healthy and ME conditions

Parameter	MRE (Healthy)	MRE (Eccentric)
L^r	9.64%	9.63%
λ^r_{PM}	N/A	0.64%

5.3 Parameter Identification for Fault Diagnosis and Condition Monitoring of SMPM Machines under Eccentricity

In this section, a parameter identification strategy for ME detection is presented. First, a parameterization which includes ME specific parameters is formulated based on the SMPM machine model under ME presented in Eq. (5.18). Note that the linear parameterization required to formulate the parameter estimators follows the form presented in Eq. (4.15). Afterwards, the input design, which guarantees sufficient conditions for accurate parameter convergence, is presented. Specifically, the conditions in which the input signals ensure the PE property are studied. The projection algorithm is used as the parameter identification algorithm, details of which can be found in the previous chapter (see Section 4.3.2).

5.3.1 Parametric Model for Fault Diagnosis and Condition Monitoring of SMPM Machines under Eccentricity

Under ME, the magnetic parameters vary with respect to the healthy ones due to the ME air-gap asymmetry (Eq. (5.21)). As shown in Fig. (5.2), the ME air-gap asymmetry increases the magnetic parameters with the main frequency corresponding to the rotor speed. This variation in the magnetic parameters can be approximately modeled as a sinusoid, in which case, the parameters are given by

$$L^r \approx L_0 + L_1 \sin\theta_r + L_2 \cos\theta_r, \tag{5.27}$$

$$\lambda^r_{PM} \approx \Lambda_0 + \Lambda_1 \sin\theta_r + \Lambda_2 \cos\theta_r. \tag{5.28}$$

Note that, for the inductance (Eq. (5.19)), the leakage term is absorbed by the constant component in Eq. (5.27).

By approximating the magnetic parameters with Eqs. (5.27) and (5.28), the linear

parameterization of the filtered dynamic model from Eq. (5.18) is given by,

$$\begin{aligned}
\vec{z} &= \begin{bmatrix} z_d & z_q \end{bmatrix}^T = \{\mathcal{F}(s)\} \begin{bmatrix} v_d^r & v_q^r \end{bmatrix}^T, \\
\vec{\theta} &= \begin{bmatrix} R & L_0 & \Lambda_0 & L_{ME_1} & L_{ME_2} & \Lambda_{ME_1} & \Lambda_{ME_2} \end{bmatrix}^T, \\
\mathbf{\Phi}^T &= \begin{bmatrix} \vec{\phi}_d^T \\ \vec{\phi}_q^T \end{bmatrix} = \{\mathcal{F}(s)\} \begin{bmatrix} i_d^r & i_q^r \\ (\frac{d}{dt} i_d^r - \omega_{re} i_q^r) & (\omega_{re} i_d^r + \frac{d}{dt} i_q^r) \\ 0 & \omega_{re} \\ \frac{d(i_d^r \sin\theta_r)}{dt} - \omega_{re} i_q^r \sin\theta_r & \frac{d(i_q^r \sin\theta_r)}{dt} + \omega_{re} i_d^r \sin\theta_r \\ \frac{d(i_d^r \cos\theta_r)}{dt} - \omega_{re} i_q^r \cos\theta_r & \frac{d(i_q^r \cos\theta_r)}{dt} + \omega_{re} i_d^r \cos\theta_r \\ \omega_r \cos\theta_r & \omega_{re} \sin\theta_r \\ -\omega_r \sin\theta_r & \omega_{re} \cos\theta_r \end{bmatrix}.
\end{aligned} \tag{5.29}$$

5.3.2 Persistently Exciting Inputs

In this section, sufficient conditions for accurate parameter estimation are studied for the estimator based on the ME model, presented in Section 5.3.1. Similar to the analysis presented in Chapter IV, the definition of persistent excitation presented in Section 2.7 (Definition 2.1) will be used to determine the sufficient conditions for PE. The following analysis assumes that the regressor is sampled with a frequency more than twice the highest-frequency component (Theorem 2.3) so that the discrete- and continuous-time regressors carry the same information. Therefore, if the continuous-time signal is PE, its discrete-time version is also PE. Additionally, the torque and rotor electrical speed are assumed constant. Similarly, since the healthy torque (Eq. (4.4)) is solely a function of the quadrature-axis current, the persistently exciting input required for accurate parameter identification will be injected through the direct-axis current. Therefore, a sinusoidal direct-axis current and a constant quadrature current will be assumed, which are given by:

$$\begin{aligned}
i_d^r &= A \sin(\omega t), \\
i_q^r &= I_q,
\end{aligned}$$

where A and ω are the amplitude and frequency of the injected PE signal, and I_q is the corresponding quadrature-axis current that achieves the desired torque (i.e., $I_q = \frac{4\tau}{3N_p\Lambda_{PM}}$). In the regressor, the low-pass filter ($\{\mathcal{F}(s)\}$) will be neglected as it has no effect on the results.

5.3.2.1 Persistency of Excitation Analysis for Estimator based on Proposed Dynamic Model

Based on the previous assumptions, the regressor of the estimator based on proposed dynamic model (Eq. (5.29)) is given by:

$$\vec{\phi}_d = \begin{bmatrix} A\sin(\omega t) \\ A\omega\cos(\omega t) - \omega_{re} I_q \\ 0 \\ A\omega\cos(\omega t)\sin(\omega_r t) + A\omega_r \sin(\omega t)\cos(\omega_r t) - \omega_{re} I_q \sin(\omega_r t) \\ A\omega\cos(\omega t)\cos(\omega_r t) - A\omega_r \sin(\omega t)\sin(\omega_r t) - \omega_{re} I_q \cos(\omega_r t) \\ \omega_r \cos(\omega_r t) \\ -\omega_r \sin(\omega_r t) \end{bmatrix}, \tag{5.30}$$

$$\vec{\phi}_q = \begin{bmatrix} I_q \\ A\omega_{re}\sin(\omega t) \\ \omega_{re} \\ I_q\omega_r \cos(\omega_r t) + \omega_{re} A\sin(\omega t)\sin(\omega_r t) \\ -I_q\omega_r \sin(\omega_r t) + \omega_{re} A\sin(\omega t)\cos(\omega_r t) \\ \omega_{re}\sin(\omega_r t) \\ \omega_{re}\cos(\omega_r t) \end{bmatrix}. \tag{5.31}$$

In this case, note that the regressor is a function of the excitation, electrical rotor, and rotor frequencies. Assuming that the regressor is periodic with $T_0 = \frac{2\pi}{\omega_0}$, it can be shown that:

$$\det\left(\frac{1}{T_0}\int_0^{T_0} \mathbf{\Phi}(\tau)\mathbf{\Phi}(\tau)^\intercal d\tau\right) = \frac{A^2\omega_{re}^6}{65536}\Big(A^2\omega^2 + \omega_{re}^2(A^2 + 2I_q^2)\Big)(20A^2\omega^2 + \omega_{re}^2(25A^2 + 18I_q^2))^2 \tag{5.32}$$

Equation (5.32) shows that the regressor, $\mathbf{\Phi}$, is persistently exciting if:

1. The rotor speed is non-zero (i.e., $\omega_r = \frac{\omega_{re}}{2} = 0$).
2. At least one sinusoidal component is injected into the direct-axis current (i.e., $A \neq 0$).

This analysis shows that the estimator based on the ME model requires the same excitation as the estimator based on the standard model. Similar to the estimator for

demagnetization presented in Chapter IV, the additional parameters for ME detection are self-excited.

5.4 Simulation Results Assuming Linear Magnetics

The performance of the parameter estimator presented in Eq. (5.29) is assessed by numerical simulations in Matlab/Simulink. The standard-model-based parameter estimator (Eq. (4.16)) presented in Section 4.3.1.1 will be used as the baseline. Both parameter estimators are evaluated with different gains while the SMPM machine operates at different current levels and a constant speed of 1000 RPM. PI regulators with cross-coupling compensation are used to regulate the two-phase currents in the rotor reference frame. The persistently exciting signal required for accurate parameter estimation is injected in the direct-axis current, as follows:

$$\tilde{i}_d^r = 10\sin(2\pi 40t), \tag{5.33}$$

where the tilde $(\tilde{\cdot})$ denotes a control reference signal.

The controller and parameter estimators are simulated with a triggered subsystem switching at $10kHz$ to capture the discrete-time practical implementation. The continuous-time SMPM dynamics are simulated with a fixed time step of 2 μs using *ode4*. The command voltages from the controller are converted into duty cycles using SVM [83]. Based on the duty cycle calculation, an ideal "average-value" VSI provides average-value voltages to the SMPM machine. An initial deviation of 20% is assumed in the estimated parameters with respect to the healthy ones. Table 5.3 presents the machine, fault, control, and adaptation parameters for the simulations. The SMPM machine used in the simulations corresponds to the one in Section 5.2.2, which is shown in Fig. 5.3. Note that the SMPM machine's magnetic parameters are calculated using Eqs. (5.19) and (5.20) and the dimensions from Table 5.1.

5.4.1 Parameter Estimator Based on Standard Dynamic Model

In Fig. 5.7, the performance of the parameter estimator from Eq. (4.16) under healthy and eccentricity conditions is presented. Under healthy conditions, the estimated parameters converge to their true values. In terms of the simulation under eccentricity condition, the parameter estimator successfully tracks the average-value variations in the magnetic parameters. Specifically, the average inductance increases by 2.99%, while the average PM flux linkage increments by 5.52% compared to the

Table 5.3: Machine, control, and adaptation parameters for simulation

Description	Value
SMPM Machine Parameters:	
R	0.785Ω
N_p	4
Eccentricity Parameters:	
δ_s	21.5%
δ_d	23.15%
α	0
Control Parameters:	
K_p	27.26
K_i	0.0785
Switching frequency (f_{sw})	$10kHz$
Sampling frequency (f_s)	$10kHz$
Adaptation Parameters:	
a	0.004/0.002/0.001
c	1

healthy case. However, the estimated parameters have noticeable oscillations that worsen as the adaptation gain increases due to unmodeled dynamics. In addition to an increased average value, the magnetic parameters experience oscillations which the parameter estimator is attempting to track. Unfortunately, as shown in Fig. 5.8, the parameter estimator is not fast enough for this purpose, even with higher adaptation gains.

The condition number of the PE condition matrix is presented in Figs. 5.9 and 5.10, as a validation for the discrete PE analysis. Note that the moving window corresponds to the period of the injected PE signal and is given by 250 samples (0.025 s). As seen in Fig. 5.9, the condition number of the PE condition matrix is not infinite, and, hence, the system is persistently excited. Fig. 5.10 shows the condition number of the PE matrix when the regressor is scaled, as previously discussed in Remark 4.1. As shown in Figs. 5.10, scaling the regressor improves the condition number of the PE condition matrix.

5.4.2 Parameter Estimator Based on Proposed Dynamic Model

The performance of the parameter estimator from Eq. (5.29) under healthy and eccentricity conditions is presented in Fig. 5.11. For the simulation under healthy conditions, the parameters achieve accurate convergence. Furthermore, the parameters related to ME are zero, which indicates that the SMPM machine is not experiencing

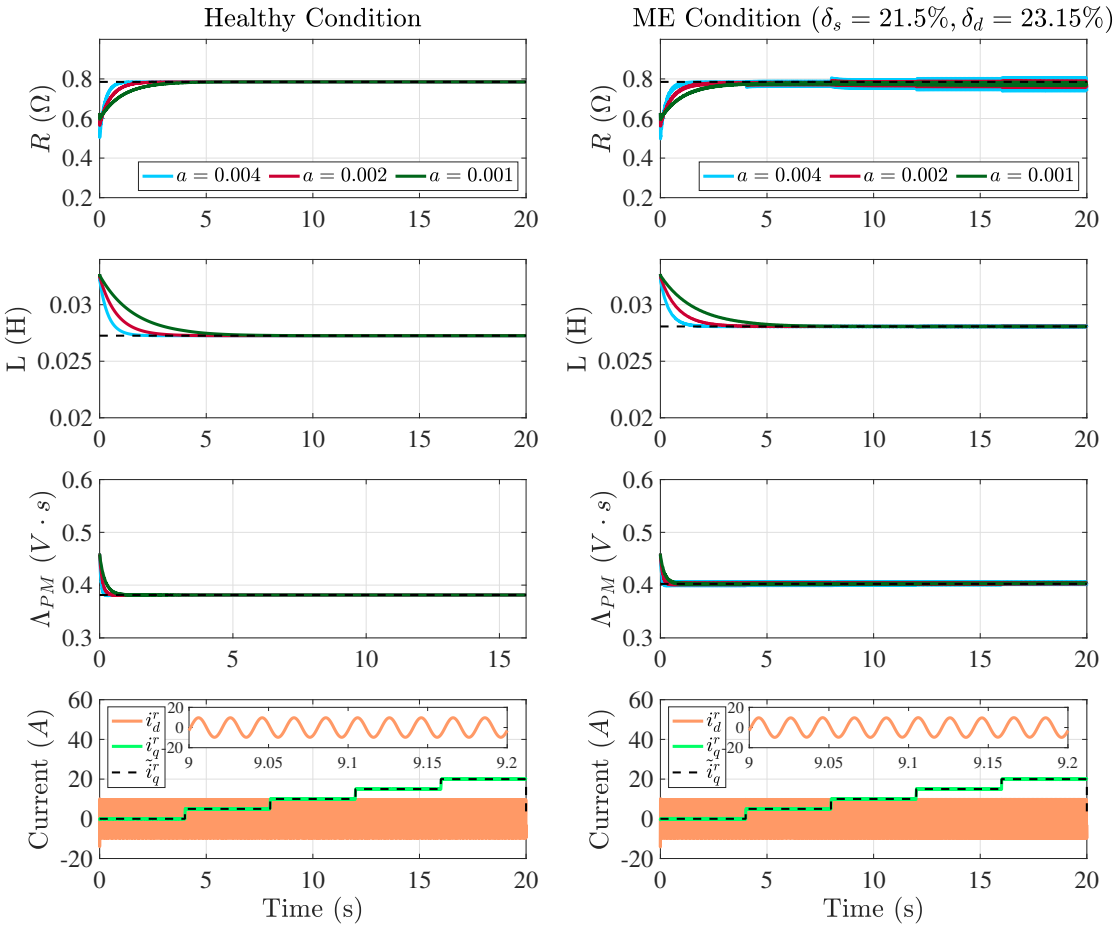

Figure 5.7: Simulation results of the parameter estimator based on the standard dynamics for different adaptation gains when the machine is operating under healthy (left) and eccentricity (right) conditions. The black dash line refers to the average true parameters.

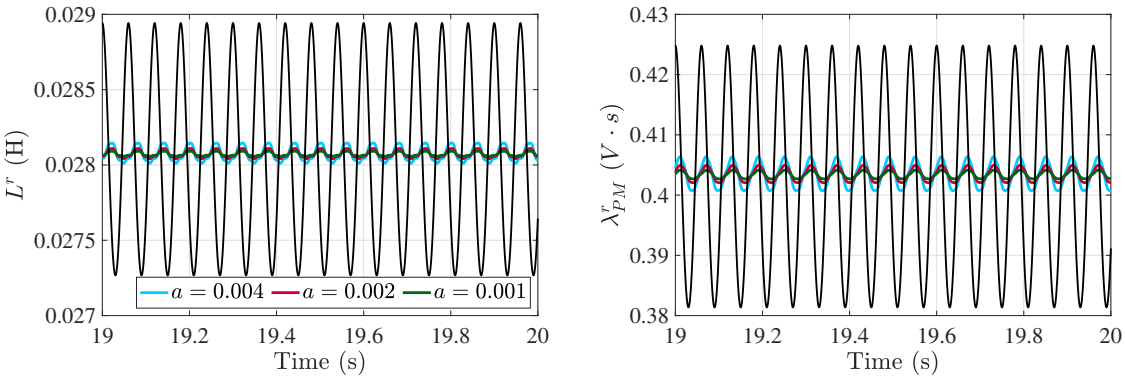

Figure 5.8: Comparison between the model magnetic parameters (black lines) and estimated parameters from the parameter estimator based on standard dynamics for different adaptation gains with the SMPM machine operating under ME conditions.

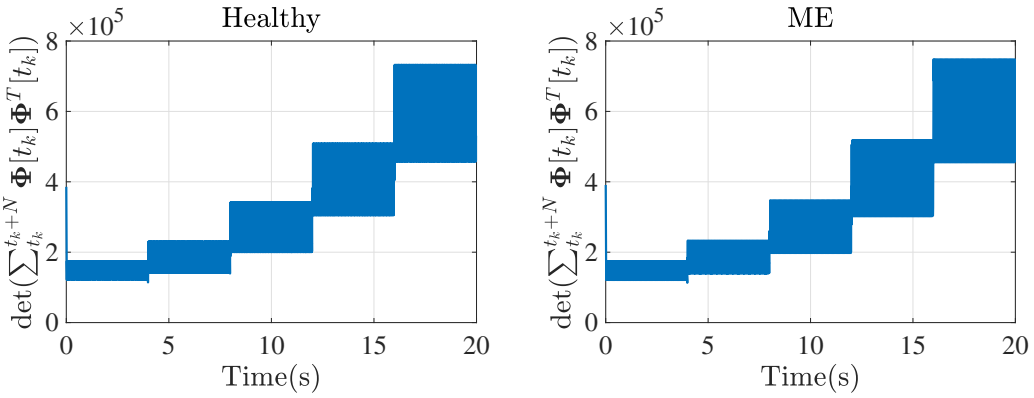

Figure 5.9: Condition number of the discrete PE condition matrix for the estimator based on the standard dynamics when the SMPM machine is operating under healthy (left) and ME (right) conditions.

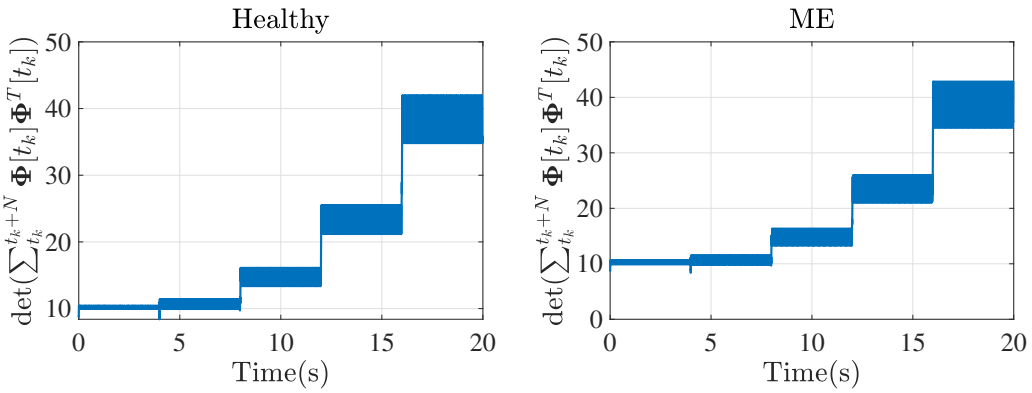

Figure 5.10: Condition number of the discrete PE condition matrix with scaled regressor for the estimator based on the standard dynamics when the SMPM machine is operating under healthy (left) and ME (right) conditions.

ME. Under eccentricity conditions, the estimated resistance, average inductance, and average PM flux linkage converge to their actual values. The parameters related to ME are non-zero, indicating that the SMPM is operating under ME conditions. Moreover, the estimated ME asymmetry parameters successfully reconstruct the frequency of interest, as shown in Fig. 5.12. Unlike the standard-model-based parameter estimator, the parameters are tracked without significant oscillations for all three adaptation gains under the eccentricity case.

In terms of the PE condition, Figs. 5.13 and 5.14 show the condition number of the PE condition for the proposed estimator. The moving window (N) is given by 3000 samples (0.3 s), corresponding to the regressor's period. Note that the regressor's period depends on the frequency of the injected PE signal and the electrical rotor frequency (See Eqs. (5.30) and (5.31)). The system is persistently excited as the condition number is not infinite, as shown in Fig. 5.13. Hence, the parameter estimator based on the eccentricity model can achieve sufficient conditions for accurate identification with the same excitation as the estimator based on the standard model. Fig. 5.14 shows the condition numbers of the PE condition matrix with the scaled regressor. Similar to the parameter estimator based on the standard model, scaling the regressor improves the condition number of the PE condition matrix.

Regarding the estimator design, smaller adaptation gains are preferable since the estimator acts as a filter under these conditions. The parameter estimator from Eq. (5.29) is based on an approximation of Eq. (5.18) and captures average-value variations and the main oscillation caused by the air-gap asymmetry. However, there are still some unmodeled dynamics that will affect the parameters as oscillations. With lower adaptation gains, the estimated parameters are more robust to these

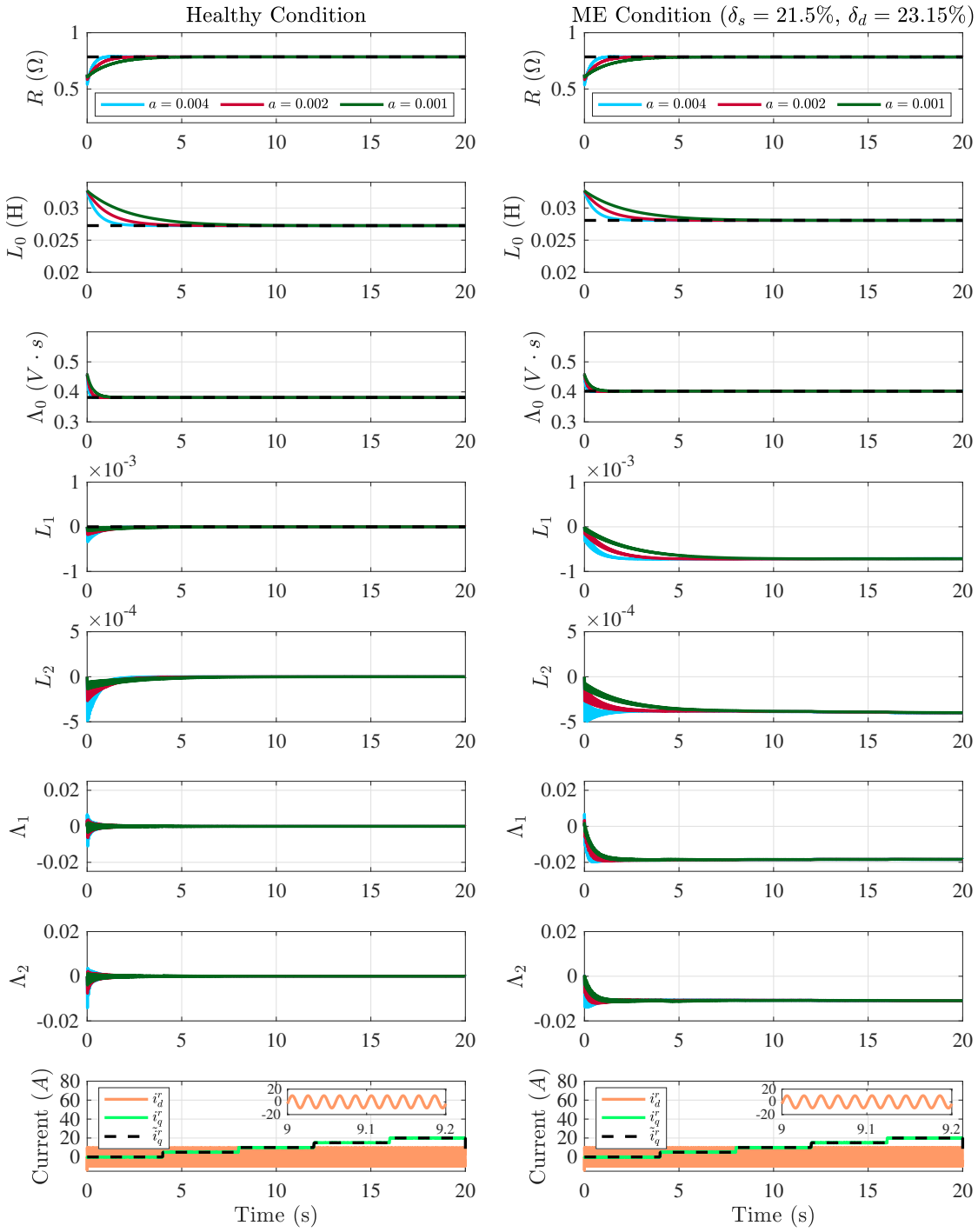

Figure 5.11: Simulation results of the proposed-model-based parameter estimator with different adaptation gains with the SMPM machine under healthy (left) and eccentricity (right) conditions. The black dash line corresponds to the actual parameters.

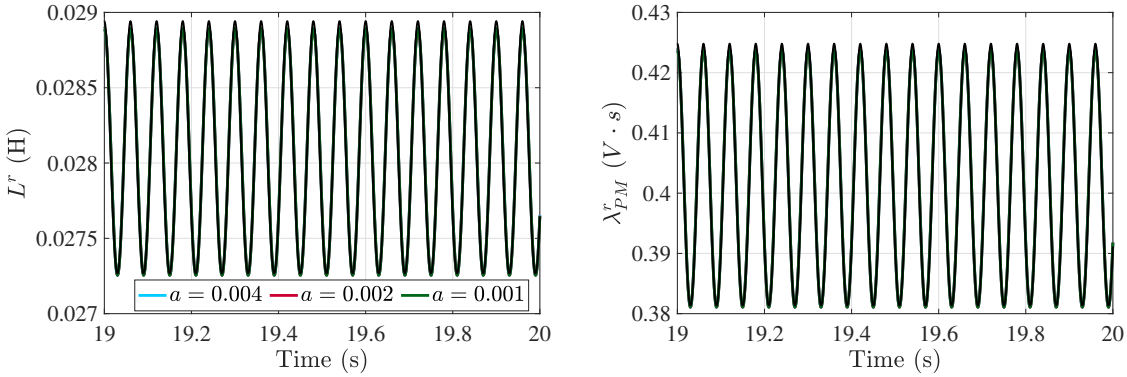

Figure 5.12: Comparison between the model and estimated magnetic parameters with the SMPM machine operating under ME conditions. The magnetic parameters are reconstructed based on the estimated parameters from the proposed parameter estimator for different adaptation gains.

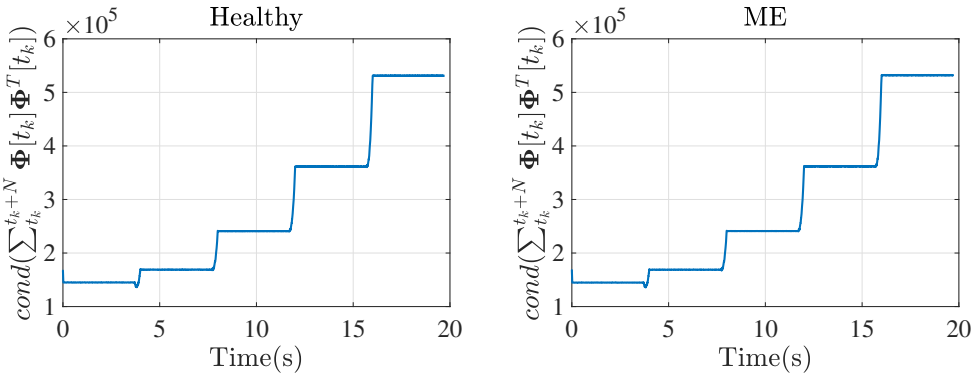

Figure 5.13: Condition number of the discrete PE condition matrix for the estimator based on the proposed dynamics when the SMPM machine is operating under healthy (left) and ME (right) conditions.

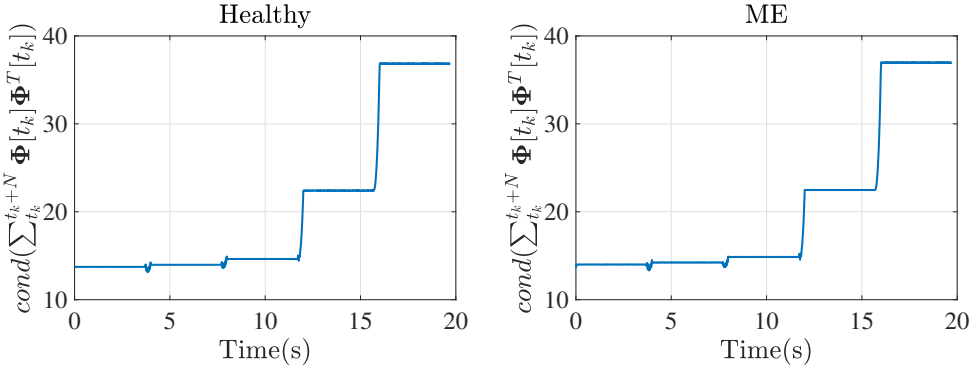

Figure 5.14: Condition number of the discrete PE condition matrix for the estimator based on the proposed dynamics with scaled regressor when the SMPM machine is operating under healthy (left) and ME (right) conditions.

unmodeled dynamics and noises [84].

5.5 Co-simulation Results Considering Nonlinearities

In this section, the effectiveness of the parameter estimators for eccentricity detection is validated through co-simulations. The co-simulations are implemented using Twin Builder, which allows integrating an FEA-based machine model with an electric drive. The FEA-based SMPM machine model corresponds to the SMPM machine presented in Section 5.2.2 and is developed and simulated in Maxwell. In the co-simulations, the steel type is changed to "M19" (See Fig. 4.23), which is a typical material for electric machines. The electric drive model, as well as the co-simulation interface, are implemented in Twin Builder. The inverter model corresponds to the "average-value" VSI. The PI regulators with cross-coupling compensation used for current regulation are developed in Matlab/Simulink and integrated as a Twin Builder component.

The FEA-based machine model and electric drive are executed at $10kHz$. The estimated parameters have an initial 20% deviation from the linear parameters presented in Section 5.2.2.2. The command current that is injected for PE purposes is given by:

$$\tilde{i}_d^r = 5\sin(2\pi 40t). \tag{5.34}$$

5.5.1 Performance of Parameter Estimator Based on Standard Dynamic Model

In Fig. 5.15, the co-simulation results for the standard-model-based parameter estimator are presented. Note that the black dashed line corresponds to the average value of the actual parameters assuming linear magnetics, as presented in Section 5.2.2.2. Regarding the co-simulation under healthy conditions, the parameters track the linear values for most current values. When the SMPM machine operates at higher currents, the magnetic parameters decrease, indicating saturation. In addition, the resistance starts drifting away from its expected value. Since the resistance drop is small compared to the total voltage, the estimated resistance is susceptible to unmodeled dynamics. Specifically, under saturation the estimated resistance gets affected by the magnetics as they are no longer linear. In terms of the ME results presented in Fig. 5.15, the magnetic parameters track their linear values at low current values and start decreasing for higher currents. Regarding the resistance, its estimate is inaccurate and has perceptible oscillations caused by the unmodeled ME

dynamics.

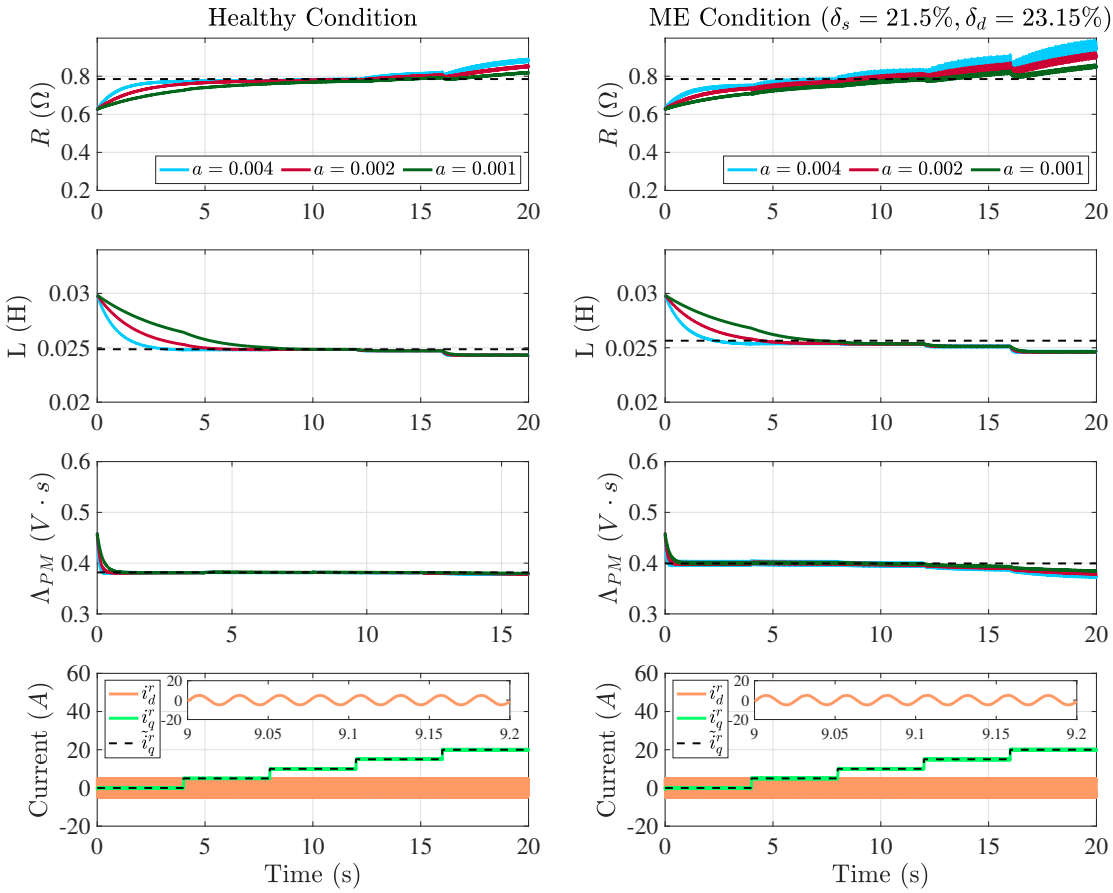

Figure 5.15: Co-simulation results of the parameter estimator based on the standard dynamics for different adaptation gains when the machine is operating under healthy (left) and eccentricity (right) conditions.

Based on these results, the standard-model-based parameter estimator can provide some information for fault diagnosis and condition monitoring of SMPM machines under ME conditions. In terms of the fundamental component of the magnetic parameters, their increase indicates an increment in ME. The PM flux linkage is more noticeably affected by eccentricity than the two-phase inductance, which is more suitable for monitoring and detection. In particular, the leakage term in the two-phase inductance weakens the eccentricity effect as it increases the average value. The main challenge of using these indicators is that, under healthy conditions, saturation and varying PM temperature also affect the magnetic parameters. Aside from the parameters' average value, the oscillations cannot be tracked by the parameter estimator and are affected by the adaptation dynamics, and, hence, the information regarding

the fault that can be extracted is unclear. Since no information can be extracted from the oscillations, smaller adaptation gains are preferable as they mitigate the impact of the unmodeled dynamics in the estimated parameters.

5.5.2 Performance of Parameter Estimator Based on Proposed Dynamic Model

The co-simulation results for the parameter estimator based on the proposed dynamics are presented in Fig. 5.16. In both cases, the magnetic parameters follow the linear values for most currents until they reach saturation and decrease. In addition, the ME-related parameters successfully indicate ME conditions. The ME-related parameters are equal to zero under healthy conditions, while they are non-zero under ME conditions. Since the air-gap asymmetry is approximately captured using the ME-related parameters, the estimated resistance is solely affected by saturation.

This parameter estimator, based on the proposed dynamics, offers more details than the standard-model-based estimator for fault diagnosis and condition monitoring of SMPM machines under ME conditions. Similar to the standard-model-based estimator, the proposed-model-based estimator can track the fundamental component of the magnetic parameters, which can be used as an indicator of ME. The ME-related parameters provide an additional indicator for the proposed model-based estimator as they capture the oscillation caused by the air-gap asymmetry. When there is no ME, the ME-related parameters are equal to zero. Similarly, under ME, these parameters become non-zero, indicating that the SMPM machine is operating under ME conditions. Therefore, these parameters can be potentially used to overcome the difficulties mentioned above for monitoring and detecting ME due to saturation and varying PM temperature. In practice, all SMPM machines have some level of ME due to the inherent tolerances in the manufacturing and assembling processes. Hence, ME-related parameters are expected to be close to zero under healthy conditions. Since eccentricity gradually increases through time, the ME-related parameters can be used to monitor this progression, and a threshold can be established for detection.

5.6 SMPM Design Limitations for Fault Detection

The SMPM machine design can affect the application of the presented approaches for fault detection. The PMs limit the degree of eccentricity that the SMPM machine can experience since they are located in the air gap. In the literature, SMPM machines with PMs that occupy approximately 50% to 90% of the air gap region can be

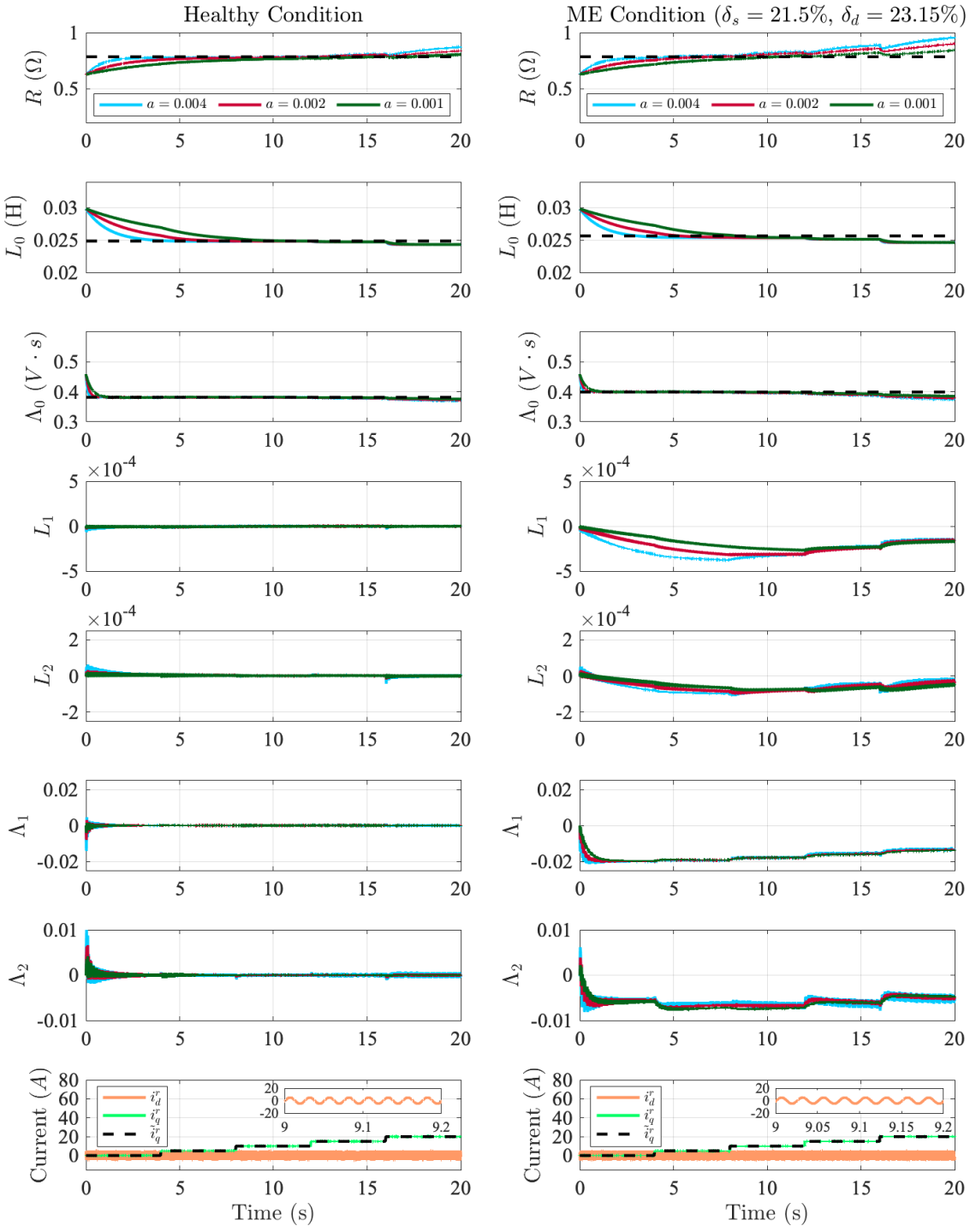

Figure 5.16: Co-simulation results of the parameter estimator based on the proposed dynamics for different adaptation gains when the machine is operating under healthy (left) and eccentricity (right) conditions.

found [101–104]. In the case that there is not much room for eccentricity, the magnetic parameters will still experience the average increase and asymmetry oscillation; however, the effects will be subtle.

5.7 Summary

In this chapter, the application of parameter identification to fault diagnosis and condition monitoring of SMPM machines under eccentricity conditions was investigated. Specifically, an equivalent two-phase model and an online parameter identification strategy for a three-phase four-pole SMPM machine with two windings in series per phase under eccentricity conditions are presented. Eccentricity mainly affects the magnetic parameters. So first, the equivalent two-phase dynamics under eccentricity were formulated by modeling the expressions for the inductances and PM flux linkages using MWF and MF theories. Then, FEA simulations were used to calibrate and validate the model's magnetic parameters for an SMPM machine design. Afterward, the parameter identification strategy for detecting eccentricity was formulated, including the parametric model and sufficient conditions for accurate convergence. Subsequently, the performance of the proposed model-based estimator and the standard-model-based parameter estimator from Section 4.3 were investigated through simulations and co-simulations. Compared to the parameter estimator based on the standard SMPM machine model, the parameter estimator based on the proposed model provided additional insight, as its ME-specific parameters capture the oscillations caused by the ME in the magnetic parameters. Moreover, the ME-related parameters are a more suitable indicator for monitoring and detecting ME as they can track a gradual increase in ME. In addition, a comparison between simulation and co-simulation results showed that the proposed model is a suitable tool for studying the SMPM machine behavior under ME in the linear operating region.

5.8 Appendix

5.8.1 Turn Functions and MWFs for the Four-Pole, Three-Phase SMPM Machine with Two Coils Per Phase

$$n_a(\phi) = A_0 + \sum_{k=1}^{\infty} A_k \cos(2k\phi) \tag{5.35}$$

$$n_b(\phi) = -A_0 - \sum_{k=1}^{\infty} A_k \cos\Big(2k\Big(\phi + \frac{\pi}{6}\Big)\Big) \tag{5.36}$$

$$n_c(\phi) = -A_0 - \sum_{k=1}^{\infty} A_k \cos\Big(2k\Big(\phi - \frac{\pi}{6}\Big)\Big) \tag{5.37}$$

$$M_a(\phi, \theta_r) = -\frac{1}{2G_0} \sum_{k=1}^{\infty} A_k G_{2k} \cos(2k\alpha_M) + \sum_{k=1}^{\infty} A_k \cos(2k\phi) \tag{5.38}$$

$$M_b(\phi, \theta_r) = \frac{1}{2G_0} \sum_{k=1}^{\infty} A_k G_{2k} \cos\Big(2k\Big(\alpha_M + \frac{\pi}{6}\Big)\Big) - \sum_{k=1}^{\infty} A_k \cos\Big(2k\Big(\phi + \frac{\pi}{6}\Big)\Big) \tag{5.39}$$

$$M_c(\phi, \theta_r) = \frac{1}{2G_0} \sum_{k=1}^{\infty} A_k G_{2k} \cos\Big(2k\Big(\alpha_M - \frac{\pi}{6}\Big)\Big) - \sum_{k=1}^{\infty} A_k \cos\Big(2k\Big(\phi - \frac{\pi}{6}\Big)\Big) \tag{5.40}$$

5.8.2 General Expressions for the Magnetic Parameters of the Four-Pole, Three-Phase SMPM Machine with Two Coils Per Phase

In the case of the four-pole, three-phase SMPM machine with two coils per phase, the general Fourier Series for turn, magnet and inverse air-gap functions are given by:

$$n_y(\phi) = A_0 + \sum_{k=1}^{\infty} A_k \cos\big(2k(\phi + \phi_y)\big), \tag{5.41}$$

$$F_{mag}(\theta_r) = \sum_{k=1}^{\infty} F_k \cos\big(2k(\phi - \theta_r)\big) - \frac{1}{2G_0} \sum_{k=1}^{\infty} F_n G_{2k} \cos(2k(\alpha_M - \theta_r)), \tag{5.42}$$

$$g^{-1}(\phi, \theta_r) = G_0 + \sum_{k=1}^{\infty} G_k \cos(k(\phi - \alpha_M)), \tag{5.43}$$

where

$$G_0 = \frac{1}{g_0\sqrt{1-\delta_M^2}},$$
$$G_k = \frac{2}{g_0\sqrt{1-\delta_M^2}}\left[\frac{1-\sqrt{1-\delta_M^2}}{\delta_M}\right]^k.$$

Note that the sign of $n_y(\phi)$ depends on the phase (see Eqs. (5.35), (5.36), and (5.37)). Using these Fourier Series expressions from Eqs. (5.41), (5.42) and (5.43), the general expressions for the inductances and permanent magnet flux linkages from Eqs. (5.9), (5.10) and (5.12) are given by,

$$\begin{aligned} L_{xy} = \mu_0\pi rl\Bigg(& G_0\sum_{k=1}^{\infty}A_k^2\cos\big(2k(\phi_y-\phi_x)\big) \\ & -\frac{1}{2}\sum_{k=1}^{\infty}\sum_{n=1}^{\infty}A_kA_nG_{2(k+n)}\cos\big(2(k\phi_y-n\phi_x+(n-k)\alpha_M)\big) \\ +\sum_{\substack{n=1\\n>k}}^{\infty}\sum_{k=1}^{\infty}& A_kA_nG_{2(n-k)}\cos\big((k+n)(\phi_y-\phi_x)\big)\cos\big((n-k)(\phi_y+\phi_x)+2(n-k)\alpha_M\big) \end{aligned} \tag{5.44}$$

$$\begin{aligned} \lambda_{PM,i} = \mu_0\pi rl\Bigg(& G_0\sum_{k=1}^{\infty}A_kF_k\cos\big(2k(\phi_i+\theta_r)\big) \\ & +\frac{1}{2}\sum_{k=1}^{\infty}\sum_{n=1}^{\infty}A_kF_n(G_{2(k-n)}-G_{2(k+n)})\cos\big(2(k\phi_i+n\theta_r+(k-n)\alpha_M)\big) \\ & +\frac{1}{2}\sum_{k=1}^{\infty}\sum_{n=1}^{\infty}A_kF_nG_{2(n-k)}\cos\big(2(k\phi_i+n\theta_r-(n-k)\alpha_M)\big)\Bigg) \end{aligned} \tag{5.45}$$

Note that L_{xx} corresponds to the case where $x = y$ in Eq. (5.44).

CHAPTER VI

Modeling and Identification for Condition Monitoring of Surface-Mount Permanent Magnet Machines Under Inter-turn Short Condition

6.1 Introduction

An Inter-Turn Short (ITS) occurs when the insulation fails between contiguous turns in a winding. In an electric machine, insulation deterioration is a natural aging process that happens gradually. However, overloads, manufacturing defects, thermal stresses, voltage stresses, and vibration-caused rubbing exacerbate insulation wear and tear [20]. Once the ITS occurs, the ITS produces additional heat, which helps its propagation. Hence, the ITS rapidly expands and escalates up to a phase-to-phase or phase-to-ground short circuit. In PMSMs, stator short-circuit faults can produce a magnetic field intensity that irreversibly demagnetizes the magnets, making this fault especially problematic [20].

This chapter studies the application of parameter identification to fault diagnosis and condition monitoring of SMPM machines under ITS conditions. Specifically, an equivalent two-phase SMPM machine model and an online parameter identification technique for a three-phase four-pole SMPM machine with two coils in series per phase are formulated. An ITS refers to an insulation failure between contiguous turns in a coil and is typically modeled with an additional resistance shorting the affected turns. First, the SMPM machine model with ITS is formulated by modeling all coils separately. Then, the three-phase SMPM machine model under ITS is formulated by integrating the coils into the different phases based on the winding connections. Afterward, the equivalent two-phase dynamics are formulated by mapping the three-phase variables into their two-phase equivalents, referenced to the rotor reference frame. Subsequently, the model's magnetic parameters are calibrated

and validated against FEA simulations for an SMPM machine design. Following the modeling section, a parameter identification strategy for monitoring and detecting ITS condition is presented, including the linear parametric model and the sufficient conditions for accurate convergence. Afterward, the effectiveness of the proposed parameter identification strategy for monitoring and detecting ITS is assessed through simulations and co-simulations. Finally, remarks on the parameters' applicability for ITS detection are presented.

6.2 Modeling SMPM Machines with Inter-Turn Short Condition

Under free-fault conditions, the standard equivalent two-phase model is typically used to analyze the electrical dynamics, as previously presented in Eq. (4.3). However, under ITS, the insulation fails between contiguous turns in a winding, and the model from Eq. (4.3) is no longer valid. In this section, a simple SMPM machine model that captures the behavior of the SMPM machine under ITS conditions is derived under the following assumptions:

A. The machine has a smooth air gap (i.e., slot effects are not considered), is balanced in construction, and is connected in an ungrounded-wye configuration.

B. Magnetic saturation, eddy current, and hysteresis effects are neglected (i.e., linear magnetics are assumed).

C. Stator and rotor irons have infinite permeability. The permanent magnets and air have equal permeability.

The three assumptions (A-C) are commonly used for control-oriented models [56]. In terms of assumption B, the magnetics of an SMPM machine are roughly linear since the effective air gap between the stator and rotor irons is large. Regarding assumption C, most magnet materials (e.g., SmCo, NdFeB) have a permeability close to that of free space, while most iron alloys used in the stator and rotor irons have a permeability that is much higher than that of free space.

Modeling SMPM machines under ITS has to be done on a case-by-case basis, since the dynamic behavior differs for different pole numbers, winding configurations, and ITS fault location. In the following analysis, the model is derived based on a four-pole, three-phase SMPM machine with two coils in series per phase, as shown in Fig. 4.1. Note that the model assumes that the ITS occurs in phase A. Following

a similar analysis, SMPM machine models with ITS in phases B and C are derived, presented in the Appendix.

6.2.1 Modeling Inter-Turn Short

An inter-turn short in a coil is typically modeled with an additional resistance shorting the affected turns [16, 71–73], as shown in Fig. 6.1. The insulation-failure resistance (R_f) is meant to capture the degradation of the insulation material. Theoretically, a perfect ITS corresponds to an insulation-failure resistance equal to zero; however, a perfect short is an ideal that is never achieved in practice. In this section, a two-phase equivalent model that captures ITS is formulated for a three-phase four-pole SMPM machine with two coils in series per phase. The derivation starts by modeling each coil from the different phases separately as the ITS fault can be easily inserted. Then, based on this coil SMPM model and winding connections, the three-phase model is formulated. Afterward, the equivalent two-phase dynamics are formulated by mapping the three-phase variables into their two-phase equivalents, referenced to the rotor reference frame.

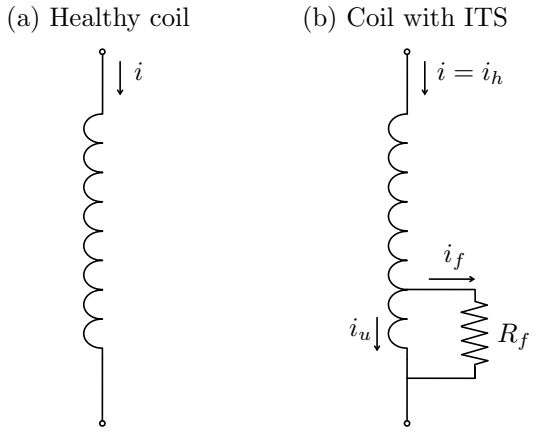

Figure 6.1: Coil model under healthy (left) and ITS (right) conditions.

6.2.1.1 Coil SMPM Machine Model under Inter-Turn Short Conditions

In this section, an SMPM machine model under ITS condition is formulated in which all coils are modeled separately. Since the ITS is modeled as an insulation-failure resistance shorting the affected turns (Fig. 6.1(b)), the electrical dynamics of the coil with ITS are separated into the dynamics related to the healthy turns (i.e., non-shorted) and the dynamics related to the shorted turns. Then, assuming that

the ITS occurs in coil a_1, the general expression describing the electrical dynamics of a four-pole three-phase SMPM machine with two coils per phase is given by

$$\begin{bmatrix} v_{a_{1h}} \\ v_{b_1} \\ v_{c_1} \\ v_{a_2} \\ v_{b_2} \\ v_{c_2} \\ v_{a_{1u}} \end{bmatrix} = \begin{bmatrix} R_{a_{1h}} & 0 & 0 & 0 & 0 & 0 & 0 \\ 0 & R_{b_1} & 0 & 0 & 0 & 0 & 0 \\ 0 & 0 & R_{c_1} & 0 & 0 & 0 & 0 \\ 0 & 0 & 0 & R_{a_2} & 0 & 0 & 0 \\ 0 & 0 & 0 & 0 & R_{b_2} & 0 & 0 \\ 0 & 0 & 0 & 0 & 0 & R_{c_2} & 0 \\ 0 & 0 & 0 & 0 & 0 & 0 & R_{a_{1u}} \end{bmatrix} \begin{bmatrix} i_{a_{1h}} \\ i_{b_1} \\ i_{c_2} \\ i_{a_2} \\ i_{b_2} \\ i_{c_2} \\ i_{a_{1u}} \end{bmatrix} + \frac{d}{dt} \begin{bmatrix} \lambda_{PM,a_{1h}} \\ \lambda_{PM,b_1} \\ \lambda_{PM,c_1} \\ \lambda_{PM,a_2} \\ \lambda_{PM,b_2} \\ \lambda_{PM,c_2} \\ \lambda_{PM,a_{1u}} \end{bmatrix} +$$

$$\begin{bmatrix} L_{a_{1h}} & L_{a_{1h}b_1} & L_{a_{1h}c_1} & L_{a_{1h}a_2} & L_{a_{1h}b_2} & L_{a_{1h}c_2} & L_{a_{1h}a_{1u}} \\ L_{a_1b_1} & L_{b_1} & L_{b_1c_1} & L_{b_1a_2} & L_{b_1b_2} & L_{b_1c_2} & L_{b_1a_{1u}} \\ L_{a_1c_1} & L_{b_1c_1} & L_{c_1} & L_{c_1a_2} & L_{c_1b_2} & L_{c_1c_2} & L_{c_1a_{1u}} \\ L_{a_1a_2} & L_{b_1a_2} & L_{c_1a_2} & L_{a_2} & L_{a_2b_2} & L_{a_2c_2} & L_{a_2a_{1u}} \\ L_{a_1b_2} & L_{b_1b_2} & L_{c_1b_2} & L_{a_2b_2} & L_{b_2} & L_{b_2c_2} & L_{b_2a_{1u}} \\ L_{a_1c_2} & L_{b_1c_2} & L_{c_1c_2} & L_{a_2c_2} & L_{b_2c_2} & L_{c_2} & L_{c_2a_{1u}} \\ L_{a_{1h}a_{1u}} & L_{b_1a_{1u}} & L_{c_1a_{1u}} & L_{a_2a_{1u}} & L_{b_2a_{1u}} & L_{c_2a_{1u}} & L_{a_{1u}} \end{bmatrix} \frac{d}{dt} \begin{bmatrix} i_{a_{1h}} \\ i_{b_1} \\ i_{c_2} \\ i_{a_2} \\ i_{b_2} \\ i_{c_2} \\ i_{a_{1u}} \end{bmatrix}, \quad (6.1)$$

where the subscript x_i denotes the coil i^{th} of phase x (e.g., a_1, a_2, b_1, b_2, c_1, or c_2), R_{x_i} is the resistance of coil x_i, L_{x_i} is the self-inductance of coil x_i, $L_{x_iy_j}$ is the mutual inductance between coils x_i and y_j, λ_{PM,x_i} is the PM flux linking coil x_i, and a_{1h} and a_{1u} denote the non-shorted and shorted parts of coil a_1, respectively.

In terms of the resistances, their values can be linearly prorated based on the three-phase resistance value and the number of shorted and non-shorted turns as follows:

$$R_{x_i} = \frac{R}{2}, \quad (6.2)$$

$$R_{a_{1h}} = \mu_h \frac{R}{2}, \quad (6.3)$$

$$R_{a_{1u}} = \mu_u \frac{R}{2}, \quad (6.4)$$

where R is the stator winding resistance, and μ_h and μ_u are the per unit healthy (i.e.,

non-shorted) and unhealthy (i.e., shorted) turns which are given by:

$$\mu_h = \frac{N_h}{N_t}, \tag{6.5}$$

$$\mu_u = \frac{N_u}{N_t}, \tag{6.6}$$

with N_t, N_h , and N_u as the total, healthy, and unhealthy number of turns in a coil. Note that:

$$N_t = N_h + N_u,$$
$$1 = \mu_h + \mu_u.$$

Regarding the inductances, the magnetizing and mutual inductances under healthy conditions can be calculated using winding function theory [96], and are given by:

$$L_{mag_{x_i}} = \frac{\mu_0 r l}{g_0} \int_0^{2\pi} n_{x_i}(\phi) N_{x_i}(\phi) d\phi = \frac{\pi \mu_0 r l}{g_0} \sum_{k=1}^{K} A_k^2, \tag{6.7}$$

$$L_{x_i y_j} = \frac{\mu_0 r l}{g_0} \int_0^{2\pi} n_{y_j}(\phi) N_{x_i}(\phi) d\phi = \frac{\pi \mu_0 r l}{g_0} \sum_{k=1}^{K} A_k^2 \cos(k(\phi_{y_j} - \phi_{x_i})), \tag{6.8}$$

where μ_0 is the magnetic constant (a.k.a., permeability of free space), r is the mean radius, l is the machine axial length, $n_{x_j}(\phi)$ and $N_{x_i}(\phi)$ are the turns and winding function for coil x_i, which are represented using Fourier Series as follows:

$$n_{x_i}(\phi) = A_0 + \sum_{k=1}^{K} A_k \cos(k(\phi + \phi_{x_i})),$$
$$N_{x_i}(\phi) = \sum_{k=1}^{K} A_k \cos(k(\phi + \phi_{x_i})).$$

The turns function for a distributed winding can be represented as a trapezoid, as shown in Fig. 6.2. In this case, the k^{th} Fourier coefficient of the turns function, $n_{x_i}(\phi)$, is given by

$$A_k = \frac{4N_t}{\pi k^2(\beta - \alpha)} \sin\Big(\frac{(\alpha + \beta)k}{2}\Big) \sin\Big(\frac{(\beta - \alpha)k}{2}\Big).$$

Then, the magnetizing and mutual inductances for the coil with the ITS can be

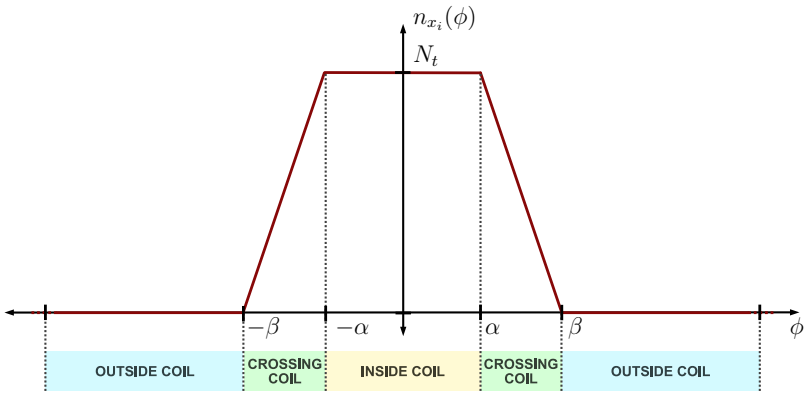

Figure 6.2: Turn function for a coil assuming distributed winding and $\phi_{x_i} = 0$.

calculated by adjusting the number of turns in Eqs. (6.7) and (6.8) as follows:

$$L_{mag_{a_{1h}}} = \frac{\pi \mu_0 r l \mu_h^2}{g_0} \sum_{k=1}^{K} A_k^2 = \mu_h^2 L_{mag_{x_i}}, \tag{6.9}$$

$$L_{mag_{a_{1u}}} = \frac{\pi \mu_0 r l \mu_u^2}{g_0} \sum_{k=1}^{K} A_k^2 = \mu_u^2 L_{mag_{x_i}}, \tag{6.10}$$

$$L_{a_{1h}a_{1u}} = \frac{\pi \mu_0 r l \mu_u \mu_h}{g_0} \sum_{k=1}^{K} A_k^2 = \mu_u \mu_h L_{mag_{x_i}}, \tag{6.11}$$

$$L_{a_{1h}y_j} = \frac{\pi \mu_0 r l \mu_h}{g_0} \sum_{k=1}^{K} A_k^2 \cos(k(\phi_{y_j} - \phi_{a_1})) = \mu_h M_{a_1 y_j}, \tag{6.12}$$

$$L_{a_{1u}y_j} = \frac{\pi \mu_0 r l \mu_u}{g_0} \sum_{k=1}^{K} A_k^2 \cos(k(\phi_{y_j} - \phi_{a_1})) = \mu_u M_{a_1 y_j}. \tag{6.13}$$

In order to determine the winding self-inductance, the leakage inductance, which does not contribute to torque generation, has to be added to the magnetizing inductance. In this analysis, the leakage inductance will be assumed to be solely the slot leakage inductance and will be modeled using the theory previously presented in Section 5.2.2.1. For the coil SMPM model, the coil slot inductance is given by:

$$L_l = 2N_t^2 l_e \mathcal{P}, \tag{6.14}$$

where l_e is the effective length defined in Eq. (5.24) and $\mathcal{P}$ is the slot leakage permeance defined in Eq. (5.25). Regarding the slot inductances for the coil with the ITS, they will be approximated based on the number of turns as:

$$L_{l_h} \approx 2N_h^2 l_e \mathcal{P} = \mu_h^2 L_l, \tag{6.15}$$

$$L_{l_u} \approx 2N_u^2 l_e \mathcal{P} = \mu_u^2 L_l. \tag{6.16}$$

where L_{l_h} and L_{l_u} are the coil slot inductances for the healthy (non-shorted) and unhealthy (shorted) turns in the coil with ITS. Note that, these slot inductances are also affected by the location of the shorted turns, which is not taken into account in Eqs. (6.15) or (6.16).

In terms of the PM flux linkages, the MF theory [98] can be used to determine the relationship between the PM flux linking the different coils and the different phases. Then, the PM flux linking the healthy coils as well as the healthy and unhealthy turns in the coil with ITS are given by:

$$\lambda_{PM,x_i} = \frac{\lambda_{PM,x}}{2},$$
$$\lambda_{PM,a_{1h}} = \frac{\mu_h \lambda_{PM,a}}{2},$$
$$\lambda_{PM,a_{1u}} = \frac{\mu_u \lambda_{PM,a}}{2}.$$

Note that a similar procedure can be followed to derive the SMPM machine model with the ITS occurring in coils from phases B or C.

6.2.1.2 Three-phase SMPM Machine Model under Inter-Turn Short Conditions

In this section, a three-phase SMPM machine model under ITS is derived based on the coil SMPM machine model presented in Eq. (6.1). Since the coils in a phase are connected in series, the coils' voltages and currents relate as follows:

$$\begin{bmatrix} v_{a_h} \\ v_b \\ v_c \\ v_{a_u} \end{bmatrix} = \begin{bmatrix} v_{a_1h} + v_{a_2} \\ v_{b_1} + v_{b_2} \\ v_{c_1} + v_{c_2} \\ v_{a_1u} \end{bmatrix}, \begin{bmatrix} i_a \\ i_b \\ i_c \end{bmatrix} = \begin{bmatrix} i_{a_1h} \\ i_{b_1} \\ i_{c_1} \end{bmatrix} = \begin{bmatrix} i_{a_2} \\ i_{b_2} \\ i_{c_2} \end{bmatrix}, i_{a_u} = i_{a_1u}. \tag{6.17}$$

Then, the electrical dynamics of the four-pole, ungrounded-wye-connected SMPM machine with two coils in series per phase under ITS are given by:

$$\begin{bmatrix} v_{a_h} \\ v_b \\ v_c \\ v_{a_u} \end{bmatrix} = \begin{bmatrix} \frac{(1+\mu_h)R}{2} & 0 & 0 & 0 \\ 0 & R & 0 & 0 \\ 0 & 0 & R & 0 \\ 0 & 0 & 0 & \frac{\mu_u R}{2} \end{bmatrix} \begin{bmatrix} i_a \\ i_b \\ i_c \\ i_{a_u} \end{bmatrix} + \frac{d}{dt} \begin{bmatrix} \frac{(1+\mu_h)}{2}\lambda_{PM,a} \\ \lambda_{PM,b} \\ \lambda_{PM,c} \\ \frac{\mu_u}{2}\lambda_{PM,a} \end{bmatrix}$$
$$+ \begin{bmatrix} L_{s_h} & \frac{\mu_h+1}{2}L_m & \frac{\mu_h+1}{2}L_m & L_{m_{hu}} \\ \frac{\mu_h+1}{2}L_m & L_s & L_m & \frac{\mu_u}{2}L_m \\ \frac{\mu_h+1}{2}L_m & L_m & L_s & \frac{\mu_u}{2}L_m \\ L_{m_{hu}} & \frac{\mu_u}{2}L_m & \frac{\mu_u}{2}L_m & L_{s_u} \end{bmatrix} \frac{d}{dt} \begin{bmatrix} i_a \\ i_b \\ i_c \\ i_{a_u} \end{bmatrix}, \quad (6.18)$$

with

$$i_0 = \frac{1}{3}(i_a + i_b + i_c) = 0. \quad (6.19)$$

where L_s is the three-phase self-inductance, L_{s_h} is the self-inductance for the non-shorted turns in the coils with ITS, L_{s_u} is the self-inductance for the shorted turns in the coil with ITS, L_m is the three-phase mutual inductance, and $L_{m_{hu}}$ is the mutual inductance between the shorted and non-shorted turns in the coil with ITS. The inductances presented in Eq. (6.18) are related to the ones from the coil SMPM machine model (Eq. (6.1)) as follows:

$$L_s = L_{mag_{x_1}} + L_{mag_{x_2}} + 2L_l + 2L_{x_1x_2} = 2(L_{mag_{x_i}} + L_l + L_{x_1x_2}),$$

$$L_{s_h} = L_{mag_{a_{1h}}} + L_{l_h} + L_{mag_{a_2}} + L_l + 2L_{x_1x_2} = (\mu_h^2 + 1)(L_{mag_{x_i}} + L_l) + 2\mu_h L_{x_1x_2},$$

$$L_{s_u} = L_{mag_{a_{1u}}} + L_{l_u} = \mu_u^2(L_{mag_{x_i}} + L_l),$$

$$L_m = L_{x_1y_1} + L_{x_1y_2} + L_{x_2y_1} + L_{x_2y_2} = 2(L_{x_iy_i} + L_{x_iy_j}),$$

$$L_{m_{hu}} = L_{a_{1h}a_{1u}} + L_{a_2a_{1u}} = \mu_u\mu_h L_{mag_{x_i}} + \mu_u L_{x_1x_2}.$$

Equation (6.18) shows the three-phase SMPM model for an ITS occurring in coil a_1. Based on Eq. (6.17), it can be shown that the three-phase SMPM machine model with an ITS in coil a_2 will be identical to the one presented in Eq. (6.18). In other words, the three-phase electrical dynamics do not distinguish in which of the phase's coils the ITS occurs.

6.2.1.3 Equivalent two-phase SMPM machine model under inter-turn short condition in the rotor reference frame

In this section, the three-phase dynamics presented in Eq. (6.18) are mapped into their equivalent two-phase variables in the rotor reference frame. In previous chapters, the Clarke transform was used to map the dynamics into their equivalent two-phase stationary ($\alpha - \beta$) variables while imposing the zero current constraint (Eq. (6.19)). However, the model under ITS has an additional state to capture the dynamics from the shorted turns. An orthonormal base can be formulated starting with the zero-sequence constraint, which can be used to enforce the wye connection between the phases and is given by

$$A_{23f} = \begin{bmatrix} \frac{1}{\sqrt{3}} & \frac{1}{\sqrt{3}} & \frac{1}{\sqrt{3}} & 0 \\ \frac{2}{\sqrt{6}} & -\frac{1}{\sqrt{6}} & -\frac{1}{\sqrt{6}} & 0 \\ 0 & \frac{1}{\sqrt{2}} & -\frac{1}{\sqrt{2}} & 0 \\ 0 & 0 & 0 & 1 \end{bmatrix}. \tag{6.20}$$

Note that this transformation includes a normalized version of the Clarke transform and an additional term for the shorted winding dynamics. Therefore, the Clarke transform can be extended for ITS condition as follows:

$$\mathbf{T_{23f}} = \begin{bmatrix} \frac{2}{\sqrt{3}} & -\frac{1}{\sqrt{3}} & -\frac{1}{\sqrt{3}} & 0 \\ 0 & \frac{\sqrt{3}}{3} & -\frac{\sqrt{3}}{3} & 0 \\ \frac{1}{3} & \frac{1}{3} & \frac{1}{3} & 0 \\ 0 & 0 & 0 & 1 \end{bmatrix}. \tag{6.21}$$

Similarly, the two-phase stationary variables can be mapped into the three-phase frame using the following extended inverse Clarke transform:

$$\mathbf{T_{23f}}^{-1} = \mathbf{T_{32f}} = \begin{bmatrix} 1 & 0 & 1 & 0 \\ -\frac{1}{2} & \frac{\sqrt{3}}{2} & 1 & 0 \\ -\frac{1}{2} & -\frac{\sqrt{3}}{2} & 1 & 0 \\ 0 & 0 & 0 & 1 \end{bmatrix}. \tag{6.22}$$

Once the dynamics are mapped into their two-phase stationary equivalents, the Park transform can be used to map these variables into the rotor reference frame. Under ITS condition, the extended version of the Park transform and its inverse are given

by:

$$\mathbf{T_{dqf}} = \begin{bmatrix} \cos(\theta_{re}) & \sin(\theta_{re}) & 0 \\ -\sin(\theta_{re}) & \cos(\theta_{re}) & 0 \\ 0 & 0 & 1 \end{bmatrix}, \mathbf{T_{dqf}}^{-1} = \begin{bmatrix} \cos(\theta_{re}) & -\sin(\theta_{re}) & 0 \\ \sin(\theta_{re}) & \cos(\theta_{re}) & 0 \\ 0 & 0 & 1 \end{bmatrix}. \quad (6.23)$$

By using the extended Clarke and Park transforms presented in Eqs. (6.21) and (6.23), the two-phase dynamics of the SMPM machine under ITS are given by,

$$\begin{aligned}
\begin{bmatrix} v_d^r \\ v_q^r \\ v_{a_u} \end{bmatrix} &= R \begin{bmatrix} (1-\frac{\mu_u}{6}) & 0 & 0 \\ 0 & (1-\frac{\mu_u}{6}) & 0 \\ 0 & 0 & \frac{\mu_u}{2} \end{bmatrix} \begin{bmatrix} i_d^r \\ i_q^r \\ i_{a_u} \end{bmatrix} + \frac{\mu_u R}{6} \begin{bmatrix} -\cos(2\theta_{re}) & \sin(2\theta_{re}) & 0 \\ \sin(2\theta_{re}) & \cos(2\theta_{re}) & 0 \\ 0 & 0 & 0 \end{bmatrix} \begin{bmatrix} i_d^r \\ i_q^r \\ i_{a_u} \end{bmatrix} \\
&+ \omega_{re}\Lambda_{PM} \begin{bmatrix} 0 \\ (1-\frac{\mu_u}{6}) \\ 0 \end{bmatrix} + \omega_{re}\Lambda_{PM} \begin{bmatrix} \frac{\mu_u \sin(2\theta_{re})}{6} \\ \frac{\mu_u \cos(2\theta_{re})}{6} \\ -\frac{\mu_u \sin(\theta_{re})}{2} \end{bmatrix} \\
&+ \begin{bmatrix} \frac{2L_s+L_{s_h}-(3-\mu_u)L_m}{3} & 0 & 0 \\ 0 & \frac{2L_s+L_{s_h}-(3-\mu_u)L_m}{3} & 0 \\ 0 & 0 & L_{a_u} \end{bmatrix} \frac{d}{dt} \begin{bmatrix} i_d^r \\ i_q^r \\ i_{a_u} \end{bmatrix} \\
&+ \begin{bmatrix} -\frac{(L_s-L_{s_h}-\mu_u L_m)\cos(2\theta_{re})}{3} & \frac{(L_s-L_{s_h}-\mu_u L_m)\sin(2\theta_{re})}{3} & \frac{2L_{m_{hu}}-\mu_u L_m}{3}\cos(\theta_{re}) \\ \frac{(L_s-L_{s_h}-\mu_u L_m)\sin(2\theta_{re})}{3} & \frac{(L_s-L_{s_h}-\mu_u L_m)\cos(2\theta_{re})}{3} & -\frac{2L_{m_{hu}}-\mu_u L_m}{3}\sin(\theta_{re}) \\ \frac{2L_{m_{hu}}-\mu_u L_m}{2}\cos(\theta_{re}) & -\frac{2L_{m_{hu}}-\mu_u L_m}{2}\sin(\theta_{re}) & 0 \end{bmatrix} \frac{d}{dt} \begin{bmatrix} i_d^r \\ i_q^r \\ i_{a_u} \end{bmatrix} \\
&+ \omega_{re} \begin{bmatrix} 0 & -\frac{2L_s+L_{s_h}-(3-\mu_u)L_m}{3} & 0 \\ \frac{2L_s+L_{s_h}-(3-\mu_u)L_m}{3} & 0 & 0 \\ 0 & 0 & 0 \end{bmatrix} \begin{bmatrix} i_d^r \\ i_q^r \\ i_{a_u} \end{bmatrix} \\
&+ \omega_{re} \begin{bmatrix} \frac{(L_s-L_{s_h}-\mu_u L_m)\sin(2\theta_{re})}{3} & \frac{(L_s-L_{s_h}-\mu_u L_m)\cos(2\theta_{re})}{3} & 0 \\ \frac{(L_s-L_{s_h}-\mu_u L_m)\cos(2\theta_{re})}{3} & -\frac{(L_s-L_{s_h}-\mu_u L_m)\sin(2\theta_{re})}{3} & 0 \\ -(L_{m_{hu}}-\frac{\mu_u L_m}{2})\sin(\theta_{re}) & -(L_{m_{hu}}-\frac{\mu_u L_m}{2})\cos(\theta_{re}) & 0 \end{bmatrix} \begin{bmatrix} i_d^r \\ i_q^r \\ i_{a_u} \end{bmatrix}. \quad (6.24)
\end{aligned}$$

Inspection of Eq. (6.24) reveals that all parameters (i.e., resistance, inductance, and PM flux linkage) reduce and have an oscillation at twice the electrical rotor speed under ITS condition. In addition, note that the dynamics from the shorted turns affect the equivalent two-phase dynamics as mutual inductances link them. Following a similar procedure, the two-phase dynamics of the SMPM machine under ITS in phases B and C are presented in the Appendix (See Eqs. (6.47) and (6.48)). Comparison between Eqs. (6.24), (6.47), and (6.48) reveals that the two-phase electrical dynamics under ITS in phases A, B, and C have identical effects on the parameters except for the oscillations at twice the electrical rotor speed, which have a phase-shift depending on the phase.

In the following section, the different components of the inductance matrix and PM flux linkage are validated. Specifically, the magnetic parameters that are validated are the equivalent magnetic parameters related to the direct and quadrature axes, which are given by:

$$L_d^r = \frac{2L_s + L_{s_h} - (3-\mu_u)L_m}{3} - \frac{(L_s - L_{s_h} - \mu_u L_m)\cos(2\theta_{re})}{3}, \tag{6.25}$$

$$L_q^r = \frac{2L_s + L_{s_h} - (3-\mu_u)L_m}{3} + \frac{(L_s - L_{s_h} - \mu_u L_m)\cos(2\theta_{re})}{3}, \tag{6.26}$$

$$M_{dq}^r = \frac{(L_s - L_{s_h} - \mu_u L_m)\sin(2\theta_{re})}{3}, \tag{6.27}$$

$$M_{da_u}^r = \frac{2L_{m_{hu}} - \mu_u L_m}{3}\cos(\theta_{re}), \tag{6.28}$$

$$M_{qa_u}^r = -\frac{2L_{m_{hu}} - \mu_u L_m}{3}\sin(\theta_{re}), \tag{6.29}$$

$$\lambda_{PMd}^r = \Lambda_{PM}(1 - \tfrac{\mu_u}{6}) - \frac{\mu_u \Lambda_{PM}\cos(2\theta_{re})}{6}, \tag{6.30}$$

$$\lambda_{PMq}^r = \frac{\mu_u \Lambda_{PM}\sin(2\theta_{re})}{6}, \tag{6.31}$$

$$\lambda_{PMu}^r = \frac{\mu_u \Lambda_{PM}\cos(2\theta_{re})}{2}. \tag{6.32}$$

where λ_{PMd}^r and λ_{PMq}^r correspond to the PM flux linking the equivalent direct and quadrature-axis windings in the rotor reference frame, λ_{PMu}^r is the PM flux linking the shorted turns in the coil with ITS, L_d^r and L_q^r are the direct- and quadrature-axis inductances in the rotor reference frame, M_{dq}^r is the mutual inductance between the equivalent direct- and quadrature-axis windings, $M_{da_u}^r$ and $M_{qa_u}^r$ are the mutual inductances between the shorted coil and the direct and quadrature windings, respectively.

6.2.2 Calibration and Validation of Proposed Model

In this section, the magnetic parameters are calibrated and validated using the dimensions of the SMPM machine and FEA simulations. The FEA simulations are performed using *Maxwell* from *Ansoft Corporation*. In the FEA simulations, the SMPM machine operates at zero current and a constant speed of $1000RPM$. Under ITS, two cases are presented in which coils a_1 and b_1 are assumed to have 5 shorted turns. The SMPM machine used in the simulations is the one presented in Section 5.2.2 (See Fig. 5.3). Figs. 6.3 and 6.4 show the cross-section of the SMPM machine from Fig. 5.3 with the ITS in coils a_1 and b_1, respectively. Additional details on the SMPM machine's dimensions and materials used for the FEA simulations can be found in Table 5.1 (Section 5.2.2).

6.2.2.1 Calibration of Magnetic Parameters

The magnetic parameters are calibrated based on the dimensions of the four-pole SMPM machine and the healthy FEA simulation results. Following the procedure previously pre-

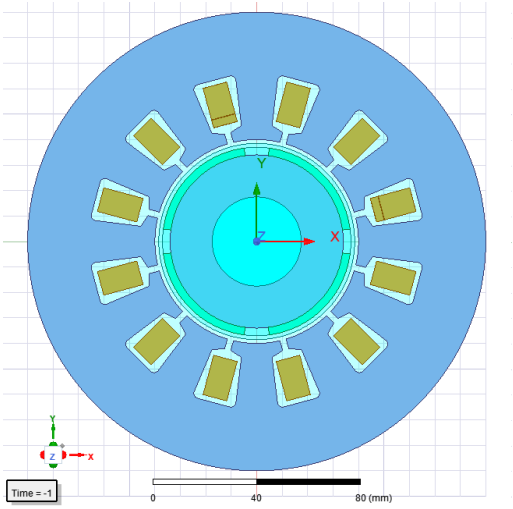

Figure 6.3: Cross-section of SMPM machine with ITS in coil a_1.

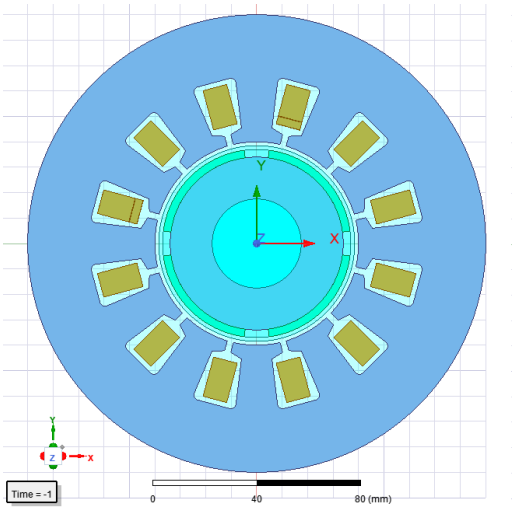

Figure 6.4: Cross-section of SMPM machine with ITS in coil b_1.

sented in Section 5.2.2.1, the slot effects are taken into account in the inductance calculations using the Carter Coefficient, as presented in Eqs. (5.8) and (5.22). The slot leakage inductance (Eq. (6.14)) is calculated by approximating the slot to a rectangle (Fig. 5.5). In terms of the PM flux linkage, its value is adjusted based on the healthy case from the FEA simulations. The left column of Figs. 6.5 and 6.6 show the calibrated inductances and PM flux linkages against the healthy FEA simulation results.

6.2.2.2 Validation of Magnetic Parameters

Based on the previous calibration, the inductance and PM flux linkages are validated against FEA simulations. Figs. 6.5 and 6.6 present the simulation results for the inductances and PM flux linkages for one mechanical period, respectively. The healthy case in Fig. 6.5 reveals a constant difference between the inductances calculated by the proposed model and the FEA results, which is carried over to the ITS case. This difference is mainly due to the leakage inductance approximation and is within a 10% MRE for the direct- and quadrature-axis inductances. In addition, Figs. 6.5 and 6.6 show a ripple in the magnetic parameters calculated through FEA simulations, which is due to the slot harmonics. The magnetic parameters calculated with the proposed model do not capture this ripple as the slot harmonics were neglected in the derivation.

The model aims to capture the "essential" aspects of the SMPM machine dynamics under ITS condition. In other words, the model is meant to capture the distinctive features of the ITS fault rather than details. In the healthy case, the inductance and PM flux

linkage are essentially constant, captured by the model. Similarly, under ITS conditions, the two-phase magnetic parameters have an oscillation at twice the electrical rotor speed as the distinctive feature, which the model also captures. Note that, in Figs. 6.5 and 6.6, the ITS in phases A and B produce identical oscillations in the magnetic parameters but phase-shifted, capture by the models presented in Eqs. (6.24) and (6.47). Regarding the magnetic parameters related to the shorted turns, the model also captures their characteristic feature corresponding to the oscillation at the electrical rotor speed.

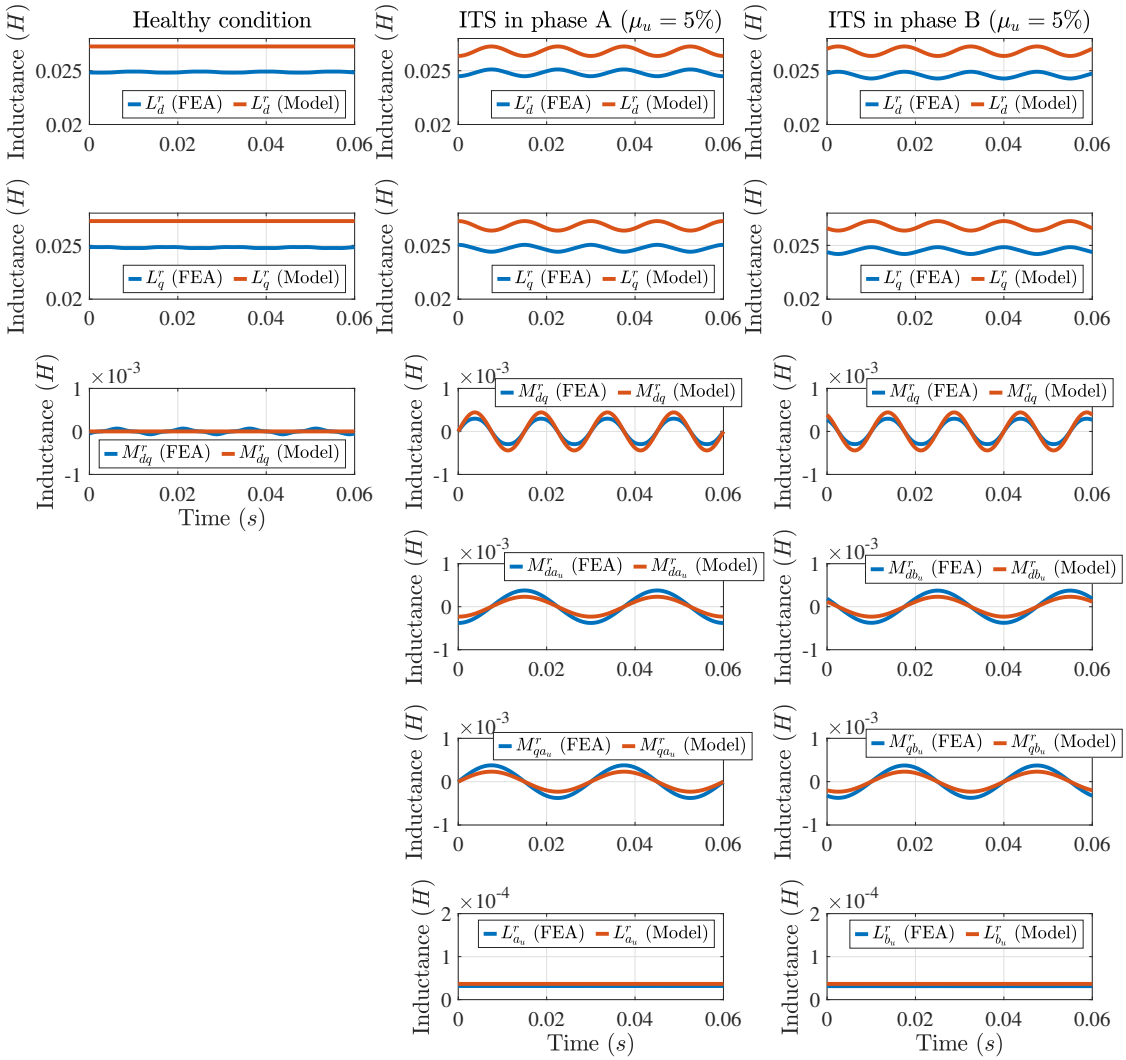

Figure 6.5: Comparison of the proposed model and FEA results for the inductances under healthy condition (left) and ITS ($\mu_u = 5\%$) in phase A (center) and phase B (right).

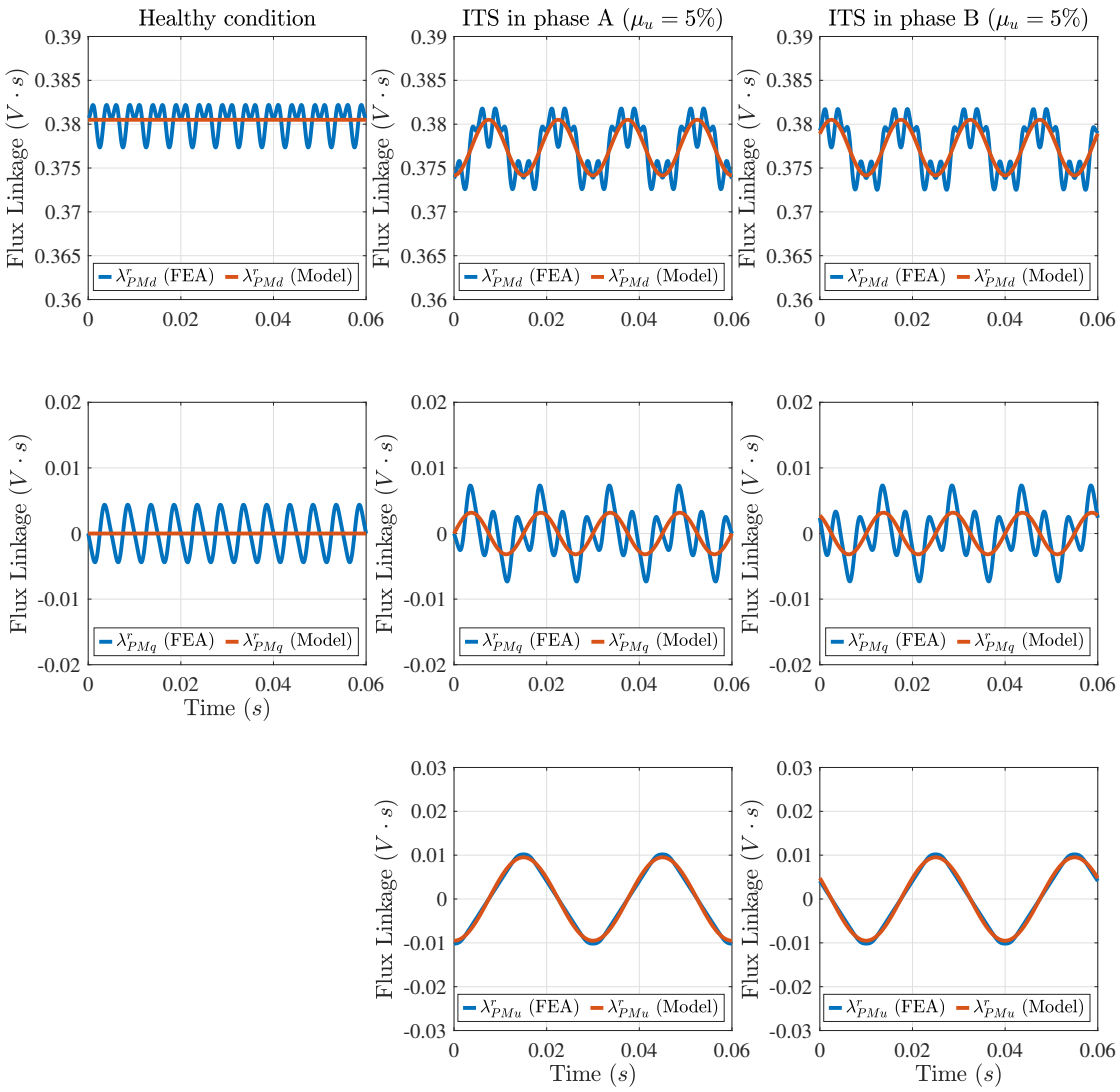

Figure 6.6: Comparison of the proposed model and FEA results for the PM flux linkage under healthy condition (left) and ITS ($\mu_u = 5\%$) in phase A (center) and phase B (right).

6.2.3 Control-Oriented Model for Simulations

An SMPM machine drive system is physically a three-phase system. The SMPM machine is typically powered through a VSI, and therefore, the inputs to the SMPM machine model corresponds to the three-phase VSI's voltages. In order to be implementable in simulations, the equations have to be written with respect to these three-phase voltages. Unfortunately, in Eq. (6.18), the voltages in the phase that experiences ITS (i.e., v_{a_h} and v_{a_u}) are unknown as they do not correspond to phase voltages. Since the phase voltage is applied to the entire winding, it contains the non-shorted and shorted coil voltages, and is given as follows:

$$v_a = v_{a_h} + v_{a_u}. \tag{6.33}$$

Similarly, the unhealthy part of the winding is shorted by the insulation-failure resistance (See Fig. 6.1(b)). Therefore, the voltage in the shorted coil is given by

$$V_{a_u} = R_f(i_a - i_{a_u}), \tag{6.34}$$

where R_f corresponds to the insulation-failure resistance. By considering Eqs. (6.33) and (6.34), the electrical dynamics presented in Eq. (6.18) can be modified as follows:

$$\begin{bmatrix} v_a \\ v_b \\ v_c \\ 0 \end{bmatrix} = \begin{bmatrix} \frac{(1+\mu_h)R}{2} & 0 & 0 & \frac{\mu_u R}{2} \\ 0 & R & 0 & 0 \\ 0 & 0 & R & 0 \\ -R_f & 0 & 0 & \frac{\mu_u R}{2} + R_f \end{bmatrix} \begin{bmatrix} i_a \\ i_b \\ i_c \\ i_{a_u} \end{bmatrix} + \frac{d}{dt} \begin{bmatrix} \lambda_{PM,a} \\ \lambda_{PM,b} \\ \lambda_{PM,c} \\ \frac{\mu_u}{2}\lambda_{PM,a} \end{bmatrix}$$
$$+ \begin{bmatrix} L_{s_h} + L_{m_{hu}} & L_m & L_m & L_{m_{hu}} + L_{s_u} \\ \frac{\mu_h+1}{2}L_m & L_s & L_m & \frac{\mu_u}{2}L_m \\ \frac{\mu_h+1}{2}L_m & L_m & L_s & \frac{\mu_u}{2}L_m \\ L_{m_{hu}} & \frac{\mu_u}{2}L_m & \frac{\mu_u}{2}L_m & L_{s_u} \end{bmatrix} \frac{d}{dt} \begin{bmatrix} i_a \\ i_b \\ i_c \\ i_{a_u} \end{bmatrix}. \tag{6.35}$$

Then, this model can be easily simulated as part of an electric drive by mapping its variables into the two-phase stationary frame by using the extended Clarke transform presented in Eq. (6.21) so that the zero current constraint can be enforced (Eq. (6.19)).

6.3 Parameter Identification for Fault Diagnosis and Condition Monitoring of SMPM Machines under Inter-Turn Short

This section presents a parameter identification strategy for monitoring and detecting ITS. First, a linear parameterization that includes ITS-specific parameters is formulated based on the SMPM machine model under ITS presented in Eq. (6.24). Note that this para-

metric model is formulated to match the linear form presented in Eq. (4.15). Afterward, the sufficient conditions in which the input signals guarantee accurate parameter convergence are studied. The parameter identification algorithm corresponds to the projection algorithm, whose details were previously presented in Section 4.3.2.

6.3.1 Parametric Model for Fault Diagnosis and Condition Monitoring of SMPM Machines under Inter-turn Short

The equivalent two-phase SMPM machine model in the rotor reference frame presented in Eq. (6.24) captures the dynamic behavior under the ITS condition. However, its application to fault diagnosis and condition monitoring requires a more convenient parameterization based on the available signals. In an electric drive, the inputs to the controller are the three-phase current, the mechanical speed, and the mechanical position, as presented in Section 2.6. Hence, unfortunately, the current flowing through the shorted turns in the ITS coil is unknown. As seen in Eq. (6.24), the dynamics from the shorted turns impact the equivalent two-phase dynamics due to their shared mutual inductances, and, therefore, a way to take into account their effect on the dynamics is required. Based on this, in order to formulate the model for identification, the two-phase SMPM machine dynamics in the rotor reference frame from Eq. (6.24) are rewritten as:

$$
\begin{aligned}
\begin{bmatrix} v_d^r \\ v_q^r \end{bmatrix} &= (1-\tfrac{\mu_u}{6})R \begin{bmatrix} 1 & 0 \\ 0 & 1 \end{bmatrix} \begin{bmatrix} i_d^r \\ i_q^r \end{bmatrix} + \frac{\mu_u R}{6} \begin{bmatrix} -\cos(2\theta_{re}) & \sin(2\theta_{re}) \\ \sin(2\theta_{re}) & \cos(2\theta_{re}) \end{bmatrix} \begin{bmatrix} i_d^r \\ i_q^r \end{bmatrix} \\
&+\omega_{re} \begin{bmatrix} 0 \\ \Lambda_{PM}(1-\frac{\mu_u}{6}) \end{bmatrix} + \frac{\mu_u \omega_{re} \Lambda_{PM})}{6} \begin{bmatrix} \sin(2\theta_{re}) \\ \cos(2\theta_{re}) \end{bmatrix} + \frac{2L_s + L_{a_h} - (3-\mu_u)L_m}{3} \begin{bmatrix} 1 & 0 \\ 0 & 1 \end{bmatrix} \frac{d}{dt} \begin{bmatrix} i_d^r \\ i_q^r \end{bmatrix} \\
&+ \frac{(L_s - L_{ah} - \mu_u L_m)}{3} \begin{bmatrix} -\cos(2\theta_{re}) & \sin(2\theta_{re}) \\ \sin(2\theta_{re}) & \cos(2\theta_{re}) \end{bmatrix} \frac{d}{dt} \begin{bmatrix} i_d^r \\ i_q^r \end{bmatrix} \\
&+ \frac{(2L_s + L_{a_h} - (3-\mu_u)L_m)\omega_{re}}{3} \begin{bmatrix} 0 & -1 \\ 1 & 0 \end{bmatrix} \begin{bmatrix} i_d^r \\ i_q^r \end{bmatrix} \\
&+ \frac{(L_s - L_{a_h} - \mu_u L_m)\omega_{re}}{3} \begin{bmatrix} \sin(2\theta_{re}) & -\cos(2\theta_{re}) \\ -\cos(2\theta_{re}) & -\sin(2\theta_{re}) \end{bmatrix} \begin{bmatrix} i_d^r \\ i_q^r \end{bmatrix} \\
&+ \frac{2L_{a_h a_u} - \mu_u L_m}{3} \begin{bmatrix} \cos(\theta_{re}) \\ -\sin(\theta_{re}) \end{bmatrix} \frac{di_{a_u}}{dt},
\end{aligned}
\tag{6.36}
$$

where the derivative of the current flowing through the shorted turns is given by:

$$\frac{di_{a_u}}{dt} = \frac{1}{L_{a_u}}\Bigg(v_{a_u} - \frac{\mu_u R}{2} i_{a_u} + \frac{\mu_u \Lambda_{PM}}{2}\omega_{re}\sin(\theta_{re}) \\ - \big(L_{a_h a_u} - \tfrac{\mu_u L_m}{2}\big)\left(\frac{d(i_d^r\cos(\theta_{re}))}{dt} - \frac{d(i_q^r\sin(\theta_{re}))}{dt}\right)\Bigg). \quad (6.37)$$

In Eq. (6.37), the voltage produced by the shorted turns (i.e., v_{a_u}) can be approximated to zero, assuming that the short creates a preferable path for the current to flow (i.e., $R_f \ll \frac{\mu_u R}{2}$). This assumption is a fair approximation since, intuitively, the voltage produced by the shorted turns represents a small portion of the total voltage applied to the phase. By substituting Eq. (6.37) into Eq. (6.36), the two-phase dynamics are given by:

$$\begin{aligned}
\begin{bmatrix} v_d^r \\ v_q^r \end{bmatrix} &= (1-\tfrac{\mu_u}{6})R\begin{bmatrix} 1 & 0 \\ 0 & 1 \end{bmatrix}\begin{bmatrix} i_d^r \\ i_q^r \end{bmatrix} + \frac{\mu_u R}{6}\begin{bmatrix} -\cos(2\theta_{re}) & \sin(2\theta_{re}) \\ \sin(2\theta_{re}) & \cos(2\theta_{re}) \end{bmatrix}\begin{bmatrix} i_d^r \\ i_q^r \end{bmatrix} \\
&+\omega_{re}\Lambda_{PM}\begin{bmatrix} 0 \\ (1-\frac{\mu_u}{6}) \end{bmatrix} + \frac{\mu_u\omega_{re}\Lambda_{PM}}{6}\begin{bmatrix} \sin(2\theta_{re}) \\ \cos(2\theta_{re}) \end{bmatrix} \\
&-\mu_u\omega_{re}\Lambda_{PM}\Big(\tfrac{2L_{a_h a_u}-\mu_u L_m}{12L_{a_u}}\Big)\begin{bmatrix} 0 \\ 1 \end{bmatrix} + \mu_u\omega_{re}\Lambda_{PM}\Big(\tfrac{2L_{a_h a_u}-\mu_u L_m}{12L_{a_u}}\Big)\begin{bmatrix} \sin(2\theta_{re}) \\ \cos(2\theta_{re}) \end{bmatrix} \\
&+\tfrac{2L_s+L_{a_h}-(3-\mu_u)L_m}{3}\begin{bmatrix} 1 & 0 \\ 0 & 1 \end{bmatrix}\frac{d}{dt}\begin{bmatrix} i_d^r \\ i_q^r \end{bmatrix} + \Big(\tfrac{(2L_{a_h a_u}-\mu_u L_m)^2}{12L_{a_u}}\Big)\begin{bmatrix} -1 & 0 \\ 0 & -1 \end{bmatrix}\frac{d}{dt}\begin{bmatrix} i_d^r \\ i_q^r \end{bmatrix} \\
&+\tfrac{(L_s-L_{a_h}-\mu_u L_m)}{3}\begin{bmatrix} -\cos(2\theta_{re}) & \sin(2\theta_{re}) \\ \sin(2\theta_{re}) & \cos(2\theta_{re}) \end{bmatrix}\frac{d}{dt}\begin{bmatrix} i_d^r \\ i_q^r \end{bmatrix} \\
&+\Big(\tfrac{(2L_{a_h a_u}-\mu_u L_m)^2}{12L_{a_u}}\Big)\begin{bmatrix} -\cos(2\theta_{re}) & \sin(2\theta_{re}) \\ \sin(2\theta_{re}) & \cos(2\theta_{re}) \end{bmatrix}\frac{d}{dt}\begin{bmatrix} i_d^r \\ i_q^r \end{bmatrix} \\
&+\omega_{re}\tfrac{2L_s+L_{a_h}-(3-\mu_u)L_m}{3}\begin{bmatrix} 0 & -1 \\ 1 & 0 \end{bmatrix}\begin{bmatrix} i_d^r \\ i_q^r \end{bmatrix} + \omega_{re}\Big(\tfrac{(2L_{a_h a_u}-\mu_u L_m)^2}{12L_{a_u}}\Big)\begin{bmatrix} 0 & 1 \\ -1 & 0 \end{bmatrix}\begin{bmatrix} i_d^r \\ i_q^r \end{bmatrix} \\
&+\tfrac{(L_s-L_{a_h}-\mu_u L_m)}{3}\omega_{re}\begin{bmatrix} \sin(2\theta_{re}) & \cos(2\theta_{re}) \\ \cos(2\theta_{re}) & -\sin(2\theta_{re}) \end{bmatrix}\begin{bmatrix} i_d^r \\ i_q^r \end{bmatrix} \\
&+\omega_{re}\Big(\tfrac{(2L_{a_h a_u}-\mu_u L_m)^2}{12L_{a_u}}\Big)\begin{bmatrix} \sin(2\theta_{re}) & \cos(2\theta_{re}) \\ \cos(2\theta_{re}) & -\sin(2\theta_{re}) \end{bmatrix}\begin{bmatrix} i_d^r \\ i_q^r \end{bmatrix} \\
&-\tfrac{2L_{a_h a_u}-\mu_u L_m}{3}\begin{bmatrix} \cos(\theta_{re}) \\ -\sin(\theta_{re}) \end{bmatrix}\frac{\mu_u R i_{a_u}}{2L_{a_u}}.
\end{aligned} \quad (6.38)$$

As seen in Eq. (6.38), the dynamics from the shorted turns presented in Eq. (6.37) alter the values of the existing magnetic parameters. In other words, in the magnetic parameters, their average component and their amplitude of the oscillation at twice the electrical rotor

speed are affected by the dynamics from the shorted turns. However, there is still a term related to the resistive drop in the shorted turns that has to be analyzed. For this purpose, the dynamics of the shorted turns are transformed into the s-domain using the Laplace transform as

$$I_{a_u}(s) \approx \frac{1}{L_{a_u}} \frac{1}{s + \frac{\mu_u R}{2L_{a_u}}} \mathcal{L}\left\{ \frac{\mu_u \Lambda_{PM}}{2} \omega_{re} \sin(\theta_{re}) - \left(L_{a_h a_u} - \frac{\mu_u L_m}{2}\right) \left(\frac{d(i_d^r \cos(\theta_{re}))}{dt} - \frac{d(i_q^r \sin(\theta_{re}))}{dt} \right) \right\}, \tag{6.39}$$

where $\mathcal{L}\{\cdot\}$ is the Laplace transform operator. Inspection of Eq. (6.39) reveals that the term associated with the resistive drop in the shorted turns affects the magnetic parameters. Specifically, a scaled and phase-shifted "version" of the terms associated with the PM flux linkage and inductances in Eq. (6.39) will be introduced to the dynamics presented in Eq. (6.38). Note that such scaling and phase-shifting depend on the short parameters.

Based on the previous analysis, a parameterization for the two-phase dynamics presented in Eq. (6.38) that captures the effect of the dynamics from the shorted turns while considering the available signals for identification is given by:

$$\begin{aligned}
\begin{bmatrix} v_d^r \\ v_q^r \end{bmatrix} &= R_0 \begin{bmatrix} 1 & 0 \\ 0 & 1 \end{bmatrix} \begin{bmatrix} i_d^r \\ i_q^r \end{bmatrix} + R_{ITS} \begin{bmatrix} -\cos(2\theta_{re}) & \sin(2\theta_{re}) \\ \sin(2\theta_{re}) & \cos(2\theta_{re}) \end{bmatrix} \begin{bmatrix} i_d^r \\ i_q^r \end{bmatrix} \\
&+ \Lambda_0 \begin{bmatrix} 0 \\ \omega_{re} \end{bmatrix} + \Lambda_1 \begin{bmatrix} \omega_{re} \\ 0 \end{bmatrix} + \omega_{re} \Lambda_{ITS_1} \begin{bmatrix} \sin(2\theta_{re}) \\ \cos(2\theta_{re}) \end{bmatrix} + \omega_{re} \Lambda_{ITS_2} \begin{bmatrix} \cos(2\theta_{re}) \\ -\sin(2\theta_{re}) \end{bmatrix} \\
&+ L_0 \begin{bmatrix} 1 & 0 \\ 0 & 1 \end{bmatrix} \frac{d}{dt} \begin{bmatrix} i_d^r \\ i_q^r \end{bmatrix} + \omega_{re} L_0 \begin{bmatrix} 0 & -1 \\ 1 & 0 \end{bmatrix} \begin{bmatrix} i_d^r \\ i_q^r \end{bmatrix} + L_1 \begin{bmatrix} 0 & 1 \\ 1 & 0 \end{bmatrix} \frac{d}{dt} \begin{bmatrix} i_d^r \\ i_q^r \end{bmatrix} - \omega_{re} L_1 \begin{bmatrix} 1 & 0 \\ 0 & 1 \end{bmatrix} \begin{bmatrix} i_d^r \\ i_q^r \end{bmatrix} \\
&+ L_{ITS_1} \begin{bmatrix} -\cos(2\theta_{re}) & \sin(2\theta_{re}) \\ \sin(2\theta_{re}) & \cos(2\theta_{re}) \end{bmatrix} \frac{d}{dt} \begin{bmatrix} i_d^r \\ i_q^r \end{bmatrix} + \omega_{re} L_{ITS_1} \begin{bmatrix} \sin(2\theta_{re}) & \cos(2\theta_{re}) \\ \cos(2\theta_{re}) & -\sin(2\theta_{re}) \end{bmatrix} \begin{bmatrix} i_d^r \\ i_q^r \end{bmatrix} \\
&+ L_{ITS_2} \begin{bmatrix} \sin(2\theta_{re}) & \cos(2\theta_{re}) \\ \cos(2\theta_{re}) & -\sin(2\theta_{re}) \end{bmatrix} \frac{d}{dt} \begin{bmatrix} i_d^r \\ i_q^r \end{bmatrix} + \omega_{re} L_{ITS_2} \begin{bmatrix} \cos(2\theta_{re}) & -\sin(2\theta_{re}) \\ -\sin(2\theta_{re}) & -\cos(2\theta_{re}) \end{bmatrix} \begin{bmatrix} i_d^r \\ i_q^r \end{bmatrix}.
\end{aligned} \tag{6.40}$$

The dynamics presented in Eq. (6.40) capture the impact that the dynamics associated with the shorted turns have in the two-phase dynamics. The parameters L_0, L_1, Λ_0, and Λ_1 capture the average component of the magnetic parameters, including the effect from the shorted-turn dynamics. Specifically, the shorted-turn dynamics introduce phase-shifted average-value magnetic parameters and, therefore, break the diagonality property of the inductance matrix and the alignment of the PM flux linkage with the direct axis. Similarly, the terms L_{ITS_1}, L_{ITS_2}, Λ_{ITS_1}, and Λ_{ITS_2} are meant to capture the oscillations at twice

the electrical rotor speed in the magnetic parameters and their phase shift. Note that the model presented in Eq. (6.40) captures any phase-shift in the magnetic parameters and, therefore, the effect of the ITS in the two-phase dynamics no matter which phase is affected by ITS. In other words, the model can be used for ITS faults occurring in any phase.

Among the ITS-specific parameters presented in the previous model, only some can be leveraged for fault diagnosis and condition monitoring. In terms of the fundamental components of the magnetic parameters (i.e., L_1 and Λ_1), their values can be used for detection as they will be zero and non-zero under healthy and ITS conditions, respectively. However, L_1 and Λ_1 can be non-zero under other circumstances, such as incorrect encoder calibration, which can lead to a wrong diagnosis. In this sense, the terms associated with the oscillations are more suitable for fault detection, as they capture the imbalance caused by the ITS. Among all the parameters associated with the oscillations at the electrical rotor speed, L_{ITS_1}, L_{ITS_2}, Λ_{ITS_1}, and Λ_{ITS_2} are the ones that will be estimated. Estimating oscillations through R_{ITS} will be in vain since the resistance drop is considerably small compared to the total voltage.

Based on the previous discussion, the linear parameterization for ITS detection is given by,

$$
\begin{aligned}
\vec{z} &= \begin{bmatrix} z_d & z_q \end{bmatrix}^T = \{\mathcal{F}(s)\} \begin{bmatrix} v_d^r & v_q^r \end{bmatrix}^T, \\
\vec{\theta} &= \begin{bmatrix} R & L_0 & \Lambda_0 & L_{ITS_1} & L_{ITS_2} & \Lambda_{ITS_1} & \Lambda_{ITS_2} \end{bmatrix}^T, \\
\mathbf{\Phi}^T &= \begin{bmatrix} \vec{\phi}_d^{\,T} \\ \vec{\phi}_q^{\,T} \end{bmatrix},
\end{aligned}
\tag{6.41}
$$

$$
\vec{\phi}_d = \{\mathcal{F}(s)\} \begin{bmatrix}
i_d^r \\
(\frac{d}{dt} i_d^r - \omega_{re} i_q^r) \\
0 \\
\frac{d(i_q^r \sin(2\theta_{re}) - i_d^r \cos(2\theta_{re}))}{dt} - \omega_{re}(i_d^r \sin(2\theta_{re}) + i_q^r \cos(2\theta_{re})) \\
\frac{d(i_d^r \sin(2\theta_{re}) + i_q^r \cos(2\theta_{re}))}{dt} + \omega_{re}(i_q^r \sin(2\theta_{re}) - i_d^r \cos(2\theta_{re})) \\
\omega_{re} \sin(2\theta_{re}) \\
\omega_{re} \cos(2\theta_{re})
\end{bmatrix},
$$

$$
\vec{\phi}_q = \{\mathcal{F}(s)\} \begin{bmatrix}
i_q^r \\
(\omega_{re} i_d^r + \frac{d}{dt} i_q^r) \\
\omega_{re} \\
\frac{d(i_d^r \sin(2\theta_{re}) + i_q^r \cos(2\theta_{re}))}{dt} + \omega_{re}(i_q^r \sin(2\theta_{re}) - i_d^r \cos(2\theta_{re})) \\
\frac{d(i_d^r \cos(2\theta_{re}) - i_q^r \sin(2\theta_{re}))}{dt} + \omega_{re}(i_d^r \sin(2\theta_{re}) + i_q^r \cos(2\theta_{re})) \\
\omega_{re} \cos(2\theta_{re}) \\
-\omega_{re} \sin(2\theta_{re})
\end{bmatrix}.
$$

6.3.2 Persistently Exciting Inputs

This section studies the sufficient conditions in which the estimator based on the ITS model achieves accurate parameter estimation. Similar to Chapters IV and V, the sufficient conditions for PE will be determined using the definition of persistent excitation presented in Section 2.7 (Definition 2.1). In the following analysis, the sampling frequency is assumed more than twice the regressor's highest-frequency component. Based on Theorem 2.3, this assumption allows the discrete-time regressor to carry the same information as the continuous-time regressor. In addition, the torque and rotor electrical speed are assumed constant. The persistently exciting input required for accurate parameter identification will be injected through the direct-axis current as the healthy torque (Eq. (4.4)) is solely a function of the quadrature-axis current. Hence, a sinusoidal direct-axis current and a constant quadrature current will be assumed, which are given by:

$$i_d^r = A\sin(\omega t),$$
$$i_q^r = I_q,$$

where I_q is the corresponding quadrature-axis current that achieves the desired torque (i.e., $I_q = \frac{4\tau_{3\phi}}{3N_p\Lambda_{PM}}$). In the regressor, the low-pass filter ($\{\mathcal{F}(s)\}$) will be neglected as it has no effect on the results.

6.3.2.1 Persistency of Excitation Analysis for Estimator based on Proposed Dynamic Model

Based on the previous assumptions, the regressor's direct and quadrature components for the estimator based on proposed dynamic model (Eq. (6.41)) are function of the excitation and electrical rotor frequencies and are given by:

$$\vec{\phi}_d = \begin{bmatrix} A\sin(\omega t) \\ A\omega\cos(\omega t) - \omega_{re} I_q \\ 0 \\ I_q\omega_{re}\cos(2\omega_{re}t) + A\omega_{re}\sin(\omega t)\sin(2\omega_{re}t) - A\omega\cos(\omega t)\cos(2\omega_{re}t) \\ A\omega\cos(\omega t)\sin(2\omega_{re}t) + \omega_{re}A\sin(\omega t)\cos(2\omega_{re}t) - \omega_{re}I_q\sin(2\omega_{re}t) \\ \omega_{re}\sin(2\omega_{re}t) \\ \omega_{re}\cos(2\omega_{re}t) \end{bmatrix}, \tag{6.42}$$

$$\vec{\phi}_q = \begin{bmatrix} I_q \\ A\omega_{re}\sin(\omega t) \\ \omega_{re} \\ A\omega\cos(\omega t)\sin(2\omega_{re}t) + A\omega_{re}\sin(\omega t)\cos(2\omega_{re}t) - \omega_{re}I_q\sin(2\omega_{re}t) \\ A\omega\cos(\omega t)\cos(2\omega_{re}t) - A\omega_{re}\sin(\omega t)\sin(2\omega_{re}t) - \omega_{re}I_q\cos(2\omega_{re}t) \\ \omega_{re}\cos(2\omega_{re}t) \\ -\omega_{re}\sin(2\omega_{re}t) \end{bmatrix}. \tag{6.43}$$

Assuming that the regressor is periodic with $T_0 = \frac{2\pi}{\omega_0}$, it can be shown that:

$$\det\left(\frac{1}{T_0}\int_0^{T_0}\mathbf{\Phi}(\tau)\mathbf{\Phi}(\tau)^\intercal d\tau\right) = \frac{A^6\omega_{re}^6}{16}\Big(A^2\omega^2 + \omega_{re}^2(A^2+2I_q^2)\Big)(\omega^2+\omega_{re}^2)^2 \tag{6.44}$$

Based on the determinant presented in Eq. (6.44), the regressor, $\mathbf{\Phi}$, is persistently exciting if:

1. The rotor speed is non-zero (i.e., $\Omega_r = \frac{\Omega_{re}}{2} = 0$).

2. At least one sinusoidal component is injected into the direct-axis current (i.e., $A \neq 0$).

This analysis shows that the estimator based on the ITS model requires the same excitation as the estimator based on the standard model. Similar to the estimators presented in Chapters IV and V, the additional parameters for ITS have a self-excitation property, which can be leveraged to guarantee sufficient conditions for accurate convergence.

6.4 Simulation Results Assuming Linear Magnetics

In this section, the performance of the parameter estimator presented in Eq. (6.41) is assessed by numerical simulations in Matlab/Simulink. In addition, the standard-model-based parameter estimator (Eq. (4.16)) presented in Section 4.3.1.1 is also evaluated for comparison. In the simulations, the SMPM machine operates at different current levels and a constant speed of 1000 RPM. Under ITS, two cases are presented in which coils a_1 and b_1 are assumed to have 5 shorted turns. PI regulators with cross-coupling compensation are used to regulate the two-phase currents in the rotor reference frame. Both parameter estimators are evaluated with different gains, and the persistently exciting signal is injected in the direct-axis current, as follows:

$$\tilde{i}_d^r = 10\sin(2\pi 40t), \tag{6.45}$$

where the tilde $(\tilde{\cdot})$ denotes a control reference signal.

The controller and parameter estimators are simulated with a triggered subsystem switching at $10kHz$ to capture the discrete-time practical implementation. The continuous-time SMPM dynamics are simulated with a fixed time step of 2 μs using *ode4*. The command voltages from the controller are converted into duty cycles using SVM [83]. Based on the duty cycle calculation, an ideal "average-value" VSI provides average-value voltages to the SMPM machine. The estimated parameters have an initial deviation of 20% with respect to their healthy ones. Table 6.1 presents the machine, fault, control, and adaptation parameters for the simulations. The SMPM machine used in the simulations corresponds to the one in Section 6.2.2, shown in Figs. 6.3 and 6.4.

Table 6.1: Machine, ITS, control, and adaptation parameters for simulation

Description	Value
SMPM Machine Parameters:	
R	0.785Ω
N_p	4
ITS Parameters:	
μ_u	5%
μ_h	95%
R_f	0.001Ω
Control Parameters:	
K_p	27.26
K_i	0.0785
Switching frequency (f_{sw})	$10kHz$
Sampling frequency (f_s)	$10kHz$
Adaptation Parameters:	
a	0.004/0.002/0.001
c	1

6.4.1 Parameter Estimator Based on Standard Dynamic Model

The simulation results for the parameter estimator based on the standard dynamic model are presented in Fig. 6.7. Under healthy conditions, the estimated parameters converge to their actual values. In terms of the simulation results under ITS conditions, all parameters were expected to decrease in theory. However, the simulation results show that the magnetic parameters slightly decrease while the resistance increases. Unfortunately, their value is affected by the dynamics from the shorted turns. Specifically, as shown in Eq. (6.40), the dynamics from the shorted turns break the diagonality of the inductance matrix and the alignment of the PM flux with the direct axis. Note that the estimated parameters have similar behavior when comparing the simulation results for ITS in phases A and B. In addition to the effect of the shorted-turns dynamics on the fundamental value

of the inductance and PM flux linkage, the ITS also introduces an oscillation at twice the electrical rotor speed, which the identification model does not capture. In the simulation results, the resistance has noticeable oscillations that worsen as the adaptation gain increases. Since the resistance represents a considerably small portion of the total voltage, its value is prone to inaccuracies due to noise or unmodeled dynamics.

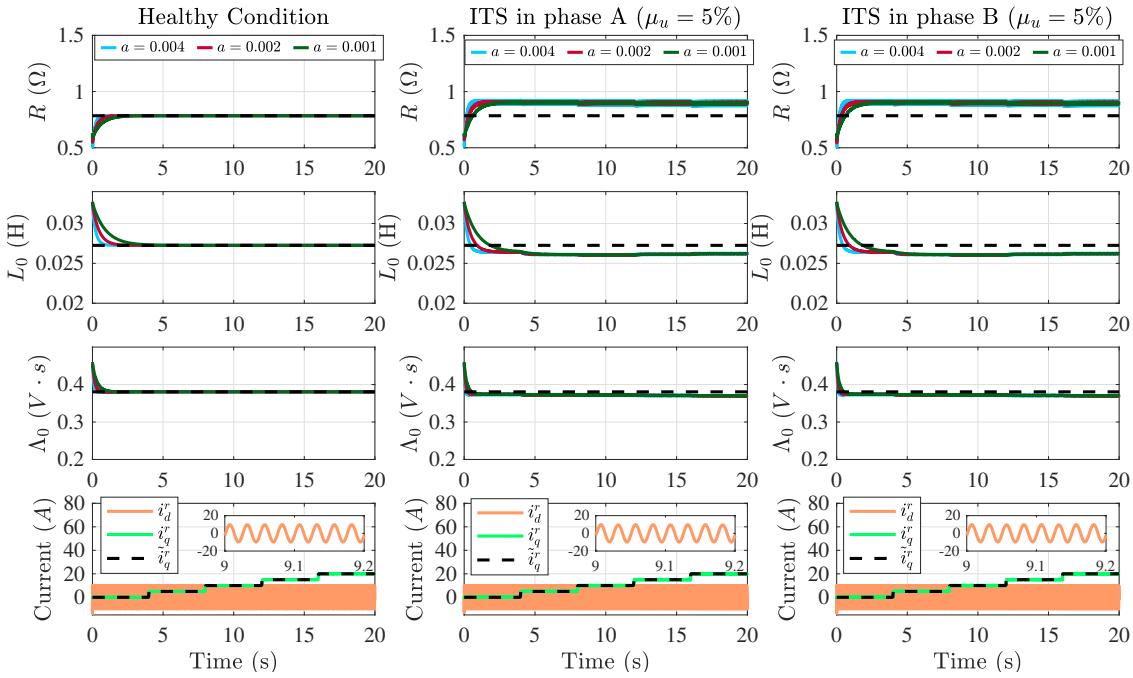

Figure 6.7: Simulation results of the parameter estimator based on the standard dynamics for different adaptation gains when the machine is operating under healthy and ITS conditions. The black dashed line refers to the average healthy parameters.

As a validation for the discrete PE analysis, the condition number of the PE condition matrix is presented in Figs. 6.8 and 6.9. Note that the moving window corresponds to the period of the injected PE signal and is given by 250 samples (0.025 s). Fig. 6.8 shows that the condition number of the PE condition matrix is not infinite, and, therefore, the inputs are persistently exciting the system. Fig. 6.9 shows the condition number of the PE matrix when the regressor is scaled, as previously discussed in Remark 4.1. As shown in Figs. 6.9, scaling the regressor improves the condition number of the PE condition matrix.

6.4.2 Parameter Estimator Based on Proposed Dynamic Model

In Fig. 6.10, the results for the parameter estimator based on the proposed model are presented. As can be seen in the left column of Fig. 6.10, the parameters converge to their actual values under healthy conditions. Regarding the parameters associated with the ITS

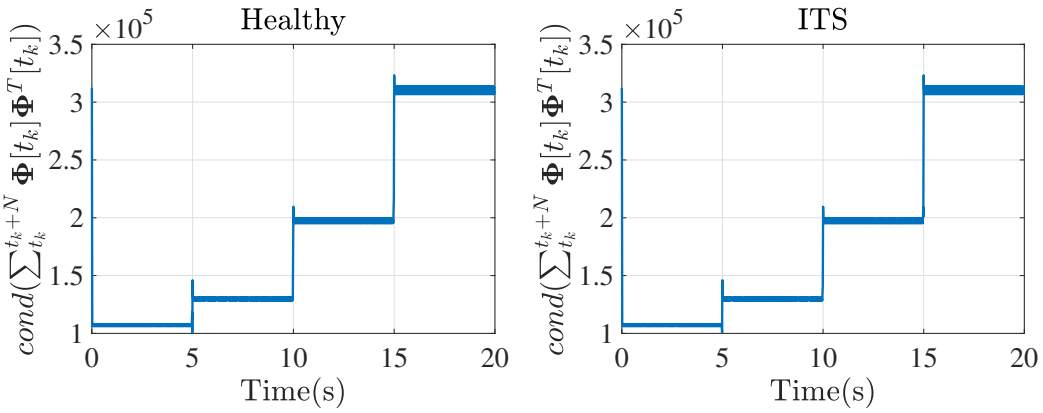

Figure 6.8: Condition number of the discrete PE condition matrix for the estimator based on the standard dynamics when the SMPM machine is operating under healthy (left) and ITS (right) conditions.

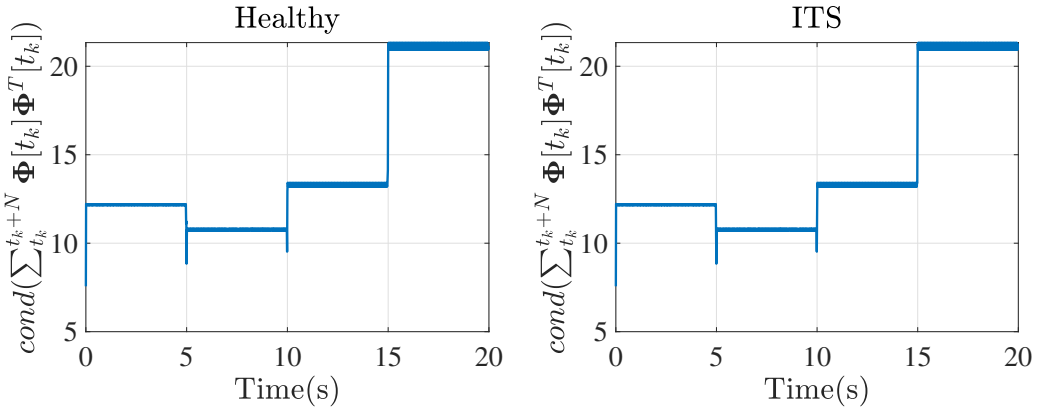

Figure 6.9: Condition number of the discrete PE condition matrix with scaled regressor for the estimator based on the standard dynamics when the SMPM machine is operating under healthy (left) and ITS (right) conditions.

condition, their values remain equal to zero, which indicates that the SMPM machine is not experiencing any ITS. Under ITS condition, the resistance, inductance, and PM flux linkage converge to values similar to those from the parameter estimator based on the standard dynamic model. As mentioned before, the dynamics from the shorted turns break the diagonality property of the inductance matrix and the alignment of the PM flux linkage with the direct axis, which affects the fundamental component of the resistance, inductance, and PM flux linkage. In terms of the ITS-specific parameters, their values are non-zero, which indicates that the SMPM machine is operating under ITS condition. Note that ITS-specific parameters have different values when comparing the simulation results for ITS in phases A and B. Depending on which phase the ITS occurs, the oscillations at twice the electrical rotor speed have a phase shift, resulting in different ITS-specific parameters for the identification model (Eq. (6.40)). In addition, the resistance has considerably smaller oscillations than those presented in the standard-model-based estimator results (Section 6.4.1). Thanks to the added parameters associated with the ITS condition, the unmodeled dynamics are reduced, alleviating the resistance from inaccuracies.

In terms of the PE condition, Figs. 6.11 and 6.12 show the condition number of the PE condition for the proposed estimator. The moving window is given by 750 samples (0.075 s), corresponding to the regressor's period. Note that the regressor period depends on the frequency of the injected PE signal and the electrical rotor frequency (See Eqs. (6.42) and (6.43)). The inputs are persistently exciting as the condition number is not infinite, as shown in Fig. 6.11. Therefore, the parameter estimator based on the inter-turn short model can achieve sufficient conditions for accurate identification with the same excitation as the estimator based on the standard model. In Fig. 6.12, the condition number of the PE condition matrix with the scaled regressor is presented. Similar to the parameter estimator based on the standard model, scaling the regressor improves the condition number of the PE condition matrix.

6.5 Co-Simulation Results Considering Nonlinearities

In this section, co-simulations are used to validate the effectiveness of the parameter estimators for ITS detection. The co-simulations consist of an FEA-based machine model connected to an electric drive and are implemented using *Twin Builder* (a.k.a., *Simplorer*), which is a simulation software from *Ansoft*. The FEA-based SMPM machine model corresponds to the SMPM machine presented in Section 6.2.2 and is simulated in *Maxwell*. In the co-simulations, the steel type is changed to "M19" (See Fig. 4.23) for the stator and rotor irons. The electric drive model, as well as the co-simulation interface, are implemented in *Twin Builder*. The inverter model corresponds to the "average-value" VSI. The PI regulators with cross-coupling compensation used for current regulation are developed

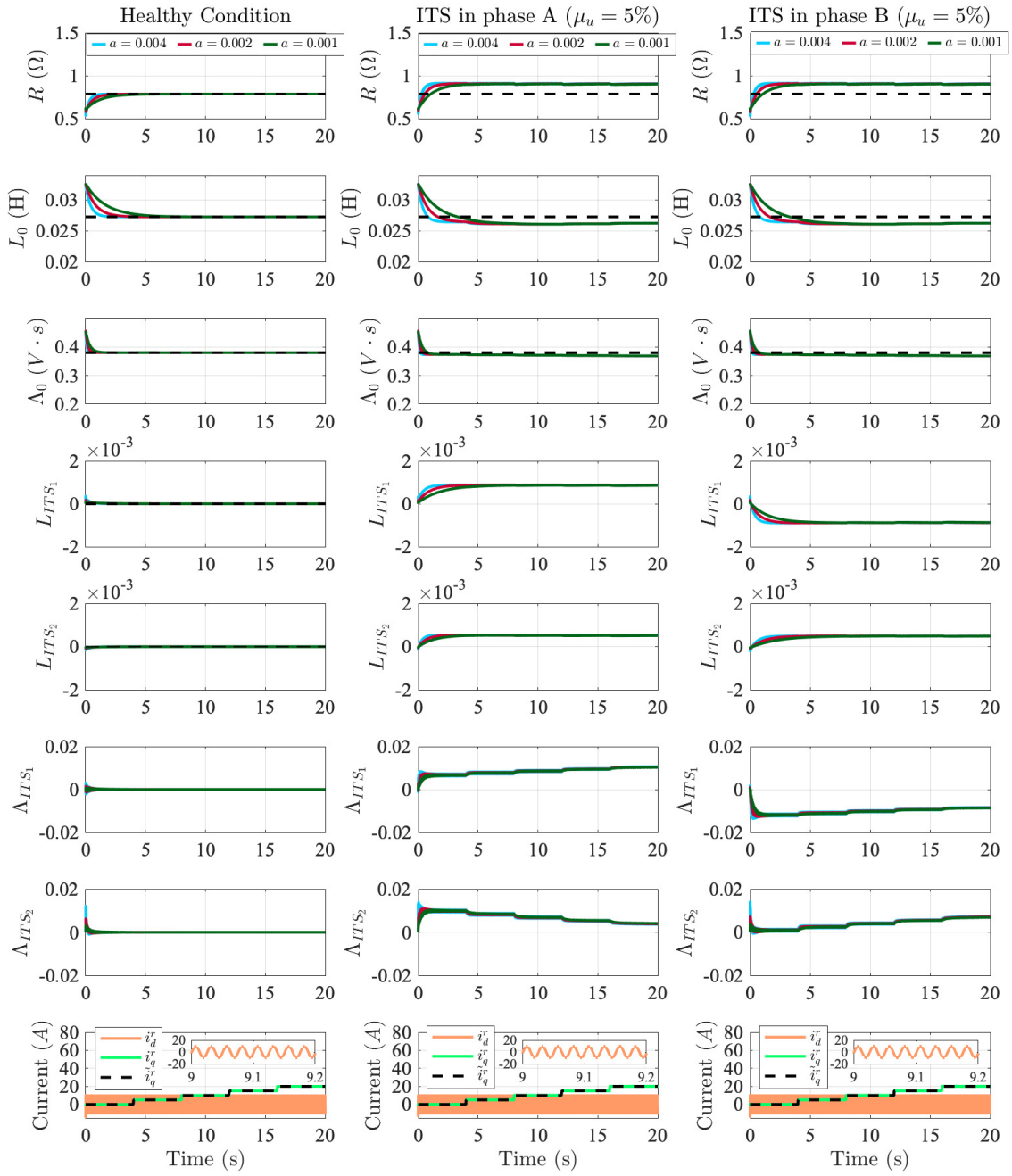

Figure 6.10: Simulation results of the proposed-model-based parameter estimator with different adaptation gains with the SMPM machine under healthy and ITS conditions. The black dashed line corresponds to the actual parameters.

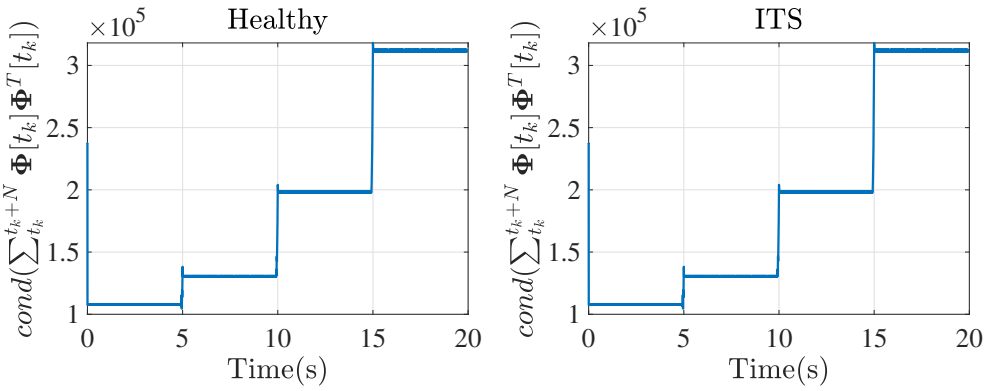

Figure 6.11: Condition number of the discrete PE condition matrix for the estimator based on the proposed dynamics when the SMPM machine is operating under healthy (left) and ITS (right) conditions.

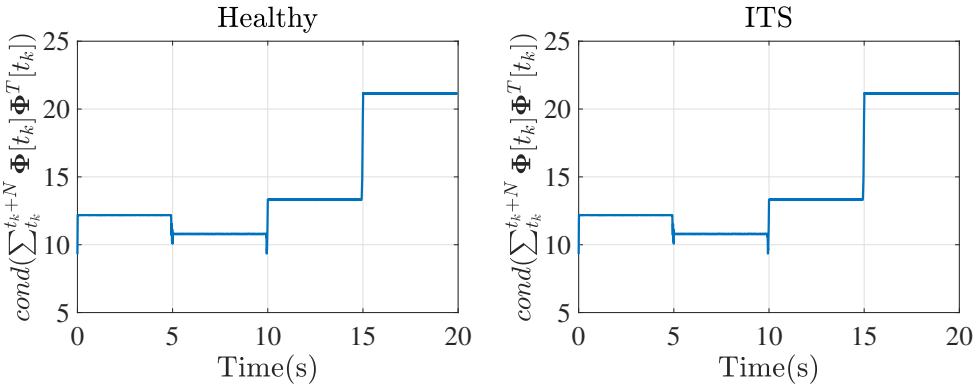

Figure 6.12: Condition number of the discrete PE condition matrix for the estimator based on the proposed dynamics with scaled regressor when the SMPM machine is operating under healthy (left) and ITS (right) conditions.

in Matlab/Simulink and integrated as a Twin Builder component.

The FEA-based machine model and electric drive are executed at $10kHz$. The estimated parameters have an initial 20% deviation from the linear parameters presented in Section 6.2.2.2. The command current that is injected for PE is given by:

$$\tilde{i}_d^r = 5\sin(2\pi 40t). \tag{6.46}$$

6.5.1 Performance of Parameter Estimator Based on Standard Dynamic Model

The co-simulation results for the parameter estimator based on the standard dynamic model are presented in Fig. 6.13. Note that the black dash line corresponds to the average value of the actual parameters assuming linear magnetics. Under healthy conditions, the estimated parameters match their linear values for most current values. Once the SMPM machine operates at higher currents, the magnetic parameters start dropping, which indicates saturation. Regarding the ITS condition, the resistance increases while the magnetic parameters slightly decrease, similar to the simulation results presented in Section 6.4.1. Note that the resistance value increases at high current values in the healthy and ITS cases. Since the magnetics are no longer linear at high currents, the resistance is affected by these unmodeled dynamics.

In terms of fault diagnosis and condition monitoring of SMPM machines under ITS, it is questionable how reliable the parameters from the standard model are for this purpose. As the resistance drop corresponds to a small portion of the total voltage, its value is susceptible to deviations due to unmodeled dynamics. Moreover, as seen in Fig. 6.13, the resistance behaves opposite to what was theoretically expected, and is affected by saturation. In terms of the magnetic parameters, their slight decrease indicates ITS. However, as shown in Fig. 6.13, their values also decrease due to saturation. In addition, the PM flux linkage varies with temperature, which can also hinder the diagnosis.

6.5.2 Performance of Parameter Estimator Based on Proposed Dynamic Model

In Fig. 6.14, the co-simulation results for the parameter estimator based on the proposed dynamic model are presented. Note that the black dashed line corresponds to the average value of the actual parameters assuming linear magnetics. Under healthy conditions, the resistance, inductance, and PM flux linkage converge to their actual linear values for most current levels. As the current increases, the magnetics reach saturation, and, therefore, the magnetic parameters slightly reduce. Additionally, the parameters associated with the ITS condition are equal to zero, indicating that the SMPM machine does not experience any ITS. Under ITS condition, the ITS-specific parameters are non-zero, indicating that

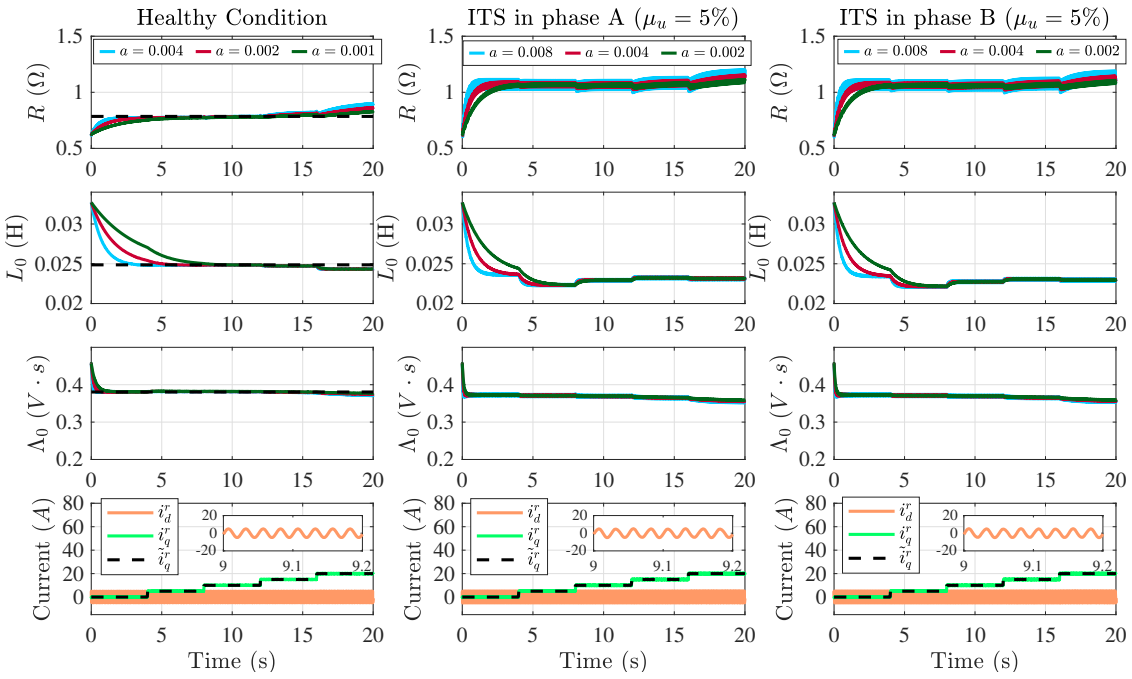

Figure 6.13: Co-simulation results of the parameter estimator based on the standard dynamics for different adaptation gains when the machine is operating under healthy and ITS conditions.

the SMPM machine has an ITS. Moreover, the ITS-specific parameters capture the phase shift in the oscillations at twice the electrical rotor speed due to the fault location, as their values are different for ITS in phases A and B. In addition, similar to the simulation results presented in Section 6.4.2, the ITS-specific parameters that capture the ITS oscillations alleviate the resistance from unmodeled dynamics. In terms of the resistance, inductance, and PM flux linkage, their average values are affected by the shorted-turns dynamics similar to the standard-model-based estimator results (See Section 6.5.1).

In terms of fault diagnosis and condition monitoring of SMPM machines under the ITS condition, the parameter estimator based on the proposed dynamics offers more information when compared with the standard-model-based estimator. The ITS-specific parameters in the proposed dynamic model are zero and non-zero under healthy and ITS conditions, respectively. Therefore, these additional parameters that capture the ITS oscillation can be used for monitoring and detecting ITS. Moreover, since the ITS-specific parameters capture the phase shift due to the fault location, they can potentially be used to detect the ITS conditions and determine which phase is experiencing the ITS. In addition, the oscillations at twice the electrical rotor speed increase with the number of shorted turns. Hence, the ITS-specific parameters can be potentially used to track the progression of the ITS.

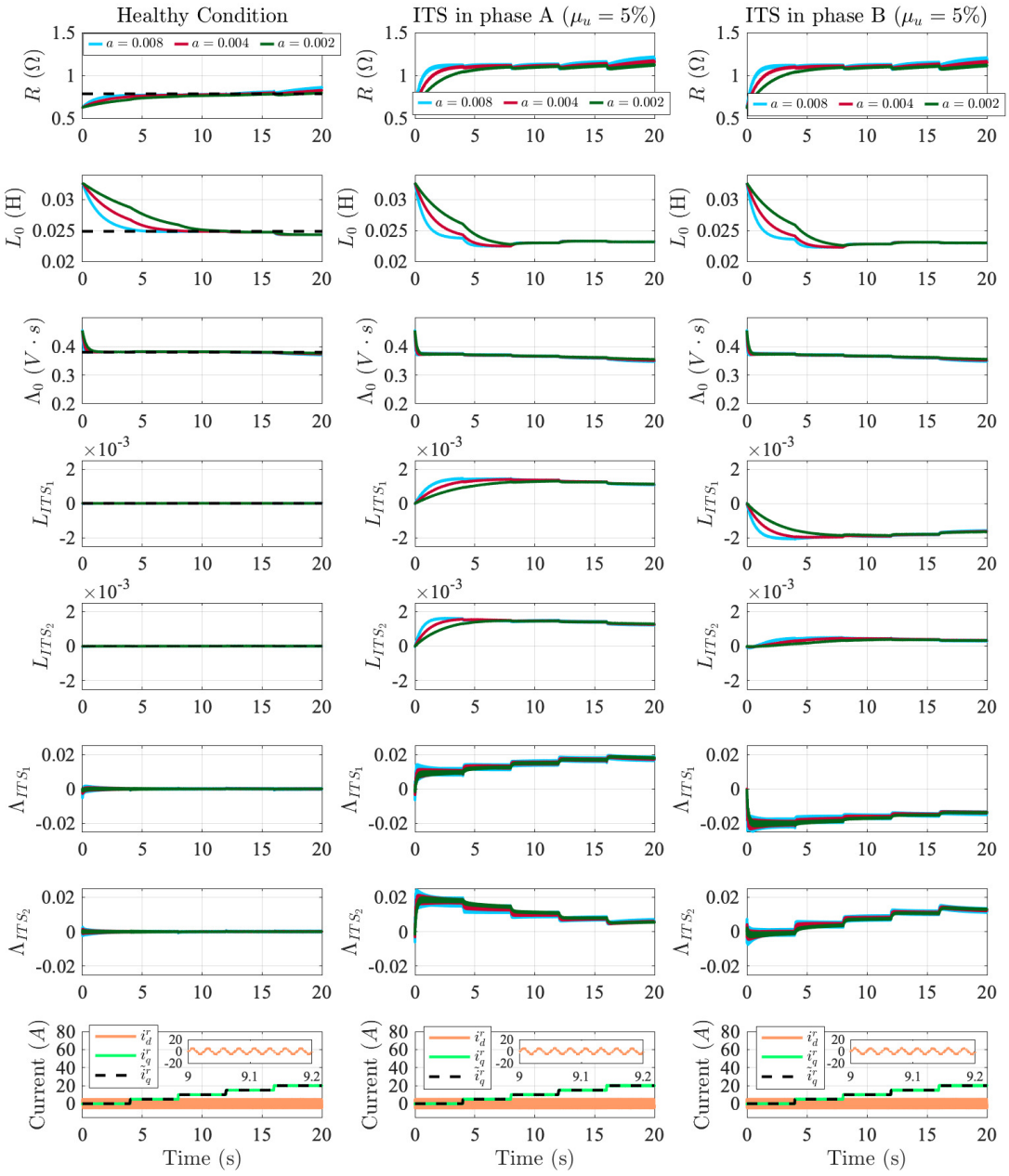

Figure 6.14: Co-simulation results of the parameter estimator based on the proposed dynamics for different adaptation gains when the machine is operating under healthy and ITS conditions.

6.6 Summary

In this chapter, the application of parameter identification to fault diagnosis and condition monitoring of SMPM machines under ITS conditions was investigated. Specifically, an equivalent two-phase parametric model and an online parameter identification technique for a three-phase four-pole SMPM machine with two coils in series per phase were formulated. An ITS refers to an insulation failure between contiguous turns in a coil and is typically modeled with an additional resistance shorting the affected turns. First, the equivalent two-phase model was formulated by modeling the different coils separately and integrating them into the different phases based on the winding connections. Afterward, FEA simulations were used to calibrate and validate the model's magnetic parameters. Then, a parameter identification strategy for ITS detection was discussed. The linear parametric model was formulated to include parameters related to ITS condition based on the proposed two-phase model while considering the available signals. To identify the sufficient conditions for accurate convergence, an analysis of the conditions in which the input signals ensure PE is presented. Simulation and co-simulation results prove the effectiveness of the proposed parameter identification strategy for monitoring and detecting ITS. In addition, a comparison between simulation and co-simulation results showed that the proposed model is a suitable tool for studying the SMPM machine behavior under ITS in the linear operating region. Finally, remarks on the parameters suitable for detecting ITS were discussed.

6.7 Appendix

6.7.1 Equivalent Two-Phase SMPM Machine Model in the Rotor Reference Frame with Inter-Turn Short in Phase B

$$
\begin{aligned}
\begin{bmatrix} v_d^r \\ v_q^r \\ v_{b_u} \end{bmatrix} &= R \begin{bmatrix} (1-\frac{\mu_u}{6}) & 0 & 0 \\ 0 & (1-\frac{\mu_u}{6}) & 0 \\ 0 & 0 & \frac{\mu_u}{2} \end{bmatrix} \begin{bmatrix} i_d^r \\ i_q^r \\ i_{b_u} \end{bmatrix} + \frac{\mu_u R}{6} \begin{bmatrix} -\cos(2(\theta_{re}-\frac{2\pi}{3})) & \sin(2(\theta_{re}-\frac{2\pi}{3})) & 0 \\ \sin(2(\theta_{re}-\frac{2\pi}{3})) & \cos(2(\theta_{re}-\frac{2\pi}{3})) & 0 \\ 0 & 0 & 0 \end{bmatrix} \begin{bmatrix} i_d^r \\ i_q^r \\ i_{b_u} \end{bmatrix} \\
&\quad + \omega_{re} \begin{bmatrix} 0 \\ \Lambda_{PM}(1-\frac{\mu_u}{6}) \\ 0 \end{bmatrix} + \omega_{re}\Lambda_{PM} \begin{bmatrix} \frac{\mu_u \sin(2(\theta_{re}-\frac{2\pi}{3}))}{6} \\ \frac{\mu_u \cos(2(\theta_{re}-\frac{2\pi}{3}))}{6} \\ -\frac{\mu_u \sin(\theta_{re}-\frac{2\pi}{3})}{2} \end{bmatrix} \\
&\quad + \begin{bmatrix} \frac{2L_s+L_{s_h}-(3-\mu_u)L_m}{3} & 0 & 0 \\ 0 & \frac{2L_s+L_{s_h}-(3-\mu_u)L_m}{3} & 0 \\ 0 & 0 & L_{b_u} \end{bmatrix} \frac{d}{dt} \begin{bmatrix} i_d^r \\ i_q^r \\ i_{b_u} \end{bmatrix} \\
&\quad + \begin{bmatrix} -\frac{(L_s-L_{s_h}-\mu_u L_m)\cos(2(\theta_{re}-\frac{2\pi}{3}))}{3} & \frac{(L_s-L_{s_h}-\mu_u L_m)\sin(2(\theta_{re}-\frac{2\pi}{3}))}{3} & \frac{2L_{m_{hu}}-\mu_u L_m}{3}\cos(\theta_{re}-\frac{2\pi}{3}) \\ \frac{(L_s-L_{s_h}-\mu_u L_m)\sin(2(\theta_{re}-\frac{2\pi}{3}))}{3} & \frac{(L_s-L_{s_h}-\mu_u L_m)\cos(2(\theta_{re}-\frac{2\pi}{3}))}{3} & -\frac{2L_{m_{hu}}-\mu_u L_m}{3}\sin(\theta_{re}-\frac{2\pi}{3}) \\ \frac{2L_{m_{hu}}-\mu_u L_m}{2}\cos(\theta_{re}-\frac{2\pi}{3}) & -\frac{2L_{m_{hu}}-\mu_u L_m}{2}\sin(\theta_{re}-\frac{2\pi}{3}) & 0 \end{bmatrix} \frac{d}{dt} \begin{bmatrix} i_d^r \\ i_q^r \\ i_{b_u} \end{bmatrix} \\
&\quad + \omega_{re} \begin{bmatrix} 0 & -\frac{2L_s+L_{s_h}-(3-\mu_u)L_m}{3} & 0 \\ \frac{2L_s+L_{s_h}-(3-\mu_u)L_m}{3} & 0 & 0 \\ 0 & 0 & 0 \end{bmatrix} \begin{bmatrix} i_d^r \\ i_q^r \\ i_{b_u} \end{bmatrix} \\
&\quad + \omega_{re} \begin{bmatrix} \frac{(L_s-L_{s_h}-\mu_u L_m)\sin(2(\theta_{re}-\frac{2\pi}{3}))}{3} & \frac{(L_s-L_{s_h}-\mu_u L_m)\cos(2(\theta_{re}-\frac{2\pi}{3}))}{3} & 0 \\ \frac{(L_s-L_{s_h}-\mu_u L_m)\cos(2(\theta_{re}-\frac{2\pi}{3}))}{3} & -\frac{(L_s-L_{s_h}-\mu_u L_m)\sin(2(\theta_{re}-\frac{2\pi}{3}))}{3} & 0 \\ -(L_{m_{hu}}-\frac{\mu_u L_m}{2})\sin(\theta_{re}-\frac{2\pi}{3}) & -(L_{m_{hu}}-\frac{\mu_u L_m}{2})\cos(\theta_{re}-\frac{2\pi}{3}) & 0 \end{bmatrix} \begin{bmatrix} i_d^r \\ i_q^r \\ i_{b_u} \end{bmatrix}
\end{aligned} \tag{6.47}
$$

6.7.2 Equivalent Two-Phase SMPM Machine Model in the Rotor Reference Frame with Inter-Turn Short in Phase C

$$
\begin{bmatrix} v_d^r \\ v_q^r \\ v_{c_u} \end{bmatrix} = R \begin{bmatrix} (1-\frac{\mu_u}{6}) & 0 & 0 \\ 0 & (1-\frac{\mu_u}{6}) & 0 \\ 0 & 0 & \frac{\mu_u}{2} \end{bmatrix} \begin{bmatrix} i_d^r \\ i_q^r \\ i_{c_u} \end{bmatrix} + \frac{\mu_u R}{6} \begin{bmatrix} -\cos(2(\theta_{re}+\frac{2\pi}{3})) & \sin(2(\theta_{re}+\frac{2\pi}{3})) & 0 \\ \sin(2(\theta_{re}+\frac{2\pi}{3})) & \cos(2(\theta_{re}+\frac{2\pi}{3})) & 0 \\ 0 & 0 & 0 \end{bmatrix} \begin{bmatrix} i_d^r \\ i_q^r \\ i_{c_u} \end{bmatrix}
$$

$$
+ \omega_{re} \begin{bmatrix} 0 \\ \Lambda_{PM}(1-\frac{\mu_u}{6}) \\ 0 \end{bmatrix} + \omega_{re}\Lambda_{PM} \begin{bmatrix} \frac{\mu_u \sin(2(\theta_{re}+\frac{2\pi}{3}))}{6} \\ \frac{\mu_u \cos(2(\theta_{re}+\frac{2\pi}{3}))}{6} \\ -\frac{\mu_u \sin(\theta_{re}+\frac{2\pi}{3})}{2} \end{bmatrix}
$$

$$
+ \begin{bmatrix} \frac{2L_s+L_{s_h}-(3-\mu_u)L_m}{3} & 0 & 0 \\ 0 & \frac{2L_s+L_{s_h}-(3-\mu_u)L_m}{3} & 0 \\ 0 & 0 & L_{c_u} \end{bmatrix} \frac{d}{dt} \begin{bmatrix} i_d^r \\ i_q^r \\ i_{c_u} \end{bmatrix}
$$

$$
+ \begin{bmatrix} -\frac{(L_s-L_{s_h}-\mu_u L_m)\cos(2(\theta_{re}+\frac{2\pi}{3}))}{3} & \frac{(L_s-L_{s_h}-\mu_u L_m)\sin(2(\theta_{re}+\frac{2\pi}{3}))}{3} & \frac{2L_{m_{hu}}-\mu_u L_m}{3}\cos(\theta_{re}+\frac{2\pi}{3}) \\ \frac{(L_s-L_{s_h}-\mu_u L_m)\sin(2(\theta_{re}+\frac{2\pi}{3}))}{3} & \frac{(L_{s_h}+\mu_u L_m-L_s)\cos(2(\theta_{re}+\frac{2\pi}{3}))}{3} & -\frac{2L_{m_{hu}}-\mu_u L_m}{3}\sin(\theta_{re}+\frac{2\pi}{3}) \\ \frac{2L_{m_{hu}}-\mu_u L_m}{2}\cos(\theta_{re}+\frac{2\pi}{3}) & -\frac{2L_{m_{hu}}-\mu_u L_m}{2}\sin(\theta_{re}+\frac{2\pi}{3}) & 0 \end{bmatrix} \frac{d}{dt} \begin{bmatrix} i_d^r \\ i_q^r \\ i_{c_u} \end{bmatrix}
$$

$$
+ \omega_{re} \begin{bmatrix} 0 & -\frac{2L_s+L_{s_h}-(3-\mu_u)L_m}{3} & 0 \\ \frac{2L_s+L_{s_h}-(3-\mu_u)L_m}{3} & 0 & 0 \\ 0 & 0 & 0 \end{bmatrix} \begin{bmatrix} i_d^r \\ i_q^r \\ i_{c_u} \end{bmatrix}
$$

$$
+ \omega_{re} \begin{bmatrix} \frac{(L_s-L_{s_h}-\mu_u L_m)\sin(2(\theta_{re}+\frac{2\pi}{3}))}{3} & \frac{(L_s-L_{s_h}-\mu_u L_m)\cos(2(\theta_{re}+\frac{2\pi}{3}))}{3} & 0 \\ \frac{(L_s-L_{s_h}-\mu_u L_m)\cos(2(\theta_{re}+\frac{2\pi}{3}))}{3} & -\frac{(L_s-L_{s_h}-\mu_u L_m)\sin(2(\theta_{re}+\frac{2\pi}{3}))}{3} & 0 \\ -(L_{m_{hu}}-\frac{\mu_u L_m}{2})\sin(\theta_{re}+\frac{2\pi}{3}) & -(L_{m_{hu}}-\frac{\mu_u L_m}{2})\cos(\theta_{re}+\frac{2\pi}{3}) & 0 \end{bmatrix} \begin{bmatrix} i_d^r \\ i_q^r \\ i_{c_u} \end{bmatrix} \quad (6.48)
$$

CHAPTER VII

Parameter Identification for Comprehensive Condition Monitoring of Surface-Mount Permanent Magnet Machines

7.1 Introduction

In Chapters IV, V, and VI, the application of parameter identification was investigated for a given fault condition. Specifically, equivalent two-phase models and online parameter identification strategies were formulated for a three-phase four-pole SMPM machine with two coils per phase under demagnetization, ME, and ITS conditions. In the previous chapters, simulation and co-simulation results demonstrated the effectiveness of the parameter identification strategies for monitoring and detecting these faults. However, in practice, the SMPM machine can experience many different faults, and the type of fault is unknown. Therefore, a more systematic and comprehensive strategy for monitoring and detecting fault conditions is required.

This chapter investigates the application of parameter identification to fault diagnosis and condition monitoring of SMPM machines under demagnetization, eccentricity, and inter-turn short conditions. First, the approach is formulated by incorporating all the previous parameter estimators into a sole strategy. Afterward, the effectiveness of the strategy for fault detection is assessed through co-simulation. Note that the results include single and mixed fault conditions. Then, remarks on the capabilities and limitations for detecting the different conditions are discussed. Finally, this chapter concludes with a summary.

7.2 Comprehensive Parameter Identification for Demagnetization, ME, and ITS Detection

This section presents a monitoring and detection strategy based on the parameter estimators for demagnetization, ME, and ITS presented in Chapters IV, V, and VI. Fig. 7.1 shows the schematic diagram. First, a parameterization that includes parameters associated with demagnetization, ME, and ITS is presented. Note that the linear parameterization required to formulate the parameter estimator follows the form presented in Eq. 4.15. Afterward, the input design, which guarantees sufficient conditions for accurate parameter convergence, is presented. Specifically, the conditions in which the input signals ensure PE are studied. The parameter identification algorithm corresponds to the projection algorithm presented in Section 4.3.2.

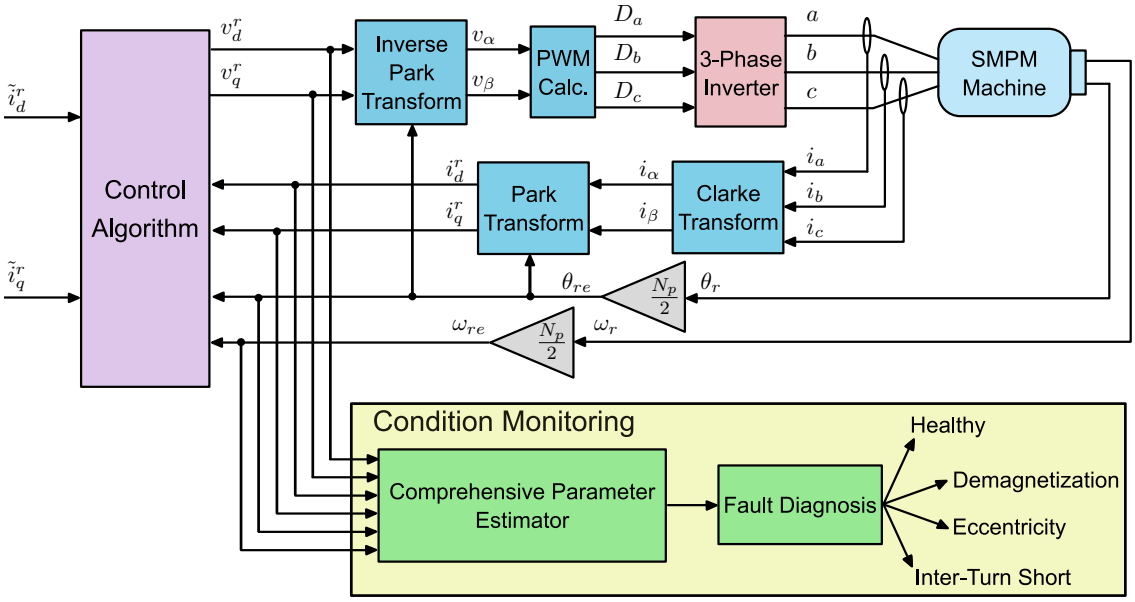

Figure 7.1: Schematic diagram of the comprehensive identification strategy for monitoring and detecting demagnetization, ME, and ITS conditions.

7.2.1 Parametric Model for Comprehensive Fault Diagnosis and Condition Monitoring of SMPM Machines under Demagnetization, ME, and ITS

In Chapters IV, V, and VI, the parameter estimators are intended to monitor and detect a specific fault and have parameters related to such fault. Table 7.1 presents the relevant parameters for each fault condition. In the parameter identi-

fication strategy for demagnetization, the fault-related parameter is the asymmetry term that captures the oscillation at three times the electrical rotor speed caused by uneven demagnetization between the north and south PM flux linkages. Similarly, the parameter identification strategy for detecting ME has fault-related parameters that capture the oscillation at the rotor speed in the magnetic parameters caused by the ME air-gap asymmetry. In the parameter identification strategy for detecting ITS, the fault-related parameters are meant to capture the oscillations at twice the electrical rotor speed in the magnetic parameters due to the ITS. Note that demagnetization, eccentricity, and ITS conditions generate oscillations with different frequencies (See Eqs. (4.17), (5.27), (5.28), and (6.40)). Hence, the fundamental value of the parameters associated with a specific fault should be non-zero only when such fault occurs. If the fault-related parameters do not match the fault condition, the estimated parameters should solely experience oscillations due to the unmodeled dynamics.

Table 7.1: Relevant parameters for Demagnetization, ME, and ITS.

Fault	Relevant Parameters
Demagnetization	Δ_{PM}
ME	L_{ME_1}, L_{ME_2}, Λ_{ME_1}, Λ_{ME_2}
ITS	L_{ITS_1}, L_{ITS_2}, Λ_{ITS_1}, Λ_{ITS_2}

A possible approach for comprehensive identification could be running the three estimators in parallel. However, a comparison between the proposed parameter estimators and the standard SMPM machine model shows that the regressor terms associated with the resistance, inductance, and PM flux linkage are identical in all cases. Therefore, the resistance, inductance, and PM flux linkage will be estimated three times by running the three proposed estimators in parallel. While this is a valid approach, having three estimates of the standard parameters adds a computational burden. Instead, by leveraging the fact that all the estimators share these dynamics, a single parameter identification strategy for the three fault conditions can be

formulated as follows:

$$\vec{z} = \begin{bmatrix} z_d \\ z_q \end{bmatrix} = \{\mathcal{F}(s)\} \begin{bmatrix} v_d^r \\ v_q^r \end{bmatrix}, \vec{\theta} = \begin{bmatrix} R \\ L_0 \\ \Lambda_0 \\ \Delta_{PM} \\ L_{ME_1} \\ L_{ME_2} \\ \Lambda_{ME_1} \\ \Lambda_{ME_2} \\ L_{ITS_1} \\ L_{ITS_2} \\ \Lambda_{ITS_1} \\ \Lambda_{ITS_2} \end{bmatrix}, \mathbf{\Phi} = \begin{bmatrix} \vec{\phi_d} & \vec{\phi_q} \end{bmatrix} \tag{7.1}$$

where the direct- and quadrature-axis components of the regressor matrix are given by,

$$\vec{\phi}_d = \{\mathcal{F}(s)\} \begin{bmatrix} i_d^r \\ (\frac{d}{dt} i_d^r - \omega_{re} i_q^r) \\ 0 \\ -2\omega_{re} \sin(3\theta_{re}) \\ \frac{d(i_d^r \sin\theta_r)}{dt} - \omega_{re} i_q^r \sin\theta_r \\ \frac{d(i_d^r \cos\theta_r)}{dt} - \omega_{re} i_q^r \cos\theta_r \\ \omega_r \cos\theta_r \\ -\omega_r \sin\theta_r \\ \frac{d(i_q^r \sin(2\theta_{re}) - i_d^r \cos(2\theta_{re}))}{dt} - \omega_{re}(i_d^r \sin(2\theta_{re}) + i_q^r \cos(2\theta_{re})) \\ \frac{d(i_d^r \sin(2\theta_{re}) + i_q^r \cos(2\theta_{re}))}{dt} + \omega_{re}(i_q^r \sin(2\theta_{re}) - i_d^r \cos(2\theta_{re})) \\ \omega_{re} \sin(2\theta_{re}) \\ \omega_{re} \cos(2\theta_{re}) \end{bmatrix},$$

$$\vec{\phi}_q = \{\mathcal{F}(s)\} \begin{bmatrix} i_q^r \\ (\omega_{re} i_d^r + \frac{d}{dt} i_q^r) \\ \omega_{re} \\ -2\omega_{re}\cos(3\theta_{re}) \\ \frac{d(i_q^r \sin\theta_r)}{dt} + \omega_{re} i_d^r \sin\theta_r \\ \frac{d(i_q^r \cos\theta_r)}{dt} + \omega_{re} i_d^r \cos\theta_r \\ \omega_{re}\sin\theta_r \\ \omega_{re}\cos\theta_r \\ \frac{d(i_d^r \sin(2\theta_{re}) + i_q^r \cos(2\theta_{re}))}{dt} + \omega_{re}(i_q^r \sin(2\theta_{re}) - i_d^r \cos(2\theta_{re})) \\ \frac{d(i_d^r \cos(2\theta_{re}) - i_q^r \sin(2\theta_{re}))}{dt} + \omega_{re}(i_d^r \sin(2\theta_{re}) + i_q^r \cos(2\theta_{re})) \\ \omega_{re}\cos(2\theta_{re}) \\ -\omega_{re}\sin(2\theta_{re}) \end{bmatrix}.$$

7.2.2 Persistently Exciting Inputs

This section analyzes the sufficient conditions in which the comprehensive parameter estimator achieves accurate convergence. Similar to Chapters IV, V, and VI, the sufficient conditions for PE will be determined using the definition of persistent excitation presented in Section 2.7 (Definition 2.1). The following analysis assumes that the sampling frequency is more than twice the regressor's highest-frequency component. In addition, the torque and rotor electrical speed are assumed constant. The persistently exciting input required for accurate parameter identification will be injected through the direct-axis current as the healthy torque (Eq. (4.4)) is solely a function of the quadrature-axis current. Therefore, a sinusoidal direct-axis current and a constant quadrature current will be assumed, which are given by:

$$i_d^r = A\sin(\omega t),$$
$$i_q^r = I_q,$$

where I_q is the corresponding quadrature-axis current that achieves the desired torque (i.e., $I_q = \frac{4\tau_{3\phi}}{3N_p\Lambda_{PM}}$). In the regressor, the low-pass filter ($\{\mathcal{F}(s)\}$) will be neglected as it has no effect on the results.

7.2.2.1 Persistency of Excitation Analysis for Estimator based on Proposed Dynamic Model

Based on the previous assumptions, the regressor's direct and quadrature components for the estimator based on proposed dynamic model (Eq. (7.1)) are function of

the excitation and electrical rotor frequencies and are given by:

$$\vec{\phi}_d = \begin{bmatrix} A\sin(\omega t) \\ A\omega\cos(\omega t) - \omega_{re} I_q \\ 0 \\ -2\omega_{re}\sin(3\omega_{re} t) \\ A\omega\cos(\omega t)\sin(\omega_r t) + A\omega_r \sin(\omega t)\cos(\omega_r t) - \omega_{re} I_q \sin(\omega_r t) \\ A\omega\cos(\omega t)\cos(\omega_r t) - A\omega_r \sin(\omega t)\sin(\omega_r t) - \omega_{re} I_q \cos(\omega_r t) \\ \omega_r \cos(\omega_r t) \\ -\omega_r \sin(\omega_r t) \\ I_q \omega_{re}\cos(2\omega_{re} t) + A\omega_{re}\sin(\omega t)\sin(2\omega_{re} t) - A\omega\cos(\omega t)\cos(2\omega_{re} t) \\ A\omega\cos(\omega t)\sin(2\omega_{re} t) + \omega_{re} A\sin(\omega t)\cos(2\omega_{re} t) - \omega_{re} I_q \sin(2\omega_{re} t) \\ \omega_{re}\sin(2\omega_{re} t) \\ \omega_{re}\cos(2\omega_{re} t) \end{bmatrix}, \quad (7.2)$$

$$\vec{\phi}_q = \begin{bmatrix} I_q \\ A\omega_{re}\sin(\omega t) \\ \omega_{re} \\ -2\omega_{re}\cos(3\omega_{re} t) \\ I_q \omega_r \cos(\omega_r t) + \omega_{re} A\sin(\omega t)\sin(\omega_r t) \\ -I_q \omega_r \sin(\omega_r t) + \omega_{re} A\sin(\omega t)\cos(\omega_r t) \\ \omega_{re}\sin(\omega_r t) \\ \omega_{re}\cos(\omega_r t) \\ A\omega\cos(\omega t)\sin(2\omega_{re} t) + A\omega_{re}\sin(\omega t)\cos(2\omega_{re} t) - \omega_{re} I_q \sin(2\omega_{re} t) \\ A\omega\cos(\omega t)\cos(2\omega_{re} t) - A\omega_{re}\sin(\omega t)\sin(2\omega_{re} t) - \omega_{re} I_q \cos(2\omega_{re} t) \\ \omega_{re}\cos(2\omega_{re} t) \\ -\omega_{re}\sin(2\omega_{re} t) \end{bmatrix}. \quad (7.3)$$

Assuming that the regressor is periodic with $T_0 = \frac{2\pi}{\omega_0}$, it can be shown that:

$$\det\left(\frac{1}{T_0}\int_0^{T_0} \mathbf{\Phi}(\tau)\mathbf{\Phi}(\tau)^\intercal d\tau\right) = \frac{A^6\omega_{re}^{12}}{65536}\Big(A^2\omega^2 + \omega_{re}^2(A^2 + 2I_q^2)\Big)(\omega^2 + \omega_{re}^2)^2(20A^2\omega^2 + \omega_{re}^2(25A^2 + 18I_q^2))^2 \quad (7.4)$$

Based on the determinant presented in Eq. (7.4), the regressor, $\mathbf{\Phi}$, is persistently

exciting if:

1. The rotor speed is non-zero (i.e., $\Omega_r = \frac{\Omega_{re}}{2} = 0$).

2. At least one sinusoidal component is injected into the direct-axis current (i.e., $A \neq 0$).

This analysis shows that the comprehensive parameter estimator requires the same excitation as the estimator based on the standard model. As previously discussed for the estimators presented in Chapters IV, V, and VI, the fault-related parameters have a self-excitation property, which can be leveraged to guarantee sufficient conditions for accurate convergence without additional excitation.

7.3 Co-Simulation Results Considering Nonlinearities

The effectiveness of the strategy presented in Section 7.2 is assessed through co-simulations. The estimator is evaluated with different gains while the SMPM machine operates at different current levels and at a constant speed of $1000RPM$. PI regulators with cross-coupling compensation are used to regulate the two-phase currents in the rotor reference frame. The co-simulations include single-fault and mixed-fault cases for DW and CW machine designs (i.e., demagnetization, ME, ITS, demagnetization+ME, demagnetization+ITS, and ME+ITS). Under demagnetization, magnet 1 is assumed to be completely demagnetized ($\Lambda_1 = 0$). Similarly, the rotor is assumed to have 21.5% of SE and 23.15% for DE under ME conditions. Under ITS condition, the DW SMPM machine is assumed to have a short in coil a_1 with $\mu_u = 5\%$, while the CW SMPM machine has a short in coil b_1 with $\mu_u = 4.5\%$.

The co-simulations integrate an FEA-based machine model with an electric drive system. The FEA-based SMPM machines correspond to the DW and CW SMPM machine models presented in Section 4.2.2 and are simulated in *Maxwell*. Note that the stator and rotor irons are modeled using "M19" as the steel type (See B-H curve in Fig. 4.23). The co-simulation interface and inverter model are implemented in *Twin Builder* from Ansoft Corporation. The inverter is modeled as an ideal "average-value" VSI. The control model is created in Matlab/Simulink and exported as a Twin Builder component.

The FEA-based machine model and electric drive are executed at $10kHz$. The estimated parameters start with an initial 20% deviation from the linear parameters under healthy conditions. For PE purposes, the command direct-axis current is set

to:

$$\tilde{i}_d^r = 5\sin(2\pi 40t). \tag{7.5}$$

7.3.1 Performance of the Comprehensive Identification Strategy for Comprehensive Detection Under Single Fault Conditions

Figures 7.2 and 7.3 present the co-simulation results for the comprehensive identification strategy when the DW and CW SMPM machine operate under demagnetization, eccentricity, and ITS. Note that, in the figures, the black dashed line corresponds to the parameters for a healthy SMPM machine. As shown in Figs. 7.2 and 7.3, under demagnetization, the PM flux linkage is reduced by 25%, tracked by the parameter estimator. Similarly, the estimated parameters track the increase in the inductance and PM flux linkage under ME. When the SMPM machine experiences ITS, the estimated magnetic parameters slightly decrease while the resistance increases. Note that all parameters were theoretically expected to decrease; however, they are affected by the dynamics from the short turns. Additionally, note that the magnetic parameters reach saturation and decrease when the SMPM machine operates at higher currents under the different fault conditions. As mentioned in previous chapters, under saturation, the magnetics become nonlinear and affect the estimated resistance since it is susceptible to unmodeled dynamics.

In terms of the fault-related parameters, they become non-zero for the specific fault they are meant to monitor and detect. Under demagnetization, the fault-related parameter is the asymmetry term that captures uneven demagnetization between the north and south PM flux linkages. Note that this asymmetry term is solely non-zero for demagnetization with the CW SMPM machine. As previously mentioned, the DW SMPM machine does not produce additional harmonics due to its design. Hence, for the DW design, demagnetization monitoring and detection relies only on the PM flux linkage decrease. Under eccentricity, the fault-related parameters capture the oscillation at the rotor speed in the magnetic parameters caused by the ME air-gap asymmetry. As seen in Figs. 7.2 and 7.3, these ME-related parameters become non-zero under eccentricity conditions for both SMPM machine designs. Under ITS condition, the fault-related parameters are intended to capture the oscillations at twice the electrical rotor speed in the magnetic parameters due to the ITS. As shown in Figs. 7.2 and 7.3, the ITS-related parameters are non-zero under ITS and zero under demagnetization and ME conditions. Therefore, the comprehensive identification approach can be used for monitoring and detecting demagnetization, ME, and ITS conditions.

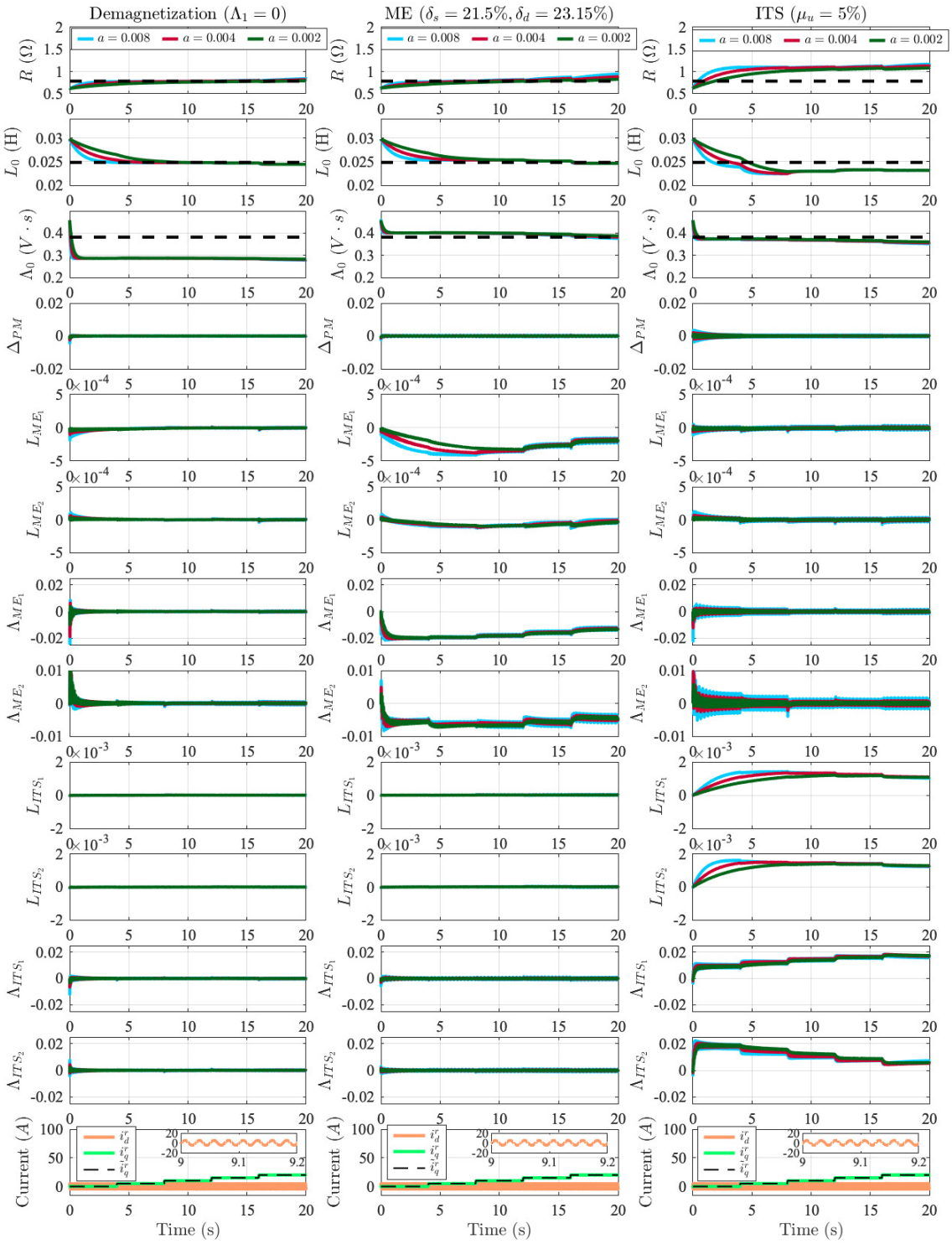

Figure 7.2: Co-simulation results of the comprehensive parameter strategy when the DW SMPM machine is operating under demagnetization, ME, and ITS.

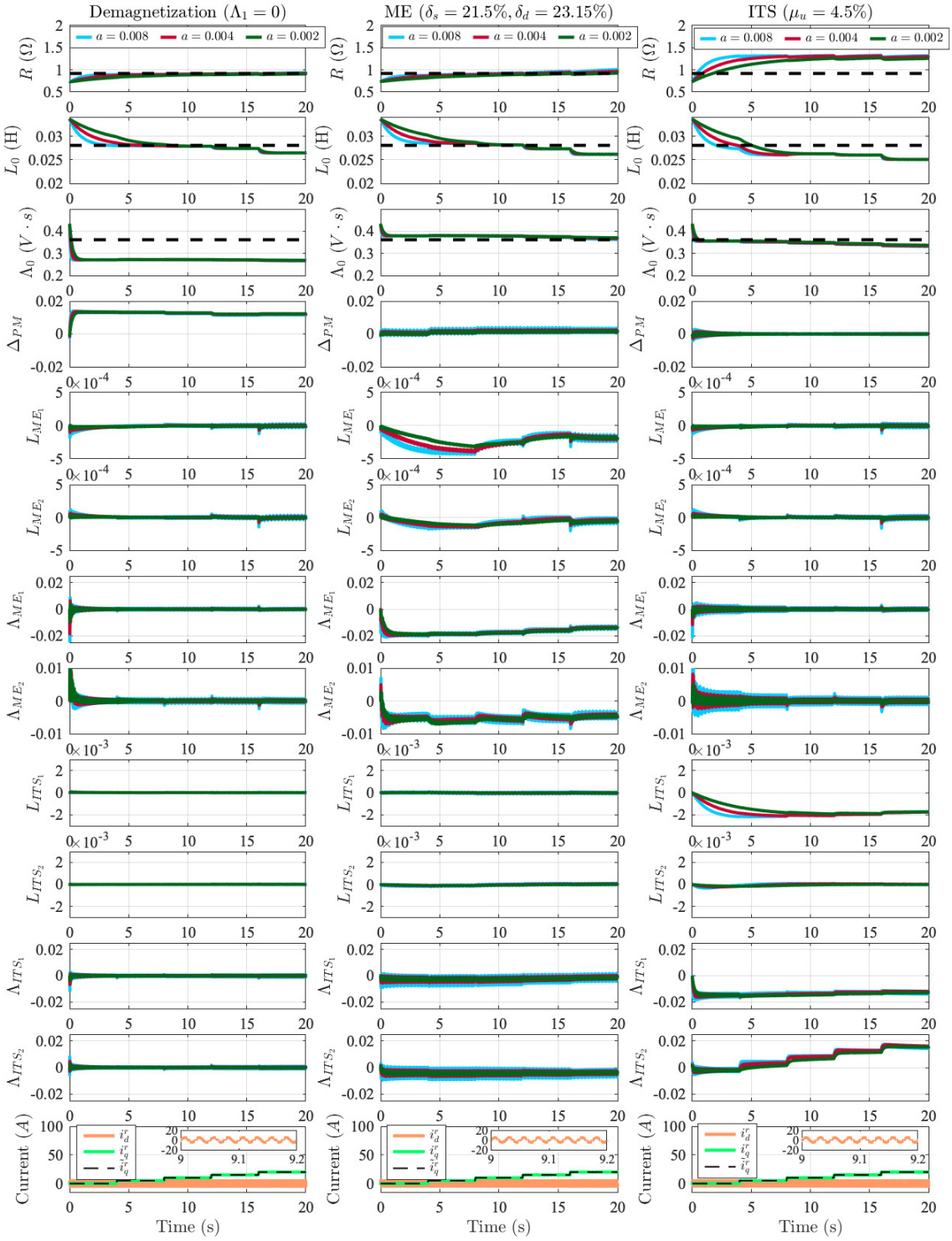

Figure 7.3: Co-simulation results of the comprehensive parameter strategy when the CW SMPM machine is operating under demagnetization, ME, and ITS.

As a validation for the discrete PE analysis, the condition number of the PE condition matrix is presented in Figs. 7.4, 7.5, 7.6 and 7.7. Note that the moving window corresponds to the period of the injected PE signal and is given by 3000 samples (0.3 s). Figs. 7.4 and 7.5 show that the condition number of the PE condition matrix is not infinite, and, therefore, the inputs are persistently exciting. Figs. 7.6 and 7.7 show the condition number of the PE matrix when the regressor is scaled, as previously discussed in Remark 4.1. As shown in Figs. 7.6 and 7.7, scaling the regressor improves the condition number of the PE condition matrix.

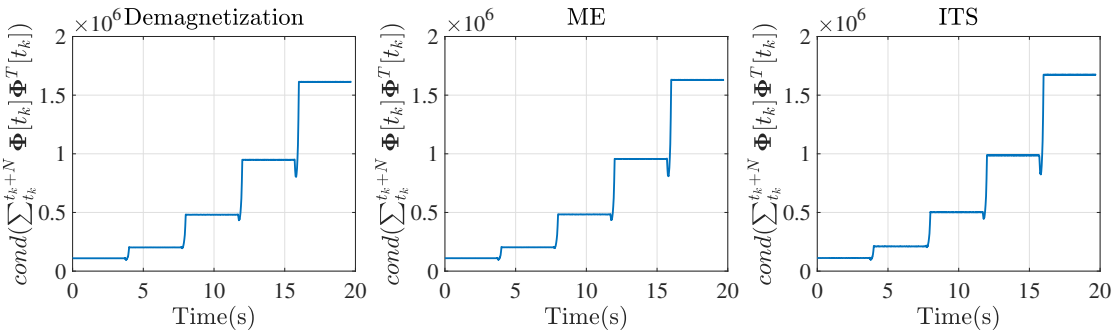

Figure 7.4: Condition number of the discrete PE condition matrix for the comprehensive identification strategy when the DW SMPM machine is operating under single fault conditions.

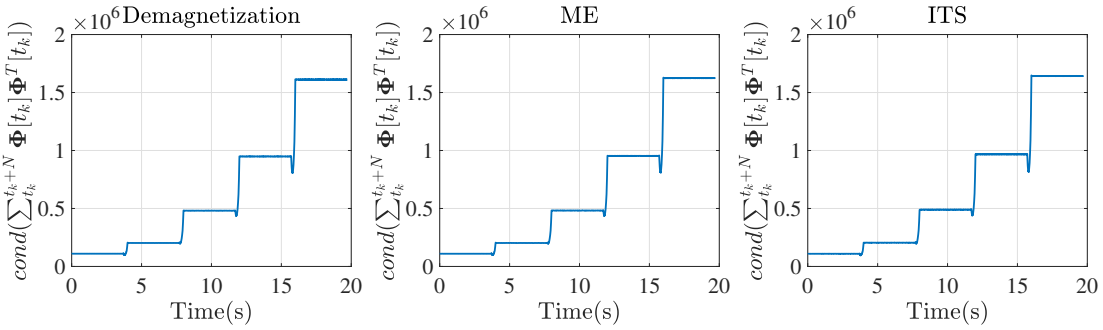

Figure 7.5: Condition number of the discrete PE condition matrix for the comprehensive identification strategy when the CW SMPM machine is operating under single fault conditions.

7.3.2 Performance of the Comprehensive Identification Strategy for Comprehensive Detection Under Mixed Fault Conditions

Figures 7.8 and 7.9 show the co-simulation results for the comprehensive identification strategy when the DW and CW SMPM machines operate under mixed fault

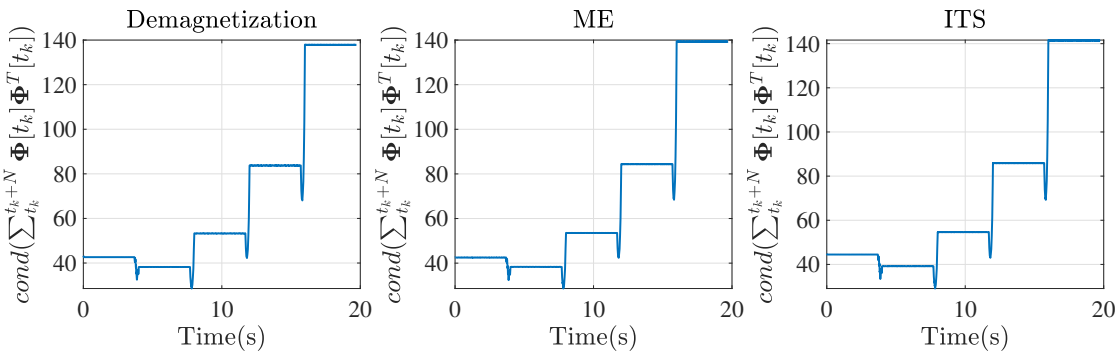

Figure 7.6: Condition number of the discrete PE condition matrix with scaled regressor for the comprehensive identification strategy when the DW SMPM machine is operating under single fault conditions.

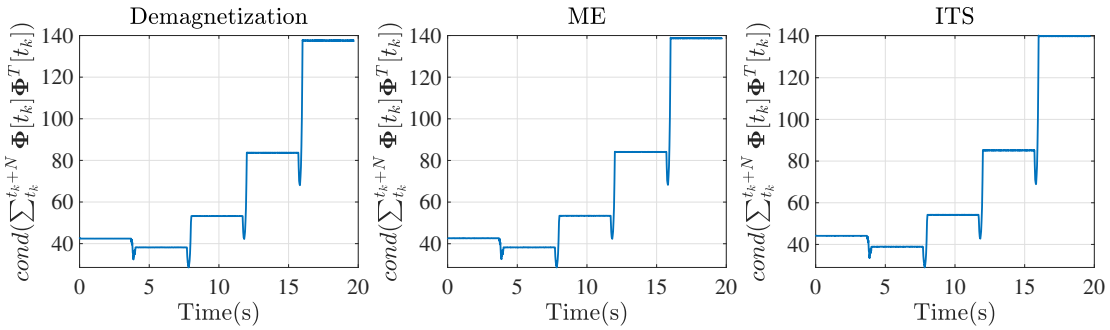

Figure 7.7: Condition number of the discrete PE condition matrix with scaled regressor for the comprehensive identification strategy when the CW SMPM machine is operating under single fault conditions.

conditions. In the figures, the black dashed line corresponds to the linear parameters under healthy conditions.

In the co-simulation results for the DW and CW SMPM machines operating under demagnetization and ITS, the resistance increases while the inductance and PM flux linkage decrease compared to the healthy values. When studied separately, demagnetization causes a reduction in the PM flux linkage while the ITS slightly decreases the magnetic parameters and increases the resistance value. When the SMPM machine operates under both faults, these parameters resemble the combined effects of demagnetization and inter-turn short. Since the SMPM machine is under demagnetization and ITS, only the fault-related parameters associated with these two faults should be non-zero. As seen in Figs. 7.8 and 7.9, the asymmetry term associated with the uneven demagnetization between the north and south poles is zero and non-zero for the DW and CW SMPM machine, respectively. As mentioned before, this is a limitation imposed by the DW design itself, as it does not produce additional harmonics under uneven demagnetization. Regarding the ITS-related parameters, their value is non-zero for both designs, indicating that the machine is experiencing ITS.

When the DW and CW SMPM machines operate under eccentricity and demagnetization, the co-simulation results show that the inductance increases while the PM flux linkage decreases. Separately, demagnetization causes a reduction in the PM flux linkage while eccentricity slightly increases the inductance and PM flux linkage. When the SMPM machine experiences simultaneously eccentricity and demagnetization, these parameters show the resultant combination of both faults. Similarly, as the SMPM machine is under demagnetization and eccentricity, the parameters related to these faults should be non-zero. As shown in Figs. 7.8 and 7.9, the asymmetry term that characterizes the uneven demagnetization between the north and south poles is zero and non-zero for the DW and CW SMPM machine, respectively. The DW design does not experience new harmonics under asymmetric demagnetization, and, therefore, the asymmetry term cannot provide fault information. In addition, the ME-related parameters are non-zero, showing that the machine is experiencing eccentricity. Similarly, since the machine does not have an ITS, the ITS-related parameters remain zero.

In the co-simulation results for the DW and CW SMPM machines operating under eccentricity and inter-turn short, the resistance and PM flux linkage increase while the inductance reduces compared to the healthy values. Individually, eccentricity causes a slight increase in the magnetic parameters, and the ITS decreases the magnetic parameters and increases the resistance value. When the SMPM machine operates

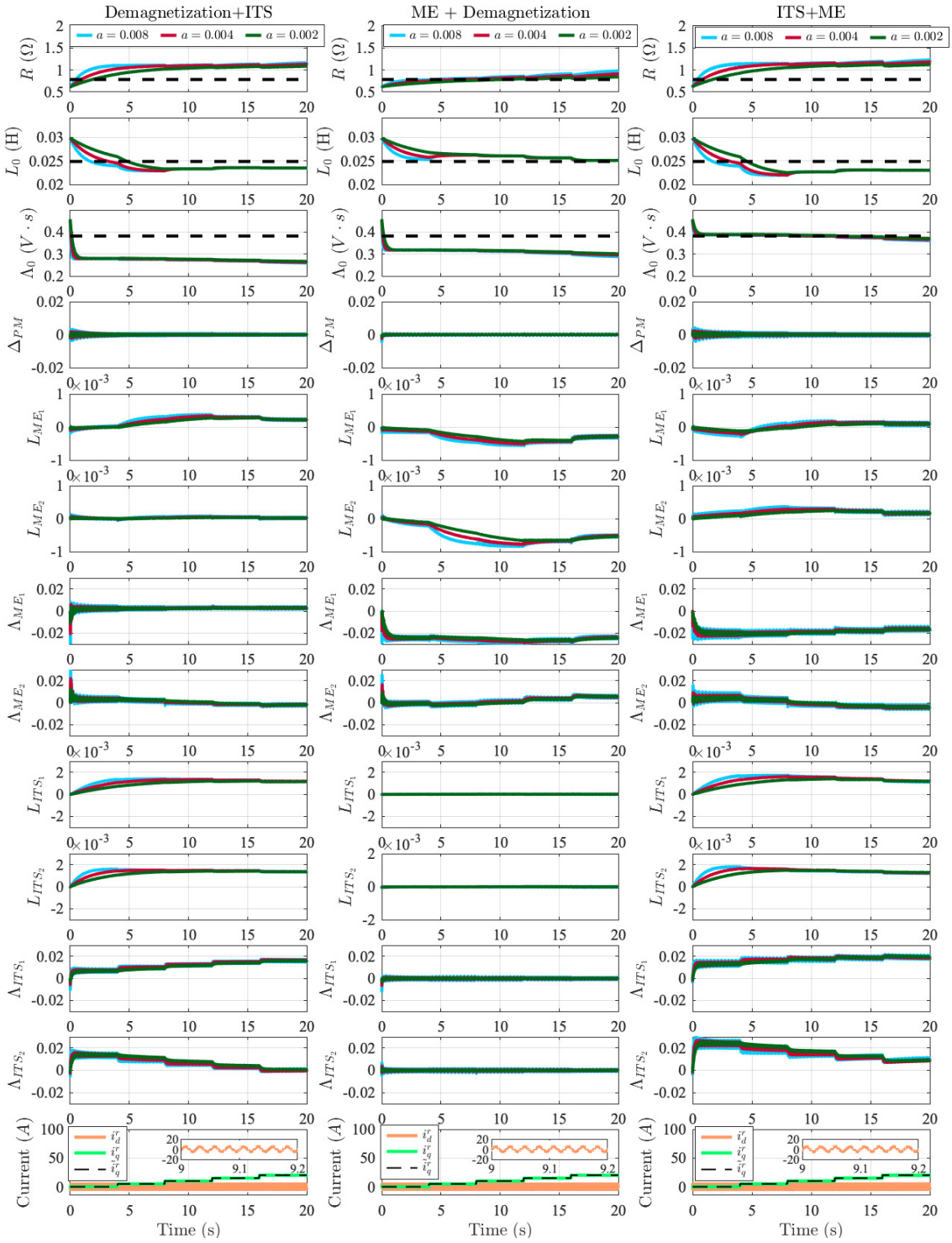

Figure 7.8: Co-simulation results of the comprehensive parameter strategy when the DW SMPM machine is operating under mixed-fault conditions.

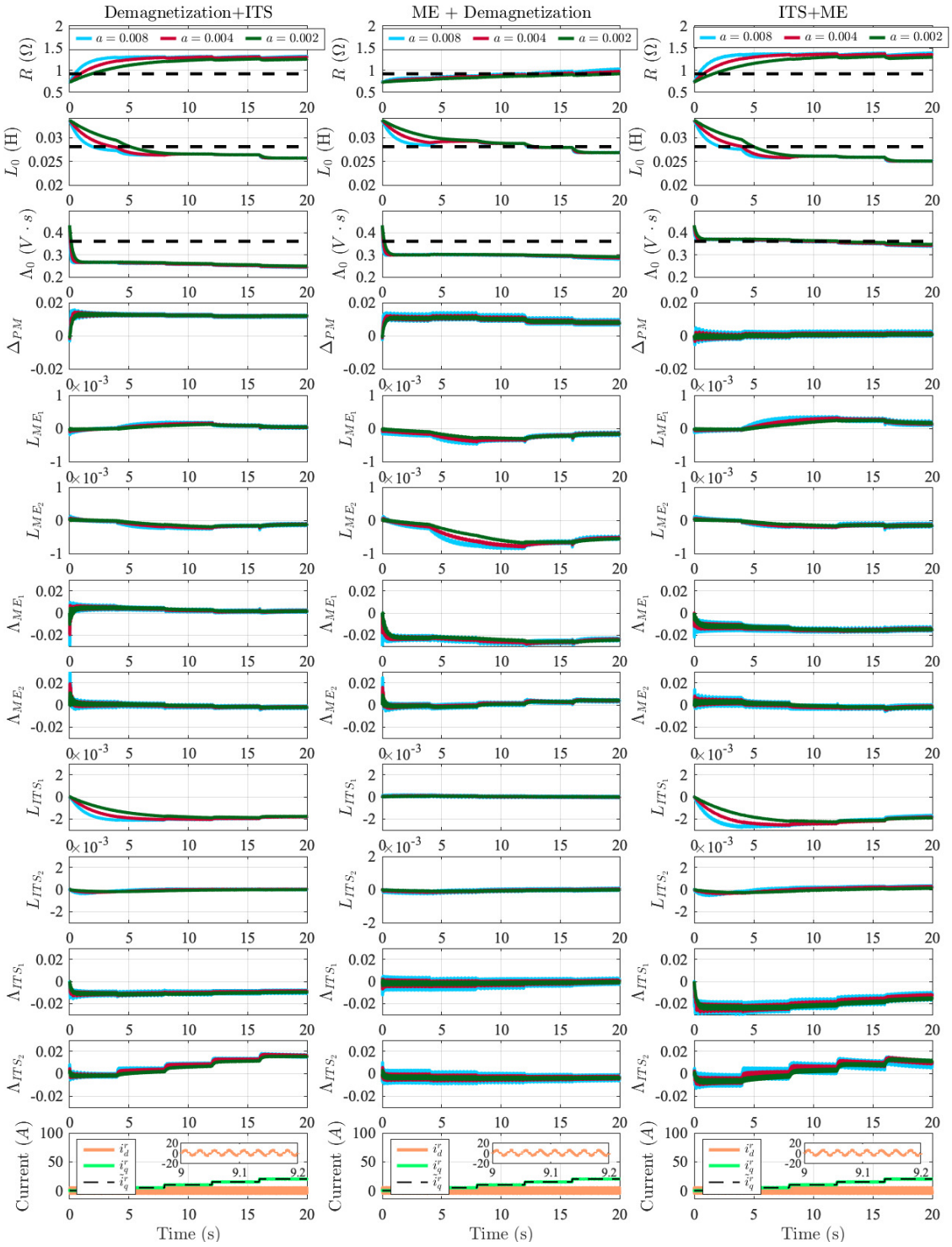

Figure 7.9: Co-simulation results of the comprehensive parameter strategy when the CW SMPM machine is operating under mixed-fault conditions.

under eccentricity and ITS faults, the parameters display the resultant combination of both faults. In addition, only the parameters related to eccentricity and ITS are non-zero.

Figures 7.10, 7.11, 7.12, and 7.13 present the condition number of the PE condition matrix for the DW and CW SMPM machines operating under mixed faults. Note that the moving window corresponds to the period of the injected PE signal and is given by 3000 samples (0.3 s). In Figs. 7.10 and 7.11, the condition number of the PE condition matrix is not infinite, and, hence, the inputs are persistently exciting. Figs. 7.12 and 7.13 show the condition number of the PE matrix when the regressor is scaled. As shown in Figs. 7.12 and 7.13, scaling the regressor improves the condition number of the PE condition matrix.

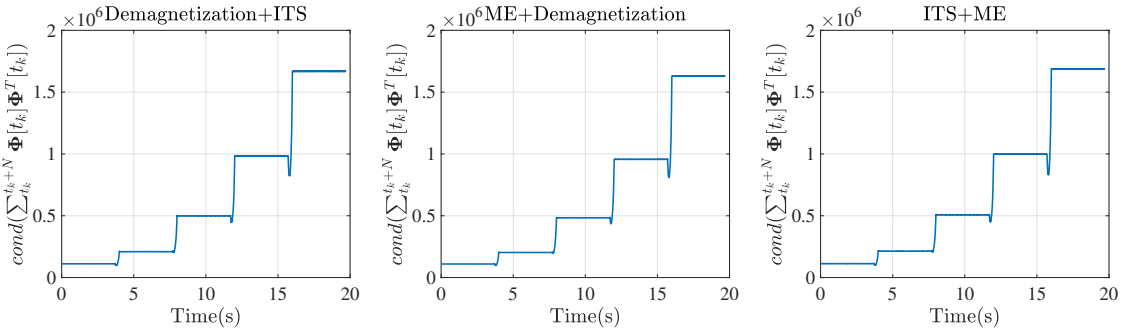

Figure 7.10: Condition number of the discrete PE condition matrix for the comprehensive identification strategy when the DW SMPM machine is operating under mixed fault conditions.

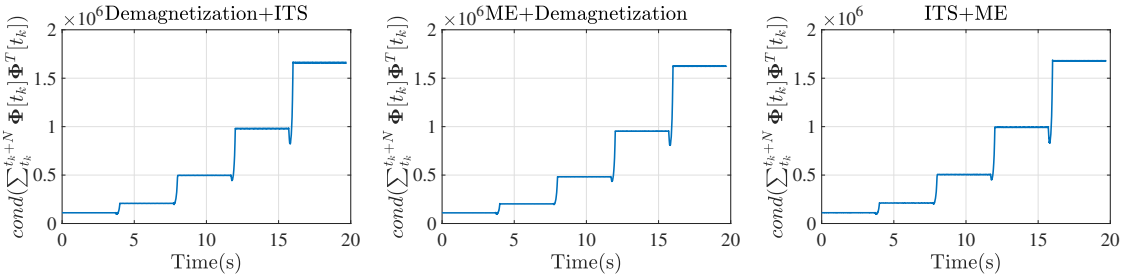

Figure 7.11: Condition number of the discrete PE condition matrix for the comprehensive identification strategy when the CW SMPM machine is operating under mixed fault conditions.

Overall, the co-simulation results show the promising aspects of the comprehensive identification strategy for monitoring and detecting faults and its limitations. As previously discussed, using the resistance, inductance, and PM flux linkage for

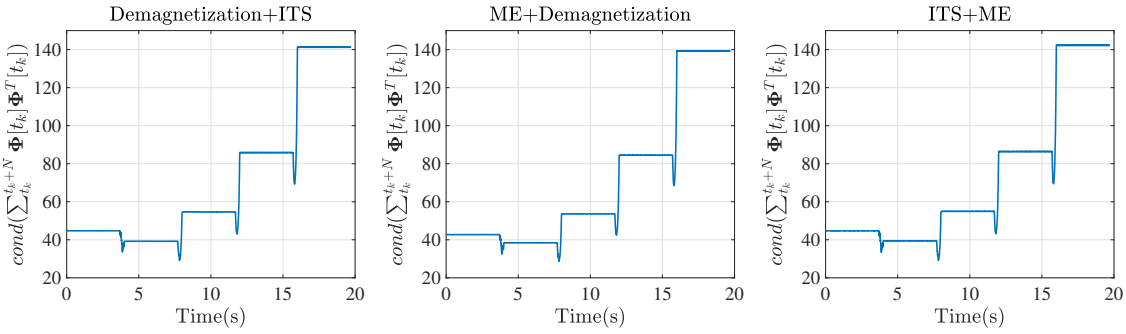

Figure 7.12: Condition number of the discrete PE condition matrix with scaled regressor for the comprehensive identification strategy when the DW SMPM machine is operating under mixed fault conditions.

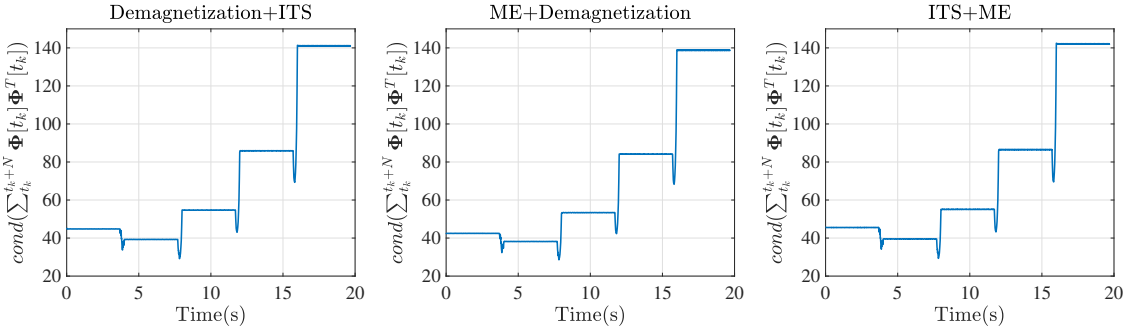

Figure 7.13: Condition number of the discrete PE condition matrix with scaled regressor for the comprehensive identification strategy when the CW SMPM machine is operating under mixed fault conditions.

detection is problematic as their value is affected by temperature, skin effect, and saturation. Moreover, since the resistance represents a considerably small portion of the total voltage, its estimated value is prone to inaccuracies. In contrast, the parameters that capture the specific fault-related oscillations offer a more systematic method for monitoring and detecting fault conditions. Demagnetization, eccentricity and ITS conditions produce oscillations at different frequencies. Consequently, the fundamental value of the fault-related parameters should be non-zero solely when such fault occurs.

As seen in the co-simulation results for single fault conditions, the fundamental component of the different fault-related parameters is non-zero solely when the specific fault occurs. Still, note that, in particular, monitoring and detecting demagnetization for the DW design is challenging as the asymmetry term for uneven demagnetization does not provide information. Hence, in this specific case, the PM flux linkage decrease is the only indicator for monitoring and detecting demagnetization.

Regarding the co-simulation results for mixed fault conditions, fault-related parameters accurately monitor and detect the eccentricity and ITS condition (ME+ITS). Similarly, the eccentricity and demagnetization condition is correctly identified for the CW SMPM machine design. Unfortunately, the eccentricity and demagnetization condition can be hard to distinguish from mere eccentricity for the DW design, as the asymmetry term for demagnetization cannot provide information. In this case, the decrease in the PM flux linkage is the sole indicator for demagnetization. The demagnetization plus ITS condition is detected for the CW SMPM machine design; however, the ME-related parameters that capture oscillations in the inductance are slightly affected. In addition, for the DW design, demagnetization and ITS condition can be difficult to distinguish from solely inter-turn short, as the DW design does not produce new harmonics under demagnetization. As previously mentioned, for the DW design, the decrease in the PM flux linkage is the only indicator for demagnetization.

7.4 Summary

This chapter investigated the application of parameter identification to fault diagnosis and condition monitoring of SMPM machines under demagnetization, ME, and ITS fault conditions. Specifically, a strategy was presented for comprehensive monitoring and fault detection. First, the parameter identification strategy was formulated by incorporating all the previous estimators into a single parameter estimator. Then, the performance of the parameter identification strategy for monitoring and detect-

ing fault conditions was assessed through co-simulations. The results included single and mixed fault conditions. In the single fault conditions, the co-simulation results demonstrated that the comprehensive approach could monitor and detect the different faults. The co-simulation results for the mixed fault conditions showed that the comprehensive approach could identify the different faults, except the demagnetization plus ITS condition. In this case, in addition to detecting demagnetization and ITS, the comprehensive estimator had non-zero ME-related inductance. The results also showed that the DW SMPM machine design imposes difficulties in monitoring and detecting demagnetization.

CHAPTER VIII

Conclusions and Future Work

This dissertation presented research that seeks to address open issues regarding the application of parameter identification to fault diagnosis and condition monitoring of PMSMs. The first part of this dissertation investigated the incorporation of operational constraints to the SIC problem. Specifically, an optimization-based SIC formulation for SMPM machines that explicitly considers the voltage and current inverter limits was presented in Chapter III. The rest of the dissertation covered research related to the parameterization and parameter identification of SMPM machines for fault detection and condition monitoring. Control-oriented models and parameter identification strategies for monitoring and detecting demagnetization, ME, and ITS were presented in Chapters IV, V, and VI, respectively. In Chapter VII, a parameter estimator was formulated by combining the parameter estimators for demagnetization, ME, and ITS. Simulation and co-simulation results demonstrated the effectiveness of the proposed estimators for fault detection and condition monitoring. This chapter presents conclusions and potential directions for future work.

8.1 Conclusions

8.1.1 Control-oriented models for analysis and fault-detection algorithm design of SMPM machines under fault conditions

Lumped-parameters models were formulated to capture the essential dynamic behavior of SMPM machines under demagnetization, ME, and ITS conditions. FEA simulations validated the proposed models. Based on the proposed models, parameterizations that included specific parameters to capture the dynamic imbalances caused by the faults were formulated. These parameterizations allowed straightforward implementation in parameter identification strategies. This section presents the

main conclusions on this topic.

In Chapter IV, an equivalent two-phase SMPM machine model under demagnetization was formulated for a three-phase four-pole SMPM machine with two windings per phase. Demagnetization mainly affects the PM flux linkage. Hence, the equivalent two-phase model was formulated by superimposing the PM flux linkage produced by the individual magnets. This model can capture the operation of the SMPM machine under healthy conditions and demagnetization affecting evenly or unevenly the different magnets. FEA simulations demonstrated that the model could capture the PM flux linkage under healthy and demagnetized conditions with reasonable accuracy when adequately calibrated. A comparison between simulation and co-simulation results showed that the proposed model is suitable for studying the SMPM machine behavior under demagnetization in the linear operating region. In addition, a comparison between the CW and DW SMPM machine results justifies the need for studying demagnetization on a case-by-case basis. The PM flux linkage contained new harmonics under demagnetization solely for the CW design studied in the simulation and co-simulation results. For identification, a parameterization was formulated based on this model, which included a parameter that captured the asymmetries between the north and south PM flux linkages.

In Chapter V, an equivalent two-phase SMPM machine model under eccentricity was formulated for a three-phase four-pole SMPM machine with two windings per phase. Eccentricity mainly affects the magnetic parameters in the three-phase SMPM machine dynamics. Thus, the equivalent two-phase dynamics under eccentricity were formulated by modeling the expressions for the inductances and PM flux linkages using MWF and MF theories. This model can capture SE, DE, and ME conditions by modifying the static and dynamic eccentricity degrees accordingly. Note that the model captures the effect of eccentricity on the fundamental Fourier coefficient of the magnetic parameters, always present regardless of the SMPM machine design. However, depending on the SMPM machine design, note that additional harmonics might exist under eccentricity. These additional harmonics can be easily incorporated into the model following the procedure previously presented, but they have to be determined on a case-by-case basis. FEA simulations demonstrated that the model captures the essential behavior of the eccentricity fault. A parameterization for identification was formulated based on this model, which included parameters that captured the ME-related oscillation at the rotor speed in the magnetic parameters.

In Chapter VI, an equivalent two-phase SMPM machine model under ITS was formulated for a three-phase four-pole SMPM machine with two windings in series

per phase. The equivalent two-phase model was formulated by modeling the different coils separately and integrating them into the different phases based on the winding connections. In this model, the insulation failure between continuous turns was modeled by an additional resistance shorting the affected turns. By phase-shifting the oscillatory components, the model can capture ITS faults affecting any of the phases. Since the effect of the ITS depends on the number of coils and winding connections, modeling other winding topologies requires a case-by-case analysis. FEA simulations showed that the model characterizes the essential behavior of the ITS fault. Based on this model, a parameterization for identification was formulated for identification purposes. Specifically, the linear parametric model included parameters related to ITS condition based on the proposed two-phase model while considering the available signals.

8.1.2 Application of parameter identification for fault detection of SMPM machines under fault conditions

Parameter identification strategies for monitoring and detecting the different faults were formulated based on the proposed lumped-parameter models. Specifically, these parameter estimators incorporated parameters that capture the dynamic asymmetries caused by demagnetization, ME, and ITS. Additionally, through PE analysis, the inputs were designed to guarantee sufficient conditions for accurate parameter convergence while avoiding control perturbations. Simulation and co-simulation results demonstrated the effectiveness of the proposed parameter estimators for monitoring and detecting the different fault conditions. This section presents the main conclusions on this topic.

In Chapter IV, an online parameter identification technique for a three-phase four-pole SMPM machine with two windings per phase under demagnetization was formulated. Specifically, a parameterization was formulated based on the proposed model, which included a parameter to capture the asymmetries between the north and south PM flux linkages. This asymmetry term allows the monitoring and detection of uneven demagnetization between the north and south poles. However, the main limitation of this approach is that under even demagnetization, the only information that can be used for monitoring and detection is the average value of the PM flux linkage. Moreover, as seen in the simulation and co-simulation results, some SMPM machine designs will not have additional harmonics under uneven demagnetization. Thus, there will be cases in which the average value of the PM flux linkage is the only fault indicator. In this sense, if no additional harmonics exist under uneven demag-

netization, there is no way to discern between even and uneven demagnetization.

In Chapter V, an online parameter identification technique was formulated for a three-phase four-pole SMPM machine with two windings per phase under ME. Concretely, a parameterization was formulated based on the proposed ME model, which included parameters that characterized the oscillations at the rotor speed in the magnetic parameters. These asymmetry terms aid the monitoring and detection of ME conditions. While DE and SE were discussed in Chapter V, solely ME exists in practice as even newly manufactured motors have some level of ME due to the inherent tolerances in the manufacturing and assembling processes. Therefore, the ME-related parameters are suitable indicators for detection as they can track a gradual increase in ME. Simulation and co-simulation results demonstrated the effectiveness of the proposed parameter identification strategy for monitoring and detecting ME. The main limitation for detection is given by the SMPM machine design, as the PMs limit the degree of eccentricity.

In Chapter VI, an online parameter identification technique was formulated for a three-phase four-pole SMPM machine with two windings in series per phase under ITS. A parameterization was formulated based on the proposed ITS model and available signals, which captured the oscillations at twice the electrical rotor speed in the magnetic parameters. These ITS-related parameters allow the detection of ITS in any of the three phases. Simulation and co-simulation results showed the effectiveness of the proposed parameter identification strategy for monitoring and detecting ITS conditions.

In Chapter VII, a comprehensive parameter identification strategy for fault diagnosis and condition monitoring was formulated by incorporating the estimators for demagnetization, ME, and ITS into a single strategy. Expressly, all the fault-related parameters were incorporated with the standard model parameters into a single model for identification. Co-simulation results demonstrated the effectiveness of the parameter identification strategy for fault detection. The results included single and mixed fault conditions. In the single fault conditions, the parameter identification strategy was successful at monitoring and detecting the different faults. In addition, the co-simulation results for the mixed fault conditions proved that the comprehensive approach could uniquely detect the different faults, except the demagnetization plus ITS condition. In this case, the comprehensive estimator could detect the demagnetization and ITS; however, a non-zero ME-related inductance was also shown. In addition, the comprehensive estimator shared the same difficulties for demagnetization detection imposed by the DW design in Chapter IV.

8.1.3 Incorporation of operational constraints to SIC methodologies for SMPM machines

Chapter III presented a simultaneous identification and torque control methodology for SMPM machines, including inverter current and voltage constraints. The current and voltage constraints for the SIC formulation were derived by mapping three-phase voltage and current constraints into their two-phase equivalents. Hexagons described the resultant feasible region for both variables. These constraints were incorporated into a SIC formulation that included an adaptive current regulator and an RHAID. The quadrature-axis current was set to achieve the desired torque, while the direct-axis current was used to inject the excitation required for accurate convergence. The inverter current and voltage constraints were incorporated as part of the RHAID, which minimized losses and maximized the excitation characteristics of the reference direct current trajectories. Accurate torque regulation was achieved through the adaptive current regulator. Simulations demonstrated the effectiveness of the SIC formulation on the constraint enforcement at different operating conditions. In particular, the simulation results showed that occasional constraint violations occurred before parameters converged within 5% of error.

8.2 Future Work

The potential directions for future work are as follows:

8.2.1 Generalization of the Proposed Two-Phase Equivalent Models in the Rotor Reference Frame for Parameter Identification-Based Fault Diagnosis and Condition Monitoring Strategies

The two-phase equivalent models under demagnetization, eccentricity, and inter-turn short were formulated for a four-pole three-phase SMPM machine with two coils per phase. Based on the intuition and knowledge gained via these case studies, some ideas on possible generalization are discussed.

In terms of demagnetization, the decrease in the overall PM flux linkage and the asymmetry term were the two indicators for the four-pole three-phase SMPM machine with two coils per phase. The overall PM flux linkage will decrease regardless of the winding configuration or number of poles, and, hence, it can be used as an indicator for other SMPM machine designs. In addition, in the analysis presented for the four-pole three-phase SMPM machine with two coils per phase, the asymmetry

term captured the oscillation at three times the electrical rotor speed caused by uneven demagnetization between the north and south PM flux linkages. As previously shown for the SMPM machine designs studied, the additional harmonics under demagnetization depended on the winding design. For example, the DW design studied did not have additional harmonics under demagnetization. However, in other SMPM machine designs, if new harmonics exist under demagnetization, we believe one will correspond to the asymmetry term. Still, a rigorous analysis should be performed to confirm this.

Regarding eccentricity, the ME air-gap asymmetry produced an oscillation at the rotor speed in the magnetic parameters for the four-pole three-phase SMPM machine with two coils per phase. This oscillation is based on the fundamental Fourier coefficient of the magnetic parameters, which is always present regardless of the SMPM machine design. Hence, these fault-related parameters can be used for SMPM machines with different winding configurations and number of poles.

The inter-turn short condition generated oscillations at twice the electrical rotor speed for the four-pole three-phase SMPM machine with two coils in series per phase. In this dissertation, an approximated model with parameters that captured these oscillations was presented. While the severity of the inter-turn short depends on the winding design, the oscillation at twice the electrical rotor speed should be present for other machines designs. Note that this should be confirmed with a rigorous analysis. In addition, note that the inter-turn short was studied only for series-connected coils. Based on the procedure presented, the effect of inter-turn short for parallel-connected windings should be studied.

The two-phase equivalent models for demagnetization, eccentricity, and inter-turn short were formulated assuming an ungrounded-wye connected SMPM machine. The effects of these faults on delta-connected SMPM machines should be investigated. While the input and output behavior should be similar, a circulating zero-sequence current should occur within the delta-connected windings.

8.2.2 Experimental Validation of Proposed Parameter Identification Strategies for Fault Diagnosis and Condition Monitoring

In this dissertation, parameter identification strategies have been formulated for monitoring and detecting demagnetization, eccentricity, and inter-turn short conditions. The performance of the parameter estimators was validated through co-simulation in which FEA machine models were integrated with an electric drive. Additional validation can be performed in actual hardware with SMPM machines

modified to replicate the fault conditions. For example, an uneven demagnetization condition can be emulated by replacing one of the magnets with a dummy block of similar shape and weight. This dummy block should be made from a material that does not produce any flux linkage to capture demagnetization. Similarly, to avoid mechanical unbalances, this dummy block should have a similar size and weight as the original magnet. In terms of eccentricity, the bearings can be designed and machined to introduce ME [36]. Regarding ITS, the stator winding can be modified to have intermediate taps for one coil. These intermediate taps can be used to insert the ITS using a resistor [27].

8.2.3 Decision Making for Fault Detection: Threshold determination

In this dissertation, parameters that capture the phenomena generated by faults were defined. Specifically, the gradual deviation from zero in these fault-related parameters is directly linked to a progressive increase in the fault condition, which can be leveraged for fault diagnosis. However, in practice a threshold for detection is required to distinguish between fault-free and faulty modes. The faults have different levels of severity and should be diagnosed after a given value is exceeded. Moreover, the threshold should be designed to avoid misdetection due to noise, unmodeled dynamics, and inherent tolerances in the manufacturing and assembling processes. Note that the performance of the fault diagnosis strategy depends on this threshold, as a trade-off for detection exists. Selecting a threshold that is too small will lead to a high false-positive rate and a low true-negative rate. Similarly, a low true-positive rate and a high false-negative rate will occur if the threshold is too large.

8.2.4 Integration of Thermal Models to the Proposed Parameter Identification Strategies

In addition to the fault-specific parameters, the standard machine parameters carry information that can be used to monitor the different faults. However, the standard parameters vary with operating conditions, hindering fault diagnosis and condition monitoring application. Thermal models offer additional information that can be used to differentiate whether faults or temperature changes are responsible for parameter variations.

Demagnetization mainly affects the PM flux linkage. As presented in Chapter IV, the fault-related parameter is the asymmetry term that captures the oscillations in the PM flux linkage due to uneven demagnetization between the north and south

poles. However, this parameter cannot provide information for even demagnetization. Moreover, there are machine designs with no asymmetry under demagnetization, such as the DW design presented in Chapter IV. In these cases, the decrease in the PM flux linkage is the sole indicator for demagnetization. The main challenge of using the PM flux linkage reduction as an indicator is that, under healthy conditions, increasing PM temperature also causes a decrease in the PM flux linkage, and so a method to distinguish the root cause is required. To distinguish the cause, the magnet temperature can be measured (which is difficult) or estimated by incorporating a thermal model, and a link between PM temperature and variations in the PM flux linkage can be established.

8.2.5 Application of the Parameter-Identification-Based Strategies to Control

In practice, there are cases in which the machine has to maintain operation even under fault conditions. In this dissertation, models in which parameters characterize oscillations caused by the faults were formulated. While these models were devised for parameter identification-based fault diagnosis and condition monitoring, the control strategy can utilize this information to adapt its strategy to continue operation and maintain performance while minimizing further machine damage. As an example, torque control is typically achieved through current regulation. Therefore, these models can be used to determine torque expressions under the different fault conditions so that the reference currents can be adjusted to maintain the torque regulation performance. Moreover, the torque capabilities can be derated based on the parameters to mitigate the fault progression and further machine damage.

8.2.6 Prognosis of SMPM machines

Predicting when the system no longer meets satisfactory performance is crucial when determining corrective measures. Prognosis analyzes the trend of machine performance so that faults can be predicted and corrected before a failure occurs [105]. Hence, the strategy should be able to detect and continuously monitor any abnormalities. In addition, the strategy should effectively predict the remaining useful life and possible failure modes of the machine [105].

This thesis presented parameters that capture demagnetization, eccentricity, and inter-turn short effects on the electrical dynamics. Specifically, the fundamental value of these fault-related parameters becomes non-zero when such a fault occurs. More-

over, the deviation of fault-related parameters from their zero values captures the gradual increase in the fault severity over time. Hence, these parameters can be used to detect and continuously monitor the machine's health and degradation.

Regarding the prediction of remaining useful life, a life prediction model is required. The fault-related parameters can be incorporated into a machine learning strategy, which can use statistical and probabilistic techniques to learn and predict from past data.

BIBLIOGRAPHY

BIBLIOGRAPHY

[1] H. Hofmann, "Electric machinery and drives," lecture notes (EECS 419).

[2] A. Boglietti, A. Cavagnino, A. Tenconi, S. Vaschetto, and P. di Torino, "The safety critical electric machines and drives in the more electric aircraft: A survey," in *2009 35th Annual Conference of IEEE Industrial Electronics*. IEEE, 2009, pp. 2587–2594.

[3] B. Sarlioglu and C. T. Morris, "More electric aircraft: Review, challenges, and opportunities for commercial transport aircraft," *IEEE Transactions on Transportation Electrification*, vol. 1, no. 1, pp. 54–64, 2015.

[4] S. J. Dale, R. E. Hebner, and G. Sulligoi, "Electric ship technologies," *Proceedings of the IEEE*, vol. 103, no. 12, pp. 2225–2228, 2015.

[5] L. Situ, "Electric vehicle development: The past, present & future," in *2009 3rd International Conference on Power Electronics Systems and Applications (PESA)*, 2009, pp. 1–3.

[6] K. G. Høyer, "The history of alternative fuels in transportation: The case of electric and hybrid cars," *Utilities Policy*, vol. 16, no. 2, pp. 63 – 71, 2008, sustainable Energy and Transportation Systems. [Online]. Available: http://www.sciencedirect.com/science/article/pii/S0957178707000768

[7] J. Staszak, K. Ludwinek, Z. Gawęcki, J. Kurkiewicz, T. Bekier, and M. Jaśkiewicz, "Utilization of permanent magnet synchronous motors in industrial robots," in *2015 International Conference on Information and Digital Technologies*, 2015, pp. 342–347.

[8] O. Ondel, E. Boutleux, and G. Clerc, "Diagnosis by pattern recognition for pmsm used in more electric aircraft," in *IECON 2011 - 37th Annual Conference of the IEEE Industrial Electronics Society*, 2011, pp. 3452–3458.

[9] M. Zeraoulia, M. E. H. Benbouzid, and D. Diallo, "Electric motor drive selection issues for hev propulsion systems: A comparative study," *IEEE Transactions on Vehicular Technology*, vol. 55, no. 6, pp. 1756–1764, 2006.

[10] B. Ebrahimi, J. Faiz, and M. Roshtkhari, "Static-, dynamic-, and mixed-eccentricity fault diagnoses in permanent-magnet synchronous motors," *IEEE Transactions on Industrial Electronics*, vol. 56, no. 11, pp. 4727–4739, 11/2009.

[11] S. Choi, M. S. Haque, M. T. B. Tarek, V. Mulpuri, Y. Duan, S. Das, V. Garg, D. M. Ionel, M. A. Masrur, B. Mirafzal, and et al., "Fault diagnosis techniques for permanent magnet ac machine and drives-a review of current state of the art," *IEEE transactions on transportation electrification*, vol. 4, no. 2, pp. 444–463, 2018.

[12] Y. Da, X. Shi, and M. Krishnamurthy, "Health monitoring, fault diagnosis and failure prognosis techniques for brushless permanent magnet machines," in *2011 IEEE Vehicle Power and Propulsion Conference*. IEEE, 9/2011, pp. 1–7.

[13] S. Nandi, H. Toliyat, and X. Li, "Condition monitoring and fault diagnosis of electrical motors-a review," *IEEE transactions on energy conversion*, vol. 20, no. 4, pp. 719–729, 12/2005.

[14] X. Dai and Z. Gao, "From model, signal to knowledge: A data-driven perspective of fault detection and diagnosis," *IEEE Transactions on Industrial Informatics*, vol. 9, no. 4, pp. 2226–2238, 11/2013.

[15] P. Tavner, L. Ran, J. Penman, and H. Sedding, *Condition monitoring of rotating electrical machines*. IET, 2008, vol. 56.

[16] Y. Qi, E. Bostanci, V. Gurusamy, and B. Akin, "A comprehensive analysis of short-circuit current behavior in pmsm interturn short-circuit faults," *IEEE Transactions on Power Electronics*, vol. 33, no. 12, pp. 10 784–10 793, 2018.

[17] M. Zhu, W. Hu, and N. C. Kar, "Torque-ripple-based interior permanent-magnet synchronous machine rotor demagnetization fault detection and current regulation," *IEEE Transactions on Industry Applications*, vol. 53, no. 3, pp. 2795–2804, 5/2017.

[18] Z. Gao, C. Cecati, and S. X. Ding, "A survey of fault diagnosis and fault-tolerant techniques-part i: Fault diagnosis with model-based and signal-based approaches," *IEEE Transactions on Industrial Electronics*, vol. 62, no. 6, pp. 3757–3767, 2015.

[19] J. Faiz and E. Mazaheri-Tehrani, "Demagnetization modeling and fault diagnosing techniques in permanent magnet machines under stationary and nonstationary conditions: An overview," *IEEE Transactions on Industry Applications*, vol. 53, no. 3, pp. 2772–2785, 5/2017.

[20] A. Gandhi, T. Corrigan, and L. Parsa, "Recent advances in modeling and online detection of stator interturn faults in electrical motors," *IEEE Transactions on Industrial Electronics*, vol. 58, no. 5, pp. 1564–1575, 2010.

[21] C. Ruschetti, C. Verucchi, G. Bossio, C. De Angelo, and G. Garca, "Rotor demagnetization effects on permanent magnet synchronous machines," *Energy Conversion and Management*, vol. 74, pp. 1–8, 10/2013.

[22] T. Ishikawa, Y. Seki, and N. Kurita, "Analysis for fault detection of vector-controlled permanent magnet synchronous motor with permanent magnet defect," *IEEE Transactions on Magnetics*, vol. 49, no. 5, pp. 2331–2334, 5/2013.

[23] Z. Gherabi, N. Benouzza, D. Toumi, and A. Bendiabdellah, "Eccentricity fault diagnosis in pmsm using motor current signature analysis," in *2019 International Aegean Conference on Electrical Machines and Power Electronics (ACEMP) and 2019 International Conference on Optimization of Electrical and Electronic Equipment (OPTIM)*. IEEE, 8/2019, pp. 205–210.

[24] B. M. Ebrahimi and J. Faiz, "Configuration impacts on eccentricity fault detection in permanent magnet synchronous motors," *IEEE Transactions on Magnetics*, vol. 48, no. 2, pp. 903–906, 2012.

[25] B. Ebrahimi, J. Faiz, and B. Araabi, "Pattern identification for eccentricity fault diagnosis in permanent magnet synchronous motors using stator current monitoring," *IET electric power applications*, vol. 4, no. 6, pp. 418–430, 2010.

[26] B. Ebrahimi and J. Faiz, "Diagnosis and performance analysis of three-phase permanent magnet synchronous motors with static, dynamic and mixed eccentricity," *IET electric power applications*, vol. 4, no. 1, pp. 53–66, 2010.

[27] S. M. Cruz and A. M. Cardoso, "Stator winding fault diagnosis in three-phase synchronous and asynchronous motors, by the extended park's vector approach," *IEEE Transactions on industry applications*, vol. 37, no. 5, pp. 1227–1233, 2001.

[28] D. Albright, "Interturn short-circuit detector for turbine-generator rotor windings," *IEEE transactions on power apparatus and systems*, no. 2, pp. 478–483, 1971.

[29] J. Hang, S. Ding, J. Zhang, M. Cheng, W. Chen, and Q. Wang, "Detection of interturn short-circuit fault for pmsm with simple fault indicator," *IEEE Transactions on Energy Conversion*, vol. 31, no. 4, pp. 1697–1699, 2016.

[30] H. Liang, Y. Chen, S. Liang, and C. Wang, "Fault detection of stator inter-turn short-circuit in pmsm on stator current and vibration signal," *Applied Sciences*, vol. 8, no. 9, p. 1677, 2018.

[31] J.-C. Urresty, J.-R. Riba, M. Delgado, and L. Romeral, "Detection of demagnetization faults in surface-mounted permanent magnet synchronous motors by means of the zero-sequence voltage component," *IEEE Transactions on Energy Conversion*, vol. 27, no. 1, pp. 42–51, 3/2012.

[32] J.-C. Urresty, J.-R. Riba, and L. Romeral, "A back-emf based method to detect magnet failures in pmsms," *IEEE Transactions on Magnetics*, vol. 49, no. 1, pp. 591–598, 1/2013.

[33] R. Z. Haddad, C. A. Lopez, S. N. Foster, and E. G. Strangas, "A voltage-based approach for fault detection and separation in permanent magnet synchronous machines," *IEEE Transactions on Industry Applications*, vol. 53, no. 6, pp. 5305–5314, 2017.

[34] Z. Ullah, S.-T. Lee, and J. Hur, "A novel fault diagnosis technique for ipmsm using voltage angle," in *2018 IEEE Energy Conversion Congress and Exposition (ECCE)*. IEEE, 2018, pp. 3236–3243.

[35] Y. Da, X. Shi, and M. Krishnamurthy, "A new approach to fault diagnostics for permanent magnet synchronous machines using electromagnetic signature analysis," *IEEE Transactions on Power Electronics*, vol. 28, no. 8, pp. 4104–4112, 8/2013.

[36] Y. Park, D. Fernandez, S. B. Lee, D. Hyun, M. Jeong, S. Kumar Kommuri, C. Cho, D. Reigosa, and F. Briz, "On-line detection of rotor eccentricity for pmsms based on hall-effect field sensor measurements," in *2017 IEEE Energy Conversion Congress and Exposition (ECCE)*, vol. 2017. IEEE, 10/2017, pp. 4678–4685.

[37] F. Çıra, "Detection of eccentricity fault based on vibration in the pmsm," *Results in physics*, vol. 10, pp. 760–765, 9/2018.

[38] B. Ebrahimi and J. Faiz, "Magnetic field and vibration monitoring in permanent magnet synchronous motors under eccentricity fault," *IET electric power applications*, vol. 6, no. 1, pp. 35–45, 2012.

[39] J. Hong, S. B. Lee, C. Kral, and A. Haumer, "Detection of airgap eccentricity for permanent magnet synchronous motors based on the d-axis inductance," *IEEE Transactions on Power Electronics*, vol. 27, no. 5, pp. 2605–2612, 2011.

[40] Z. Liu, J. Huang, and B. Li, "Diagnosing and distinguishing rotor eccentricity from partial demagnetisation of interior pmsm based on fluctuation of high-frequency d-axis inductance and rotor flux," *IET Electric Power Applications*, vol. 11, no. 7, pp. 1265–1275, 2017.

[41] S. Moon, J. Lee, H. Jeong, and S. W. Kim, "Demagnetization fault diagnosis of a pmsm based on structure analysis of motor inductance," *IEEE transactions on industrial electronics (1982)*, vol. 63, no. 6, pp. 3795–3803, 6/2016.

[42] J. Lee, Y.-J. Jeon, D.-c. Choi, S. Kim, and S. W. Kim, "Demagnetization fault diagnosis method for pmsm of electric vehicle," in *IECON 2013-39th Annual Conference of the IEEE Industrial Electronics Society*. IEEE, 2013, pp. 2709–2713.

[43] W. le Roux, R. Harley, and T. Habetler, "Detecting rotor faults in low power permanent magnet synchronous machines," *IEEE Transactions on Power Electronics*, vol. 22, no. 1, pp. 322–328, 1/2007.

[44] K. Liu, Z. Q. Zhu, and D. A. Stone, "Parameter estimation for condition monitoring of pmsm stator winding and rotor permanent magnets," *IEEE Transactions on Industrial Electronics*, vol. 60, no. 12, pp. 5902–5913, 12/2013.

[45] K. Liu and Z. Q. Zhu, "Position-offset-based parameter estimation using the adaline nn for condition monitoring of permanent-magnet synchronous machines," *IEEE Transactions on Industrial Electronics*, vol. 62, no. 4, pp. 2372–2383, 4/2015.

[46] G. Feng, C. Lai, K. Mukherjee, and N. C. Kar, "Online pmsm magnet flux-linkage estimation for rotor magnet condition monitoring using measured speed harmonics," *IEEE Transactions on Industry Applications*, vol. 53, no. 3, pp. 2786–2794, 5/2017.

[47] M. A. Mazzoletti, G. R. Bossio, C. H. De Angelo, and D. R. Espinoza-Trejo, "A model-based strategy for interturn short-circuit fault diagnosis in pmsm," *IEEE Transactions on Industrial Electronics*, vol. 64, no. 9, pp. 7218–7228, 2017.

[48] B.-G. Gu, "Study of ipmsm interturn faults part ii: Online fault parameter estimation," *IEEE Transactions on Power Electronics*, vol. 31, no. 10, pp. 7214–7223, 2015.

[49] S. Underwood and I. Husain, "Online parameter estimation and adaptive control of permanent-magnet synchronous machines," *IEEE Transactions on Industrial Electronics*, vol. 57, no. 7, pp. 2435 – 2443, July 2010.

[50] D. M. Reed, J. Sun, and H. F. Hofmann, "Simultaneous identification and adaptive torque control of permanent magnet synchronous machines," *IEEE Transactions on Control Systems Technology*, vol. 25, no. 4, pp. 1372–1383, 2017.

[51] D. M. Reed, J. Sun, and H. F. Hofmann, "A robust adaptive controller for surface-mount permanent magnet synchronous machines," in *2014 American Control Conference*, June 2014, pp. 5236–5241.

[52] D. M. Reed, J. Sun, and H. F. Hofmann, "A receding horizon approach to simultaneous identification and torque control of permanent magnet synchronous machines," in *American Control Conference (ACC)*, July 2016, pp. 2211–2216.

[53] D. M. Reed, "Identification and adaptive control for high-performance ac drive systems," Ph.D. dissertation, University of Michigan, 2016.

[54] S. Ruoho, J. Kolehmainen, J. Ikaheimo, and A. Arkkio, "Interdependence of demagnetization, loading, and temperature rise in a permanent-magnet synchronous motor," *IEEE Transactions on Magnetics*, vol. 46, no. 3, pp. 949–953, 3/2010.

[55] H. He, N. Zhou, and C. Sun, "Efficiency decrease estimation of a permanent magnet synchronous machine with demagnetization faults," *Energy Procedia*, vol. 105, pp. 2718–2724, 5/2017.

[56] R. Krishnan, *Permanent Magnet Synchronous and Brushless DC Motor Drives*. CRC Press, 19/12/2017.

[57] S. Hamidizadeh, N. Alatawneh, R. R. Chromik, and D. A. Lowther, "Comparison of different demagnetization models of permanent magnet in machines for electric vehicle application," *IEEE Transactions on Magnetics*, vol. 52, no. 5, pp. 1–4, 2016.

[58] P. Zhou, D. Lin, Y. Xiao, N. Lambert, and M. A. Rahman, "Temperature-dependent demagnetization model of permanent magnets for finite element analysis," *IEEE Transactions on Magnetics*, vol. 48, no. 2, pp. 1031–1034, 2/2012.

[59] S. Sharouni, P. Naderi, M. Hedayati, and P. Hajihosseini, "Demagnetization fault detection by a novel and flexible modeling method for outer rotor permanent magnet synchronous machine," *International Journal of Electrical Power and Energy Systems*, vol. 116, p. 105539, 3/2020.

[60] M. Zafarani, T. Goktas, B. Akin, and S. E. Fedigan, "An investigation of motor topology impacts on magnet defect fault signatures," *IEEE Transactions on Industrial Electronics*, vol. 64, no. 1, pp. 32–42, 1/2017.

[61] E. Mazaheri-Tehrani, J. Faiz, M. Zafarani, and B. Akin, "A fast phase variable abc model of brushless pm motors under demagnetization faults," *IEEE Transactions on Industrial Electronics*, vol. 66, no. 7, pp. 5070–5080, 7/2019.

[62] C. R. Ruschetti, C. J. Verucchi, G. R. Bossio, and G. O. Garcia, "A model for permanent magnet synchronous machines with demagnetization faults," *IEEE Latin America Transactions*, vol. 11, no. 1, pp. 414–420, 2/2013.

[63] J. Farooq, A. Djerdir, and A. Miraoui, "Analytical modeling approach to detect magnet defects in permanent-magnet brushless motors," *IEEE Transactions on Magnetics*, vol. 44, no. 12, pp. 4599–4604, 12/2008.

[64] M. Zafarani, T. Goktas, B. Akin, and S. E. Fedigan, "Modeling and dynamic behavior analysis of magnet defect signatures in permanent magnet synchronous motors," *IEEE Transactions on Industry Applications*, vol. 52, no. 5, pp. 3753–3762, 9/2016.

[65] S. Moosavi, A. Djerdir, Y. Amirat, and D. Khaburi, "Demagnetization fault diagnosis in permanent magnet synchronous motors: A review of the state-of-the-art," *Journal of Magnetism and Magnetic Materials*, vol. 391, pp. 203–212, 1/10/2015.

[66] J.-R. Ruiz, J. Rosero, A. Espinosa, and L. Romeral, "Detection of demagnetization faults in permanent-magnet synchronous motors under nonstationary conditions," *IEEE Transactions on Magnetics*, vol. 45, no. 7, pp. 2961–2969, 7/2009.

[67] D. Torregrossa, A. Khoobroo, and B. Fahimi, "Prediction of acoustic noise and torque pulsation in pm synchronous machines with static eccentricity and partial demagnetization using field reconstruction method," *IEEE Transactions on Industrial Electronics*, vol. 59, no. 2, pp. 934–944, 2/2012.

[68] M. Zhang, A. Macdonald, K.-J. Tseng, and G. M. Burt, "Magnetic equivalent circuit modeling for interior permanent magnet synchronous machine under eccentricity fault," in *2013 48th International Universities' Power Engineering Conference (UPEC)*. IEEE, 2013, pp. 1–6.

[69] I. Hussein, Z. Al-Hamouz, M. Abido, and A. Milhem, "On the mathematical modeling of line-start permanent magnet synchronous motors under static eccentricity," *Energies*, vol. 11, no. 1, p. 197, 2018.

[70] J.-P. Wang and D. K. Lieu, "Magnetic lumped parameter modeling of rotor eccentricity in brushless permanent-magnet motors," *IEEE transactions on magnetics*, vol. 35, no. 5, pp. 4226–4231, 1999.

[71] I. Jeong, B. J. Hyon, and K. Nam, "Dynamic modeling and control for spmsms with internal turn short fault," *IEEE Transactions on Power Electronics*, vol. 28, no. 7, pp. 3495–3508, 2012.

[72] B. Vaseghi, N. Takorabet, F. Meibody-Tabar, A. Djerdir, J. Farooq, and A. Miraoui, "Modeling and characterizing the inter-turn short circuit fault in pmsm," in *2011 IEEE International Electric Machines & Drives Conference (IEMDC)*. IEEE, 2011, pp. 551–556.

[73] L. Romeral, J. C. Urresty, J.-R. R. Ruiz, and A. G. Espinosa, "Modeling of surface-mounted permanent magnet synchronous motors with stator winding interturn faults," *IEEE Transactions on Industrial Electronics*, vol. 58, no. 5, pp. 1576–1585, 2010.

[74] M. Fitouri, Y. Bensalem, and M. N. Abdelkrim, "Modeling and detection of the short-circuit fault in pmsm using finite element analysis," *IFAC-PapersOnLine*, vol. 49, no. 12, pp. 1418–1423, 2016.

[75] J. Faiz, A. Exiri, and H. Nejadi-Koti, "Simulation of permanent magnet synchronous motors under short circuit fault," in *2016 18th Mediterranean Electrotechnical Conference (MELECON)*. IEEE, 2016, pp. 1–6.

[76] B.-G. Gu, "Study of ipmsm interturn faults part i: Development and analysis of models with series and parallel winding connections," *IEEE Transactions on Power Electronics*, vol. 31, no. 8, pp. 5931–5943, 2015.

[77] J. Faiz, H. Nejadi-Koti, and Z. Valipour, "Comprehensive review on inter-turn fault indexes in permanent magnet motors," *IET Electric Power Applications*, vol. 11, no. 1, pp. 142–156, 2017.

[78] M. Lovera, *Control-oriented modelling and identification: theory and practice*. IET, 2015, vol. 80.

[79] F. Pinto Delgado, Z. Song, H. F. Hofmann, and J. Sun, "Modeling and parameter identification for condition monitoring of surface-mount permanent magnet machines under magnet demagnetization," in *Dynamic Systems and Control Conference*, vol. 84270. American Society of Mechanical Engineers, 2020, p. V001T21A002.

[80] F. A. Pinto Delgado, D. M. Reed, H. F. Hofmann, and J. Sun, "Simultaneous identification and torque control of surface-mount permanent magnet synchronous machines with inverter current and voltage constraints," in *2018 IEEE Conference on Control Technology and Applications (CCTA)*. IEEE, 8/2018, pp. 1185–1190.

[81] W. C. Duesterhoeft, M. W. Schulz, and E. Clarke, "Determination of instantaneous currents and voltages by means of alpha, beta, and zero components," *Transactions of the American Institute of Electrical Engineers*, vol. 70, pp. 1248–1255, 1951.

[82] R. H. Park, "Two-reaction theory of synchronous machines generalized method of analysis-part i," *Transactions of the American Institute of Electrical Engineers*, vol. 48, no. 3, pp. 716–727, 7/1929.

[83] B. Bose, *Modern Power Electronics and AC Drives*. New Jersey: Prentice Hall PTR, New Jersey, 2002.

[84] P. Ioannou and J. Sun, *Robust Adaptive Control*. New Jersey: Prentice Hall, 1996.

[85] G. Tao, *Adaptive control design and analysis*. John Wiley & Sons, 2003, vol. 37.

[86] C. L. Phillips, H. T. Nagle, and A. Chakrabortty, *Digital control system analysis and design, (Global Edition)*. Pearson Education Limited, 2015.

[87] I. Kolmanovsky and D. P. Filev, *Optimal Finite and Receding Horizon Control for Identification in Automotive Systems*. London: Springer London, 2012, pp. 327–348.

[88] G. Marafioti, R. Bitmead, and M. Hovd, "Persistently exciting model predictive control using fir models," in *International Conference Cybernetics and Informatics*, 2010.

[89] H. Genceli and M. Nikolaou, "New approach to constrained predictive control with simultaneous model identification," *AIChE Journal*, vol. 42, no. 10, pp. 2857–2868, 1996.

[90] A. Weiss and S. D. Cairano, "Robust dual control mpc with guaranteed constraint satisfaction," in *53rd IEEE Conference on Decision and Control*, Dec 2014, pp. 6713–6718.

[91] F. Leve and M. Jah, "Spacecraft actuator alignment determination through null motion excitation," in *Proceedings of 62nd International Astronautical Congress*, 2011.

[92] A. Weiss, F. Leve, I. Kolmanovsky, and M. Jah, "Reaction wheel parameter identification and control through receding horizon-based null motion excitation," in *Bar-Itzhack Memorial Symposium*, October 2012.

[93] G. Goodwin and K. Sin, *Adaptive Filtering Prediction and Control*, ser. Dover Books on Electrical Engineering. Dover Publications, 2014.

[94] S. Silvey, *Optimal Design*, 1st ed. New York: Springer Netherlands, 1980.

[95] I. R. Manchester, "Input design for system identification via convex relaxation," in *49th IEEE Conference on Decision and Control (CDC)*. IEEE, 2010, pp. 2041–2046.

[96] H. A. Toliyat, S. Choi, H. Meshgin-Kelk, and S. Nandi, *Electric machines: modeling, condition monitoring, and fault diagnosis*. CRC Press, 10/10/2012.

[97] S. Nandi, R. Bharadwaj, and H. Toliyat, "Mixed eccentricity in three phase induction machines: analysis, simulation and experiments," in *Conference Record of the 2002 IEEE Industry Applications Conference. 37th IAS Annual Meeting (Cat. No.02CH37344)*, vol. 3. IEEE, 2002, p. 1525?1532 vol.3.

[98] S. Saied, K. Abbaszadeh, and A. Tenconi, "Improvement to winding function theory for pm machine analysis," in *2011 International Conference on Power Engineering, Energy and Electrical Drives*. IEEE, 5/2011, pp. 1–6.

[99] T. A. Lipo, *Introduction to AC machine design*. John Wiley & Sons, 2017.

[100] T. Lipo, *Analysis of Synchronous Machines*. CRC Press, 19/12/2017.

[101] F. Lin, S. Zuo, and W. Deng, "Impact of rotor eccentricity on electromagnetic vibration and noise of permanent magnet synchronous motor," *Journal of Vibroengineering*, vol. 20, no. 2, pp. 923–935, 2018.

[102] W. Tong, S. Li, X. Pan, S. Wu, and R. Tang, "Analytical model for cogging torque calculation in surface-mounted permanent magnet motors with rotor eccentricity and magnet defects," *IEEE Transactions on Energy Conversion*, vol. 35, no. 4, pp. 2191–2200, 2020.

[103] C. Schumann, T. Müller, E. Stein, and M. Pacas, "Analytical calculation of the induced emf in pm-machines with arbitrary arranged surface mounted magnets using the winding function theory," in *2014 International Conference on Electrical Machines (ICEM)*. IEEE, 2014, pp. 994–1000.

[104] H. Mahmoud and N. Bianchi, "Analytical comparison of synchronous reluctance and surface permanent magnet machines with rotor eccentricity," in *2015 IEEE Energy Conversion Congress and Exposition (ECCE)*. IEEE, 2015, pp. 1765–1772.

[105] O.-S. Yang and A. Widodo, *Introduction of intelligent machine fault diagnosis and prognosis*. Nova Science Publishers, Incorporated, 2010.